Die approbierte Originalversion dieser Dissertation ist in der Hauptbibliothek der Technischen Universität Wien aufgestellt und zugänglich.
http://www.ub.tuwien.ac.at

The approved original version of this thesis is available at the main library of the Vienna University of Technology.
http://www.ub.tuwien.ac.at/eng

TECHNISCHE UNIVERSITÄT WIEN

Dissertation

Development of a Geant4 Based Electromagnetic Background Model for the CRESST Experiment

ausgeführt zum Zwecke der Erlangung des akademischen Grades eines Doktors der technischen Wissenschaften unter der Leitung von

Univ.Prof. Dipl.-Phys. Dr.rer.nat. Jochen Schieck

und

Univ.Ass. Dipl.-Phys. Dr.rer.nat. Holger Kluck

am Institut für Hochenergiephysik (HEPHY)
der Österreichischen Akademie der Wissenschaften (ÖAW)
und am Atominstitut (E141)

eingereicht an der
Technischen Universität Wien
Fakultät für Physik

von

Cenk Türkoğlu, M.Sc.
Matrikelnummer: 1529732

Wien, im Juli 2018

Swan song, a declaration of endlessness
I swear I will not look back as I return into the black
When the veil lifts, how will I know, how will I know?
Will I see God?

- Architects, *Memento Mori*

Contents

Abstract **23**

1. Introduction **25**

2. Dark Matter **27**
2.1. Observational Evidence for the Existence of Dark Matter 27
2.2. Alternatives to Dark Matter 30
2.3. Dark Matter Particle Candidates 31
2.4. Search Strategies for Dark Matter 34
2.4.1. Dark Matter Production 34
2.4.2. Indirect Search 35
2.4.3. Direct Search 35
2.5. Details on Direct Searches for Dark Matter 36
2.5.1. Nuclear Recoils 36
2.5.2. Detection Techniques 39
2.5.3. Current Status 40

3. The CRESST Experiment **43**
3.1. The Experimental Setup of CRESST 43
3.2. Detector Design 45
3.3. Low-Threshold Cryogenic Detectors 49
3.4. Event Categories 52
3.5. Background Sources and Their Management 53
3.5.1. Muons 53
3.5.2. Ambient Gamma Radiation 54
3.5.3. Cosmogenic Activation 54
3.5.4. Ambient Neutrons 55
3.5.5. Radon Gas 56
3.5.6. Near-Surface Alpha-Decays 56
3.5.7. Internal Contamination of $CaWO_4$ 57
3.6. Previous Work on Background Sources in CRESST 60
3.7. Reference Data 61
3.7.1. Low Energy Reference Data 62
3.7.2. Medium Energy Reference Data 63
3.7.3. High Energy Reference Data 65

4. Radioactive Background Simulations **69**
4.1. Simulation of Electromagnetic Interactions in $CaWO_4$ . . . 69
4.1.1. Geant4 Framework . . . 69
4.1.2. Particle Interactions by Nuclear Reactions . . . 71
4.1.3. Energy Deposition via Electromagnetic Interactions . . . 73
4.2. Geometry Model . . . 75
4.3. Detector Response Model . . . 76
4.3.1. Energy Resolution . . . 76
4.3.2. Time Resolution . . . 80
4.4. Simulation of Spectral Templates . . . 81
4.4.1. Internal Radiogenic Backgrounds . . . 82
4.4.2. Internal Cosmogenic Backgrounds . . . 84
4.4.3. External Near Radiogenic Backgrounds . . . 86
4.4.4. External Distant Radiogenic Backgrounds . . . 90

5. Electromagnetic Background Spectra **95**
5.1. Internal Radiogenic Backgrounds . . . 95
5.1.1. Normalisation via Sideband Measurements . . . 95
5.1.2. Determination of Alpha Activities . . . 97
5.1.3. Scaling of β/γ Templates . . . 102
5.2. Internal Cosmogenic Backgrounds . . . 104
5.2.1. Determination of ^{181}W Activity . . . 104
5.2.2. Determination of ^{3}H Activity . . . 105
5.2.3. Determination of ^{179}Ta Activity . . . 106
5.3. External Near Radiogenic Backgrounds . . . 106
5.3.1. Calculation of Activities . . . 106
5.3.2. Scaling of β/γ Templates . . . 108
5.4. External Distant Radiogenic Backgrounds . . . 108
5.4.1. Determination of Gamma Activities . . . 109
5.4.2. Scaling of β/γ Templates . . . 110

6. Results and Discussion **117**
6.1. Reproduction of the Observed Background . . . 117
6.2. The Composition of the Background . . . 120
6.3. Comparison with the Previous Work . . . 121
6.4. Comparison with Another Experiment . . . 121

7. Future Works **133**
7.1. Improvements for Future Simulations . . . 133
7.1.1. Full Experimental Setup . . . 133
7.1.2. Neutron Simulation . . . 134
7.1.3. Copper Screenings . . . 134
7.1.4. A More Detailed Study of Cosmogenic Activation . . . 134
7.1.5. Improved Detector Response Model . . . 135

7.1.6. Free-Floating Template Fit . . . 135
7.2. Impacts on the CRESST Experiment . . . 137
7.2.1. Likelihood-Based Dark Matter Analysis . . . 137
7.2.2. Detector Development . . . 137

8. Conclusion **141**

Acknowledgements **145**

A. Appendices **147**
A.1. Abbreviations . . . 147
A.2. Simulated Templates of Internal Radiogenic Backgrounds . . . 148
A.2.1. Templates of Alpha Decays . . . 148
A.2.2. Templates of Beta-/Gamma-Decays . . . 157
A.3. Simulated Templates of Internal Cosmogenic Backgrounds . . . 173
A.4. Simulated Templates of Near External Radiogenic Backgrounds . . . 176
A.5. Simulated Templates of Distant External Radiogenic Backgrounds . . . 191
A.6. Comparison of Observed Peak Positions with Literature . . . 196
A.7. Composition of the Background Sources . . . 198
A.8. Natural Decay Chains . . . 208

List of Figures

2.1. Rotation curve of the galaxy NGC 6503: orbital velocity as a function of the orbit's radius. Figure taken from [57]. 28

2.2. Upper panel: CMB power as function of the multipole moment l (blue data points) obtained by the Planck Space Telescope shown in angular scale and compared with a fit based on the standard cosmological model (red line). Lower panel: the residuals between data and fit. Figure taken from [6]. . . . 29

2.3. The X-ray image of the Bullet Cluster was taken by Chandra X-ray Observatory and shows the distribution of the hot intergalactic medium. The green contours show the total mass density deduced from the gravitational lensing. Figure taken from [50]. 31

2.4. Dark matter-nucleon cross-sections σ_{int} vs dark matter particle mass $\mathrm{m_{DM}}$. The colour indicates the temperature of the candidates at production in the early Universe: red, pink and blue represent hot, warm and cold dark matter, respectively. Neutralinos are highlighted in green. Figure taken from [36]. 32

2.5. A simplified Feynman diagram illustrating different approaches to detect dark matter χ. If the time flows to the right side (blue), two dark matter particles annihilate into SM particles. If the time flows to the left (green), a pair of dark matter is produced from the annihilation of SM particles. If the time flows up (purple), dark matter particle scatters off a nucleus. Figure adapted from [108]. 34

2.6. Event rate R drawn with respect to the recoil energy E_{R} for various WIMP masses m_χ for targets Ge and Xe. A nucleon-WIMP cross-section of $\sigma_{\chi \mathrm{n}} = 10^{-8}$ pb is assumed. Figure adapted from [43]. 37

2.7. Different dark matter direct detection mechanisms: while some experiments use only one signal channel, others use a combination of two different signal channels to reject backgrounds. Figure taken from [84]. 39

2.8. Current upper limits on dark matter particle-nucleon cross-sections with respect to the dark matter particle mass for spin-independent elastic scattering. Results from different stages of various experiments are shown: CRESST-III 2017 (prelim) [95], CRESST-II 2016 [25], CRESST-II 2014 [26], CDEX 2014 [111], CDMSlite 2015 [9], SuperCDMS 2014 [11], DAMIC 2016 [13], EDELWEISS-III 2016 [32], DarkSide-50 2015 [7], DarkSide 2018 - binom. (tbp) [8], LUX 2016 combined [14], NEWS-G 2018 [33], PandaX-II 2016 [107], XENON1T 2018 (tbp) [28], XENON100 Low-Mass 2016 [30], PICO-60 C_3F_8 2016 [21]. Also shown are the DM interpretations of the signal excess observed with CDMS-Si 2013 [10], and CoGeNT 2013 [1]. The bottom left shows the region for coherent neutrino scattering on $CaWO_4$ [67]. 41

3.1. Technical drawing of the CRESST experimental setup [76]. The cryostat holding the liquid helium and liquid nitrogen can bee seen at the top. Below the cryostat, the carousel holds the detector modules. The shielding consists of polyethylene, lead, an active muon veto and the air-tight radon box used against radon contamination from air. 46

3.2. Schematics of some detector modules operated in the CRESST experiment: The *Lise* (a) and *TUM40* (b) modules were operated in CRESST-II Phase 2, whereas *Detector A* (c) was operated in CRESST-III Phase 1. Figures provided by CRESST. 47

3.3. The scaling law (eq. (3.2)) of the theoretical achievable energy threshold as function of the target mass for Al_2O_3 (blue dashed line) and $CaWO_4$ (green dashed line) targets fitted to data obtained with cryogenic Al_2O_3 (triangles) and $CaWO_4$ (cross) detectors [25, 26, 86]. $M^{\frac{2}{3}}$ behaviour can be observed for most data points, except "this work" [106], which was obtained in a non-optimized environment. Red stars show the expected values for the prototype described in [106] under low-background conditions. Figure taken from [106]. 50

3.4. The plane of dark matter particle-nucleon cross-section as a function of the dark matter particle mass for spin-independent scattering with focus on the low-mass range below 20 $\mathrm{GeV/c^2}$. CRESST-III 2017 (prelim) [95], CRESST-II 2016 [25], CRESST-II 2014 [26], CDEX 2014 [111], CDMSlite 2015 [9], SuperCDMS 2014 [11], DAMIC 2016 [13], EDELWEISS-III 2016 [32], DarkSide-50 2015 [7], DarkSide 2018 - binom. (tbp) [8], LUX 2016 combined [14], NEWS-G 2018 [33], PandaX-II 2016 [107], XENON100 Low-Mass 2016 [30], PICO-60 C_3F_8 2016 [21]. Also shown are the DM interpretations of the signal excess observed with CDMS-Si 2013 [10], and CoGeNT 2013 [1]. 51

3.5. An example light yield plot with different bands showing different event types: electromagnetic interactions (grey) alpha interactions (red), oxygen (green) and tungsten (blue) recoils. The calcium recoil band between these two is not shown for the purposes of clarity. Also shown is the region of interest (ROI, cyan) for a possible signal of dark matter particle. 52

3.6. An illustration of a $^{210}Po \longrightarrow {}^{206}Pb + \alpha$ decay taking place close to the surface of the target crystal or in the surrounding material (a) and the change in the resulting light yield value when a scintillating housing is used (b). Figures taken from [104]. 58
3.7. Count rate spectra for detector modules with commercial $CaWO_4$ crystals and those grown at *Technische Universität München*: *VK31* is a typical commercial crystal with an average rate of 30 counts/(kg · keV · day) (dashed black line). With an average 6 counts/(kg · keV · day) *Daisy* is the commerical crystal with the lowest background rate (dashed red line). The black histogram shows the events recorded with *TUM40* with an average rate of 3.51 counts/(kg · keV · day) [105]. Most prominent peaks are labelled. Figure taken from [105]. 59
3.8. Comparison of the semi-empirical background analysis [105] with data (black) recorded with TUM40: internal beta/gamma radiation from natural radioactive decay chains (blue) the contributions from the external gamma rays (green), both based on a Geant4 simulation. The grey band shows an empirical fit which stands for external betas. Finally, the red line shows the sum of these individual contributions as well as fits to the observed peaks caused by cosmogenic activation (2.6009 keV, 10.74 keV and 11.271 keV) and the copper fluorescence line (8.04 keV). Figure taken from [105]. 60
3.9. Top panel: the rescaling function obtained from the fitted values of the peaks of the low energy reference data set. Bottom panel: relative residual between fit values and literature. 63
3.10. The signal survival probability (a) related to the low energy reference data set: below an energy of 92.36 keV, a varying signal survival probability is used whereas above this energy, the signal survival probability is set to the constant value of 85.0 %. The corresponding energy spectrum (b) between 0.6 keV and 495 keV, after the rescaling in section 3.7.1 was applied. Data provided by [97, 98]. 64
3.11. Top panel: the rescaling function obtained from the fitted values of the peaks of the medium energy reference data set. Bottom panel: relative residual between fit values and literature. 65
3.12. Energy spectrum of the medium energy reference data set between 510 keV and 4000 keV, after the rescaling in section 3.7.2 was applied. Data provided by [90]. 66
3.13. Energy spectrum of the high energy reference data set between 4000 keV and 7000 keV, without any rescaling applied. Data provided by [37]. 67

4.1. Nuclear, electronic and total stopping power of $CaWO_4$ with respect to the energy of a ^4_2He nucleus. Figure provided by [77] based on [113] 71
4.2. Total stopping power of $CaWO_4$ with respect to the energy of beta particles. Figure taken from [40, 92]. 72
4.3. Total attenuation of gamma rays inside the $CaWO_4$ with respect to the energy of gammas. Figure taken from [92]. 73

4.4. Photo of TUM40 detector module. Figure provided by the CRESST collaboration [52]. 75

4.5. Visualisation of the TUM40 detector module as implemented in Geant4: cut-away views parallel to the X-Z plane fig. 4.5a and parallel to the X-Y plane fig. 4.5b. Main components are the $CaWO_4$ target crystal (purple box), Cu holders (brown/orange) and the BC408 plastic ring (red). For the sake of visibility, the implemented scintillating foil is not visualised. 77

4.6. Energy resolution function (red) for the low energy reference data used in the detector response model. The function is retrieved by parametrizing the variance values of Gaussian fits to known peaks. 78

4.7. Energy resolution function (red) for the medium energy reference data used in the detector response model. The function is retrieved by parametrizing the variance values of Gaussian fits to known peaks. 79

4.8. Energy resolution function (red) for the high energy reference data used in the detector response model. The function is retrieved by parametrizing the variance values of Gaussian fits to known peaks. 79

4.9. Simulated energy depositions of ^{223}Ra bulk contamination inside the $CaWO_4$ crystal with (purple, left scale) and without (red, right scale) applied detector response model. 80

4.10. Simulated template of ^{234}Th decaying inside the $CaWO_4$ crystal without applied detector response model. It shows several spectral features such as beta-spectra, gamma-lines and a pile-up of both. For a detailed description, see section 4.4.1. 83

4.11. Simulated distribution of N=$5 \cdot 10^5$ EC decays of ^{179}Ta in the E_{kin} vs E_{dep} plane, where E_{kin} is the kinetic energy of the recoiling daughter nucleus ^{179}Hf and E_{dep} is the deposited energy. Clearly visible are distinct band corresponding to EC from the K-, L- and M- shells. 84

4.12. Simulated energy deposition in $CaWO_4$ caused by EC of ^{179}Ta separated according to the involved atomic shells. The inset shows a zoom to the EC-peaks for the M- and L-shells. 85

4.13. Simulated energy deposition in $CaWO_4$ for an internal decay of ^{234}Th (red), i.e. placed inside the $CaWO_4$ crystal, and an external decay of ^{234}Th (purple), i.e. placed inside a spherical Cu shell around the crystal. In the external case, betas emitted via $^{234}\text{Th} \rightarrow {}^{234\text{m}}\text{Pa}$, $^{234\text{m}}\text{Pa} \rightarrow {}^{234}\text{U}$ (BR = 99.84 %), and $^{234}\text{Pa} \rightarrow {}^{234}\text{U}$ are strongly attenuated. On the contrary, a gamma emission from ^{234}Th is visible in both cases. 86

4.14. Visualisation of gamma rays (green) are started on a sphere around (a) the bare, cuboid $CaWO_4$ crystal and (b) TUM40 detector module, and sent inwards. The red points show the energy depositions caused by hits of the gamma rays. 89

4.15. Simulated energy deposition in $CaWO_4$ caused by 2614.0 keV gamma rays from ^{208}Tl for a bare $CaWO_4$ crystal (red) and a $CaWO_4$ crystal inside the TUM40 detector module (black). Both data sets were normalized to the integrals of the photopeaks. The inset shows a zoom to the Cu fluorescence line at 8.04 keV. 89

4.16. Simulated energy depositions in the $CaWO_4$ crystal caused by ^{234}Th decays in different parts of the crystal holder made out of Cu. Each individual histogram is normalised to the number of decays. 90

4.17. A visualisation of the spherical shell made out of copper around the TUM40 detector module. 91

4.18. Energy deposition inside the $CaWO_4$ crystal caused by ^{234}Th inside one of the copper holder parts (black) and in the copper spherical shell around the TUM40 detector module (red). 92

4.19. Attenuation of gamma rays in Cu. 92

4.20. Simulated decay of ^{234}Th inside the copper sphere without applied detector response model. 93

5.1. Alpha lines in the energy range between 4 and 7 MeV from the TUM40 training data-set. Figure taken from [105]. 97

5.2. Experimental data (black) and scaled simulated template (red) for the alpha peak corresponding to ^{238}U. 101

5.3. Top panel: comparison of simulated templates for alpha decays (dark red) and the experimental energy spectrum of TUM40 (black) [37]. Light red shows the band of statistical errors and with the pale red the band of statistical and systematical errors. Bottom panel: relative residual between simulation and data. 111

5.4. Combination of all simulated templates for internal beta-decays (a) and zoom on the first 40 keV (b). 112

5.5. Combination of all simulated templates for internal decays caused by cosmogenic activation (a) and zoom on the first 40 keV (b). 113

5.6. Combination of all simulated templates for external contaminations in the near copper parts (a) and zoom on the first 40 keV (b). 114

5.7. Combination of all simulated templates of external contaminations in the distant copper parts (a) and zoom on the first 40 keV (b). 115

6.1. Top panel: sum of all simulated templates with statistical and systematical uncertainties with respect to the experimental data with statistical errors in the medium energy range. Bottom panel: relative residual between simulation and data. 124

6.2. Identified gamma peaks in the medium energy reference data. Gamma emissions originating from the same nuclides are labeled with arrows of the same colour. 125

6.3. Top panel: sum of all simulated templates with statistical and systematical uncertainties with respect to the experimental data with statistical errors in the low energy range. Bottom panel: relative residual between simulation and data. . . . 126
6.4. Top panel: sum of all simulated templates with statistical and systematical uncertainties with respect to the experimental data with statistical errors in the ROI both for this work (1-40 keV) and for the dark matter analysis of TUM40 (0.6-40 keV). Bottom panel: relative residual between simulation and data. . . . 127
6.5. Identified gamma peaks in the low energy reference data. Gamma emissions originating from the same nuclides are labeled with arrows of the same colour. 128
6.6. Top panel: individual background components and their sum compared to the medium energy reference data set. Bottom panel: relative residual between simulation and data. . . . 129
6.7. Top panel: individual background components and their sum compared to the low energy reference data set. Bottom panel: relative residual between simulation and data. . . . 130
6.8. Top panel: individual background components and their sum compared to the low energy reference data zoomed on the ROI (1-40 keV). Bottom panel: relative residual between simulation and data. . . . 131

7.1. Visualisation of a CRESST3 detector module as implemented in Geant4: cut-away views parallel to the X-Z plane fig. 7.1a and parallel to the Y-Z plane fig. 7.1b. Main components are the $CaWO_4$ target crystal (big blue box), silicon on sapphire light detector (thick blue line in fig. 7.1b) and Cu holder (brown/orange). . . . 138
7.2. Simulated energy deposition of a bare $CaWO_4$ crystal (red), TUM40 (black) and a CRESST-III (purple) detector modules caused by irradiation with 2614.0 keV gamma rays (e.g from ^{208}Tl): (a) shows all spectra normalised to the photopeak at 2614.0 keV whereas (b) shows all spectra normalised by the number of all simulated events for each geometry. . . . 139

A.1. Decay of ^{232}Th inside the $CaWO_4$ crystal. Detector response function is not applied. . . . 149
A.2. Decay of ^{238}U inside the $CaWO_4$ crystal. Detector response function is not applied. . . . 149
A.3. Decay of ^{235}U inside the $CaWO_4$ crystal. Detector response function is not applied. . . . 150
A.4. Decay of ^{230}Th inside the $CaWO_4$ crystal. Detector response function is not applied. . . . 150
A.5. Decay of ^{234}U inside the $CaWO_4$ crystal. Detector response function is not applied. . . . 151
A.6. Decay of ^{226}Ra inside the $CaWO_4$ crystal. Detector response function is not applied. . . . 151

A.7. Decay of ^{231}Pa inside the $CaWO_4$ crystal. Detector response function is not applied. . . . 152
A.8. Decay of ^{210}Po inside the $CaWO_4$ crystal. Detector response function is not applied. . . . 152
A.9. Decay of ^{228}Th inside the $CaWO_4$ crystal. Detector response function is not applied. . . . 153
A.10. Decay of ^{222}Rn inside the $CaWO_4$ crystal. Detector response function is not applied. . . . 153
A.11. Decay of ^{224}Ra inside the $CaWO_4$ crystal. Detector response function is not applied. . . . 154
A.12. Decay of ^{223}Ra inside the $CaWO_4$ crystal. Detector response function is not applied. . . . 154
A.13. Decay of ^{218}Po inside the $CaWO_4$ crystal. Detector response function is not applied. . . . 155
A.14. Decay of ^{227}Th inside the $CaWO_4$ crystal. Detector response function is not applied. . . . 155
A.15. Decay of ^{220}Rn inside the $CaWO_4$ crystal. Detector response function is not applied. . . . 156
A.16. Decay of ^{211}Bi inside the $CaWO_4$ crystal. Detector response function is not applied. . . . 156
A.17. Decay of ^{234}Th inside the $CaWO_4$ crystal. Detector response function is not applied. . . . 158
A.18. Decay of ^{234}Pa inside the $CaWO_4$ crystal. Detector response function is not applied. . . . 158
A.19. Decay of ^{214}Pb inside the $CaWO_4$ crystal. Detector response function is not applied. . . . 159
A.20. Decay of ^{218}At inside the $CaWO_4$ crystal. Detector response function is not applied. . . . 159
A.21. Decay of ^{214}Bi inside the $CaWO_4$ crystal. Detector response function is not applied. . . . 160
A.22. Decay of ^{210}Tl inside the $CaWO_4$ crystal. Detector response function is not applied. . . . 160
A.23. Decay of ^{214}Po inside the $CaWO_4$ crystal. Detector response function is not applied. . . . 161
A.24. Decay of ^{210}Pb inside the $CaWO_4$ crystal. Detector response function is not applied. . . . 161
A.25. Decay of ^{206}Hg inside the $CaWO_4$ crystal. Detector response function is not applied. . . . 162
A.26. Decay of ^{210}Bi inside the $CaWO_4$ crystal. Detector response function is not applied. . . . 162
A.27. Decay of ^{206}Tl inside the $CaWO_4$ crystal. Detector response function is not applied. . . . 163
A.28. Decay of ^{231}Th inside the $CaWO_4$ crystal. Detector response function is not applied. . . . 163

A.29. Decay of ^{227}Ac inside the $CaWO_4$ crystal. Detector response function is not applied. . . . 164
A.30. Decay of ^{223}Fr inside the $CaWO_4$ crystal. Detector response function is not applied. . . . 164
A.31. Decay of ^{219}At inside the $CaWO_4$ crystal. Detector response function is not applied. . . . 165
A.32. Decay of ^{215}Bi inside the $CaWO_4$ crystal. Detector response function is not applied. . . . 165
A.33. Decay of ^{219}Rn inside the $CaWO_4$ crystal. Detector response function is not applied. . . . 166
A.34. Decay of ^{215}Po inside the $CaWO_4$ crystal. Detector response function is not applied. . . . 166
A.35. Decay of ^{211}Pb inside the $CaWO_4$ crystal. Detector response function is not applied. . . . 167
A.36. Decay of ^{215}At inside the $CaWO_4$ crystal. Detector response function is not applied. . . . 167
A.37. Decay of ^{207}Tl inside the $CaWO_4$ crystal. Detector response function is not applied. . . . 168
A.38. Decay of ^{211}Po inside the $CaWO_4$ crystal. Detector response function is not applied. . . . 168
A.39. Decay of ^{228}Ra inside the $CaWO_4$ crystal. Detector response function is not applied. . . . 169
A.40. Decay of ^{228}Ac inside the $CaWO_4$ crystal. Detector response function is not applied. . . . 169
A.41. Decay of ^{216}Po inside the $CaWO_4$ crystal. Detector response function is not applied. . . . 170
A.42. Decay of ^{212}Pb inside the $CaWO_4$ crystal. Detector response function is not applied. . . . 170
A.43. Decay of ^{212}Bi inside the $CaWO_4$ crystal. Detector response function is not applied. . . . 171
A.44. Decay of ^{208}Tl inside the $CaWO_4$ crystal. Detector response function is not applied. . . . 171
A.45. Decay of ^{212}Po inside the $CaWO_4$ crystal. Detector response function is not applied. . . . 172
A.46. Decay of ^{179}Ta inside the $CaWO_4$ crystal. Detector response function is not applied. . . . 174
A.47. Decay of ^{181}W inside the $CaWO_4$ crystal. Detector response function is not applied. . . . 174
A.48. Decay of ^{3}H inside the $CaWO_4$ crystal. Detector response function is not applied. . . . 175
A.49. Decay of ^{234}Th inside the copper holder part "Stäbchenring". Detector response function is not applied. . . . 177
A.50. Decay of ^{234}Pa inside the copper holder part "Stäbchenring". Detector response function is not applied. . . . 177

A.51.Decay of ^{226}Ra inside the copper holder part "Stäbchenring". Detector response function is not applied. 178
A.52.Decay of ^{214}Pb inside the copper holder part "Stäbchenring". Detector response function is not applied. 178
A.53.Decay of ^{218}At inside the copper holder part "Stäbchenring". Detector response function is not applied. 179
A.54.Decay of ^{214}Bi inside the copper holder part "Stäbchenring". Detector response function is not applied. 179
A.55.Decay of ^{210}Tl inside the copper holder part "Stäbchenring". Detector response function is not applied. 180
A.56.Decay of ^{210}Pb inside the copper holder part "Stäbchenring". Detector response function is not applied. 180
A.57.Decay of ^{206}Hg inside the copper holder part "Stäbchenring". Detector response function is not applied. 181
A.58.Decay of ^{210}Bi inside the copper holder part "Stäbchenring". Detector response function is not applied. 181
A.59.Decay of ^{206}Tl inside the copper holder part "Stäbchenring". Detector response function is not applied. 182
A.60.Decay of ^{231}Th inside the copper holder part "Stäbchenring". Detector response function is not applied. 182
A.61.Decay of ^{231}Pa inside the copper holder part "Stäbchenring". Detector response function is not applied. 183
A.62.Decay of ^{223}Fr inside the copper holder part "Stäbchenring". Detector response function is not applied. 183
A.63.Decay of ^{227}Th inside the copper holder part "Stäbchenring". Detector response function is not applied. 184
A.64.Decay of ^{223}Ra inside the copper holder part "Stäbchenring". Detector response function is not applied. 184
A.65.Decay of ^{215}Bi inside the copper holder part "Stäbchenring". Detector response function is not applied. 185
A.66.Decay of ^{219}Rn inside the copper holder part "Stäbchenring". Detector response function is not applied. 185
A.67.Decay of ^{211}Pb inside the copper holder part "Stäbchenring". Detector response function is not applied. 186
A.68.Decay of ^{211}Bi inside the copper holder part "Stäbchenring". Detector response function is not applied. 186
A.69.Decay of ^{207}Tl inside the copper holder part "Stäbchenring". Detector response function is not applied. 187
A.70.Decay of ^{228}Ra inside the copper holder part "Stäbchenring". Detector response function is not applied. 187
A.71.Decay of ^{228}Ac inside the copper holder part "Stäbchenring". Detector response function is not applied. 188
A.72.Decay of ^{228}Th inside the copper holder part "Stäbchenring". Detector response function is not applied. 188

A.73. Decay of ^{224}Ra inside the copper holder part "Stäbchenring". Detector response function is not applied. . . . 189
A.74. Decay of ^{212}Pb inside the copper holder part "Stäbchenring". Detector response function is not applied. . . . 189
A.75. Decay of ^{212}Bi inside the copper holder part "Stäbchenring". Detector response function is not applied. . . . 190
A.76. Decay of ^{208}Tl inside the copper holder part "Stäbchenring". Detector response function is not applied. . . . 190
A.77. Decay of ^{234}Th inside the copper sphere. Detector response function is not applied. . . . 192
A.78. Decay of ^{228}Ac inside the copper sphere. Detector response function is not applied. . . . 192
A.79. Decay of ^{226}Ra inside the copper sphere. Detector response function is not applied. . . . 193
A.80. Decay of ^{214}Bi inside the copper sphere. Detector response function is not applied. . . . 193
A.81. Decay of ^{212}Pb inside the copper sphere. Detector response function is not applied. . . . 194
A.82. Decay of ^{210}Pb inside the copper sphere. Detector response function is not applied. . . . 194
A.83. Decay of ^{208}Tl inside the copper sphere. Detector response function is not applied. . . . 195
A.84. Decay of ^{40}K inside the copper sphere. Detector response function is not applied. . . . 195
A.85. Top panel: individual background components and their sum compared to the low energy reference data set between 0 keV and 125 keV. Bottom panel: relative residual between simulation and data. . . . 199
A.86. Top panel: individual background components and their sum compared to the low energy reference data set between 125 keV and 250 keV. Bottom panel: relative residual between simulation and data. . . . 200
A.87. Top panel: individual background components and their sum compared to the low energy reference data set between 250 keV and 375 keV. Bottom panel: relative residual between simulation and data. . . . 201
A.88. Top panel: individual background components and their sum compared to the low energy reference data set between 375 keV and 500 keV. Bottom panel: relative residual between simulation and data. . . . 202
A.89. Top panel: individual background components and their sum compared to the medium energy reference data set between 500 keV and 950 keV. Bottom panel: relative residual between simulation and data. . . . 203
A.90. Top panel: individual background components and their sum compared to the medium energy reference data set between 950 keV and 1400 keV. Bottom panel: relative residual between simulation and data. . . . 204

A.91. Top panel: individual background components and their sum compared to the medium energy reference data set between 1400 keV and 1850 keV. Bottom panel: relative residual between simulation and data. 205
A.92. Top panel: individual background components and their sum compared to the medium energy reference data set between 1850 keV and 2300 keV. Bottom panel: relative residual between simulation and data. 206
A.93. Top panel: individual background components and their sum compared to the medium energy reference data set between 2300 keV and 2800 keV. Bottom panel: relative residual between simulation and data. 207
A.94. ^{238}U natural decay chain. Figure provided by [77]. 209
A.95. ^{235}U natural decay chain. Figure provided by [77]. 210
A.96. ^{232}Th natural decay chain. Figure provided by [77]. 211

List of Tables

3.1. An overview of different stages of the CRESST experiment in terms of data taking period, target material and references for details [98]. 44

3.2. Properties of different detector modules used in the CRESST experiment: crystal mass M, detection threshold E_{th}, exposure $T \cdot M$ and background B between 1 keV and 40 keV. 48

4.1. Parts of the TUM40 detector module as as implemented in the Geant4 simulation. 81

5.1. An overview of the nuclides of the ^{238}U decay chain. Decay modes, branching ratios, half-lives and activities are included. Nuclides presented in the same colour are in secular equilibrium. Activities of each nuclide are given with systematical errors as deduced in this work. 98

5.2. An overview of the nuclides of the ^{235}U decay chain. Decay modes, branching ratios, half-lives and activities are included. Nuclides presented in the same colour are in secular equilibrium. Activities of each nuclide are given with systematical errors as deduced in this work. 99

5.3. An overview of the nuclides of the ^{232}Th decay chain. Decay modes, branching ratios, half-lives and activities are included. Nuclides presented in the same colour are in secular equilibrium. Activities of each nuclide are given with systematical errors as deduced in this work. 100

5.4. Gaussian fit values (mean E, amplitude A and variance σ) of the alpha lines observed in the high energy reference data of TUM40. The number of observed events ($N_{\alpha,\mathrm{obs}}$) and the corresponding activities (A_α) are calculated from the integral of the fit. The statistical uncertainties for $N_{\alpha,\mathrm{obs}}$ and A_α are calculated using the fit values as described in the text. 103

5.5. Gaussian fit values (mean E, amplitude A and variance σ) of cosmogenic X-ray lines observed in the experimental data of TUM40. The number of observed events ($N_{\mathrm{X-ray,obs}}$) and the corresponding activities ($A_{\mathrm{X-ray}}$) are calculated from the integral of the fit. The statistical uncertainties for $N_{\mathrm{X-ray,obs}}$ and $A_{\mathrm{X-ray}}$ are calculated using the fit values as described in the text. Based on simulations, η is the ratio between the activities of the photo peak $A_{\mathrm{X-ray}}$ and the complete spectrum. 107

5.6. Gaussian fit values (mean E, amplitude A and variance σ) of gamma lines observed in the experimental data of TUM40. The number of observed events ($N_{\gamma,\mathrm{obs}}$) and the corresponding activities (A_γ) are calculated from the integral of the fit. The statistical uncertainties for $N_{\gamma,\mathrm{obs}}$ and A_γ are calculated using the fit values as described in the text. Based on simulations, η is the ratio between the activities of the photo peak A_γ and the complete spectrum $\mathrm{A_{Total}}$. 116

6.1. Disentanglement of the background sources for TUM40, comparing this work with the previous [105]. Numbers for this work are given rounded up to significant digits. 122

A.1. Lines corresponding to X-ray and gamma emissions, and alpha decays observed in the TUM40 data. The literature values of the energies of these lines are given along with the mean values of the peaks obtained through fitting. 197

Abstract

One of the biggest unknowns of our Universe is the nature of dark matter. The existence of dark matter was proven by many astrophysical and cosmological observations and it is known that it constitutes 27 % of the energy budget of our Universe. Many theories were proposed to explain the nature of the dark matter which may be a particle. In order to detect dark matter particles, there are three different mechanisms: production, indirect searches and direct searches.

Direct searches look for recoils in a detector induced by the scatter off of a dark matter particle. There are different types of direct search experiments focusing on different mass ranges.

In the past years, the attention was extended towards possible low mass dark matter particles. In this mass range, the leading experiment is CRESST. The CRESST experiment uses scintillating $CaWO_4$ crystals as target while simultaneously measuring the scintillation light with a light detector and the phonon excitation of the crystal lattice with a thermometer. It is able to differentiate between different types of particle interactions. CRESST focuses its search efforts for dark matter in the $\sim \mathcal{O}(100\,\mathrm{MeV/c^2})$ mass region. In order to be able to detect possible dark matter particles in this mass region, CRESST can measure recoil energies down to $\mathcal{O}(100\,\mathrm{eV})$.

However, in this energy region, beta and gamma particles are hardly distinguishable from nuclear recoils which makes the search for a possible dark matter signal very difficult. These beta and gamma particles originate from radioactive backgrounds inside and outside the target crystal. Since it is not possible to remove all of this background physically, it is vital to have a background model predicting the contributions of these backgrounds to the region of interest. In order to do this, simulations based on the Geant4 framework are used.

In this thesis, the electromagnetic background of CRESST is studied and simulated. Based on this model, the overall background is decomposed into contributions from individual sources, their isotopic compositions and locations. The validity of the model is assessed in comparison with the experimental data recorded in-situ with the detector module TUM40 of CRESST-II Phase 2. In this first full Monte Carlo study of electromagnetic backgrounds in CRESST, we were able to successfully reproduce (75 ± 19) % of the observed backgrounds in this detector module. Furthermore, we decomposed the background into three basic components: internal contamination of $CaWO_4$, both radiogenic and cosmogenic, and contamination of external copper parts. Finally, we discussed the implication of these findings on the CRESST experiment and outline possible future improvements.

1. Introduction

As confirmed by many astrophysical and cosmological observations, such as galactic rotation curves and temperature fluctuations of the *cosmic microwave background* (CMB), there exists a deviation between astronomical observation and predictions based on our well established theories about gravitation and matter. Since the first observations, there have been many different hypotheses trying to explain what these effects could be caused by. There have been attempts at explaining this phenomenon using modifications of the dynamical laws derived by Newton. However, these attempts failed to explain all observations. Other hypotheses assume that the effect can be explained by a new type of matter, called *dark matter* (DM), because it is not directly visible in astronomical observations. In this interpretation, the total mass of dark matter would constitutes 26.6 % of the matter-energy budget of the Universe [6]. The things we know about dark matter are limited as it does not emit light which means it does not interact electromagnetically. In addition, we know that it does not interact strongly [71]. The only interaction dark matter is known to have is gravity because we see its effects. To be able to detect dark matter, it needs to interact with baryonic matter via a weak interaction, i.e. dark matter would consist out of WIMPs, which stands for *Weakly Interacting Massive Particles*. A classic possibility would be that dark matter is made up of the superposition of the supersymmetric twins of some elementary *Standard Model* (SM) particles. This interaction can occur in three different mechanisms: production, annihilation and scattering. The production search looks for Standard Model particles creating dark matter particles by collisions with each other whereas the indirect detection search looks for two dark matter particles annihilating into Standard Model particles. The direct detection search is in pursuit of the dark matter particle through its interaction with a target detector.

The direct search explores a broad range of possible dark matter masses m_χ which range from a few $\mathrm{MeV/c^2}$ to hundreds of $\mathrm{GeV/c^2}$. Different mass ranges require different detection techniques. For masses ranging from a few $\mathrm{GeV/c^2}$ and on, a high amount of exposure is significant whereas for masses below a few $\mathrm{GeV/c^2}$, the detection threshold is critical. The multistage *Cryogenic Rare Event Search with Superconducting Thermometers* (CRESST) experiment is currently the most sensitive experiment for $m_\chi \leq 1.7\,\mathrm{GeV/c^2}$ and set leading limits on the DM-SM cross-section [95]. As it will be explained later in detail, CRESST is able to identify nuclear recoils in its targets as predicted for most types of DM. In addition, it can also distinguish electron recoils induced by background reaction from natural radioactivity. However, for low mass DM search, where one needs to consider recoil energies below 40 keV, the discrimination power between electron recoils and nuclear recoils decline dramatically. In order to be able to discriminate between nuclear and electron recoils and, accordingly, make a discovery, one needs to understand

the backgrounds in the experimental data. In the past, CRESST was searching for WIMPs at the GeV/c^2 mass scale, which means recoil energies in the regime of $\mathcal{O}(10\,\text{keV})$. Hence, the backgrounds could be discriminated and this lead to an easier dark matter analysis. However, in the last few years, CRESST started to look for the low-mass dark matter particles. This endeavour started in 2014 with a CRESST detector module called TUM40 [89]. Since one has to look at low energies, where the region of interest lies, there is background leaking from the electron recoils into the nuclear recoils. If one can quantify the background, only then a possible observation of a dark matter signal will be possible. This can be done via creating a background model based on simulations. An effort was put into determining the type and the amount of backgrounds in the past [105]. Even though it created a basis for the background research at CRESST, it used a simplistic design of the TUM40 detector module. Hence, an extended analysis of the backgrounds with the full detector geometry is needed. In order to be able to create this background model, simulations produced using the Geant4 framework with all necessary physics interactions considered are used.

This thesis describes a background model based on the Geant4 framework [12, 17, 18], aiming to quantify the radioactive backgrounds of the CRESST experiment. We are focusing on one of the detector modules in CRESST-II Phase 2 named TUM40. Based on this model, the overall electromagnetic background is decomposed into contributions from individual sources, their isotopic compositions and locations. The validity of the model is assessed in comparison with the experimental data recorded in-situ with the detector module under investigation.

The observational evidence for the existence of dark matter with possible particle explanations, different mechanisms to detect it and a detailed explanation on direct detection technique will be given in Chapter 2. A concise description of the experimental setup, working principle and the technical properties of the CRESST Experiment will be given in Chapter 3. In Chapter 4, the methodology of the simulations and assessment of the radioactive background activities will be explained. A summary of how the simulations are scaled and combined will be presented in Chapter 5. In Chapter 6, the results of the background analysis and the comparison with reference data will be given. The results and the future implications will be discussed in Chapter 7. Finally, a brief conclusion will be given in Chapter 8.

2. Dark Matter

In this chapter, first, a selection of observational evidence for the existence of dark matter at different length scales will be discussed in section 2.1. Alternatives and candidates for dark matter will be summarised in section 2.2 and in section 2.3, respectively. Different detection approaches, i.e. direct searches, indirect searches and searches at particle colliders will be presented in section 2.4. The topic of this work is related to the CRESST experiment, a direct search for dark matter, and will be explained in detail in section 2.5.

2.1. Observational Evidence for the Existence of Dark Matter

The Swiss astrophysicist Fritz Zwicky was one of the first who used the modern concept of dark matter. In 1933, he investigated the velocity distribution of a group of galaxies in the Coma Cluster. His objective was to calculate the total mass of the cluster via the virial theorem [115, 116]:

$$M \sim \frac{5R < v^2 >}{3\mathrm{G}} \tag{2.1}$$

which connects the squared velocity averaged over all cluster members $< v^2 >$ with cluster mass M; R is the cluster radius and G is Newton's gravitational constant. However, he detected a discrepancy between the dynamical mass determined above and the luminous mass, i.e. the mass interfered from the luminous content of the cluster: if both would be equal, the obtained $< v^2 >$ would be lower than the observed one [116]. Zwicky concluded that additional mass was needed to explain the observation and since this extra mass cannot be luminous, he attributed it to *dark matter*.

Further evidence following Zwicky's findings came from Vera Rubin and W. Kent Ford in 1970. They measured the velocity curve of spiral galaxies using a high precision spectrograph [100]. The expectation for stars in galaxies was to have a Keplerian velocity decrease as their radii go higher which can be calculated from

$$m \cdot a = \frac{\mathrm{G}mM}{r^2}, \text{ where } a = \frac{v^2}{r}. \tag{2.2}$$

Here, v stands for the velocity of the star in question, r for the distance from the center of the galaxy to the star, m for the mass of the star, M for the mass of the galaxy within the star's orbit and G for the gravitational constant. When the equation for the acceleration is inserted into the Newton's second law, the equation

$$v = \sqrt{\frac{\mathrm{G}M}{r}} \tag{2.3}$$

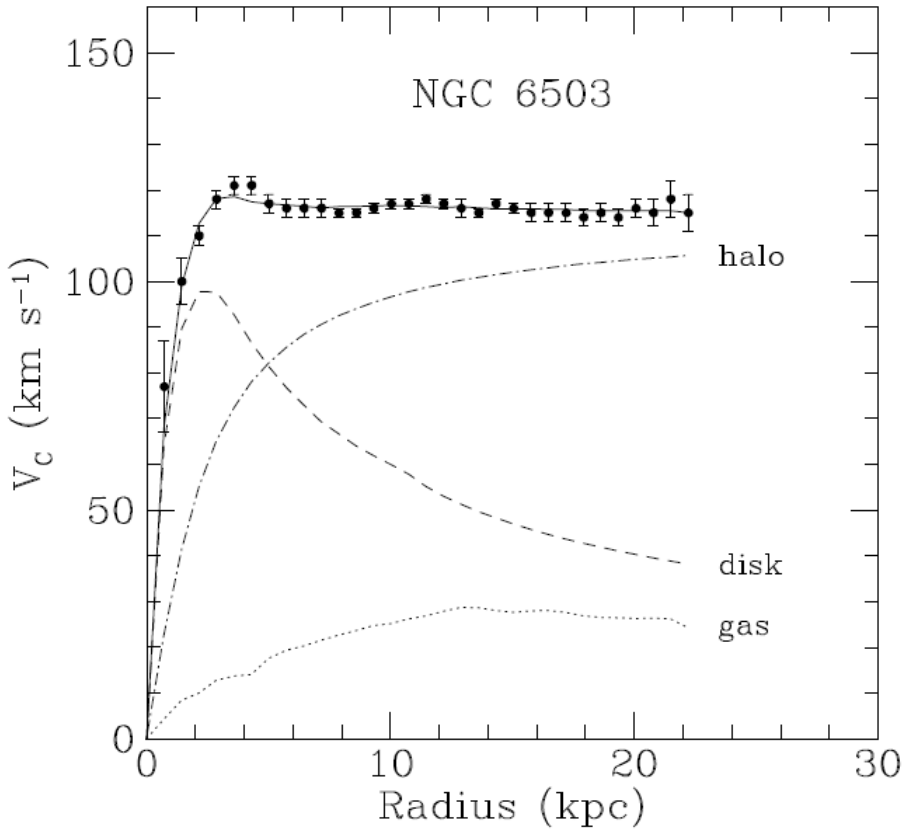

Figure 2.1.: Rotation curve of the galaxy NGC 6503: orbital velocity as a function of the orbit's radius. Figure taken from [57].

predicts a decrease in velocity as $1/\sqrt{r}$. However, they found that the rotational curves of the galaxies stay flat well beyond their visible boundaries [99]. With this in mind, they concluded the existence of non-luminous matter in addition to the visible galaxy. To obtain the flat rotation curve that was observed, it was necessary to add a halo of dark matter to the galaxies. The contribution of a halo in addition to the galactic disk and gas clouds can be seen in fig. 2.1 on the example of the galaxy NGC 6503. This research was one major step towards the extablishment of dark matter halos around galaxies. Observation imply also a dark halo around our galaxy [102, 103].

Another indication for dark matter can be deduced from the *cosmic microwave background* (CMB). In 1965, Amo Penzias and Woodrow Wilson discovered a thermal radiation filling the Universe [93]. Roughly 30 years later, John C. Mather and George F. Smoot showed with data obtained by NASA's *Cosmic Background Explorer* (COBE) that the radiation features a blackbody spectrum with anisotropies at the μK-scale. For these discoveries, both were awarded with the Nobel Prize in physics in 2006 [44]. Over the years, more accurate measurements of the CMB were performed using the *Wilkinson Microwave Anisotropy Probe* (WMAP) [39] and most recently with ESA's *Planck Space Telescope*

[6]. The power spectrum of the temperature anisotropy of the CMB, as observed by the Planck Space Telescope in fig. 2.2, was created in the early times of the Universe via baryonic acoustic oscillations. In this figure, baryonic matter participated in this oscillation via electromagnetic coupling, whereas dark matter doesn't take any part in it. Different cosmological parameters can be determined from the power spectrum [6]. The curvature of the Universe can be deduced from the angular scale of the first acoustic peak (the highest peak on the left). The reduced baryon density can be deduced from the amplitudes of even vs odd numbered peaks. The total mass density, i.e. baryonic matter plus dark matter, affects the amplitude of all peaks. Finally, the dark matter density can be calculated as the difference between total mass density and baryonic mass density. Up to now, Planck provides the most precise measurements of the mass-energy budget of the Universe: $\Omega_b = (4.91 \pm 0.05)$ % baryons, $\Omega_{CDM} = (26.6 \pm 1.3)$ % dark matter and $\Omega_\Lambda = (68.5 \pm 1.3)$ % dark energy [6].

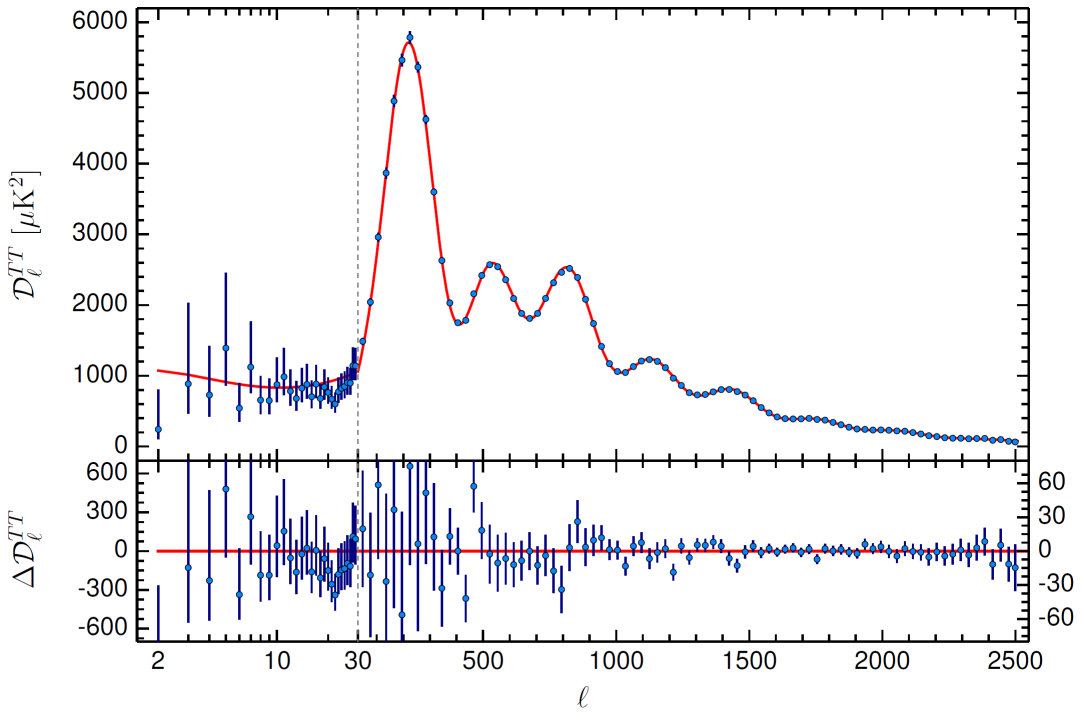

Figure 2.2.: Upper panel: CMB power as function of the multipole moment l (blue data points) obtained by the Planck Space Telescope shown in angular scale and compared with a fit based on the standard cosmological model (red line). Lower panel: the residuals between data and fit. Figure taken from [6].

2.2. Alternatives to Dark Matter

The observation discussed in the previous section points to the existence of dark matter, an additional type of matter that interacts gravitationally but not via electromagnetism. Alternatively, one can doubt the validity of Newton's second law of mechanics (eq. (2.2)). Either, there is something which is not known regarding the mass M, e.g. dark matter, or regarding the acceleration a.

A theory to modify the acceleration was suggested by Mordehai Milgrom in 1983 as *Modified Newtonian Dynamics* (MOND) [87]. Milgrom advocated that modifying Newton's second law can make up for the unexpectedly high orbital velocities of stars in galaxies. Whereas Newton's laws have been tested for high acceleration cases such as the Earth and the Solar System, they were not tested for objects with low acceleration such as stars in outer parts of galaxies. With this idea in mind, Milgrom proposed that if the gravitational force a star in the outer part of a galaxy experiences is proportional to the square of its centripetal acceleration, whereas it should be proportional to its centripetal acceleration, this could explain why the speeds of stars are much higher than calculated. The modification he made had the form

$$\vec{F} = \vec{a} \cdot \mu \left(\frac{a}{a_0} \right) \cdot m \tag{2.4}$$

where m is the gravitational mass of a moving body under the influence of an arbitrary static force field $\vec{F}$ with an acceleration $\vec{a}$. In this equation, μ is a function which is defined via its limits [87]:

$$\mu(x) \approx \begin{cases} 1, & \text{for } x \gg 1. \\ x, & \text{for } x \ll 1. \end{cases} \tag{2.5}$$

This theory claims to explain most galactic rotation curves with $a_0 \approx 2 \cdot 10^{-8} \mathrm{cm} \cdot \mathrm{s}^{-2}$ [87].

Another astronomical indication for dark matter is the Bullet Cluster, 1E 0657-558, which consists of two clusters of galaxies colliding with each other [50]. An X-ray image of the Bullet Cluster is shown in fig. 2.3 together with the green contours of the mass density obtained via weak lensing study. These contours correspond to the gravitational centers of the galaxy clusters. However, these regions do not coincide with the majority of the baryonic matter content, i.e. the hot intergalactic medium, of the clusters visible via their X-ray emissions. During the collision of these two clusters, the baryonic content slows down and emits X-rays because of friction. On the other hand, dark matter, which has no friction, continues to move on its path with nearly constant velocity. The spatial difference between the centers of the baryonic components and the centers of the total masses cannot be expressed with theories like MOND: also in these theories, like in Newtonian gravity, the place of the source of gravitation and the place of the caused action coincide. Hence, if in a MOND scenario, the baryonic mass would cause all the observed gravitational interaction and, then, the centers of the X-ray images and the contours of the weak graviational lensing should coincide. Therefore, it indicates that most of the matter in the system has to be non-baryonic dark matter [50].

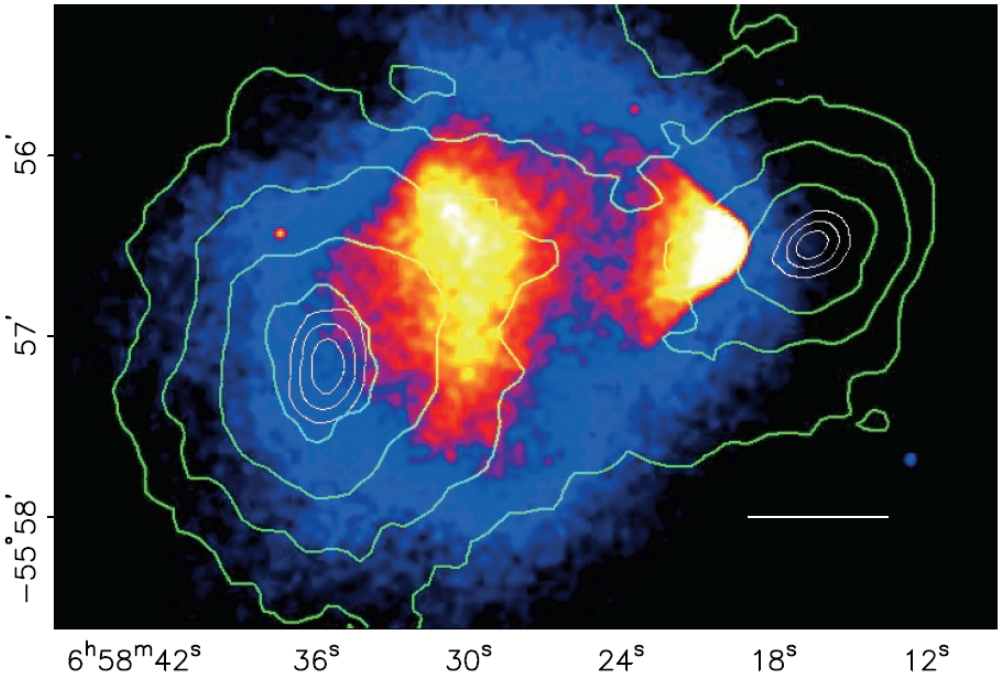

Figure 2.3.: The X-ray image of the Bullet Cluster was taken by Chandra X-ray Observatory and shows the distribution of the hot intergalactic medium. The green contours show the total mass density deduced from the gravitational lensing. Figure taken from [50].

Another attempt to find a solution to observed discrepancies in galactic dynamics without relying on dark matter was made by adding more baryonic mass to M in eq. (2.2). A possibility for additional, non-luminous baryonic matter are *Massive Compact Halo Objects* (MACHOs). A MACHO is an object made of baryonic matter which emits little to no light, e.g. black holes, brown dwarfs and neutron stars [64]. This theory also fails as proven by observations with the NICMOS instrument of the Hubble Space Telescope because the amount of red dwarfs [63] and brown dwarfs [49] only stood for a negligible percentage of the mass of the dark matter halo.

As MOND and MACHOs failed, the most favored theory so far that can explain all the effects mentioned in the last section is that dark matter exists and consists of a non-baryonic particle, possible properties of which will be discussed in the next section.

2.3. Dark Matter Particle Candidates

Over the years, many different theories proposed particle candidates to explain dark matter. The current consensus is that dark matter should be non-baryonic and cold which means non-relativistic during the early Universe. Some dark matter particle candidates are shown in fig. 2.4 together with their expected interaction strength with nucleons, their

mass and their temperature at production in the early Universe.

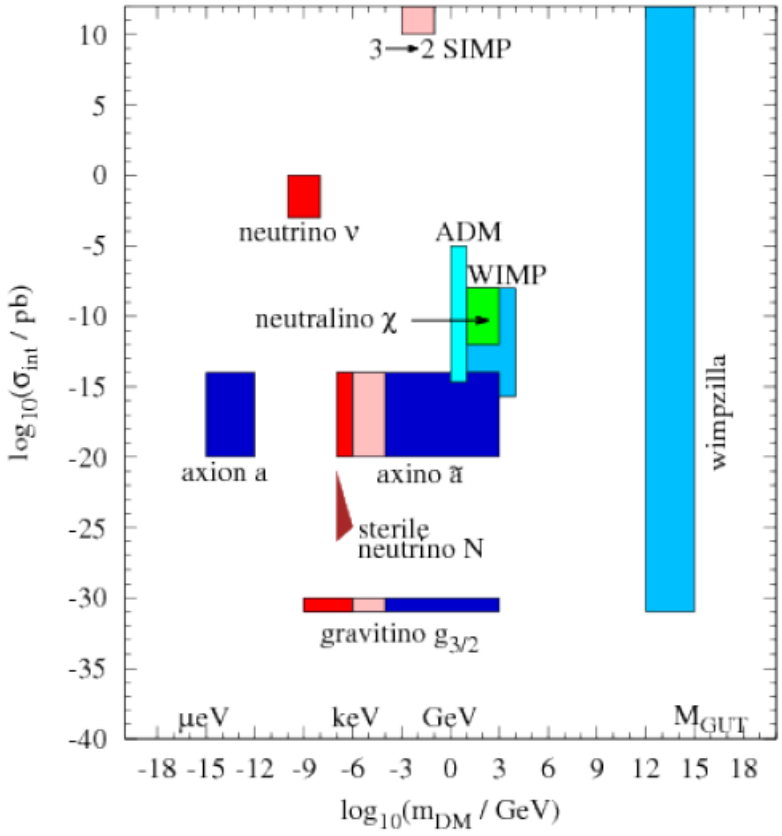

Figure 2.4.: Dark matter-nucleon cross-sections σ_{int} vs dark matter particle mass m_{DM}. The colour indicates the temperature of the candidates at production in the early Universe: red, pink and blue represent hot, warm and cold dark matter, respectively. Neutralinos are highlighted in green. Figure taken from [36].

So far, the most well-studied theories of dark matter involves *Weakly Interacting Massive Particles* (WIMPs). The main reason why WIMPs are one of the most favored dark matter candidates is that WIMPs which are thermally produced in the early Universe results in the correct dark matter density observed today, i.e. 26.6 % (see section 2.1). When the temperature was high enough in the early Universe, the dark matter particles could have been formed from and annihilated into particles of the *Standard Model* (SM) of particle physics. During the expansion of the Universe, the creation of dark matter particles becomes Boltzman suppressed because the temperature of the Universe drops below the mass of the dark matter particles. On the contrary, the annihilation of the dark matter and anti-dark matter particles continued and the amount of dark matter particles decreased exponentially [74]. However, when the expansion of the Universe accelerate beyond the annihilation rate of the dark matter particles, the annihilation becomes sup-

pressed and the number density of dark matter particles would remain nearly constant as the Universe continued with its expansion; the dark matter *freeze-out* occurs [65]. Dark matter candidates with higher annihilation cross-sections would continue to annihilate for a longer time than those with a smaller cross-section. Consequently, their number density would be even lower when the interaction stops [74].

Based on the observations by the Planck Space Telescope, the relic dark matter density is $\Omega_{CDM} = 0.266$ [6]. Calculations showed that the relic abundance is related to the annihilation cross-section of dark matter particles $\langle \sigma_{\mathrm{A}} v \rangle$ averaged over their velocity distribution by [43]

$$\Omega_{\mathrm{CDM}} h^2 \simeq \frac{3 \cdot 10^{-27} \mathrm{cm}^3 \mathrm{s}^{-1}}{\langle \sigma_{\mathrm{A}} v \rangle} \tag{2.6}$$

where h is Hubble constant in units of 100 $\mathrm{kms}^{-1}\mathrm{Mpc}^{-1}$. When this equation is solved for the annihilation cross-section, the result is $\langle \sigma_{\mathrm{A}} v \rangle \approx 3 \cdot 10^{-26}\,\mathrm{cm}^3\mathrm{s}^{-1}$. A weakly interacting particle within the mass range of $\sim 100\,\mathrm{GeV/c}^2$ fits this model [72]. This is the so-called *WIMP Miracle*.

One of the most favored WIMP candidates are supersymmetric neutralinos [54]. *Supersymmetry* (SUSY) is a beyond SM theory that relates fermions and bosons. SUSY suggests that every fermion in the SM has a yet-undiscovered bosonic super partner and vice versa. Often, the neutralino [54] is the lightest supersymmetric particle which is stable, making it a prime candidate for dark matter.

In the past years, light dark matter particles which are below the WIMP scale gained more attraction. One model in this mass scale is *Asymmetric Dark Matter* (ADM). ADM [45, 94, 114] is based on a possible asymmetry between dark matter and anti-dark matter particles, similar to the asymmetry in baryonic matter. In this model, the relic density of dark matter is calculated through the asymmetry in the initial dark matter populations instead of a thermal freeze-out. For ADM, the asymmetry between dark matter and their anti-particle is related to the baryon asymmetry [75]. The particle mass for ADM m_{ADM} can be estimated using this simple relation [36]:

$$m_{\mathrm{ADM}} = \frac{\eta_{\mathrm{B}}}{\eta_{\mathrm{ADM}}} \frac{\Omega_{\mathrm{ADM}}}{\Omega_{\mathrm{B}}} m_{\mathrm{B}} = \mathcal{O}(1 - 10\, m_{\mathrm{p}}), \tag{2.7}$$

where m_{B} stands for the mass of baryonic particles, which in this calculation is taken as the mass of the proton, η_{ADM} and η_{B} are the asymmetries in the number densities of ADM and baryons, respectively. If all dark matter consists of ADM, then the relation between the energy density of baryons and ADM is nearly $\frac{\Omega_{\mathrm{ADM}}}{\Omega_{\mathrm{B}}} \approx 5$ [4] (see section 2.1). The ADM and baryon asymmetries are parametrized by [36]

$$\eta_i \equiv \frac{n_i - n_{\bar{i}}}{s} \text{ for } i = \mathrm{B} \text{ or ADM} \tag{2.8}$$

where s stands for entropy density, and n_i and $n_{\bar{i}}$ are the number densities of the particles and antiparticles of type i, respectively. Should the asymmetry of baryons and ADM be roughly the same, $\eta_{\mathrm{ADM}} \approx \eta_{\mathrm{B}}$, this would suggest a light dark matter particle with a mass of nearly 5 $\mathrm{GeV/c}^2$ [36].

2.4. Search Strategies for Dark Matter

There are three different experimental strategies to search for dark matter if it has a particle nature and if it interacts with baryonic matter also non-gravitationally: production of dark matter (section 2.4.1), indirect search for dark matter via its annihilation products (section 2.4.2) and direct search of dark matter interacting with baryonic matter (section 2.4.3). A simplified Feynman diagram illustrating these approaches can be seen in fig. 2.5. Only when there is a consensus of results from all of these three strategies, then one can claim to have discovered dark matter particle undoubtedly. In this section, these three strategies will be explained.

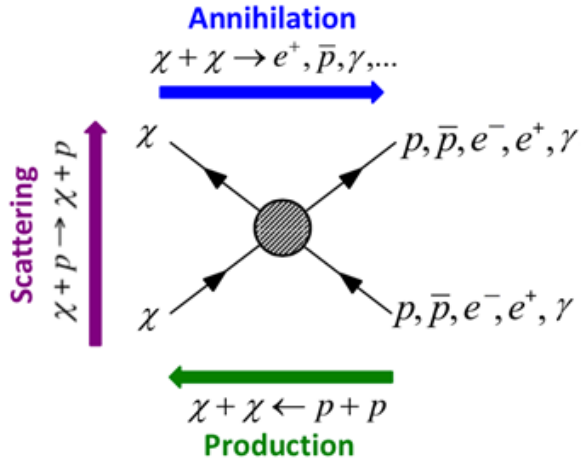

Figure 2.5.: A simplified Feynman diagram illustrating different approaches to detect dark matter χ. If the time flows to the right side (blue), two dark matter particles annihilate into SM particles. If the time flows to the left (green), a pair of dark matter is produced from the annihilation of SM particles. If the time flows up (purple), dark matter particle scatters off a nucleus. Figure adapted from [108].

2.4.1. Dark Matter Production

Dark matter particles can be potentially produced in accelerators, like LHC [73, 88] and Belle [70], using the collision and annihilation of Standard Model particles, such as protons. Since the dark matter particles produced in the collision have by definition a tiny interaction cross-section with baryonic matter, they will leave the detector without giving a signal. One can only determine their existence through the Missing Transverse Energy [61]. However, to trigger and measure dark matter at all, an additional SM particle must be produced. Different dark matter models can be tested experimentally with this approach.

2.4.2. Indirect Search

Indirect searches look for the cosmic rays originating from the annihilation of dark matter particles. Potential dark matter annihilations can produce various particle-anti particle pairs such as $q\bar{q}$, $\mu^-\mu^+$, ZZ, W^-W^+ or HH [43]. These particles go through different processes after their production, such as hadronization, and create a flux of cosmic rays including $\bar{p}$, e^-, e^+, ν and γ.

An excess of anti-particles in the cosmic rays can be caused by dark matter annihilation. The actual energy spectrum of the anti-particles depends strongly on the initially-created SM particles after the dark matter annihilation. However, a common signature for a possible dark matter signal would be a bump in the energy spectrum followed by a hard cut-off at the mass of the dark matter particle.

Another type of particles important for the indirect search are γ rays. Gamma rays can be produced in annihilation either through virtual internal Bremsstrahlung [46], initial state radiation or hadronisation followed by decay into γ rays. All of these processes result in characteristic γ-ray spectra. The annihilation, in particular, leads to a line signal at the mass of the dark matter particle. The highest gamma-ray flux would be expected from the *Galactic Center* (GC) (which coincide with the center of the dark halo) due to the high dark matter density. However, also several "normal" astrophysical processes in the GC can mimic such a signal. Currently, FermiLAT is looking for such a signal [3].

The last type of particle being searched for are neutrinos. Just like with γ rays, neutrinos produced in the dark matter annihilation leads to a line signal at the mass of the dark matter particle. However, the location of a potential neutrino signal is different from the location of a potential γ ray signal. A particular interest is given to the neutrinos coming from the center of the Sun because the neutrino flux may not be related to the dark matter annihilation cross-section but to the dark matter-nucleon scattering cross-section. As we mentioned in the beginning, dark matter-nucleon scattering is also searched for by direct detection experiments. The reason for this is that dark matter particles might scatter on protons in the Sun, thereby losing kinetic energy. Depending on the energy loss, they might be captured by the gravitational field of the Sun. Then, they are accumulated in the center of the Sun which leads to a locally magnified rate of annihilations. In the case of an equilibrium between the annihilation and the capture of the dark matter particles, the emitted neutrino flux is independent of the annihilation cross-section. The neutrinos which originate from these annihilations then reach detectors on Earth and could be measured. One experiment searching for these neutrinos is IceCube [2].

2.4.3. Direct Search

Direct searches for dark matter particle are performed with Earth-bound experiments. These experiments aim to measure the scattering of the dark matter particles off nuclei of the target material of the detector. In a simplified approach, most of the experiments assume that dark matter particles scatter coherently and elastically. Another feature

shared by most experiments is their location at underground sites in order to protect them from cosmic rays as background source.

Since this thesis will deal specifically with a direct detection experiment, namely CRESST, direct detection will be explained thoroughly in the next section.

2.5. Details on Direct Searches for Dark Matter

As we pointed out in Section section 2.1, there is also a dark matter halo surrounding our galaxy. Therefore, Earth-based experiments can search for dark matter-induced interactions in their detectors. In this work, we are focusing on the direct search for dark matter via nuclear recoils (section 2.5.1). Afterwards, different detection techniques will be explained (section 2.5.2) and, finally, the current status of the direct searches will be discussed (section 2.5.3).

2.5.1. Nuclear Recoils

The rate R of expected recoiling nuclei per target mass m is given by

$$R = \Phi_\chi \cdot \sigma_{\chi\mathrm{N}} \cdot \frac{N_\mathrm{T}}{m} \tag{2.9}$$

where $\sigma_{\chi\mathrm{N}}$ stands for the dark matter-nucleon cross-section[1], Φ_χ stands for the incident flux of dark matter particles and N_T for the number of nuclei in the target. The incident flux is equal to $n_\chi \cdot v_{\chi\mathrm{N}}$ with the velocity $v_{\chi\mathrm{N}}$ of dark matter particles relative to the target nucleus and the particle density $n_\chi = \frac{\rho_0}{m_\chi}$ where ρ_0 is the local density of the dark matter halo and m_χ is the mass of the dark matter particle. The number of nuclei in the target, $N_\mathrm{T} = \frac{m \cdot N_\mathrm{A}}{A}$, can be expressed with Avogadro's constant N_A and the atomic weight A. Since dark matter particles are considered to be non-relativistic today with a speed relative to the Earth's movement in the order of $v_\chi \approx 10^{-3}$ c, the recoil energy can be given as [43]

$$E_\mathrm{R} = \frac{\mu^2 v_{\chi\mathrm{N}}^2}{m_\mathrm{N}} \cdot (1 - \cos\theta),\ \mu = \frac{m_\chi m_\mathrm{N}}{m_\chi + m_\mathrm{N}} \tag{2.10}$$

where θ is the scattering angle and m_N is the mass of the nucleus. This leads to a transferred momentum of $q^2 = 2 m_\chi E_\mathrm{R}$ [82]. In fig. 2.6, the relation between the dark matter rate with respect to the recoil energy is shown. Blue lines stand for Ge target nuclei whereas the orange ones stand for Xe target. Same coloured lines show the change of the relation between the event rate and the recoil energy for possible dark matter particles with different masses [43].

Generally, the cross-section depends on the recoil energy E_R. In addition, $v_{\chi\mathrm{N}}$ is not constant but it is weighted by a distribution $f(\vec{v}_{\chi\mathrm{N}})$. Therefore, the event rate per unit

[1] Usually given in units of barn ($1\,\mathrm{barn} = 10^{-28}\,\mathrm{m}^2$).

target mass has to be modified [43]:

$$R = \int_{E_\mathrm{T}}^{\infty} dE_R \cdot \frac{\rho_0}{m_\mathrm{N} m_\chi} \int_{v_{min}}^{v_{esc}} v_{\chi\mathrm{N}} \cdot f(\vec{v}_{\chi\mathrm{N}}) \frac{d\sigma_{\chi\mathrm{N}}}{dE_R}(E_R, v_{\chi\mathrm{N}}) \cdot d^3\vec{v}_{\chi\mathrm{N}} \tag{2.11}$$

where $v_{min} = v_{min}(E_\mathrm{R})$ is the minimum velocity required to produce a recoiling nucleus with energy E_R, E_T is the energy threshold which corresponds to the minimum measurable energy and v_{esc} is the minimum velocity required for a dark matter particle to escape the gravitation well of the galaxy.

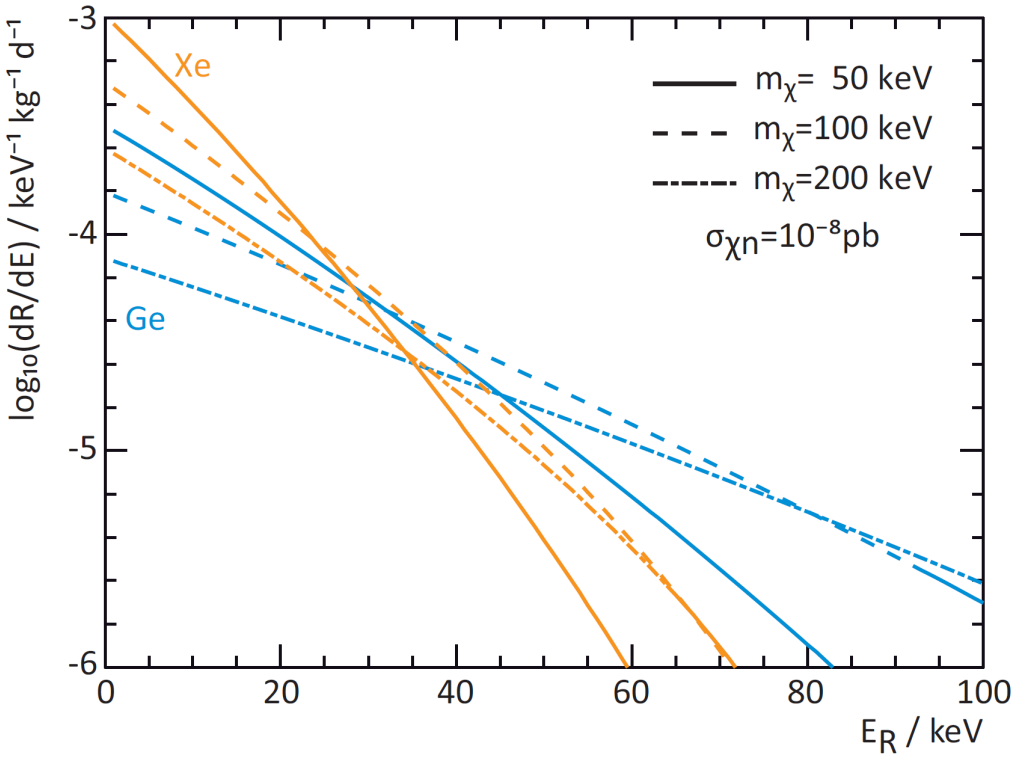

Figure 2.6.: Event rate R drawn with respect to the recoil energy E_R for various WIMP masses m_χ for targets Ge and Xe. A nucleon-WIMP cross-section of $\sigma_{\chi\mathrm{n}} = 10^{-8}$ pb is assumed. Figure adapted from [43].

All of these parameters depend either on different theoretical models, astronomical observations, or parameters of experimental setups.

Astrophysical parameters, such as ρ_0, $v_{\chi\mathrm{N}}$ and v_{esc}, depend on the applied halo model and are calculated according to the astrophsyical observations. In order to simplify comparisons between different experiments, common values for ρ_0, v_{esc} and v_χ are used [43]:

$$\rho_\chi = 0.3\,\mathrm{GeV/cm^3},\ v_{esc} = 544\,\mathrm{km\,s^{-1}},\ v_\chi = 220\,\mathrm{km\,s^{-1}} \tag{2.12}$$

In addition, usually for the distribution function $f(\vec{v}_{\chi\mathrm{N}})$, a Maxwell-Boltzman distribution is used.

If one assumes that the Milky Way has a dark matter halo, a WIMP flux of the order of $10^5(100\,\mathrm{GeV}/m_\chi)\,\mathrm{cm}^{-2}\mathrm{s}^{-1}$ is expected on Earth due to its motion through the galaxy [43].

Particle parameters, such as m_χ and $\sigma_{\chi\mathrm{N}}$, depend on the dark matter particle model. The cross-section, $\sigma_{\chi\mathrm{N}}$ can be separated into spin-independent (SI) and spin-dependent (SD) contributions [43]:

$$\frac{d\sigma_{\chi\mathrm{N}}}{dE_R} = \left(\frac{d\sigma_{\chi\mathrm{N}}}{dE_R}\right)_{SI} + \left(\frac{d\sigma_{\chi\mathrm{N}}}{dE_R}\right)_{SD} \tag{2.13}$$

The spin-dependent cross-section is given by [43]

$$\left(\frac{\mathrm{d}\sigma_{WN}}{\mathrm{d}E_\mathrm{R}}\right)_{SD} = \frac{16 m_N}{\pi v^2}\Lambda^2\, G_\mathrm{F}^2\, J(J+1)\frac{S(E_\mathrm{R})}{S_0} \tag{2.14}$$

where J is the total angular momentum, S is the spin form factor and Λ is defined as [43]

$$\Lambda = \frac{1}{J}[a_p\langle S_p\rangle + a_n\langle S_n\rangle] \tag{2.15}$$

Here, S_p and S_n stand for the expectation values of the spin content of the proton and the neutron groups in the nucleus, respectively and a_p and a_n are the coupling constants to the proton and neutron spin, respectively. Should the target nuclei have little or no net spin, as for the case of CRESST which uses $CaWO_4$ as the target, then the spin-dependent part can be neglected.

The spin-independent cross-section, on the other hand, follows

$$\left(\frac{\mathrm{d}\sigma_{WN}}{\mathrm{d}E_\mathrm{R}}\right)_{SI} = \frac{m_N\sigma_0 F^2(E_\mathrm{R})}{2\mu_N^2 v^2} \tag{2.16}$$

where F is the nuclear form factor for coherent interactions.

If one considers the contribution from the scalar coupling, then the WIMP-nucleon cross-section at zero-momentum transfer becomes [43]

$$\sigma_0 = \frac{4\mu_N^2}{\pi}[Z\, f^p + (A-Z)f^n] \tag{2.17}$$

where Z is the atomic number, A is the atomic mass number, and f^p and f^n are the coupling constants to proton and neutron mass, respectively.

The last type of parameters are the detector parameters, such as A, m and E_T, and these depend on the selected target material and the experimental setup. The detection threshold E_T becomes significant; especially if the search is focused on low-mass dark matter particles. As E_T goes down, the capability of detecting low-energy nuclear recoils improves (see also fig. 2.6). The parameters A and m of the target material are also important as they have a direct effect on the interaction of the particles with the target. According to different mass ranges, various types of detectors have been built over the years which will be the topic of next section.

The parameters $\sigma_{\chi N}$ and m_χ are free parameters, i.e. they should be determined by the outcome of the experiment. In case of no observation, direct detection experiments set limits on $\sigma_{\chi N}$ with respect to m_χ. To provide a comparability between experiments using different target materials, one has to scale $\sigma_{\chi N}$ to the dark matter particle-nucleon cross-section $\sigma_{\chi n}$.

2.5.2. Detection Techniques

The energy transfer which occurs through a dark matter scattering off of a nuclei can be usually observed via three different signal channels: heat (phonons) production, emission of scintillation photons after the target atom is excited and direct ionization of target atoms. Either one channel or a combination of two channels are used in the direct detection experiments. Figure 2.7, gives and overview of different channels and their combinations in several direct detection experiments. Although all three signals can be used together, there is no experiment currently making use of three of them at the same time.

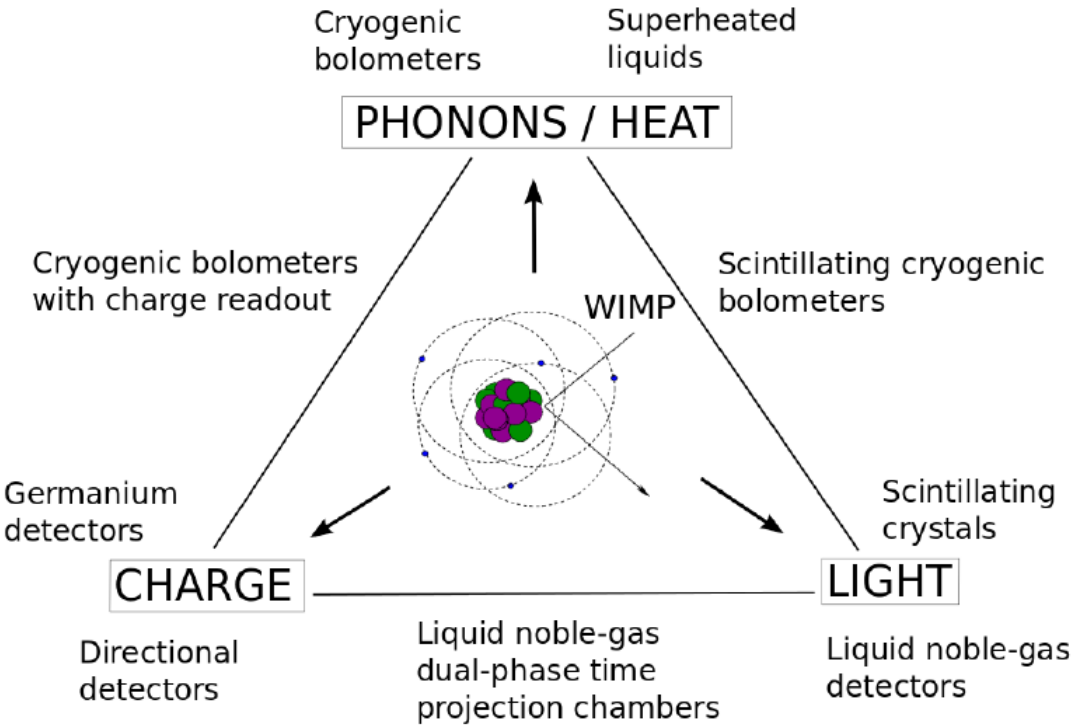

Figure 2.7.: Different dark matter direct detection mechanisms: while some experiments use only one signal channel, others use a combination of two different signal channels to reject backgrounds. Figure taken from [84].

There are many experiments which use only one channel to search for a dark matter particle signal. DAMA/LIBRA [41, 42], XMASS [110] and DEAP-3600 [19] use only the

light channel whereas CoGeNT [1], DAMIC [13] and CDEX [111] use only the ionization channel.

However, using two signal channels at the same time can be a powerful tool to reject background, i.e. SM processes which mimic the searched-for dark matter induced signal. The partition of the total deposited energy on the different signal channels depend on the type of interacting particles [84]. This makes it possible to discriminate between electronic recoils, e.g. caused by Compton scattering or beta-decays, and nuclear recoils, e.g. caused by a potential dark matter scattering. However, it is not possible to distinguish a potential dark matter induced nuclear recoil from a neutron induced nuclear recoil on an event-by-event basis. Hence, neutrons are usually a very dangerous background. SuperCDMS [11] and EDELWEISS [32] are using the combination of heat (phonons) and ionization. XENON1T [28, 29], LUX [14] and DarkSide-50 [7] are using a combination of light and ionization signals. Finally, the CRESST [95] experiment is the only experiment so far to put a combination of heat and light signals into use in the search for dark matter.

2.5.3. Current Status

Over the years, several direct detection experiments were operated in different labs using different detector technologies. With the data they gathered, these experiments set upper limits on the cross-sections between dark matter particles and nucleons. Such an exclusion plot showing the latest results from different direct detection experiments searching for spin-independent elastic dark matter-nucleon scattering can be seen in fig. 2.8. Currently, the lowest cross-section with $\sigma_{\chi N} \leq 7.7 \cdot 10^{-47}\,\mathrm{cm}^2$ at $m_\chi = 35\,\mathrm{GeV/c}^2$ is obtained by XENON1T [29]. So far, no dark matter signal has been unambigously observed. The DM interpretations of the signals observed with CoGeNT [1], CDMS-Si [10] and most famously DAMA/LIBRA [41, 42][2] are not unanimously accepted by the community.

As mentioned earlier section 2.3, different models have been developed to provide a particle explanation of dark matter. Consequently, the mass of the predicted dark matter particle is model dependent, e.g. $\mathcal{O}(100\,\mathrm{GeV/c}^2)$ for the WIMP or $\sim 5\mathrm{GeV/c}^2$ for ADM (see section 2.3). Masses above roughly 5 GeV are mostly considered belonging to a *high mass* range whereas below this energy, the possible dark matter particle is considered as *low mass*.

On the one hand, for high-mass dark matter particles, the most important parameter is a high exposure because the incident dark matter flux decrease with increasing particle mass if the dark matter density is fixed (see section 2.5.1). This leads to liquid noble gas detectors (e.g. XENON1T [28], DarkSide-50 [7], PandaX-II [107]) taking the lead in the search as the amount of liquids which are used as target in these experiments can be at the level of tons. The multistage XENON experiment is one of the lead experiments in the search for high-mass dark matter, its latest results from its XENON1T is shown in fig. 2.8 as blue dashed line.

[2] DAMA/LIBRA does not provide an official analysis of their observation in the $\sigma_{\chi N}$ vs m_χ plane. Therefore, it is not shown in fig. 2.8.

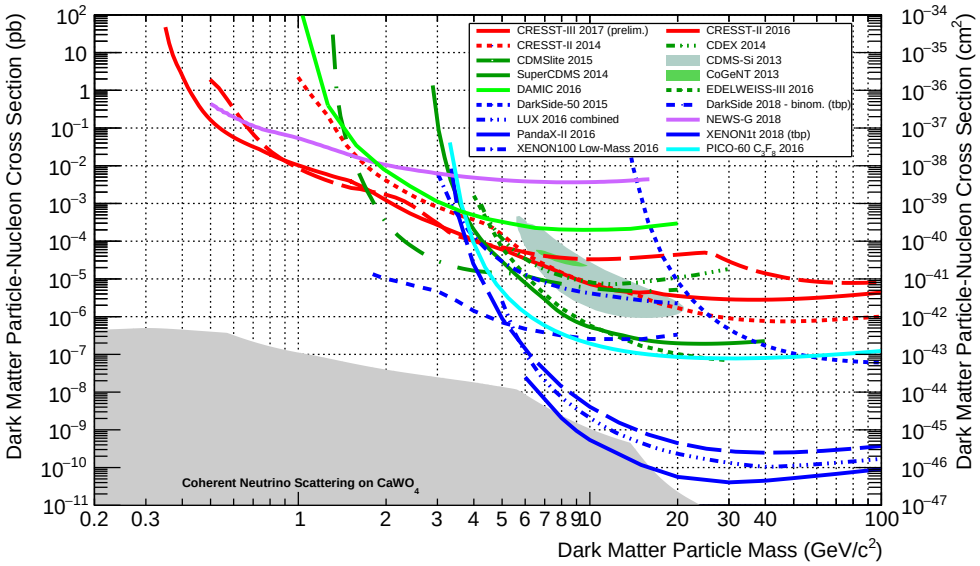

Figure 2.8.: Current upper limits on dark matter particle-nucleon cross-sections with respect to the dark matter particle mass for spin-independent elastic scattering. Results from different stages of various experiments are shown: CRESST-III 2017 (prelim) [95], CRESST-II 2016 [25], CRESST-II 2014 [26], CDEX 2014 [111], CDMSlite 2015 [9], SuperCDMS 2014 [11], DAMIC 2016 [13], EDELWEISS-III 2016 [32], DarkSide-50 2015 [7], DarkSide 2018 - binom. (tbp) [8], LUX 2016 combined [14], NEWS-G 2018 [33], PandaX-II 2016 [107], XENON1T 2018 (tbp) [28], XENON100 Low-Mass 2016 [30], PICO-60 C_3F_8 2016 [21]. Also shown are the DM interpretations of the signal excess observed with CDMS-Si 2013 [10], and CoGeNT 2013 [1]. The bottom left shows the region for coherent neutrino scattering on $CaWO_4$ [67].

On the other hand, for low-mass dark matter searches, the most important parameter is the energy threshold of the detector which has to be lower than the deposited recoil energy which scales with the dark matter particle mass (see eq. (2.10)). Cryogenic detectors (e.g. SuperCDMS [11], EDELWEISS-III [32], CRESST-III Phase 1 [95]) achieve very low detection thresholds $E_{\mathrm{th}} \lesssim 1\,\mathrm{keV}$ and take the lead in this mass range. The CRESST experiment is the current lead in the low-mass direct dark matter search and is sensitive down to $350\,\mathrm{MeV/c^2}$ [95], its latest result can be seen in fig. 2.8 as solid red curve. In the next chapter, information regarding the experimental setup, the search for dark matter and the backgrounds of the CRESST experiment will be given.

3. The CRESST Experiment

In this chapter, an overview of the experimental setup of the CRESST experiment (section 3.1) and of the used detector modules will be given (section 3.2). Afterwards, we outline the working principle of low-threshold cryogenic detectors (section 3.3) and the definitions of event categories (section 3.4). Finally, we discuss the background management in the CRESST experiment (section 3.5), and introduce the data sets (section 3.7) we will use as reference for background simulation (chapter 4).

3.1. The Experimental Setup of CRESST

The construction of the CRESST Experiment dates back to 1995. The first stage of the experiment, namely CRESST-I, was significantly different from the current setup, using sapphire (Al_2O_3) crystals as target material. Since sapphire does not scintillate, only phonon signals were recorded [23]. With CRESST-II, the target material was changed to scintillating $CaWO_4$ crystals and the simulatenous readout of phonon and scintillation signals (see section 2.5.2) was established. Since then, the detector modules are equipped also with a dedicated light detector [25, 26, 27]. The Phase 2 of CRESST-II introduced new detector designs [104] and some of the crystals were produced at Technische Universität München with reduced background [89]. Based on the experience in CRESST-II Phase 2, the design of the CRESST-III detector modules was adapted and, most importantly, the mass of the $CaWO_4$ crystal was reduced in order to be able to explore the low dark matter mass regime [98]. The relation between detection threshold and target mass will be discussed in section 3.3. An overview of different phases of the CRESST experiment is given in table 3.1.

CRESST stands for *Cryogenic Rare Event Search with Superconducting Termometers*. For low-background rare event search experiments, protection from cosmic rays is a must. Hence, CRESST is operated at Hall A of the *Laboratori Natizonali del Gran Sasso* (LNGS) in the Apennine Mountains in central Italy.

To achieve a low detection threshold, the detectors are operated at $\mathcal{O}(10\,\mathrm{mK})$. Therefore, an important part of the CRESST experiment is placed inside a cryostat. A commercial dilution refrigerator provides the required temperature by circulating a mixture of He^3/He^4. A detailed description of this type of cryostat can be found in [53, 96].

A rare event search requires a low-background setup aiming to reduce dead time and improve signal-to-noise ratio. Even though most of the materials close to the detectors

Table 3.1.: An overview of different stages of the CRESST experiment in terms of data taking period, target material and references for details [98].

Stage	**Phase**	**Data Taking**	**Material**	**Comments**
CRESST-I	-	2000	Al_2O_3	only phonon detector [23]
CRESST-II	Commissioning	2007	$CaWO_4$	from now on with phonon and light detectors [22, 47]
	Phase 1	2009-2011	$CaWO_4$	first extensive science run [27]
	Phase 2	2013-2015	$CaWO_4$	upgraded detector modules with improved radiopurity [89] and background rejection capability [104] (see for dark matter analysis results [25, 26])
CRESST-III	Phase 1	2016-2018	$CaWO_4$	new detector modules optimized for low detection threshold [95]
	Phase 2	$\sim$ 2020	$CaWO_4$	planned future stage, aiming for a further improvement of the radiopurity of the crystals and an increase in exposure [24]

are selected for *radiopurity*, i.e. low contamination with radioactive nuclides, some not-so-radiopure materials, such as stainless steel, are unavoidable because of the cryogenic requirement [23]. Therefore, the design used for the CRESST setup (see fig. 3.1) features radiation shields against the dirtier parts of the cryostat, as well as a shielding against ambient backgrounds from natural radioactivity.

In this design, the outermost part of the setup is a polyethylene shield against neutrons. Inside the upper part of the polyethylene (PE) shield hangs the dilution refrigerator, which is partially filled with liquid nitrogen and liquid helium. The lower part of the cryostat extends to the *cold box*, which is made out of low-background copper. In addition, high-purity lead is used for vacuum seals [23]. As we will describe later, the cold box contains the detectors. Therefore, it is surrounded by additional shields inside the PE. The first layer inside the PE is the active muon veto which tags when a charged particle penetrates through it. The next layer is a gas-tight container, the so-called *radon box*, which insulates its interior from ambient radon gas by being constantly flushed by N_2 gas. The radon box contains a lead shield for protection from gamma rays. Since radiopure lead is not available, a copper shielding is placed inside the lead shielding. As copper is relatively easy to purify, it is used to protect the detectors from the beta, gamma and alpha decays occuring inside the lead shield without producing a similar amount of background. The copper shielding is the direct enclosing of the cold box which includes layers of internal copper and internal polyethylene shields. The detector modules are placed in the core of the setup, the so-called *carousel*. The carousel is held by the *cold finger* which provides the coupling between the carousel and the actual cryostat [98]. The effect of the shieldings on the backgrounds will be discussed in the section 3.5 in more detail, as it is directly related to this thesis.

3.2. Detector Design

As already mentioned, CRESST-II and CRESST-III utilize scintillating $CaWO_4$ crystals as targets. They are operated as cryogenic detectors at a temperature of $\mathcal{O}(10\,\mathrm{mK})$. Each interaction in the target crystal produces a phonon signal as well as a light signal which is measured by a nearby *Silicon-on-Sapphire* (SOS) disk. Signals from both the $CaWO_4$ crystal and the SOS disk are read-out by two separated *Transition Edge Sensors* (TES). A TES is a thin tungsten film operated in the steep transition region between normal conduction and superconduction. A small increase in the temperature results in measurably large increase of resistivity. This signal is read-out by SQUID sensors [22]. By using TES, a $CaWO_4$ crystal is turned into a *phonon detector* and the SOS disk into a *light detector*. Both detectors are surrounded by a reflective and scintillating plastic foil to increase the light collection efficiency. All these components form a detector module. Phonon and light detectors are equipped with a heater which stabilizes the temperature at the desired point between normal and super-conducting state and injects electrical pulses needed for energy calibration.

In its different phases, CRESST has used various detector designs. Designs of recent

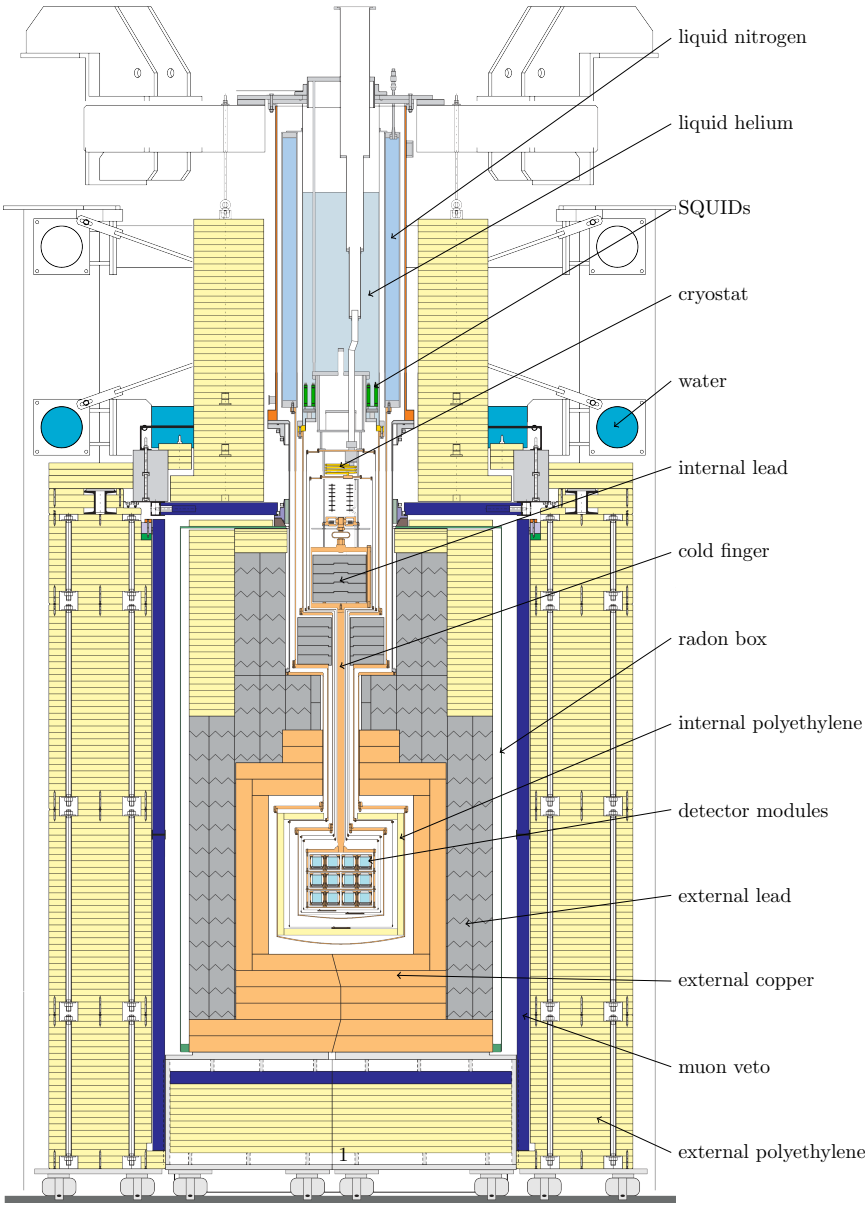

Figure 3.1.: Technical drawing of the CRESST experimental setup [76]. The cryostat holding the liquid helium and liquid nitrogen can bee seen at the top. Below the cryostat, the carousel holds the detector modules. The shielding consists of polyethylene, lead, an active muon veto and the air-tight radon box used against radon contamination from air.

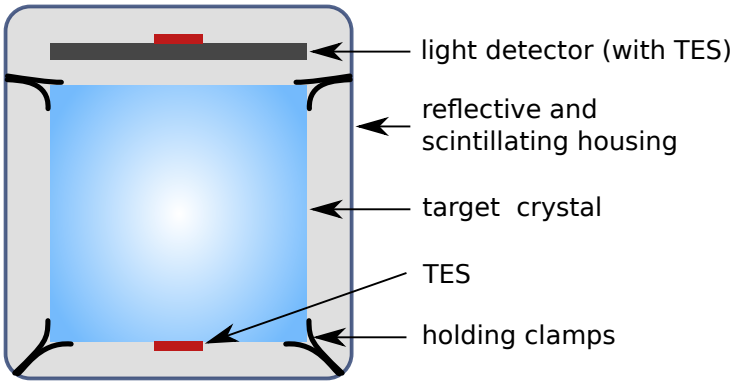

(a)

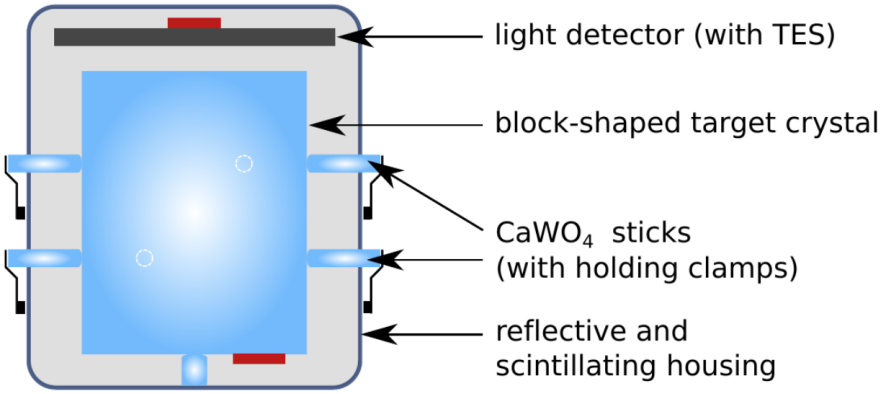

(b)

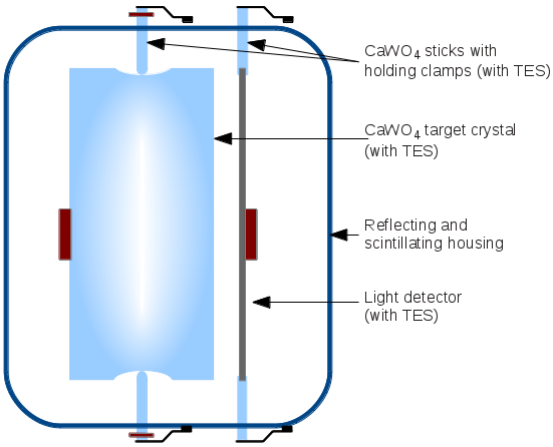

(c)

Figure 3.2.: Schematics of some detector modules operated in the CRESST experiment: The *Lise* (a) and *TUM40* (b) modules were operated in CRESST-II Phase 2, whereas *Detector A* (c) was operated in CRESST-III Phase 1. Figures provided by CRESST.

Table 3.2.: Properties of different detector modules used in the CRESST experiment: crystal mass M, detection threshold E_{th}, exposure $T \cdot M$ and background B between 1 keV and 40 keV.

Detector Module	M (g)	E_{th} (eV)	B ($\mathrm{kg}^{-1} \cdot \mathrm{keV}^{-1} \cdot \mathrm{day}^{-1}$)	Comments
Lise	300	307.3	8.5 [a]	crystal held by bronze clamps [25] (see also fig. 3.2a)
TUM40	249	603	3.51	crystal held by $CaWO_4$ sticks [26, 105] (see also fig. 3.2b)
Detector A	24	100 [c]	3.85 [b]	both crystal and light detector held by $CaWO_4$ sticks, which are instrumented [91, 95] (see also fig. 3.2c)

[a] Without background from an accidental irradiation with a ^{55}Fe source.
[b] Measured between 10-40 keV.
[c] The analysis threshold for Detector A of CRESST-III Phase 1 is 100 eV but the optimal detection threshold for this detector can go down to $\sim$ 26 eV [83, 95]. An analysis using the optimal threshold is currently under preparation.

detector modules used for dark matter searches can be seen in fig. 3.6: the design mostly used in the current CRESST-III Phase 1 is shown in fig. 3.2c and the designs shown in fig. 3.2a and fig. 3.2b were used in the previous CRESST-II. To illustrate the difference between these designs, table 3.2 gives the properties of one exemplary detector module (Lise, TUM40, Detector A) per design. For reasons which will be explained in the next chapter, the focus of this thesis will be on the TUM40 detector module. A detailed description of its geometry will be given in section 4.2, when we will be discussing its implementation into the simulation code.

As pointed out in the previous chapter, the CRESST experiment focuses on the low-mass regime in the search for dark matter particles. In order to be able to detect a low-mass signal, the detector in question should be able to detect very low recoil energies. The two main factors affecting the analysis of very low energies will be explained in the next section.

3.3. Low-Threshold Cryogenic Detectors

The rise of the temperature ΔT of a target material after an energy deposition of ΔE is given in a simplified model by

$$\Delta T = \frac{\Delta E}{C} \ , \ C = c \cdot m \tag{3.1}$$

and this constitutes the basis of cryogenic calorimetry. Here, C stands for the heat capacity and c for the specific heat of the target material. Since the heat capacity is approximately proportional to T^3, because it follows the Debye law[1], calorimetric measurements of very small energy depositions are possible if used with a low-heat-capacity absorber at low-enough temperatures [43]. With crystalline materials working at mK-temperatures, a small heat capacity can be achieved. A decrease in heat capacity leads to a temperature increase for a given energy deposit, which results in high sensitivity to small energy changes [106].

Another factor affecting the detection threshold is the mass of the target detector. A study of cuboid target crystals [106] found that the energy threshold E_{th} for phonon detection and the detector mass M is related as follows:

$$E_{\text{th}} = \text{const.} \times M^{\frac{2}{3}} \tag{3.2}$$

The *constant* in this equation depends on the material and the geometry of the crystal, but not on the size. The results of the study for Al_2O_3 and $CaWO_4$ calorimeters, with respect to the target mass, can be seen in fig. 3.3. By decreasing their mass down to $\mathcal{O}(10\,\text{g})$, cryogenic detectors can achieve energy thresholds as low as $\mathcal{O}(100\,\text{eV})$ [95].

[1] According to the Debye model, at low temperatures, the heat capacity takes the form $C_V(T) = \frac{12}{5}\pi^4 \cdot N \cdot k_B \frac{T^3}{T_D^3}$ where N is the number of unit cells of the crystal, k_B is Boltzmann's constant and T_D is the Debye temperature. This model is valid for $T \ll T_D$ [66].

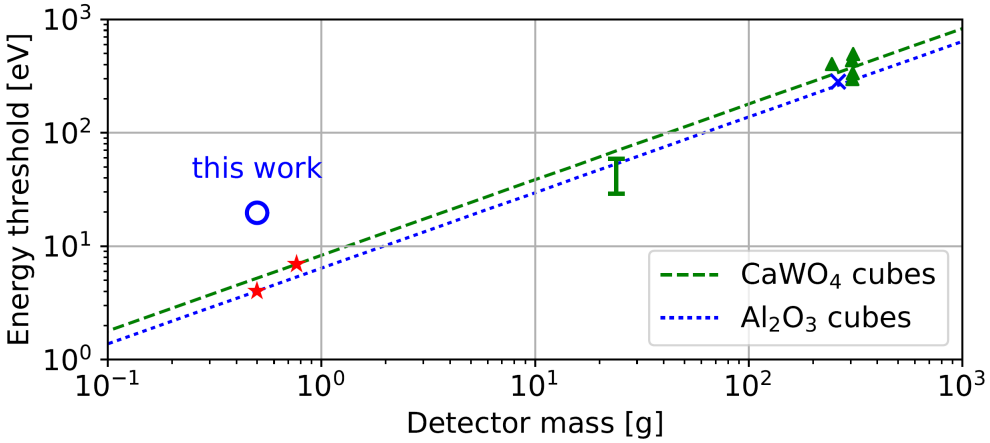

Figure 3.3.: The scaling law (eq. (3.2)) of the theoretical achievable energy threshold as function of the target mass for Al_2O_3 (blue dashed line) and $CaWO_4$ (green dashed line) targets fitted to data obtained with cryogenic Al_2O_3 (triangles) and $CaWO_4$ (cross) detectors [25, 26, 86]. $M^{\frac{2}{3}}$ behaviour can be observed for most data points, except "this work" [106], which was obtained in a non-optimized environment. Red stars show the expected values for the prototype described in [106] under low-background conditions. Figure taken from [106].

How a decreased detection threshold affects the dark matter analysis can be seen by looking at the latest results from the CRESST Experiment in fig. 3.4: the red dashed line is the upper limit on dark matter-nucleon cross-section resulted from the analysis of the detector *Lise* which is the detector with the lowest detection threshold operated in CRESST-II Phase 2 [25]. The *Lise* detector module had $\sim 300\,\mathrm{g}$ of $CaWO_4$ crystal as the target and featured a detection threshold of $E_{\mathrm{th}} = (307.3 \pm 3.6)\,\mathrm{eV}$ [25]. In CRESST-III Phase 1, the CRESST experiment uses new detector modules with $CaWO_4$ crystals of 24 g each as targets, aiming for a detection threshold of 100 eV. The first results from one of the new detector modules can be seen on fig. 3.4 as solid red line [95]. As can be seen here, decreasing the detection threshold improves the sensitivity for low-mass dark matter. Lise can detect dark matter particle masses down to $500\,\mathrm{MeV/c^2}$ with its detection threshold of $E_{\mathrm{th}} = (307.3 \pm 3.6)\,\mathrm{eV}$ [25]; using an analysis threshold[2] of 100 eV the CRESST-III detector module *Detector A* used in [95] could improve its sensitivity for dark matter particles with masses down to $350\,\mathrm{MeV/c^2}$.

The significance of reaching a lower energy threshold comes from the fact that the count rate of possible low-mass dark matter particles increases strongly as the energy threshold of the detector decreases as discussed in section 2.5.

[2]The analysis threshold for Detector A of CRESST3 Phase 1 is 100 eV but the optimal detection threshold for this detector can go down to $\sim$ 26 eV [83, 95]. An analysis using the optimal threshold is currently under preparation.

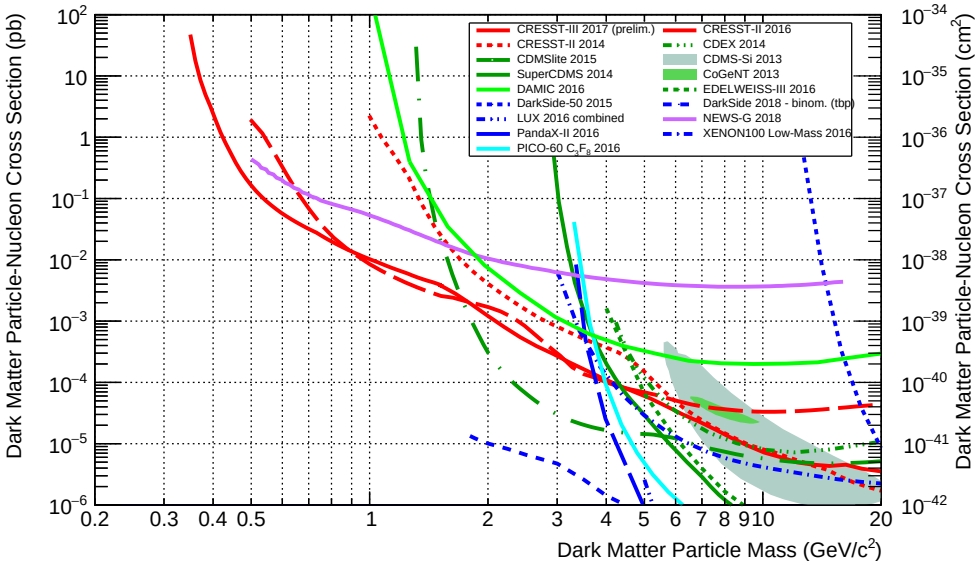

Figure 3.4.: The plane of dark matter particle-nucleon cross-section as a function of the dark matter particle mass for spin-independent scattering with focus on the low-mass range below 20 GeV/c^2. CRESST-III 2017 (prelim) [95], CRESST-II 2016 [25], CRESST-II 2014 [26], CDEX 2014 [111], CDMSlite 2015 [9], SuperCDMS 2014 [11], DAMIC 2016 [13], EDELWEISS-III 2016 [32], DarkSide-50 2015 [7], DarkSide 2018 - binom. (tbp) [8], LUX 2016 combined [14], NEWS-G 2018 [33], PandaX-II 2016 [107], XENON100 Low-Mass 2016 [30], PICO-60 C_3F_8 2016 [21]. Also shown are the DM interpretations of the signal excess observed with CDMS-Si 2013 [10], and CoGeNT 2013 [1].

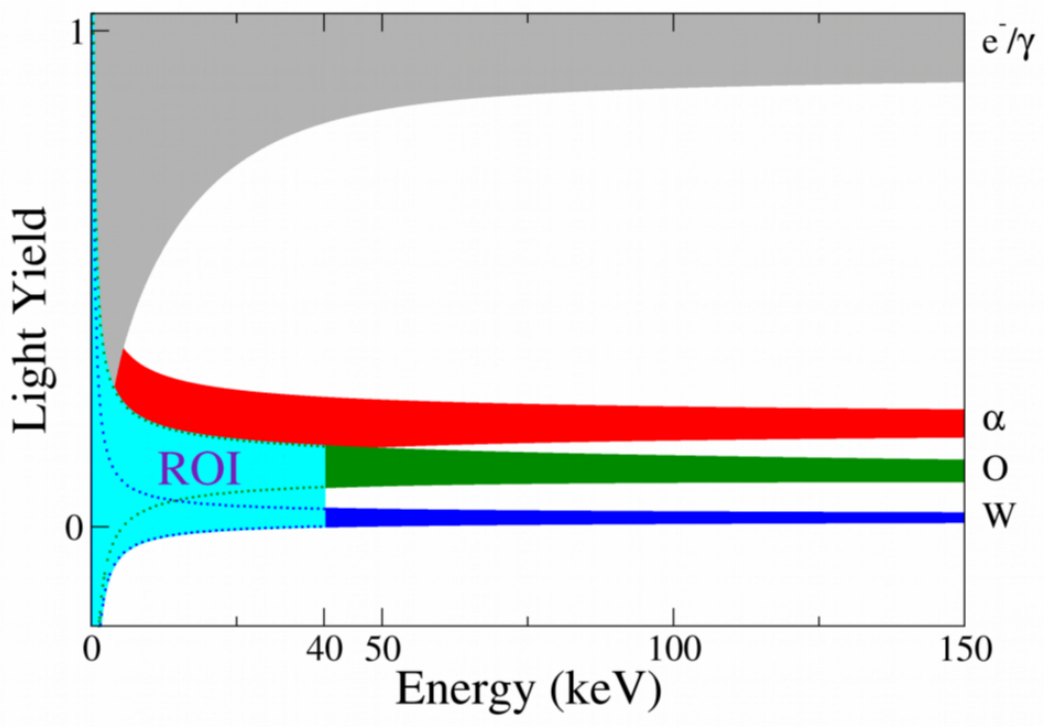

Figure 3.5.: An example light yield plot with different bands showing different event types: electromagnetic interactions (grey) alpha interactions (red), oxygen (green) and tungsten (blue) recoils. The calcium recoil band between these two is not shown for the purposes of clarity. Also shown is the region of interest (ROI, cyan) for a possible signal of dark matter particle.

3.4. Event Categories

As briefly discussed in section 2.5.2, the combination of the two signal channels allows a particle identification in cryogenic detectors. In case of CRESST-II and CRESST-III, the two signal channels are the phonon and light channels. Using the combination of these two signals, one can identify the type of recoil via the *Light Yield* (LY), defined by the following equation:

$$LY = \frac{\text{Light Energy}}{\text{Phonon Energy}}. \tag{3.3}$$

Figure 3.5 shows Figure 3.5 shows the expected light yield with respect to the deposited energy. As can be seen, a number of bands emerge, separated by their respective light yields. For calibrating the light yield, a ^{57}Co source is used. The light yield caused by the 122-keV gamma-line is normalised to $LY = 1$. Then, electronic test pulses with different equivalent energies are used to linearise the detector response. Test pulses are periodically injected throughout the whole data taking period to account for the potential time variations of the detector response. Different bands indicate the interaction of incident particles

with the different target particles in the detector: starting from high light yield values to lower ones, these are e^-/γ scattering off electrons, interaction of alphas and finally dark matter particles or neutrons recoiling from O-, Ca- and W-nuclei. The latter three are collectively called nuclear recoil bands. A signal from a potentially dark matter scattering is expected in the nuclear recoil bands. The exact area for this *region of interest* (ROI)[3], depends on the actual analysis. The ROI in fig. 3.5 is only for illustration. The e^-/γ band includes most of the radioactive background, well-separated from nuclear recoil bands at high energies. However, the purity of the ROI suffers from a leakage of events from the electron/gamma band at lower energies. This complicates the dark matter analysis performed in this region since the expected rate of dark matter particle is low, a signal may not be seen because of the leakage, or an unknown background can be mistaken for a signal event.

3.5. Background Sources and Their Management

As discussed in section 3.4, CRESST can distinguish the nuclear recoils, which may be a signal for dark matter, from the electromagnetic interaction due to radioactive background via the light yield. However, the expected rate of dark matter events is low compared to the usual rate of radioactive decays in the environment and other sources producing nuclear recoils, as well. The detectors have to be shielded against these background sources and the remaining backgrounds have to be carefully studied. In this section, the main background sources and the applied methods to reduce and analyse them will be discussed in detail.

3.5.1. Muons

One important source of background for rare event search experiments above ground are cosmic rays. Specifically, high energetic atmospheric muons can easily penetrate through meters-thick layers of shielding. For this reason, the CRESST experiment is located in the LNGS in Italy, which is covered approximately by minimum 1400 meters of rock. This provides (3.1 ± 0.2) kilometers of water equivalent shielding [85]. The remaining muon rate is approximately $\mathcal{O}(1\,\mathrm{h}^{-1}\mathrm{m}^{-2})$ [20], i.e. it is reduced by about six orders of magnitude compared to the surface of the Earth.

Even though the amount of muons which can penetrate through the rock and reach the detectors is very low, they can still induce background events in detectors. One way this could happen is by producing secondary particles in their interactions with rock or the material of the experimental setup. Furthermore, they can directly deposit energy in the detectors. To be able to reject such events, CRESST is equipped with a *muon veto* which can be seen in fig. 3.1. The veto consists of 20 plastic scintillator panels, read out by photomultipliers and covering 98.7 % of the solid angle around the detectors. The reason

[3] For the dark matter analysis with the TUM40 detector, a ROI between 0.6 keV and 40 keV is used [26]. However, in order to make a one-to-one comparison with the previous background analysis [105] possible, the ROI for this work is chosen between 1 keV and 40 keV.

why the coverage is not 100 % is that an opening is needed on the top to leave space for the cryostat [27]. If an event is detected by this system, all events within a certain time window are rejected.

3.5.2. Ambient Gamma Radiation

Another type of backgrounds are gamma rays, originating from the rock and concrete of the site where CRESST is located. The sources of this radiation are gamma-decays along the natural radioactive decay chains of ^{238}U, ^{235}U and ^{232}Th, but also individual radioactive nuclides like ^{40}K. The integrated gamma ray flux in Hall A of LNGS for energies below 3000 keV was measured to be $(0.28 \pm 0.02)\,\mathrm{cm}^{-2}\mathrm{s}^{-1}$ [68].

To shield the experiment against this radiation in Hall A of LNGS, CRESST detectors are surrounded by lead shield of 24 tons and 20cm-thickness. In addition, 98 kg of lead is placed directly below the mixing chamber of the cryostat followed by an additional 232 kg below this. Most of this 330 kg of lead is produced by the company Boliden in Sweden. However, the lowest layers of lead bricks are produced by the company Plombum in Poland [81]. With its high density and atomic number, it is ideally suited to absorb gamma rays. However, lead is not a very radio-clean material and its naturally occuring radioactive nuclides like ^{210}Pb can create backgrounds of its own, contributing to the background observed in the experiment.

In order to prevent this, a copper shield of 10 tons and 14 cm thickness is placed between the cold box which contains the detectors and the lead shield (see fig. 3.1). In contrast to lead, copper can be produced with a very low level of internal radioactivity as it has no naturally occuring radiactive isotopes. This makes copper not only a more expensive but also a more favorable shielding material which can be used closer to the detectors. In addition, it is also used for the structures inside the cold box, such as holders for the detectors of the CRESST experiment (see section 4.2). However, even if copper can be produced with low contamination levels, it stays a non-negligible background source due to its closeness to the detectors [105].

3.5.3. Cosmogenic Activation

As explained before, rare event search experiments operate underground to protect them from cosmic rays. However, there is a chance that some long-lived radioactive impurities in the experimental material might be activated due to exposure to cosmic rays [48]. This phenomenon is called *cosmogenic activation*.

One of the processes causing cosmogenic activation is spallation of nucleons in parts of the experimental setup by highly energetic nucleons from the cosmic rays. In addition, reactions such as induced fusion, capture and fragmentation can also be significant for the occurances of cosmogenic activation [48].

For $CaWO_4$, two X-ray lines below 80 keV are reported [80, 105] caused by the decays of cosmogenic nuclides.

One line occurs due to cosmogenic activation of ^{182}W. The process, proton capture followed by EC, leads to the occurance of the line as follows [80]:

$$^{182}\mathrm{W} + \mathrm{p}^{+} \longrightarrow {}^{179}\mathrm{Ta} + \alpha \tag{3.4a}$$

$$^{179}\mathrm{Ta} + \mathrm{e}^{-} \longrightarrow {}^{179}\mathrm{Hf}^{*} + \upsilon_{\mathrm{e}} \tag{3.4b}$$

$$^{179}\mathrm{Hf}^{*} \longrightarrow {}^{179}\mathrm{Hf} + \mathrm{X-ray} \tag{3.4c}$$

The *electron capture* (EC) signatures in TUM40 is equal to the binding energy of the shell electrons of ^{179}Hf. Peaks originated from this decay can be seen clearly in fig. 3.7 at energies 2.60 keV (M1-shell), 10.74 keV (L2-shell), 11.27 keV (L1-shell) and 65.35 keV (K shell).
Another cosmogenically activated nuclide is ^{183}W. The activation occurs as follows [80]:

$$^{183}\mathrm{W} + \mathrm{p}^{+} \longrightarrow {}^{181}\mathrm{W} + {}^{3}\mathrm{H} \tag{3.5a}$$

$$^{181}\mathrm{W} + \mathrm{e}^{-} \longrightarrow {}^{181}\mathrm{Ta}^{*} + \upsilon_{\mathrm{e}} \tag{3.5b}$$

$$^{181}\mathrm{Ta}^{*} \longrightarrow {}^{181}\mathrm{Ta} + \gamma + \mathrm{X-ray} \tag{3.5c}$$

Activation through $^{183}\mathrm{W}(p,t)$ results in the nuclide ^{181}W. This then decays into an excited state of ^{181}Ta through EC and it de-excites with a 6.2 keV gamma emission. Thus, the most prominent energy signature for this decay is the binding energy of the K-shell electron of Tantalum with energy 67.4 keV and 6.2 keV coming from the energy of the gamma. They add up to give 73.7 keV [80].

An already mentioned (see eq. (3.5a)) common nuclide which can be cosmogenically produced in a wide range of target materials is ^{3}H [112]. Albeit, it is not yet experimentally observed for $CaWO_4$, eq. (3.5a) indicates that the observed ^{181}W should be accompanied by a ^{3}H component. Other reaction paths to create ^{3}H in $CaWO_4$ may also be possible. A study [48] based on the TALYS simulation code [78] predicts a total ^{3}H production rate of 45.5 $\mathrm{kg}^{-1}\mathrm{day}^{-1}$ for $CaWO_4$. Given the low end point of the ^{3}H decay spectrum of 18.592 keV [69], we note that any significant ^{3}H contribution to the CRESST background would be of great interest for the search of low-mass dark matter.

3.5.4. Ambient Neutrons

Neutrons constitute a significant background source, as neutron induced nuclear recoils can mimic a possible signal, i.e. dark matter induced nuclear recoils. One way neutrons can be produced is through muons (see section 3.5.1), interacting in the rock or with the material of the experiment. As the production yield for muon-induced neutrons increases with the atomic number, lead is an ideal neutron source. The other neutron production mechanisms include fission of heavy nuclei or (α, n)-reactions on light elements. The total neutron flux measurements in LNGS shows a value of nearly $19 - 30\,\mathrm{m}^{-2}\mathrm{h}^{-1}$ [38].

The muon veto described in section 3.1 enables CRESST to reject events potentially caused by neutrons which are produced by muons inside the experimental setup. To

protect the detectors from neutrons produced outside the experimental setup, a PE shield of 50 cm thickness is installed (see fig. 3.1). Elastic scatterings of the incoming neutron on the hydrogen in the PE can help to decrease the kinetic energy of neutrons. These slowed-down neutrons can be captured by the hydrogen, with a subsequent release of a 2.2 MeV-gamma, or if they reach the detector, their reduced kinetic energy is ideally below the detection threshold [101]. Since CRESST-II Phase 2 also *internal* PE shields are installed inside the cold box. They attenuate neutrons originating in the Pb and Cu shields. Since their installation, no distinct neutron signal, i.e. multiple nuclear recoils, were observed anymore.

3.5.5. Radon Gas

An additional background source is ^{222}Rn, created via the ^{238}U natural decay chain. It diffuses out of rocks and the radon activity in LNGS was measured to be $\sim 50\,\mathrm{Bq}\cdot\mathrm{cm}^{-3}$ [34]. Even though the origin of radon is similar to the origin of the ambient gamma rays, the effect is different: It can get attached to surfaces close to the detector and, therefore, expose the detector to relatively short range alpha and beta radioactivity caused by its decay products, e.g. alpha-decay from ^{210}Po and beta-decay from ^{210}Pb.

To stop radon from penetrating through the shielding and reaching the detectors, copper and lead shieldings are placed inside a gas-tight container the so-called *radon box* (see fig. 3.1). This container is flushed constantly with clean nitrogen gas and the pressure of the gas is kept slightly at overpressure [101].

However, radon gas in the air can pose problems during the production and installation of the detectors. Therefore, measures have been taken to minimize the exposure of the detectors to air. With additional efforts, such as electro-polishing, the surface contamination of copper can be reduced [101].

3.5.6. Near-Surface Alpha-Decays

Most detector modules in CRESST-II had a background coming from surface contaminations, mostly caused by ^{210}Po alpha-decays. A possible source for ^{210}Po is the contamination of the surface with radon (see section 3.5.5). If a ^{210}Po nucleus decays on the surface of the target crystal or on the surface of the crystal holder, the daughter nucleus ^{206}Pb can enter the crystal and deposit up to 103 keV. Since the light emission from these types of events is very low, they turn out to be similar to W-recoils. Hence, this would look like a possible dark matter signal. These ^{206}Pb events are only distinguishable if the emitted alpha generates light in a scintillating material around the target crystal (see section 4.2). This additional scintillation light would increase the light yield of the event and move it above the W-recoil band. However, most of the detector modules previous to CRESST-II Phase 2 hold the crystal with bronze clamps (see fig. 3.2a), which do not scintillate. Hence, if the alpha hits by chance the bronze clamp and not the scintillating foil around the target, the ^{206}Pb event is indistinguishable from W-recoils. In order to remove this type of background, scintillating $CaWO_4$ sticks were introduced as crystal holders with TUM40

(see fig. 3.2b). When a ^{206}Pb surface event happens in TUM40, additional scintillation light is produced, even if the produced alpha hits the crystal holder, and increases the light yield. This helps to differentiate the surface events from W recoils. That was the main advantage of the TUM40 detector module being based on this new *stick design* [104].

3.5.7. Internal Contamination of $CaWO_4$

As discussed earlier, all $CaWO_4$ crystals in CRESST-II Phase 1 and some in Phase 2 were commercial crystals produced by the Scientific Research Company "Carat" (SRC "Carat") in Ukraine and the General Physics Institute of the Russian Academy of Sciences (GPI RAS) in Russia. A series of measurements found the contamination of these crystals by alpha-emitters from the natural decay chains in the energy range between 1.5 MeV and ∼7 MeV to be between $(3.05 \pm 0.02)\,\mathrm{mBq\,kg^{-1}}$ and $(107.13 \pm 0.14)\,\mathrm{mBq\,kg^{-1}}$, depending on the actual crystal [89]. Even though the energy of alpha decays are outside the ROI for the dark matter searches, i.e. <40 keV, the subsequent decay chains contain also beta- and gamma-decays that deposit energy in the ROI. With the aim to improve the radiopurity and scintillation properties (e.g. light output of the crystals) by screening and purifying the raw materials, as well as to prevent contaminations during the crystal growth and after-growth treatment, it was decided to produce the $CaWO_4$ crystals within the collaborationt [89]. A Czochralski furnace at the crystal laboratory of *Technische Universität München* was used [55]. After a series of growth processes, the TUM40 crystal was produced and installed in a detector module of the same designation (see fig. 3.2b). A measurement of the alpha-activities showed an activity as low as $(1.23 \pm 0.06)\,\mathrm{mBq\,kg^{-1}}$, with the TUM40 crystal having an activity of $(3.07 \pm 0.11)\,\mathrm{mBq\,kg^{-1}}$ [89]. The effect of the reduced alpha-activity on the energy region below 80 keV can be seen in fig. 3.7. The beta and gamma emissions, e.g. caused by the decay of ^{210}Pb, are also reduced since they originate from the same natural decay chains as the measured alpha decays. Depending on which commercial crystal TUM40 is compared to, a factor of 2 to 10 decrease in the beta/gamma background in the region of interest was obtained. After all the cleaning efforts and production steps, the average rate of background events in the energy range between 1 and 40 keV amounts to 3.51 $\mathrm{kg^{-1}\,keV^{-1}\,day^{-1}}$ [105].

Even though the amount of background reduction at TUM40 is significant, there still remains an irreducible amount of beta/gamma background at low energies, with the potential to leak into the ROI for dark matter searches. Therefore, a further background reduction is planned for the future CRESST-III phase, via improved radiopurity and improved detector designs [24]. However, these efforts are time consuming and complicated. Hence, it is of great importance to understand the contribution of each background source using the experimental data in hand. For this, the construction of a background model is crucial. The next chapter will focus on the construction of a background model using the Monte Carlo framework Geant4. The topic of the next section will be the already existing semi-empirical background study for CRESST [105].

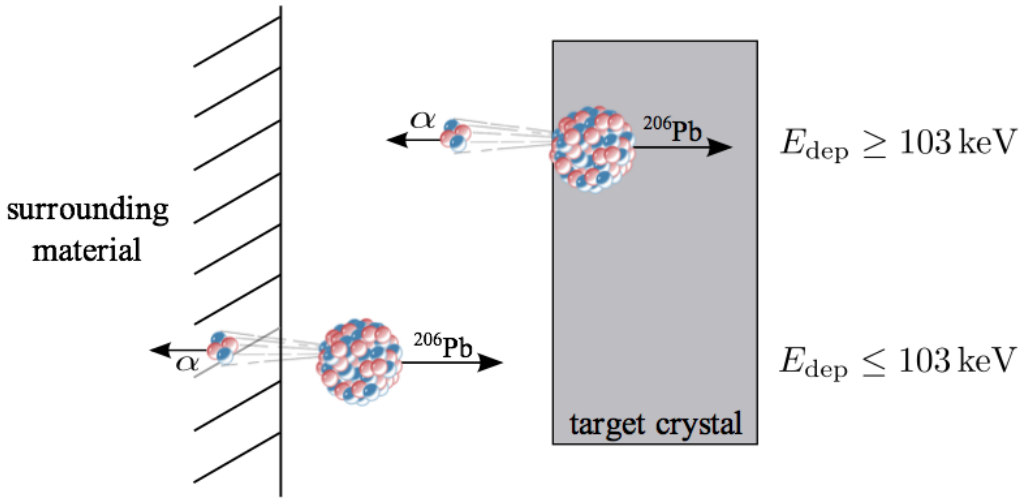

(a)

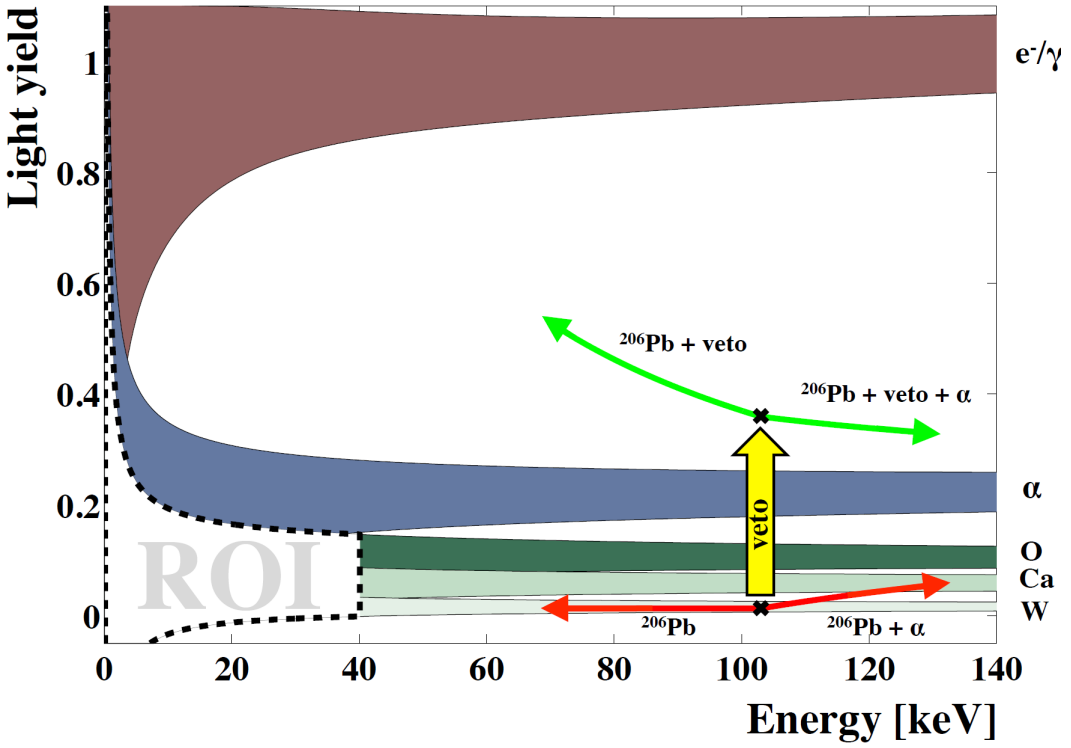

(b)

Figure 3.6.: An illustration of a ^{210}Po $\longrightarrow$ ^{206}Pb+α decay taking place close to the surface of the target crystal or in the surrounding material (a) and the change in the resulting light yield value when a scintillating housing is used (b). Figures taken from [104].

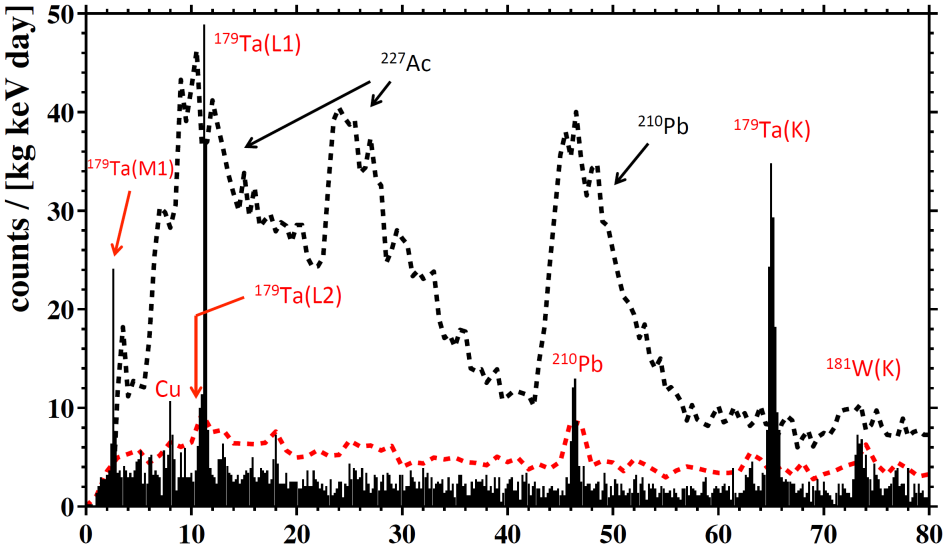

Figure 3.7.: Count rate spectra for detector modules with commercial $CaWO_4$ crystals and those grown at *Technische Universität München*: *VK31* is a typical commercial crystal with an average rate of 30 counts/(kg · keV · day) (dashed black line). With an average 6 counts/(kg · keV · day) *Daisy* is the commerical crystal with the lowest background rate (dashed red line). The black histogram shows the events recorded with *TUM40* with an average rate of 3.51 counts/(kg · keV · day) [105]. Most prominent peaks are labelled. Figure taken from [105].

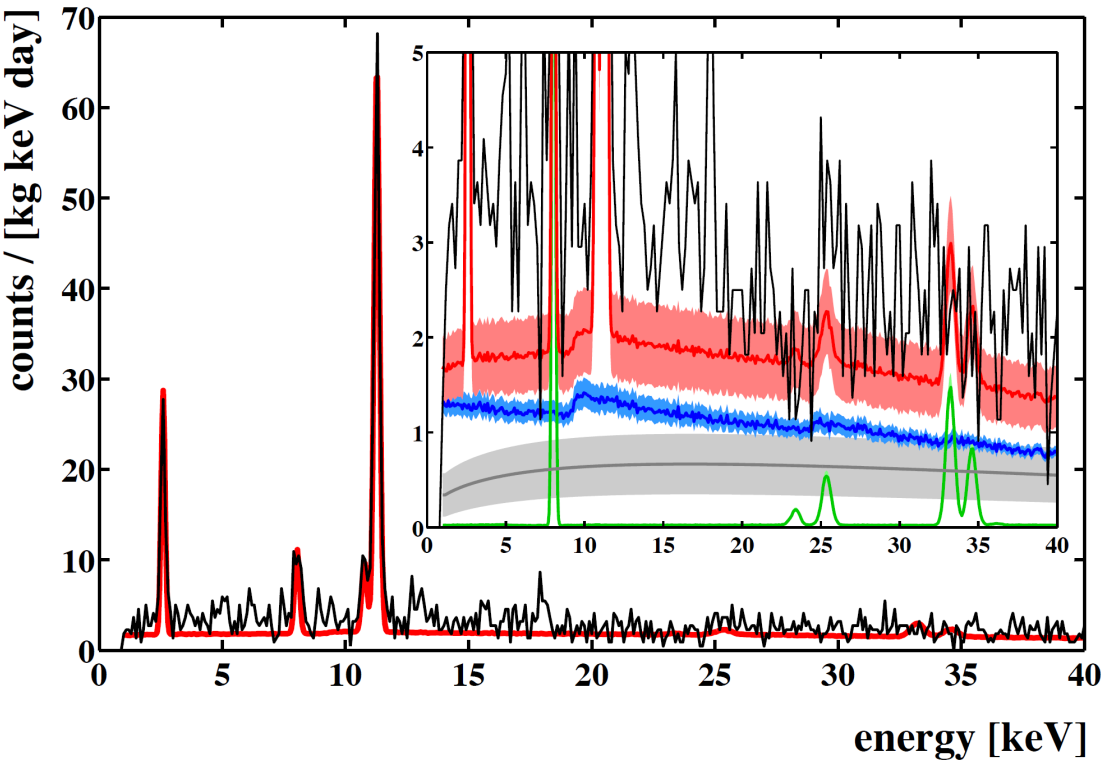

Figure 3.8.: Comparison of the semi-empirical background analysis [105] with data (black) recorded with TUM40: internal beta/gamma radiation from natural radioactive decay chains (blue) the contributions from the external gamma rays (green), both based on a Geant4 simulation. The grey band shows an empirical fit which stands for external betas. Finally, the red line shows the sum of these individual contributions as well as fits to the observed peaks caused by cosmogenic activation (2.6009 keV, 10.74 keV and 11.271 keV) and the copper fluorescence line (8.04 keV). Figure taken from [105].

3.6. Previous Work on Background Sources in CRESST

So far, there have been two different background analyses performed for CRESST: one for CRESST-II Phase 1 [80] and one for CRESST-II Phase 2 [105]. The latter work holds great importance, as this work is a continuation of it and the analysis performed for [105] is specific to the TUM40 detector module. In [105], a simple geometry implementing only the $CaWO_4$ crystal of TUM40 was used for a Geant4 (see section 4.1.1) based study of backgrounds. Identified alpha lines in the high energy region (4-7 MeV), belonging to the natural decay chains, were used as a starting point to get the activities of internal beta/gamma-decays assuming a secular equilibrium between them (see section 5.1). After simulating fourteen most-prominent beta-/gamma-decays from the natural decay chains, they were scaled according to the activities calculated from the sideband measurements

of their alpha-decaying parents.

In the previous work, only a bare $CaWO_4$ crystal is used, but no other detector parts around the crystal. In order to simulate these eight identified external contaminants, the following approach is used: Since the external contaminants are identified by their characteristic gamma emissions, these gamma rays are simulated to approximate the external contaminants instead of using the nuclides they originate from. An imaginary spherical shell around the $CaWO_4$ crystal is created. From the inner surface of this spherical shell, gamma rays are shot to the crystal with the energies of the identified lines. Once a gamma ray hits the crystal, the deposited energy is collected. An image of the visualisation of this simulation is shown in fig. 4.14a.

However, there are events in the experimental data with light yields higher than expected. These events are called *excess light events* and they are thought to come from external betas, hitting the scintillating foil and creating additional light. Based on dedicated measurements, it was understood that beta particles produce nearly a fixed amount of scintillation light with an energy of $\mathcal{O}(1\text{keV})$, and considering the deposited light energy from these events is fixed, the excess in light yield increases as the energy goes down [105]. Since the geometry used in [105] only includes the crystal but not the foil, these events could not be seen as a direct result of the simulation. In order to include the contribution of these events, an empirical fit was used.

The result of this earlier work is shown in fig. 3.8. Here, the colours blue, green and grey stand for individual contributions from internal radiogenic backgrounds, external gammas and excess light events, respectively. The red shows the sum of all these contributions as well as fits to the observed cosmogenic lines and the copper fluorescence line at 8.04 keV.

It is clear that, even though the semi-empirical background model in [105] explains a lot, the result presented there is not sufficient. The main task of this work is to improve the background model of [105] by developing a full Monte Carlo based model, with the details of the differences will be explained in section 4.2 and section 4.4. For the normalisation of the model developed for this work, experimental reference data are necessary and this will be the topic of the next section.

3.7. Reference Data

For different ranges of deposited energy, different analyses are performed for each detector module. This is mainly caused by the fact that the pulse shapes of particle event change with energy due to the non-linear detector response. In addition, the resolution of the detectors varies with energy. In this work, we are using the complete data recorded with the TUM40 module with a gross exposure of 129.912 kg · days[4][5]. Three analyses are performed in [37, 90, 97, 98], each optimised for a different energy range: energies between 0.6 keV and 495 keV (i.e. *low energy reference data set*, see section 3.7.1), energies between 500 keV and 4000 keV (i.e. *medium energy reference data set*, see section 3.7.2) and energies

[4]We note that for the dark matter analysis in [26], only a part, 29.35 kg · days, of this data was used.
[5]The uncertainty of this value is at negligible levels.

between 4 MeV and 7 MeV (i.e. *high energy reference data set*, see section 3.7.3). The specifics of the analyses performed in [37, 90, 97, 98] will be summarised below.

3.7.1. Low Energy Reference Data

The first data set, the *low energy reference data set*, covers the energy range between 0.6 keV and 495 keV, discussed in [97, 98]. The lower limit of this spectrum is equal to the detection threshold of the TUM40 detector module whereas the upper limit of the spectrum comes from the fact that energy reconstruction works differently for this energy range and the one higher. This spectrum is very important since it contains the ROI for dark matter search with TUM40 in CRESST-II Phase 2. In this work, we will identify each background contribution and simulate the corresponding decay. In Chapter 5, the obtained decay spectra will be compared to this data set and the contribution to the background in the ROI will be quantified in Chapter 6.

In order to get the spectrum, four categories of cuts are applied, which are described in detail in [97, 98][6]: a *rate and stability cut*, a *coincidence cut*, a *carrier cut*, *quality cuts* and an *RMS cut*.

The first one, the rate and stability cut, is energy independent and removes periods of abnormal high rate as well as periods of unstable detector operation.

The next cut is the so-called anti-coincidence cut. Events coincident with muon veto events and events from other detector modules are removed, and this cut is also energy independent.

The next cut is the carrier cut. TUM40 features a glued TES carrier and events in this carrier show faster rise and decay times compared to the events in the target. The resulting different pulse shapes are used to differentitate between carrier and target events.

The first group of cuts to introduce energy-dependence are quality cuts. Quality cuts remove events which are affected by well-known artifacts, like *delta voltage-RMS cut* and *right-left baseline cut*. Delta voltage-RMS cut removes delta-spikes that might be caused by an electrical origin. Right-left baseline cut removes events with pulses rising too fast for the SQUID to be able to detect as well as decaying baselines. In addition, this cut also removes the so-called *stick events* caused by the energy depositions in the $CaWO_4$ sticks holding the $CaWO_4$ target crystal. Stick events take longer time than other events since phonons have to propagate from the stick to the target crystal, and then to the TES.

The last cut is the so-called RMS cut. RMS quantifies the deviation between an actual event pulse and a standardised template fitted to this pulse. It is similar to the quality cuts but as a more general cut it removes all events which deviate from the nominal pulse shape whereas the quality cuts require knowledge of a certain type of artifact [98].

Combining all these cuts together gives the energy dependent signal survival probability ε_l that is shown in fig. 3.10a. The resulting recoil energy spectrum can be seen in fig. 3.10b.

[6] We note that in [98], the analysis is applied to a data set with an exposure of 97.989 kg · days before cuts whereas the data set used in this work was obtained in [97] by applying the same analysis to 129.912 kg · days, i.e. the full exposure recorded with TUM40.

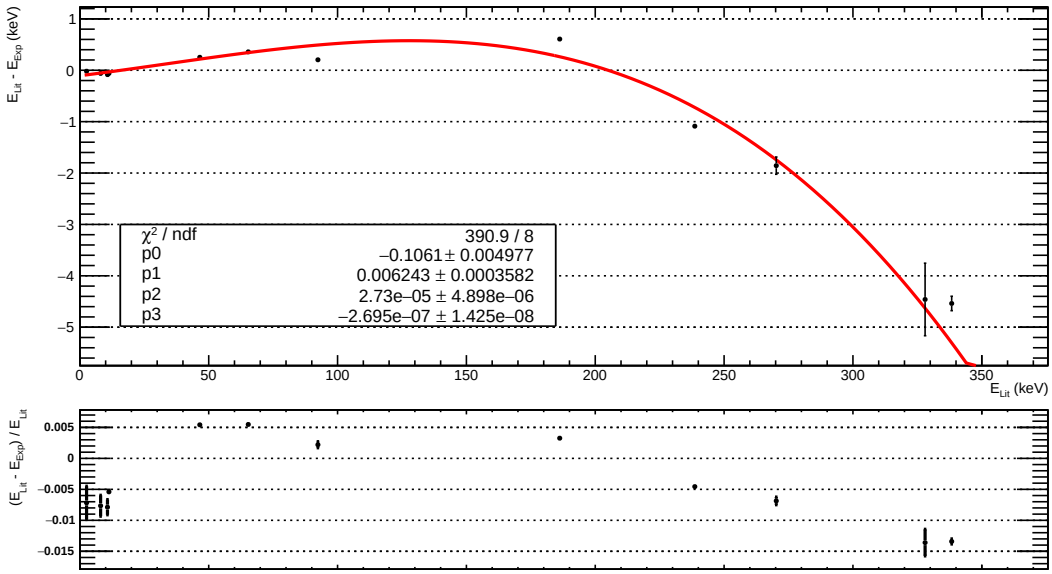

Figure 3.9.: Top panel: the rescaling function obtained from the fitted values of the peaks of the low energy reference data set. Bottom panel: relative residual between fit values and literature.

When we fit some of the known peaks, the mean values turned out to be shifted with respect to the literature values of these peaks. In order to correct this shift, a rescaling is performed:

$$\begin{aligned} E' = E - (0.106 \pm 0.005)\,\mathrm{keV} + (6.2 \pm 0.4) \cdot 10^{-3} \cdot E \\ +(2.7 \pm 0.5) \cdot 10^{-5}\,\mathrm{keV}^{-1} \cdot E^2 - (2.7 \pm 0.1) \cdot 10^{-7}\,\mathrm{keV}^{-2} \cdot E^3 \end{aligned} \tag{3.6}$$

where E' stands for the rescaled energy and E stands for the measured energy of the original data set [97]. The rescaling function eq. (3.6) (see also fig. 3.9) is obtained from the fitting of the energy shift in the low energy reference data with respect to the literature values of the peaks in question. This can be seen in fig. 3.9. After this rescaling, the means of the fit results turned out to be in close proximity to the literature values.

3.7.2. Medium Energy Reference Data

The second data set, the *medium energy reference data set*, used in this work covers the energies between 511 keV to 4000 keV and is provided by [90]. This spectrum will be used in section 5.4 to normalise the simulation of gamma decays originated from ^{208}Tl, ^{40}K, ^{228}Ac and ^{214}Bi.

In order to get this spectrum, only the stability cut and some quality cuts are applied. The resulting spectrum has an exposure of 129.912 kg · days before the cuts. The signal

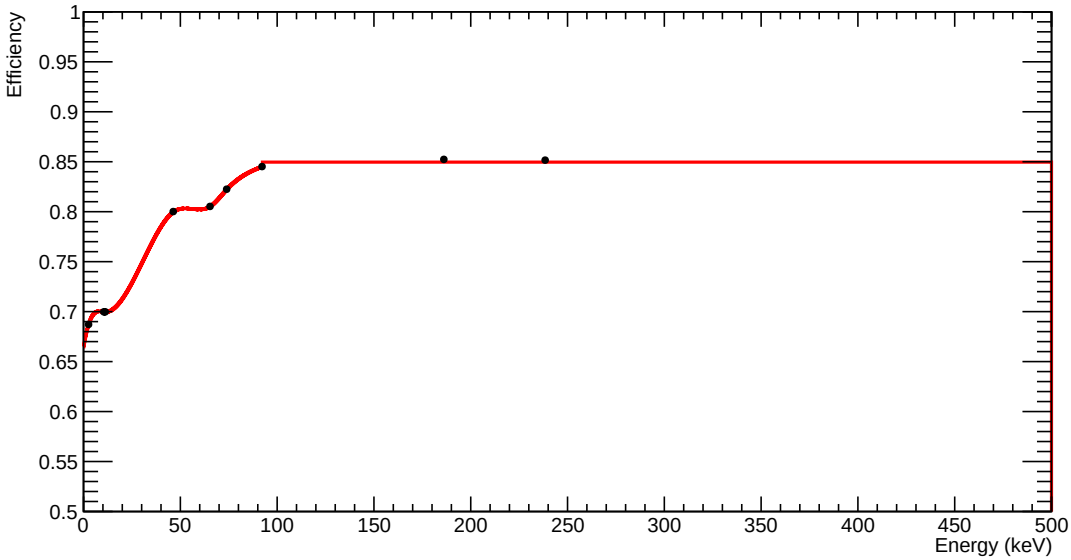

(a)

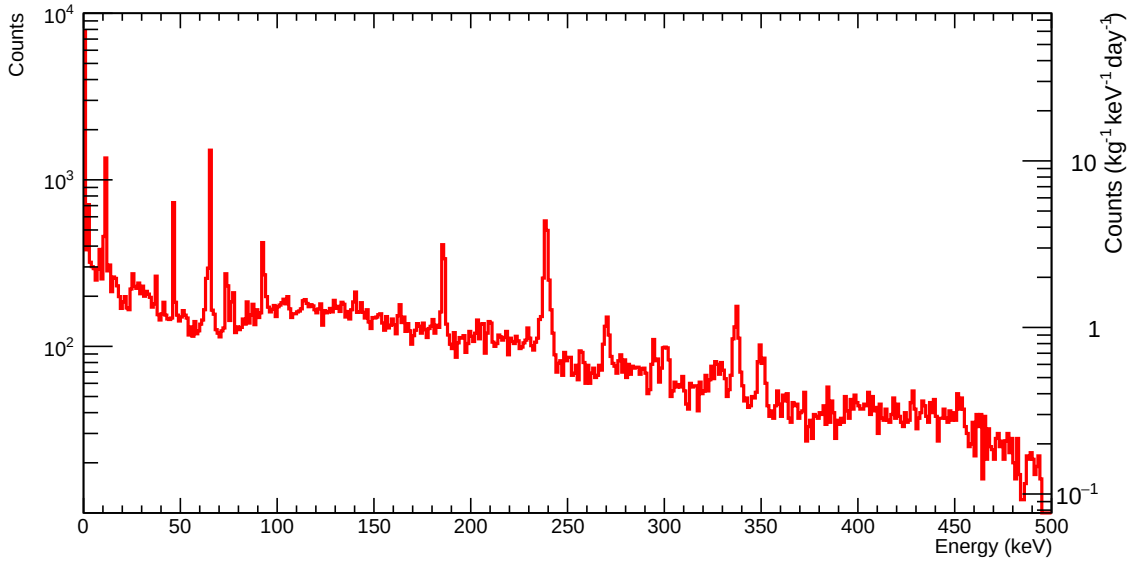

(b)

Figure 3.10.: The signal survival probability (a) related to the low energy reference data set: below an energy of 92.36 keV, a varying signal survival probability is used whereas above this energy, the signal survival probability is set to the constant value of 85.0 %. The corresponding energy spectrum (b) between 0.6 keV and 495 keV, after the rescaling in section 3.7.1 was applied. Data provided by [97, 98].

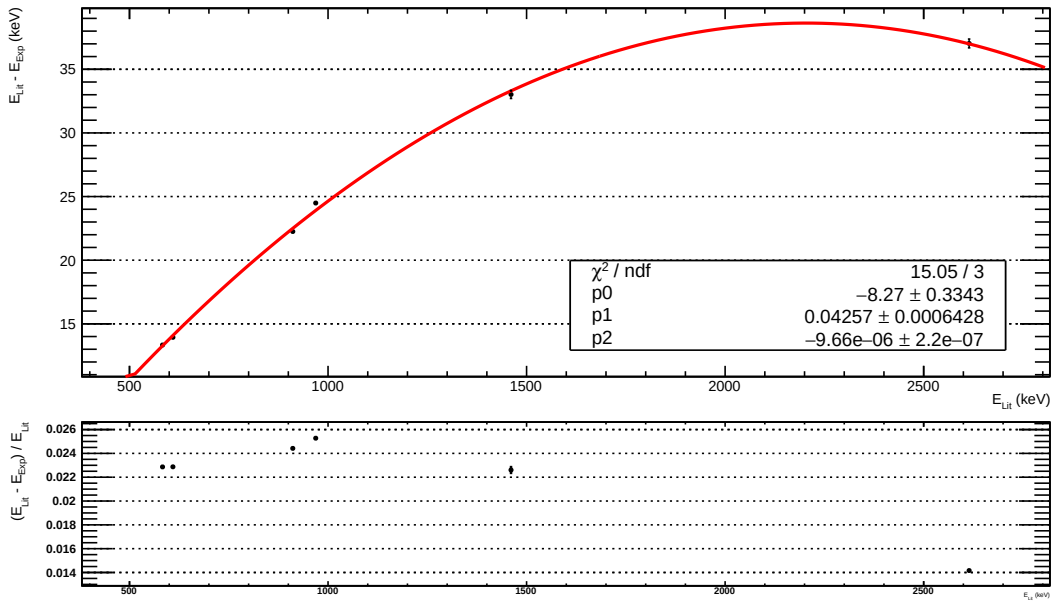

Figure 3.11.: Top panel: the rescaling function obtained from the fitted values of the peaks of the medium energy reference data set. Bottom panel: relative residual between fit values and literature.

survival probability is estimated by the ratio of events surviving the cuts to the total number of candidate events, resulting in a signal survival probability of $\varepsilon_{\mathrm{m}} = 98.1\,\%$ [90].

Here, just as with the low energy reference data set, we identified a shift between the mean energies of the known peaks and their literature values. In order to correct this shift, we performed a rescaling:

$$E' = E - (8.1 \pm 0.9)\,\mathrm{keV} + (0.042 \pm 0.001) \cdot E - (9.6 \pm 0.4) \cdot 10^{-6}\,\mathrm{keV}^{-1} \cdot E^2 \qquad (3.7)$$

where E' stands for the rescaled energy and E stands for the measured energy. The function eq. (3.7) (see also fig. 3.11) is obtained from the fitting of the energy shift in medium energy reference data with respect to the literature values of the peaks in question. After this calibration, the means of the fit results turned out to be in close proximity to the literature values.

3.7.3. High Energy Reference Data

The last data set, the *high energy reference data set*, contains events with energies between 4 MeV and 7 MeV and is provided by [37]. This range includes sharp peaks which belong to alpha decays within the ^{238}U, ^{235}U and ^{232}Th decay chains. Except for a few events in this energy range, there is no continuous spectrum accompanying the alpha lines. At these energies, the TES is nonlinear, the recorded pulses saturate. Since the saturation of

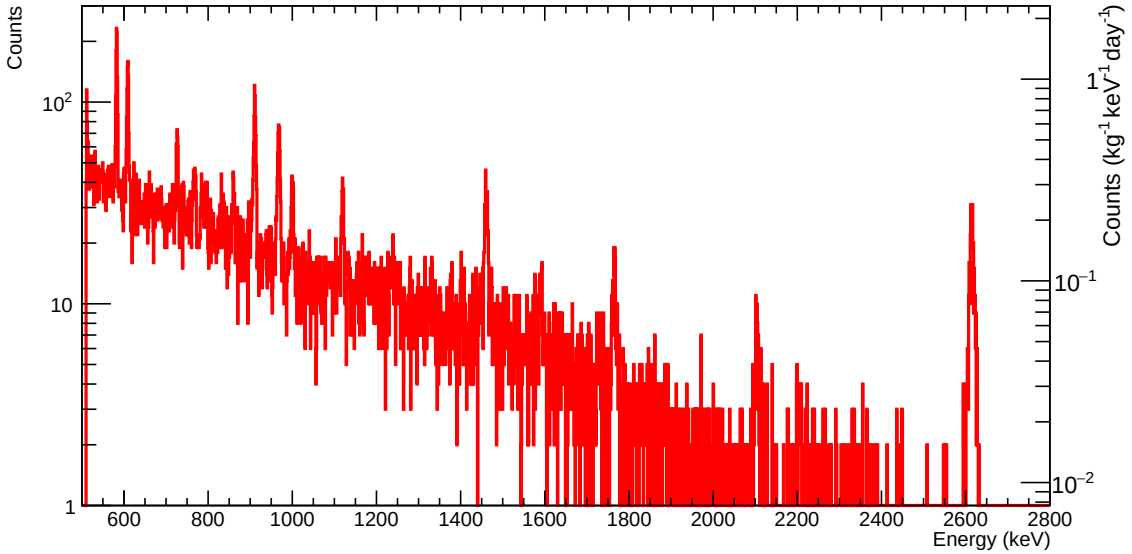

Figure 3.12.: Energy spectrum of the medium energy reference data set between 510 keV and 4000 keV, after the rescaling in section 3.7.2 was applied. Data provided by [90].

the pulses makes the energy calibration more difficult, and potentially a little less precise, the standard energy calibration is not working properly and the calibration was corrected [37] by assigning Q values from literature [69] to well identified peaks. The result of the high energy analysis is shown in fig. 3.13. The spike at the middle of the highest energetic peak, which belongs to ^{211}Bi, is an artifact of the energy calibration of the data [37]. The analysis has an energy-independent signal survival probability of $\varepsilon_{\mathrm{h}} = 86.5\,\%$ calculated the same way as for the medium energy reference data set: estimating the fraction of events surviving the cuts to the total number of candidate alpha events [37].

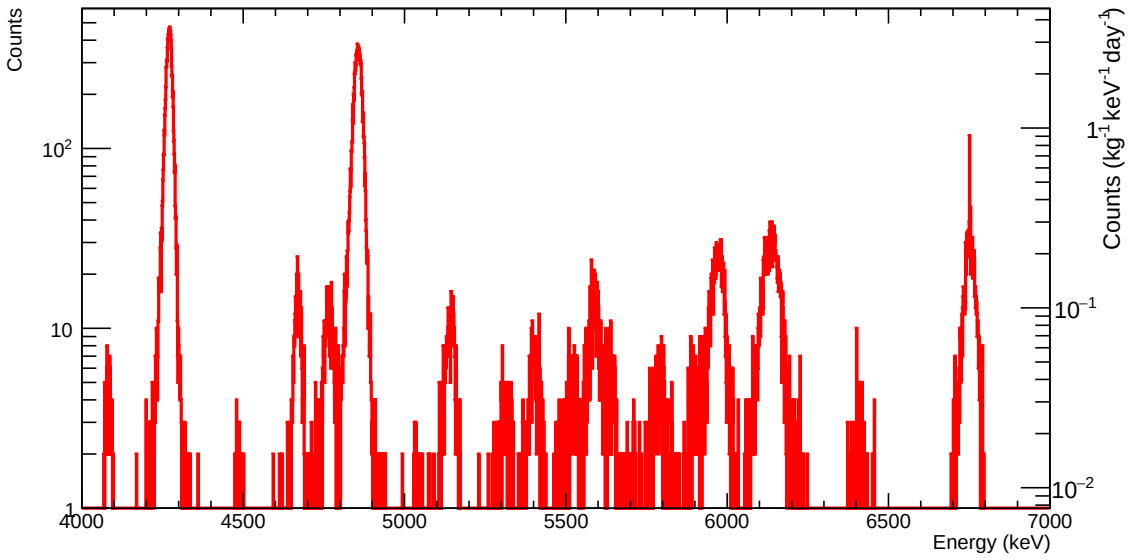

Figure 3.13.: Energy spectrum of the high energy reference data set between 4000 keV and 7000 keV, without any rescaling applied. Data provided by [37].

4. Radioactive Background Simulations

As pointed out in the previous chapter, experimental data retrieved with the TUM40 detector module still shows contamination by background sources even after improved purification of the crystal. Background coming from the electron recoil band[1] is at a constant level of 3.51 counts/(kg · keV · day) between recoil energies of 1-40 keV [105]. The dark matter recoils are expected in the nuclear recoil bands of the light yield-recoil energy plane. However, the electron recoil band leaks into the nuclear recoil bands at low energies. This makes the discovery of a possible low-mass dark matter particle impossible as an unknown background can mimic or conceal a dark matter signal. In order to understand the backgrounds, the construction of a Monte Carlo based background model is of great importance, which will be the topic of this chapter.

In this chapter, a detailed description of the applied physics (section 4.1), the implemented geometry (section 4.2), the applied detector response model (section 4.3) and finally how the simulations are performed (section 4.4) will be given.

4.1. Simulation of Electromagnetic Interactions in $CaWO_4$

In this work, we are using the Monte Carlo framework Geant4 [12, 17, 18] in version 10.2 patch 1 to simulate the radioactive decay of contaminants inside the $CaWO_4$ crystal of TUM40 and the Cu parts close to it. The simulation code propagates the produced decay products through a detailed geometry of the TUM40 detector module. Finally, the energy deposits in the $CaWO_4$ crystal are recorded.

4.1.1. Geant4 Framework

Geant4 is a Monte Carlo toolkit that is used to simulate the production of particles, their passage through matter and their final decay or capture. Geant4 can be used for applications in particle and nuclear physics, medical physics, accelerator design and space engineering. It is implemented in C++. For this work, we used and extended the simulation code *ImpCRESST*[2] that is based on Geant4 (version 10.2 patch 1) and the analysis package ROOT (version 6.04.00).

Geant4 is based on four basic concepts:

[1] The total background is assumed to be coming from the electron recoil band [105].
[2] Internally developed and used by the CRESST collaboration.

- **Geometry Models:** In order to simulate detectors, a detailed geometry should be implemented. A particular geometry results in specific results. There are various features one has to consider while implementing a detector, such as geometry or material. In order to implement variations of these for a particular simulation, one may use the so-called *macro files*. Macro files can include information as to which geometry with its specific materials will be simulated as well as the starting values of the particles to be simulated.
- **Primary Particle Generation:** At the beginning of the simulation, the particles have to be created at their designated places. In the context of this work, the radioactive nuclides are placed inside $CaWO_4$ and Cu with zero kinetic energy. This is called *primary particle generation*. The next step after the generation is the interaction of particles.
- **Physics Lists:** There are various interactions a particle can go through. However, in the simulations, one can select which ones to include depending on the study. These interactions are included in Geant4 via the so-called *physics lists*. These lists include interaction types of many particles and the corresponding interaction cross-sections. In this work, we will use a physics lists which follows mainly the *Shielding* physics list of Geant4 version 10.2 patch 1 with two physics modifications: *G4RadioactiveDecay* and *G4EmStandardPhysics_option4*. ImpCRESST treats also ^{3}H as unstable [59] which is not the case if only the standard G4RadioactiveDecay is used. In addition, the more accurate [60] G4EmStandardPhysics_option4 is used instead of *G4EmStandardPhysics*.
- **Particle Tracking:** When the simulation generates the particles, particle tracking starts. Geant4 tracks the particles according to a step length it calculates. This calculation is based on the interactions allowed through the physics lists. For example, if a particle can go through electromagnetic interactions such as photoelectric effect, Compton scattering and pair production, Geant4 calculates the free path length of this particle for all of these interactions. The shortest free path length calculated out of these interactions is used as the effective free path length, which means that this particle travels this much distance in the medium until the next step is calculated. Its energy loss inside the medium is calculated according to the physical process associated with the effective free path. For the particular Geant4 code used for this work, the tracking works for particles with kinetic energies as low as 250 eV inside all the materials used to construct the geometry of TUM40 detector module (see table 4.1). Below this energy, particles are not propagated and they instantly deposit their energies at the position they are at. The only exceptions are the products of nuclear and atomic de-excitation, e.g. gammas, fluorescence X-rays or Auger electrons, which will be tracked regardless of their energies.
- **Hit Generation:** After the primary particle generation, when a particle goes through interactions allowed in the physics lists, it loses energy. However, this energy loss or the related energy deposition in the surrounding material is not always recorded; the energy deposition is only recorded as a so-called *hit* in parts of the medium which are designated as *sensitive volumes* by the user. In the context of this work, sensitive

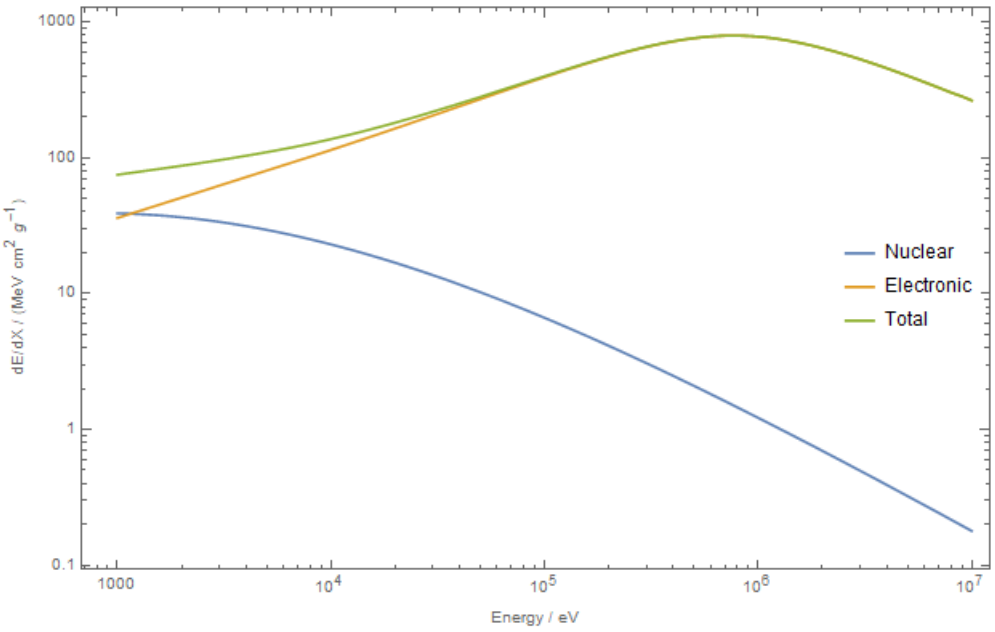

Figure 4.1.: Nuclear, electronic and total stopping power of $CaWO_4$ with respect to the energy of a $^4_2$He nucleus. Figure provided by [77] based on [113]

volumes are the following parts of the geometry model which will be introduced in section 4.2: $CaWO_4$ crystal, light detector, scintillating foil and $CaWO_4$ holder sticks.

Since we are interested in radioactive decays and the resulting interactions in this work, physics processes including *radioactive decays* and *electromagnetic interactions* are used [58] and they will be explained in the next two sections.

4.1.2. Particle Interactions by Nuclear Reactions

The radioactive decays can be simulated either at rest or in flight. The radioactive decay in Geant4 includes processes of α, β, γ emissions and EC [58]. For the simulation model, the data from the *Evaluated Nuclear Structure Data File* (ENSDF) [109] are used. The data retrieved from this database includes nuclear half-lives, nuclear level structure of the parent and the daughter nuclide, branching ratios of decays and the energy of the decay processes [58].

In the simulation, the nuclide is placed inside a volume ($CaWO_4$ crystal of TUM40 or the Cu parts around the crystal) with zero kinetic energy. There are three primary decays simulated in this work:

- **Alpha Decay:** Here, a nuclide $^{A}_{Z}$X decays into a $^4_2$He nucleus along with another nuclide $^{A-4}_{Z-2}$Y, where X and Y are called parent and daughter nuclides, respectively. The internal bulk alpha decays are mostly contained inside their respective mother

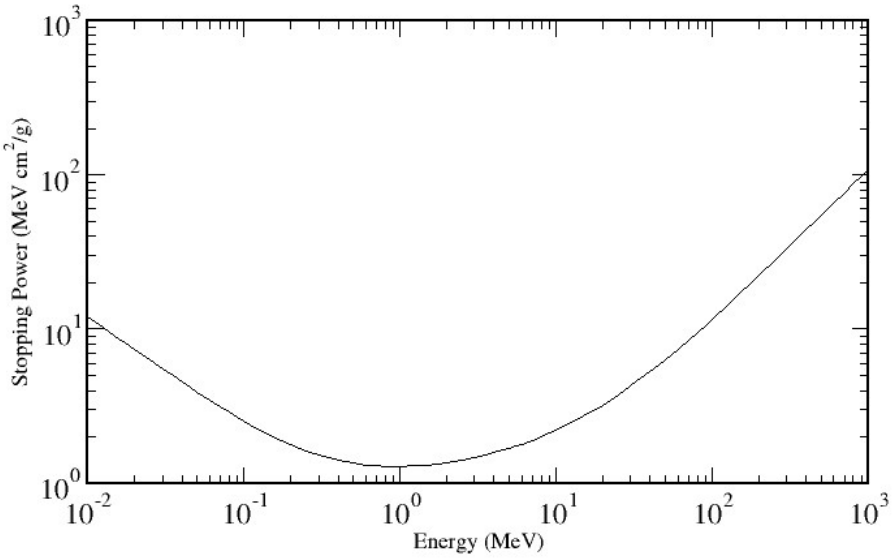

Figure 4.2.: Total stopping power of $CaWO_4$ with respect to the energy of beta particles. Figure taken from [40, 92].

volumes. If one wants to calculate how far an alpha particle can travel in $CaWO_4$ before being absorbed, the nuclear stopping power dE/dX values shown in fig. 4.1 should be used in conjunction with the following equation:

$$d(E_\alpha) = \int_0^{E_\alpha} \frac{1}{\frac{dE}{dX}(E') \cdot \rho_{CaWO_4}} \cdot dE' \tag{4.1}$$

Using this equation and the values from fig. 4.1, the amount of distance a 7 MeV[3] alpha-particle can travel inside the $CaWO_4$ crystal is $d = 23.74\,\mu m$. Since the $CaWO_4$ crystal of TUM40 detector module has the dimensions of $40 \times 40 \times 32\,mm^3$, the alphas will be contained inside the crystal unless they are closer to the surface of the crystal than the aforementioned distance.

- **Beta Decay:** Here, a nuclide ${}^{A}_{Z}X$ emits a β^- particle as well as a $\bar{\nu}_e$, and turn into another nuclide ${}^{A}_{Z+1}Y$. Similar to the alpha decays, internal beta decays are also contained inside the crystal. The same equation eq. (4.1) can be used to obtain the free path length $d(E_\beta)$ of beta particles in different materials.

  For betas, we choose, as an example, the highest energy beta particles expected in the experimental reference data of TUM40 with energies around 5 MeV[4]. At this energy, based on fig. 4.2, stopping power is $1.692\,MeV\,cm^2\,g^{-1}$. Hence, the maximum amount of distance betas can travel inside a $CaWO_4$ crystal before they

[3] The highest energy alpha decay seen in the experimental data of TUM40 crystal belongs to ^{211}Bi, with an energy of (6750.4 ± 0.5) keV [69].

[4] The highest energy beta decay seen in the experimental data of TUM40 crystal belongs to ^{208}Tl, with an energy of (4998.5 ± 1.7) keV [69].

are absorbed is d = 5.6 mm. Again, just as with alpha-particles, beta-particles are contained inside the crystal as long as the decay does not occur close the crystal less than the distance given above.

- **Electron Capture (EC)** Here, an orbital electron is captured by the nucleus of ${}^{A}_{Z}X$ and then, it changes into ${}^{A}_{Z-1}X$ and a ν.

After the decay begins, the secondaries are emitted and the tracks of these particles are propagated. Then, the nucleus may de-excite, e.g. via gamma emission, which may be followed by the de-excitation of its atomic shells. The atomic de-excitations give out Auger electrons or X-rays. These gammas or X-rays might result in the so-called escape peaks if these emissions leave the $CaWO_4$ crystal without being fully absorbed. After these processes occur, electromagnetic interactions of the produced secondaries start, which will be the topic of next part.

4.1.3. Energy Deposition via Electromagnetic Interactions

After the atomic and nuclear de-excitation occurs, electromagnetic interactions of the secondaries start in the simulation. For this work, we used the electromagnetic physics as defined by Geant4 in the class G4EmStandardPhysics_option4, which is claimed by Geant4 [60] to be the most accurate one at low energies. The interactions and their outcomes in the simulation depend on the particle type:

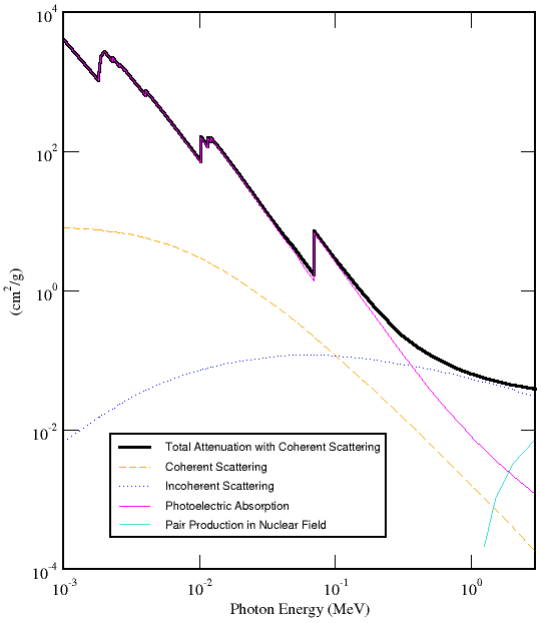

Figure 4.3.: Total attenuation of gamma rays inside the $CaWO_4$ with respect to the energy of gammas. Figure taken from [92].

- **Gamma:** This particle can interact via the photoelectric effect, Compton scattering, gamma conversion and Rayleigh scattering as well as pair production. The *photopeaks* of gamma emission being fully absorbed inside the crystal result from the photoelectric effect. At lower energies, the Compton continuum of partially absorbed gammas follows. Gamma rays are highly penetrative and they may not be contained inside the crystal. Gamma attenuation in $CaWO_4$ crystal with respect to the gamma energy is shown in fig. 4.3. Different from the stopping powers calculated for alpha- and beta-particles, how much of the

gamma rays entering a medium are absorbed inside can be calculated using [79]:

$$I = I_0\, e^{-\mu_m \rho x} \tag{4.2}$$

where I_0 and I stand for initial and transmitted intensities, respectively, μ_m is the attenuation coefficient and ρ is the density of the absorber material. The distance to be traveled throughthe absorber material is x. For our case, we choose $x = 4\,\mathrm{cm}$[5] and $\rho = 6.01\,\mathrm{g/cm^3}$. From the fig. 4.3, we take $\mu_m \approx 0.1\,\mathrm{cm^2/g}$ for gammas with energies around 2.6 MeV [6]. Inserting these into eq. (4.2), one finds:

$$\frac{I}{I_0} = e^{-(0.1\,\mathrm{cm^2/g})\,\cdot\,(6.01\,\mathrm{g/cm^3})\,\cdot\,(4\,\mathrm{cm})} = 9\,\% \tag{4.3}$$

The result shows that only 9 % of the gamma rays can go through the $CaWO_4$ crystal without being absorbed. However, these are for external gamma rays entering the crystal. For gamma rays produced due to beta-/gamma-decays inside the crystal, this percentage can be higher as the length of the gamma trajectory inside the medium may be smaller than the value we used in eq. (4.3).

- **Electron/Positron:** For electrons, we have interactions such as multiple scattering, ionisation and bremsstrahlung with an additional process of pair-annihilation for positrons.

  Also, we see may delta rays in the energy spectrum as a small bump-like feature below $\sim$ 500 keV. Delta rays are caused by primary ionizing particle colliding head-on with an electron, and transferring a large amount of energy to the electron, which then produces secondary ionization while traveling through the medium [79].

  In addition, single and double electron escape peaks are direct results of pair production and pair annihilation. In these cases, a gamma ray with an energy higher than 1022 keV enters the crystal and produces an electron-positron pair. When the positron annihilates with another electron, two gamma rays are produced each with the energy of the rest mass of an electron, namely 511 keV. If one of these gamma rays escape from the crystal, the remaining deposited energy results in the so-called single electron escape peak; if both of them escape, it results in the so-called double electron escape peak. These peaks show themselves in the energy spectrum in the form of peaks at 511 keV and 1022 keV below energy of the photopeak.

These interactions will be shown in detail through examples of simulation results in section 4.4 and fig. 4.15.

[5] The dimensions of the $CaWO_4$ crystal is $40 \times 40 \times 32\,\mathrm{mm^3}$ and here we chose one of the edges as the length.

[6] The highest energy gamma rays observed in the experimental data of TUM40 belongs to ^{208}Tl with an energy of (2614.511 ± 0.010) keV [69].

4.2. Geometry Model

The design of the TUM40 detector module, as discussed earlier, is called the *stick design* and it can be seen in fig. 3.2b. A photo of the detector module are shown in fig. 4.4. As described in section 3.2, the main components of the TUM40 detector module are the $CaWO_4$ target crystal, the light detector, the scintillating foil and the copper parts. There are also minor components such as the $CaWO_4$ sticks, plastic scintillator and bronze clamps. The Geant4 simulation implements these six parts as following (see also table 4.1 and fig. 4.5):

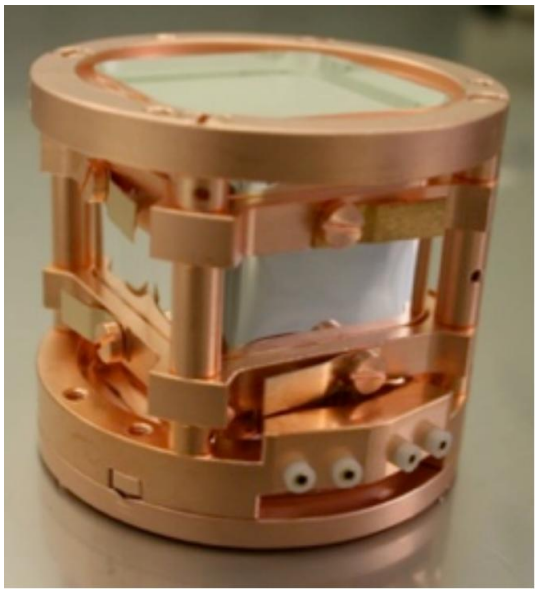

Figure 4.4.: Photo of TUM40 detector module. Figure provided by the CRESST collaboration [52].

The target is modeled as a cubic $CaWO_4$ crystal with a size of $40 \times 40 \times 32\,\mathrm{mm}^3$. The sticks holding the $CaWO_4$ crystal are also made out of the same material. They are constucted both in real life and in simulation in the shape of a hemisphere attached to one endcap of a cylinder.

The light detector has the shape of a disc with a radius of 20 mm and a height of 0.5 mm. The light detector is constructed in simulation from sapphire (i.e. Al_2O_3) even though in reality, it is made up from silicon-on-sapphire because since the silicon layer is too thin, we neglected it in a first approximation.

Scintillating foils[7] cover the crystal and the light detector with the exception of the holes cut for the $CaWO_4$ sticks to be able to penetrate. As we do not know the exact composition of the scintillating foil used in CRESST, our literature search showed that we could approximate the foil used in reality as Mylar, with a chemical composition $C_{10}H_8O_4$.

There is a plastic ring which holds the scintillating foil around the light detector implemented as an empty cylinder with open endcaps. It is made out of the plastic scintillator *BC408* and it has a chemical composition of $C_{10}H_{11}$. The reason why this material was used is to have a fully scintillating surface around the crystal.

In addition, three bronze clamps are used to hold the light detector. Bronze has a material composition of 6 % Sn and 94 % Cu.

Finally, the holders keeping all these aforementioned parts in place and make it into a detector module are made out of Cu. The dominating mass of the detector module comes

[7] Due to geometrical restrictions, the implemented scintillating foil is made up of four different parts in the simulation, whereas in reality, a foil with a complicated shape is used.

from these Cu holders (see table 4.1). The copper holder part "Stäbchenring", which can be seen in fig. 4.5, will have a specific importance in section 4.4.3.

We simplify the implemented geometry in three instances with respect to the real detector:

- One of them is that the screws used in connecting the copper parts with each other are not implemented as these screws fit the holes drilled for them perfectly. Hence, the copper holders are implemented without any holes for screws.
- Another exception is that TESs made out of tungsten are not implemented in the simulations as these pieces would not affect the results since they are pretty small ($\mathcal{O}(10\,\mathrm{mm}^3)$).

The implemented volumes and the corresponding materials used for the simulation are listed in table 4.1. For the isotope composition of the materials, we assume a natural abundance as implemented in Geant4.

4.3. Detector Response Model

After the Geant4 simulations are finished, one obtains data which includes the energy, position and time information for each hit in one of the sensitive volumes of the implemented TUM40 model. However, these results are missing two important factors that should be included: the detector's energy and time responses. Only by applying these, a comparability between the simulation and the experimental reference data can be obtained. In order to do this, we post-process the simulated data sets and apply the energy resolution of the TUM40 target crystal and the time response of the detector. Once the detector response model is applied to a simulated background spectrum and the spectrum is normalised to the total number of simulated decays[8], we will refer to this as a *template* for a given decay spectrum.

4.3.1. Energy Resolution

In order to find a suitable energy resolution at energies[9], we re-analysed the reference data in a four-step process:

1. First, we identify peaks in the energy region of interest.
2. After the peaks are selected, a Gaussian function (eq. (5.8)) or a Gaussian function with a polynomial (eq. (5.13)) to adapt to a linear background is fitted to each of these peaks.
3. The variance σ of each analysed peak is plotted with respect to its mean energy E.
4. Finally, a polynomial function is fitted to this plot.

[8] Therefore, it is the *probability density function* (PDF) for observing a detector event at a given energy which originate from the background source under investigation.

[9] That is the sum of phonon and light energies as described in section 3.4.

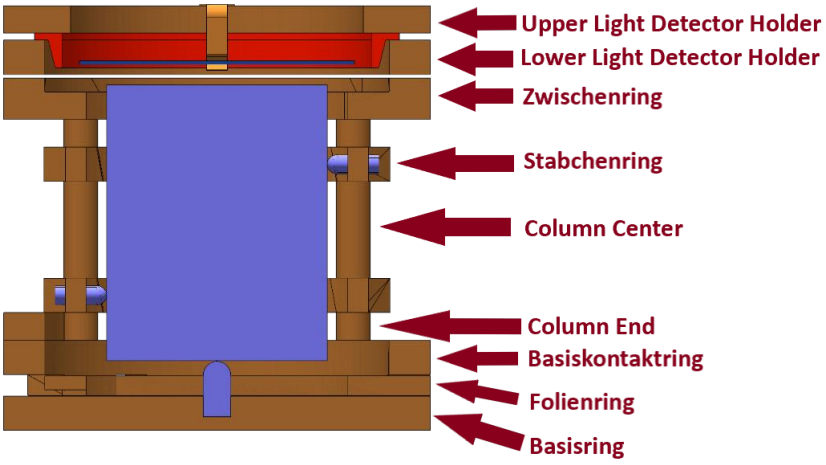

(a)

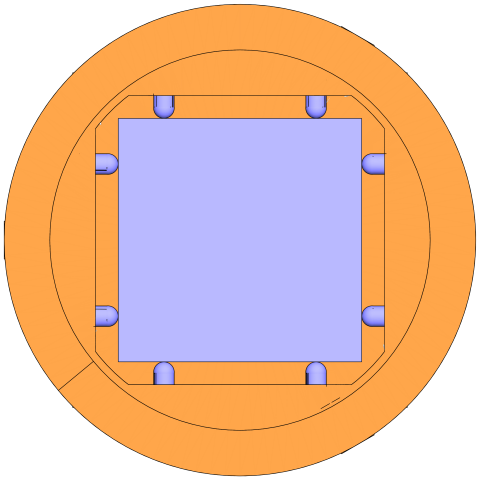

(b)

Figure 4.5.: Visualisation of the TUM40 detector module as implemented in Geant4: cut-away views parallel to the X-Z plane fig. 4.5a and parallel to the X-Y plane fig. 4.5b. Main components are the $CaWO_4$ target crystal (purple box), Cu holders (brown/orange) and the BC408 plastic ring (red). For the sake of visibility, the implemented scintillating foil is not visualised.

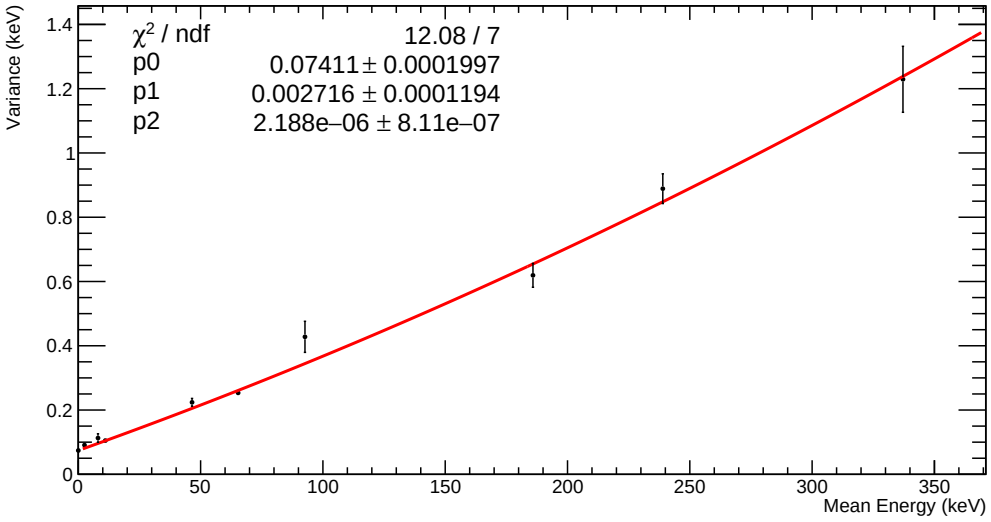

Figure 4.6.: Energy resolution function (red) for the low energy reference data used in the detector response model. The function is retrieved by parametrizing the variance values of Gaussian fits to known peaks.

For the low energy range $E < 495$ keV (see section 3.7.1), the obtained σ_l(E) correlation is shown in fig. 4.6 and we find:

$$\sigma_\mathrm{l} = (0.0741 \pm 0.0002)\,\mathrm{keV} + (2.7 \pm 0.1) \cdot 10^{-3} \cdot E + (2.2 \pm 0.8) \cdot 10^{-6}\,\mathrm{keV}^{-1} \cdot E^2 \quad (4.4)$$

For the medium energy range 511 keV $< E \leq$ 4000 keV (section 3.7.2), the obtained σ_m(E) correlation is shown in fig. 4.7 and we find:

$$\begin{aligned} \sigma_\mathrm{m} = -(1.6 \pm 1.3)\,\mathrm{keV} + (7.5 \pm 3.8) \cdot 10^{-3} \cdot E \\ -(4.0 \pm 3.3) \cdot 10^{-6}\,\mathrm{keV}^{-1} \cdot E^2 + (8.5 \pm 7.6) \cdot 10^{-10}\,\mathrm{keV}^{-2} \cdot E^3 \end{aligned} \quad (4.5)$$

For the high energy range 4 MeV $< E \leq$ 7 MeV (section 3.7.3), the obtained σ_h(E) correlation is shown in fig. 4.8 and we find:

$$\begin{aligned} \sigma_\mathrm{h} = (0.10 \pm 0.01)\,\mathrm{keV} + (0.0057 \pm 0.0004) \cdot E \\ -(1.7 \pm 0.2) \cdot 10^{-6}\,\mathrm{keV}^{-1} \cdot E^2 + (2.3 \pm 0.2) \cdot 10^{-10}\,\mathrm{keV}^{-2} \cdot E^3 \end{aligned} \quad (4.6)$$

Uncertainties of the energy resolutions are only shown here for illustration; they are not taken into account when we apply these resolutions in the simulations.

Given the experimentally determined energy resolutions σ_l, σ_m and σ_h, we applied them to the simulated energy depositions, i.e. *hits* in Geant4 as follows:

1. The observable energy E_obs of a hit is randomly chosen from a Gaussian distribution with width σ, which is centered around the deposited energy $E_\mathrm{deposited}$ as simulated by Geant4.

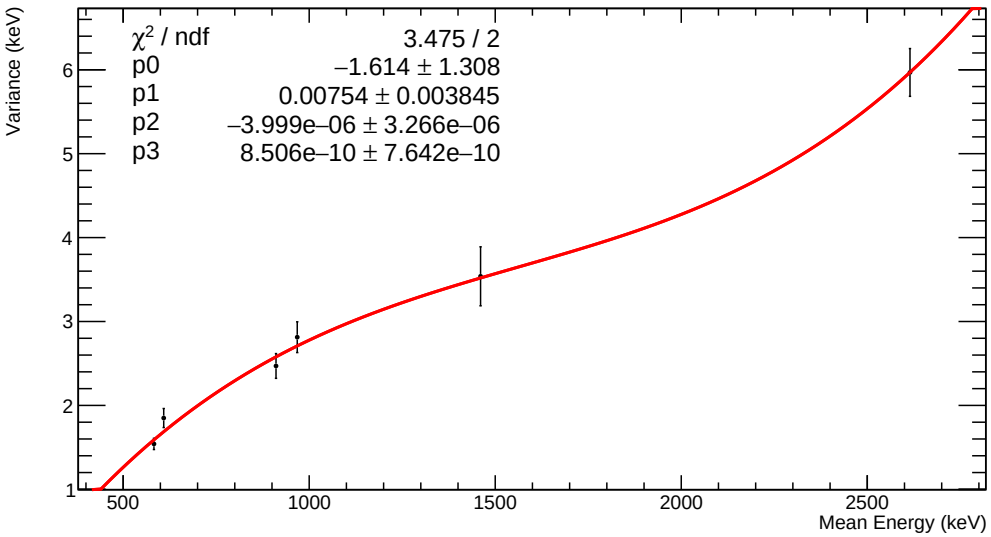

Figure 4.7.: Energy resolution function (red) for the medium energy reference data used in the detector response model. The function is retrieved by parametrizing the variance values of Gaussian fits to known peaks.

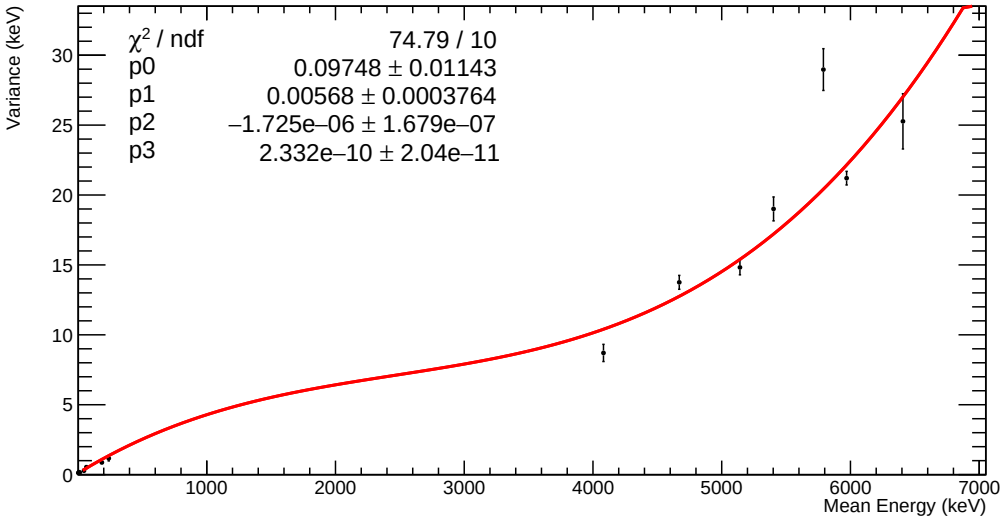

Figure 4.8.: Energy resolution function (red) for the high energy reference data used in the detector response model. The function is retrieved by parametrizing the variance values of Gaussian fits to known peaks.

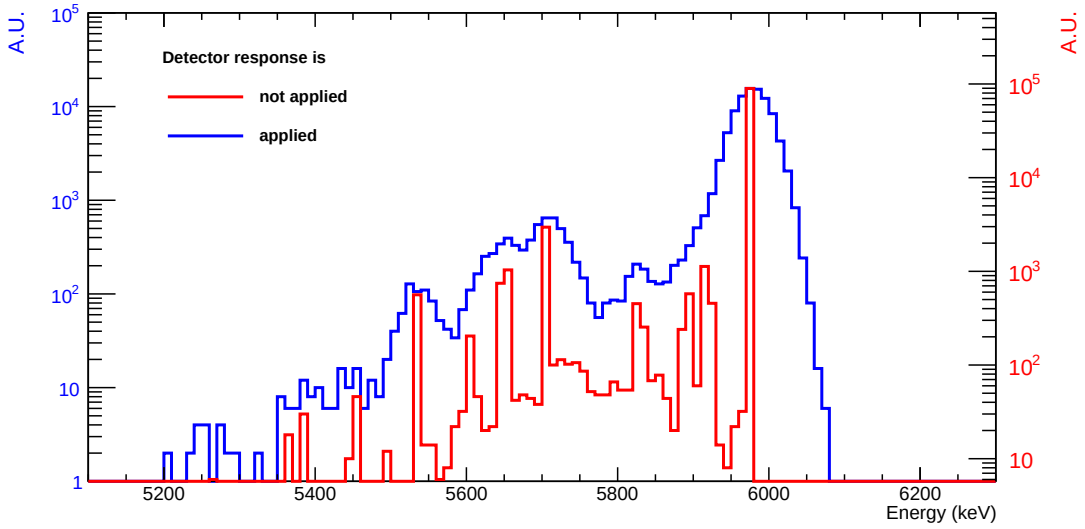

Figure 4.9.: Simulated energy depositions of ^{223}Ra bulk contamination inside the $CaWO_4$ crystal with (purple, left scale) and without (red, right scale) applied detector response model.

2. Depending on which energy range we want to compare the simulation with, we choose the σ accordingly.

An example of the effect of the energy response is shown in fig. 4.9 through the alpha-decay of ^{223}Ra: with (purple) and without (red) detector response applied. The case of no detector response model (red) is equivalent to an infinite energy resolution which shows the alpha-line at its literature value [69]. On the other hand, with the finite energy resolution of the detector response model (purple), the energy deposition of each alpha-decay is distributed according to eq. (4.6).

4.3.2. Time Resolution

The other important aspect of the detector response which is needed to be considered is the time resolution. For the time resolution, a constant value of 2 ms is used for most of the nuclides. This value corresponds to the minimum time difference for two different particle pulses to be distinguished from each other. Hence, in the post-processing we sum-up all Geant4 hits which happen within 2ms with respect to the first hit of a simulated decay to create one "experimental event". If hits happen after 2 ms, e.g. via a delayed isomeric decay, it will create the next experimental event of 2 ms length and so on.

There are two exceptions for this:

1. For some of the nuclides, an infinite time resolution should be used, i.e. the previously mentioned time window is of infinite length. Therefore, all Geant4 hits are

Table 4.1.: Parts of the TUM40 detector module as as implemented in the Geant4 simulation.

Detector Part	**Material**	**Mass** (g)	**Density** (g/cm^3)
Phonon Detector	$CaWO_4$	246.2	6.01
Sapphire Light Detector	Al_2O_3	2.5	3.99
Copper Parts (20 pieces)	Cu	469.2	8.92
Mylar Scintillating Foil (4 pieces)	$C_{10}H_8O_4$	1.3	1.37
BC408 Plastic Ring	$C_{10}H_{11}$	1.3	1.032
Holder Sticks (9 sticks)	$CaWO_4$	2.5	6.01
Bronze Clamps (3 clamps)	Sn (6 %), Cu (94 %)	0.4	8.82

summed up to one "experimental" event. This is a work-around for a technical problem: to manage short-lived isotopes, the simulation stores the absolute time stamps of the Geant4 hits as nanoseconds with double precision. If now a decay has a half-life of more than a couple of thousand years, already the offset of the first time stamps in nanoseconds exceeds the double precision and comparison operation produces meaningless results. This is the case for the following nuclides: ^{238}U, ^{235}U, ^{234}U, ^{232}Th, ^{231}Pa, ^{230}Th, ^{226}Ra and ^{40}K. However, this work-around does not affect the physical results because any of these decays is a prompt one, i.e. all hits happen on time scale below 1 μs. Therefore, the same result is obtained either if the hits are summed up over a time window of 2 ms or infinite time.

2. The second exception are fast subsequent nuclear decays. Beta-decays of ^{214}Bi and ^{212}Bi along with alpha-decays of ^{219}Rn have a high probability that also their daughter nuclides decay within the 2 ms started by the decay of its respective parent. However, in reality this will result in pile-up events observed in [105]. Due to the cuts described in section 3.7, those events are not included in the experimental reference data used in this work. Hence, these nuclides are not simulated.

4.4. Simulation of Spectral Templates

The experimental data show that the contaminants differ by where they originate from or the type of processes they go through (see section 3.6). Hence, we will divide this section into four parts with respect to the aforementioned differences. First, we will talk about the *internal radiogenic backgrounds* (section 4.4.1). Then, we will talk about the processes that lead to the *cosmogenic activation* of nuclei inside the $CaWO_4$ crystal (section 4.4.2). Next, we will talk about the different ways taken in order to simulate *external near radiogenic backgrounds* (section 4.4.3). Finally, we will discuss what way is used to simulate *external*

distant radiogenic backgrounds (section 4.4.4).

We used a Geant4 code with the implemented geometry and physics list as described in the previous sections. In macro files, we specified physical features such as atomic and mass numbers of the decaying nuclide, and where the decaying nuclide should be placed. Then, we set its initial kinetic energy to zero.

In this work, the surface contaminations are not taken into account, only bulk contaminations are considered. This means, the decaying nuclides are placed inside the volume under investigation. The parts of the TUM40 detector module which were investigated in this work are the $CaWO_4$ crystal, the crystal holders made of copper and a spherical copper shell around the detector module which approximate the copper of the cryostat (see section 4.4.4 for details). Within each of these parts, the placement of nuclides is done homogeneously throughout the volume.

In addition, the beginning and the end of a decay chain can be arranged using the macro file. In this case, after the parent decayed to its daughter(s), the decay ends. In the post-processing, we weigh the template of each decay with its activity and sum them up to the final background spectrum. This way, one can easily adapt the contamination levels by changing the activities of individual nuclides. The templates of each simulated nuclide can be found in appendices A.2 to A.5.

4.4.1. Internal Radiogenic Backgrounds

As it was discussed earlier in section 3.5.7, the main source of contamination comes from the natural raidoactivity associated with the ^{238}U, ^{235}U and ^{232}Th decay chains. However, it is important to understand where these contaminants originate from. In order to understand the source of these backgrounds, the recoil energies of the alpha peaks in the MeV region, i.e. the high energy reference data set (section 3.7.3), should be compared to the Q-values of these lines in literature as we will do it in section 5.1. After a one-to-one check of experimental and literature values, it was understood that all of the lines in this region deposit nearly the full energy created in the alpha decay. Therefore, the energy depositions of each decay are contained inside the crystal and the contaminating nuclide causing these decay should originate from inside the $CaWO_4$ crystal. This is expected based on the stopping power of alphas as discussed in section 4.1.2.

After the initial alpha decay at the top of the decay chain emits the daughter along with a ^4He nuclide, the daughter decays either through an alpha or a beta decay, and this process is repeated until the stable nuclide at the end of the decay chain is reached. Hence, the beta decays originating from the daughter nuclides in these decay chains also deposit approximately all their energy inside the crystal, making them internal contaminants. The characteristic difference in the decay spectrum between an internal and an external beta-decay will be discussed in section 4.4.3 and section 4.4.4.

The alpha-decaying nuclides considered in this work are the same as identified in the previous work [105]. However, the difference between [105] and this work is that all of the internal beta-decaying nuclides are included in this work whereas only fourteen of

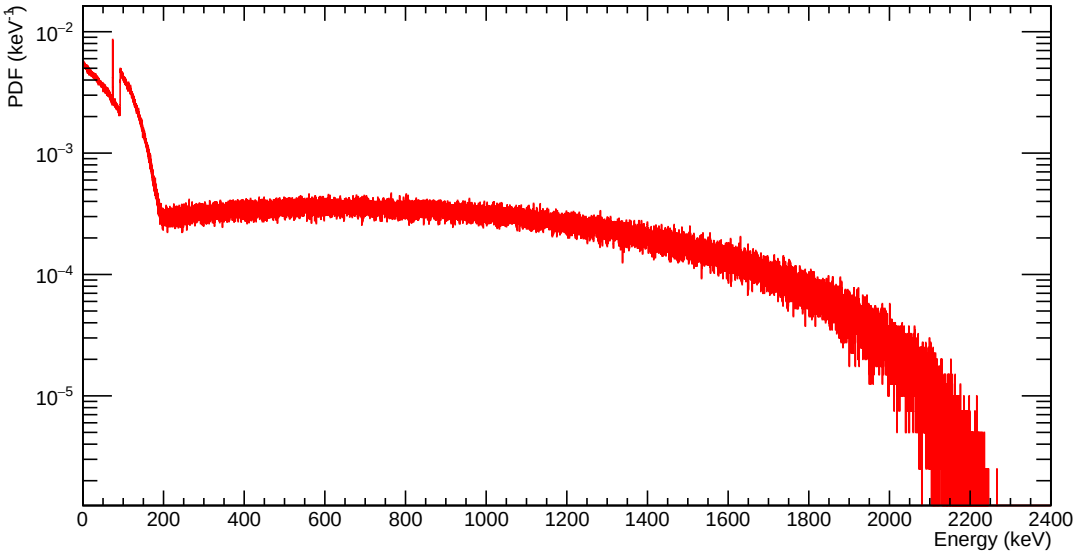

Figure 4.10.: Simulated template of ^{234}Th decaying inside the $CaWO_4$ crystal without applied detector response model. It shows several spectral features such as beta-spectra, gamma-lines and a pile-up of both. For a detailed description, see section 4.4.1.

these nuclides are used in [105] as discussed in section 3.6. This way, a wider range of decays are included to construct the background model. Detailed information regarding the simulated nuclides and their activities are given in tables 5.1 to 5.3.

In order to implement the internal radiogenic decays in the Geant4 simulation code, the placement of the nuclides is constrained to the $CaWO_4$ crystal, since these are internal contaminants. No particular part of the crystal is favoured so the placement of nuclides is homogeneous throughout the crystal. We simulate each step ($X \rightarrow Y$) in the decay chain individually, i.e. we place nuclide X in the crystal and stop the simulation after the decay to nuclide Y. Then, we place nuclide Y in the crystal, let it decay and so on. The advantage of this approach compared to the simulation of the complete decay chain is that we can easily change the activity of a specific nuclide by rescaling just one decay spectrum. A potential disadvantage, the difficulties to simulate pile-up of fast subsequent decays, is of no concern because such events are excluded from the experimental reference data (section 4.3.2).

As an example of an internal beta-decay, the simulated template of ^{234}Th can be seen in fig. 4.10. This nuclide (Q-value of (274 ± 3) keV [69]), decays in $\sim 14\,\%$ of the cases to the 166.30 keV-level of ^{234}Pa and in $\sim 6.4\,\%$ of the cases to the nearby 166.72 keV-level [69]. Both of these energy levels decay via gamma-emission to the isomeric 73.92 keV-state $^{234\mathrm{m}}$Pa with a half-life of 1.159 minutes [69]. In $\sim 78\,\%$ of the cases ^{234}Th makes a direct beta-decay to $^{234\mathrm{m}}$Pa. The latter case is seen as a beta-spectrum between 0 and 200.08

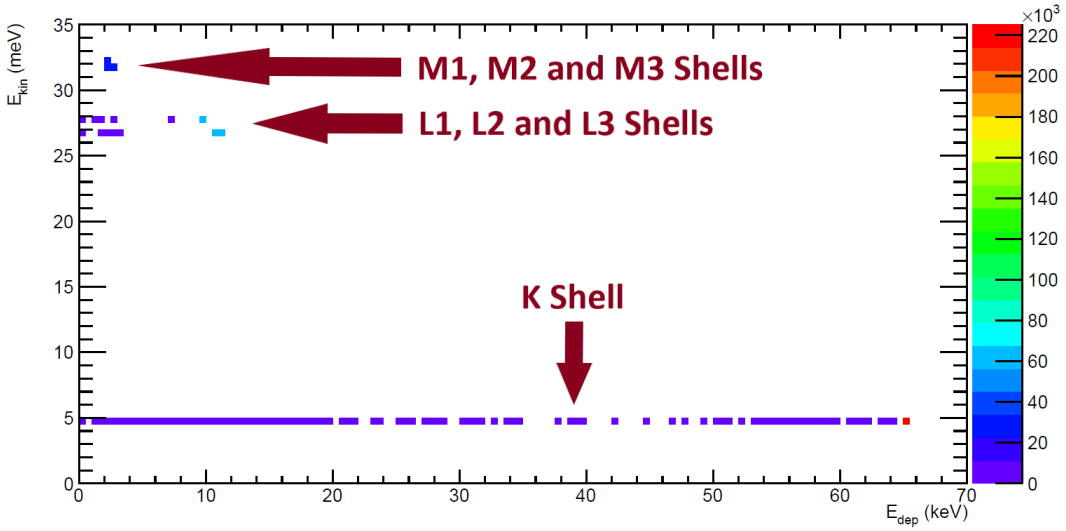

Figure 4.11.: Simulated distribution of N=$5 \cdot 10^5$ EC decays of ^{179}Ta in the E_{kin} vs E_{dep} plane, where E_{kin} is the kinetic energy of the recoiling daughter nucleus ^{179}Hf and E_{dep} is the deposited energy. Clearly visible are distinct band corresponding to EC from the K-, L- and M- shells.

keV (= 274 keV - 73.92 keV) in fig. 4.10. The former case, which is the beta-decay with subsequent gamma-emission, results in a pile-up due to the slow response of the cryogenic detector: this results in an "edge-like" feature starting at the energy of the gamma-lines (166.72 keV - 73.92 keV = 92.8 keV, 166.30 keV - 73.92 keV = 92.38 keV) going up until 200.08 keV. The isomeric state decays in 0.16 % of the cases to the ground state of ^{234}Pa, resulting in a gamma-line at 73.92 keV. In the remaining 99.84 % of the cases, the isomeric state undergoes a beta-decay to the ground state of ^{234}U (2194 keV[10] + 73.92 keV = 2267.92 keV). Again, due to the slow detector response, both decay channels of ^{234m}Pa gives rise to another event in the detector. Both of them are seen in fig. 4.10 either as a sharp line at 73.92 keV or as a continuous beta-spectrum up to 2267.92 keV. A more detailed discussion of the difference between internal and external contaminations is given in section 4.4.3.

Spectra of internal radiogenic decays simulated for all the nuclides used in this work can be found in appendix A.2. How the results of these individual decays are combined is explained in the next chapter (section 5.1).

4.4.2. Internal Cosmogenic Backgrounds

As discussed in section 3.5.3, we expect ^{3}H, ^{179}Ta and ^{181}W as cosmogenically activated radionuclides in $CaWO_4$. In order to add this component to the background model, these nuclides are placed homogeneously inside the $CaWO_4$ crystal, similar to the internal

[10]The Q-value of the beta-decay of ^{234}Pa to ^{234}U is (2194 ± 4) keV [69].

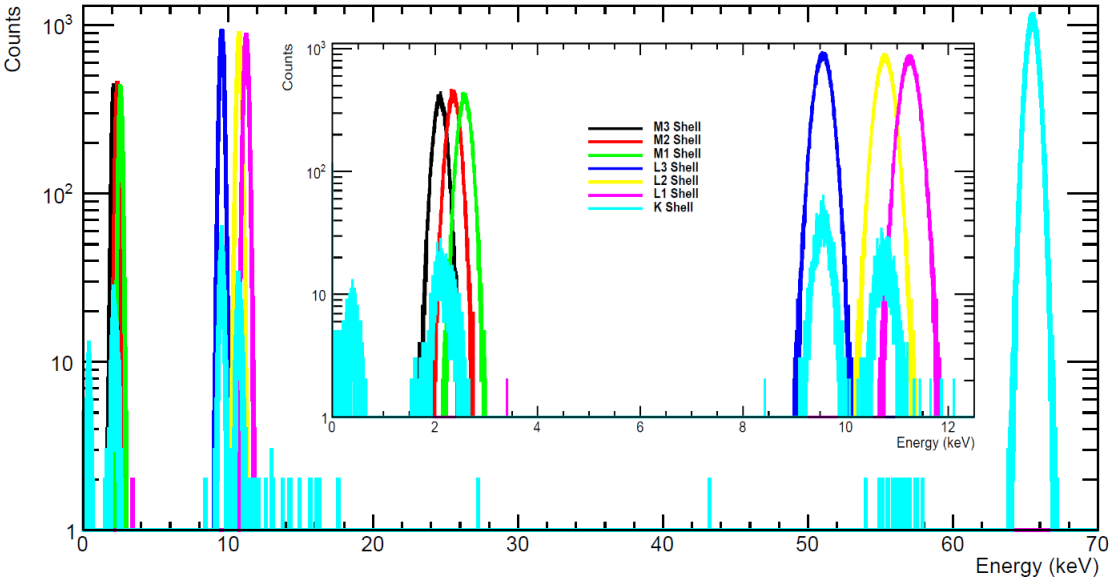

Figure 4.12.: Simulated energy deposition in $CaWO_4$ caused by EC of ^{179}Ta separated according to the involved atomic shells. The inset shows a zoom to the EC-peaks for the M- and L-shells.

radiogenic backgrounds of the previous section. The resulting spectra can be seen in appendix A.3.

When a comparison was made between the experimental reference data and the simulated template, it was found that the branching ratio for EC from the different shells of ^{179}Ta, e.g. K-, L1-, L2-, M2-shell, does not obviously correspond to the amplitude ratio of the K-, L1-, L2-, M2- peaks in the experimental reference data. This problem was also encountered in [105]. At this stage, we can only speculate about the reasons: it may be an experimental issue, e.g. an overlap of the ^{179}Ta peaks with other background components, or it may point to an uncertainty in the branching ratios used by Geant4. Regardless of the reason, the practical problem is that we cannot fit the simulated spectrum with fixed branching ratios to the experimental data: if we would match the peak corresponding to one shell, the height of the other peaks from the simulation will not fit to the ones from experimental data. To solve this problem, we have to find a way to decompose the simulated spectrum into individual spectra, one for each decay branch, e.g. EC from K-shell, L1-shell, etc. Unfortunately, Geant4 does not provide the information to the user from which shell an EC has occured. To reconstruct the involved shell for each EC, the kinetic energy of the daughter nuclide ^{179}Hf is plotted with respect to the total energy deposited by this decay, see fig. 4.11. Based on this, we were able to decompose the simulated spectrum of the total EC decay of ^{179}Ta into the individual shells that make it up as can be seen in fig. 4.12. Each colour correspond to a decay of this nuclide through a different shell. With templates for each involved shell, it is now possible to fit each corresponding peak independently.

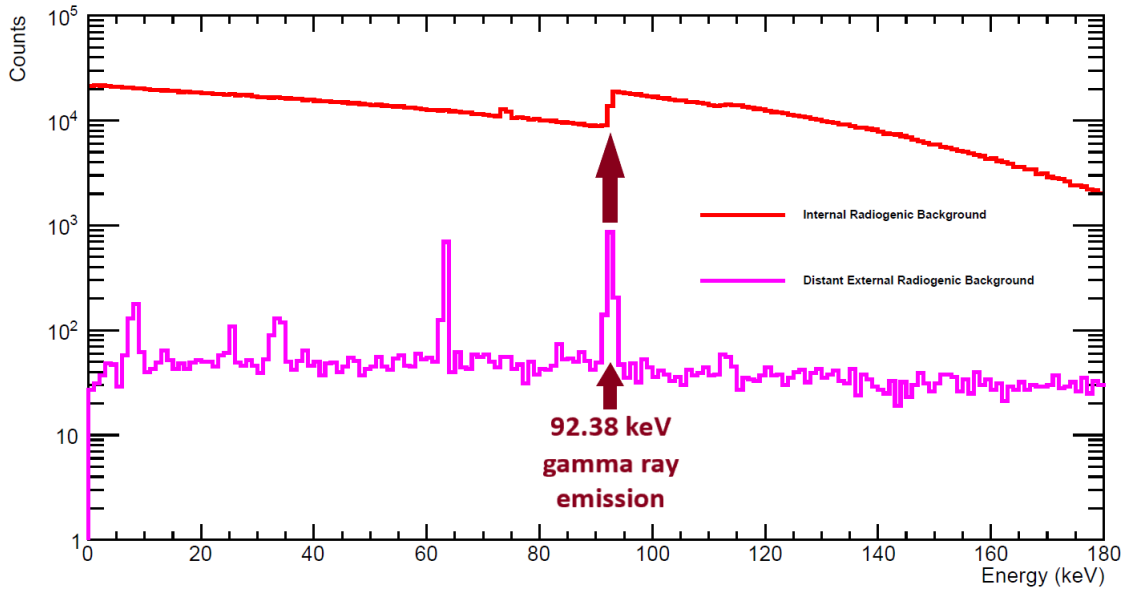

Figure 4.13.: Simulated energy deposition in $CaWO_4$ for an internal decay of ^{234}Th (red), i.e. placed inside the $CaWO_4$ crystal, and an external decay of ^{234}Th (purple), i.e. placed inside a spherical Cu shell around the crystal. In the external case, betas emitted via $^{234}\text{Th} \rightarrow {}^{234\text{m}}\text{Pa}$, $^{234\text{m}}\text{Pa} \rightarrow {}^{234}\text{U}$ (BR = 99.84 %), and $^{234}\text{Pa} \rightarrow {}^{234}\text{U}$ are strongly attenuated. On the contrary, a gamma emission from ^{234}Th is visible in both cases.

We note that the full absorption peaks for the EC from the L1-, L2- shells are overlapping with X-ray escape peaks of the EC from K-shell. This may contribute to the above mentioned apparent deviation of the branching ratios from literature.

Spectra of internal cosmogenic decays simulated for all the nuclides used in this work can be found in appendix A.3. How the results of these individual decays are combined is explained in the next chapter (section 5.2).

4.4.3. External Near Radiogenic Backgrounds

In addition to the internal contamination of the $CaWO_4$ crystal in TUM40, there are additional contributions coming from external sources. The distinction between an internal and an external source in case of a combined beta-/gamma-decay comes from the fact that betas mostly are not energetic enough to pass through the scintillating foils and copper holders around the $CaWO_4$ crystal to be able to deposit energy inside the crystal. On the other hand, gamma rays can penetrate through these parts of the detector module and can be seen in the experimental data.

Therefore, the way the gamma lines are observed in the data from internal and external contaminants is different from each other: considering the poor time resolution of the

detector (see section 4.3.2), an internal beta-/gamma-decay is the pile-up of a gamma-peak and a beta spectrum, whereas from an external beta-/gamma-decay only the gamma-peak is visible. An example of this can be seen in fig. 4.13. Here, the energy deposited in the $CaWO_4$ crystal as a result of beta-/gamma-decay of an internal (red, cf. also fig. 4.10) and an external (purple) ^{234}Th nucleus is shown. In both cases, the features at 92.38 keV belong to the same gamma emissions.

In the internal case, since some percentage of the beta decays occur with the emission of a gamma ray, an edge occurs at the energy of the gamma ray, on top of the continuous beta spectrum. Figure 4.13 contains two different decay modes of this nuclide: a pure beta decay with a Q-value of (274 ± 3) keV and a beta decay associated with the emission of a gamma ray, also with the same Q-value.

For the external case, since most of the beta particles cannot penetrate through the copper holders and the scintillating foil, their energy deposition inside the crystal is relatively low. This leads to a sharp, prominent gamma peak.

Based on this reasoning, the previous study [105] identified ten gamma lines belonging to a total of eight radionuclides (see table 5.6), which had to be originating from outside the $CaWO_4$ crystal. Even though it is known that there are radioactive contaminants outside the crystal, it is not known exactly where they originate from. Considering the experimental setup including the mass of each part, the most likely candidates of contaminated parts include the copper holders of the TUM40 module and copper parts of the cryostat. The holders are the Cu parts which are closest to the crystal, only separated by the scintillating foil. Betas originating in these parts may have the highest probability of all external betas to be seen by the crystal. Therefore, we study this *external near radiogenic backgrounds* separately in this section. The *external distant radiogenic backgrounds* originating from the more distant Cu parts of the cryostat, which are shielded by the parts of the copper holders, are the topic of the next section.

We investigate the external near radiogenic backgrounds under two approaches: as secondaries produced in the near Cu parts which acts as targets and as primaries from contaminants in the near Cu parts.

Approach 1: Secondaries produced in near Cu

Similar to the work in [105] (see the description in section 3.6), gamma rays with energies identified in the experimental data (see table 5.6) are shot towards the detector module and the energy depositions are collected. However, here the full TUM40 geometry (see fig. 4.5) built for this work is used, i.e. the inpinging gamma rays are attenuated by the different parts of the detector module before they hit the $CaWO_4$ crystal.

As an example, a gamma ray with 2614.0 keV, e.g. originating from an external ^{208}Tl decay, is chosen for comparing this work with [105]. In both works, gamma rays with initial energies of 2614.0 keV are shot from the inner surface of an imaginary spherical shell around the $CaWO_4$ crystal to its center. We chose the 2614.0 keV line as an example because it is the most prominent part of the experimental spectrum that can be clearly

identified. We will only analyse the energy deposition in the $CaWO_4$ crystal but we note that external background can deposit energy also in other active parts of the detector module such as the light detector, the scintillating $CaWO_4$ sticks or scintillating foils. In order to compare our work with the findings of [105], we rerun the above described simulation also with the geometry used in [105], i.e. a bare $CaWO_4$ crystal. Figure 4.15 shows the energy deposition in the $CaWO_4$ crystal for both geometries after the events under the photopeak at 2614.0 keV are normalised to 1 in both cases.

Photopeaks indicate that the gamma rays entering the $CaWO_4$ crystal deposit all of their energies, which means they are completely absorbed. The smaller peaks on the left of the photopeaks show the X-ray escape lines, i.e. partial energy depositions caused by X-ray fluorescence originating from the W nucleus which escaped the $CaWO_4$ crystal.

Also in both geometries, we see clearly peaks at 2103 keV and 1592 keV, i.e. the single and double electron escape peaks, respectively (see section 4.1.3).

Three different phenomena occur only in the geometry including the detector holders (black in fig. 4.15). The first one is the 511 keV peak from electron/positron annihilations in the copper. When an incoming gamma ray hits a copper holder, it can produce an electron/positron pair. When the positron from this pair annihilates with an electron, it emits two gamma rays, energies of each that is equal to the rest mass of the electron. This phenomenon gives a peak at 511 keV if one these gamma rays enters the crystal and is completely absorbed. There is no peak at 1022 keV since in order to preserve momentum, the gamma rays should travel in exactly opposite directions.

The second phenomena occur when a gamma ray hits a copper holder, X-rays are emitted and then they enter the crystal, depositing all of their energy. This is called copper fluorescence and the peak related to it can be seen at 8.04 keV. Especially, the 8.04 keV fluorescence line of Cu is well within the ROI of CRESST and, therefore, highlight the importance of a detailed geometry for the simulation of external backgrounds.

The third phenomena involves knock-off electrons (e.g. delta rays, see section 4.1.3). This phenomena can be probably seen in fig. 4.15 at energies of around $\mathcal{O}(100\,\mathrm{keV})$ for the simulation which includes the full detector geometry whereas the same feature is absent for the simulation which includes only the $CaWO_4$ crystal.

Approach 2: Primary background radiation from the near Cu

The previous approach only considers the influence of the module parts as attenuators and targets for more distant gamma rays. Here, we study also the Cu of the detector holders as source for beta-/gamma-background. To do so, we place all the beta emitters, as well as some alpha emitters with associated beta-decays, from the three natural decay chains inside the copper holders.

Since there are various copper parts making up TUM40, as a first trial, one of the nuclides, ^{234}Th, is simulated in sufficient amounts in each copper part to see if there is a position dependency. We chose ^{234}Th as an example because it is one of the most prominent contaminants according to [105]. As can be seen in fig. 4.16, there is nearly

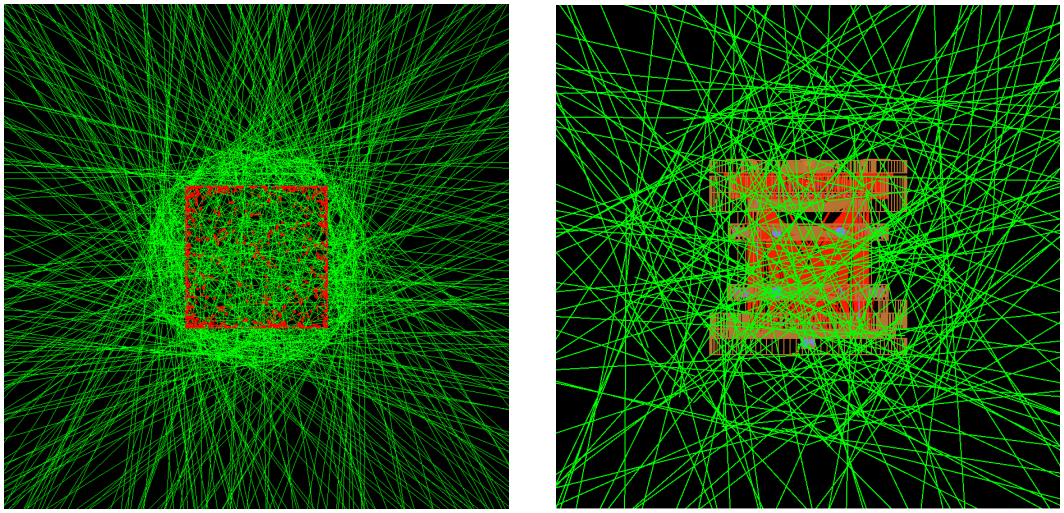

(a) (b)

Figure 4.14.: Visualisation of gamma rays (green) are started on a sphere around (a) the bare, cuboid $CaWO_4$ crystal and (b) TUM40 detector module, and sent inwards. The red points show the energy depositions caused by hits of the gamma rays.

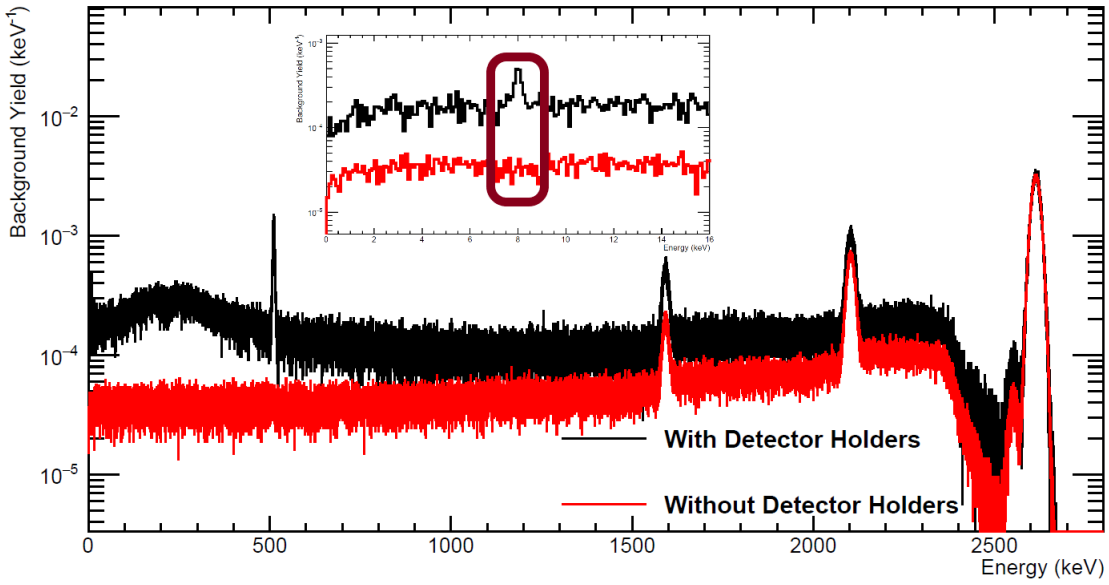

Figure 4.15.: Simulated energy deposition in $CaWO_4$ caused by 2614.0 keV gamma rays from ^{208}Tl for a bare $CaWO_4$ crystal (red) and a $CaWO_4$ crystal inside the TUM40 detector module (black). Both data sets were normalized to the integrals of the photopeaks. The inset shows a zoom to the Cu fluorescence line at 8.04 keV.

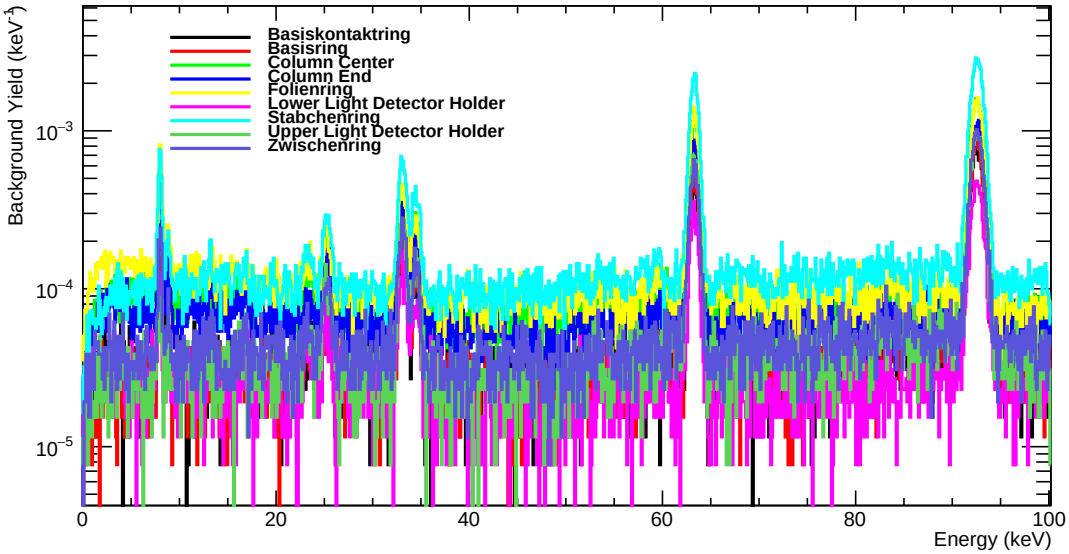

Figure 4.16.: Simulated energy depositions in the $CaWO_4$ crystal caused by ^{234}Th decays in different parts of the crystal holder made out of Cu. Each individual histogram is normalised to the number of decays.

no spectral difference between different copper parts but only a difference in the absolute rate. This occurs due to how far the different parts are to the crystal and how much copper is between them and the crystal. The holder part which contributes most to the background budget is "Stäbchenring" (cf. fig. 4.5a), probably because it is close to the crystal and it surrounds it. Hence, the statistics of the amount of hits coming from this part is expected to be higher than the other parts. Because simulating each nuclide for each of the copper parts is too time consuming given the limited amount of time for this work, we make the following approximation: we simulated all three decay chains but only for Stäbchenring. However, as it will be explained in section 5.3.1, we scaled the obtained background spectra to the mass of all holder parts. As Stäbchenring has the highest background contribution, this approximation may overestimate the contribution of the external near radiogenic background. However, as it will be shown in section 6.2, this background is only a minor component to the overall background budget.

Spectra of near external radiogenic decays simulated for all the nuclides used in this work can be found in appendix A.4. How the results of these individual decays are combined is explained in the next chapter (section 5.3).

4.4.4. External Distant Radiogenic Backgrounds

In addition to the copper holder of TUM40, it is known that also the copper structure of the cryostat has radioactive contamination. However, the implementation of the full

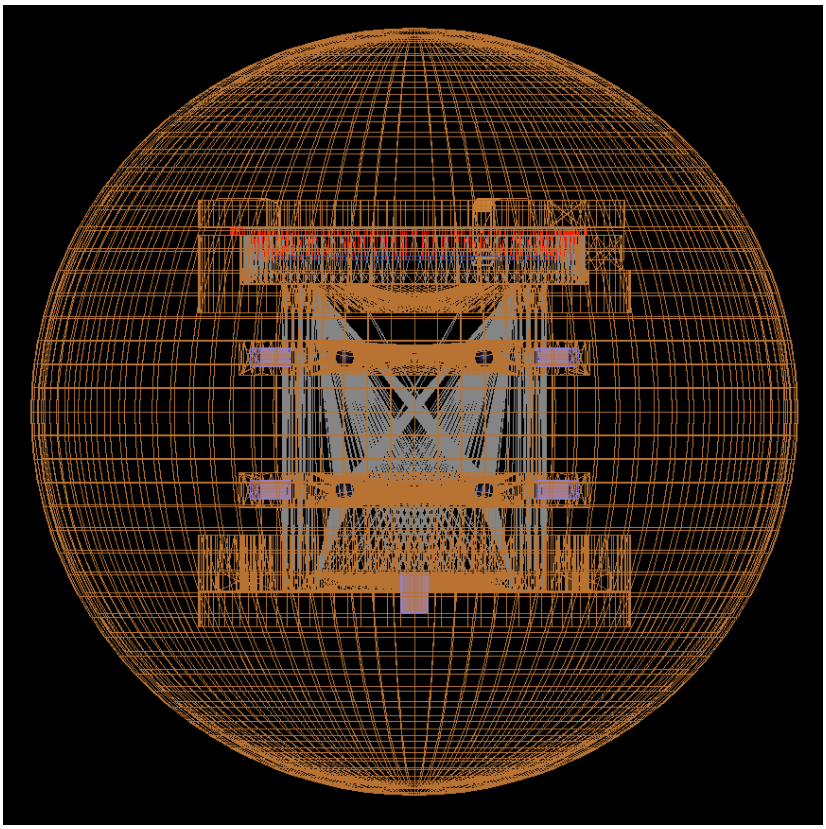

Figure 4.17.: A visualisation of the spherical shell made out of copper around the TUM40 detector module.

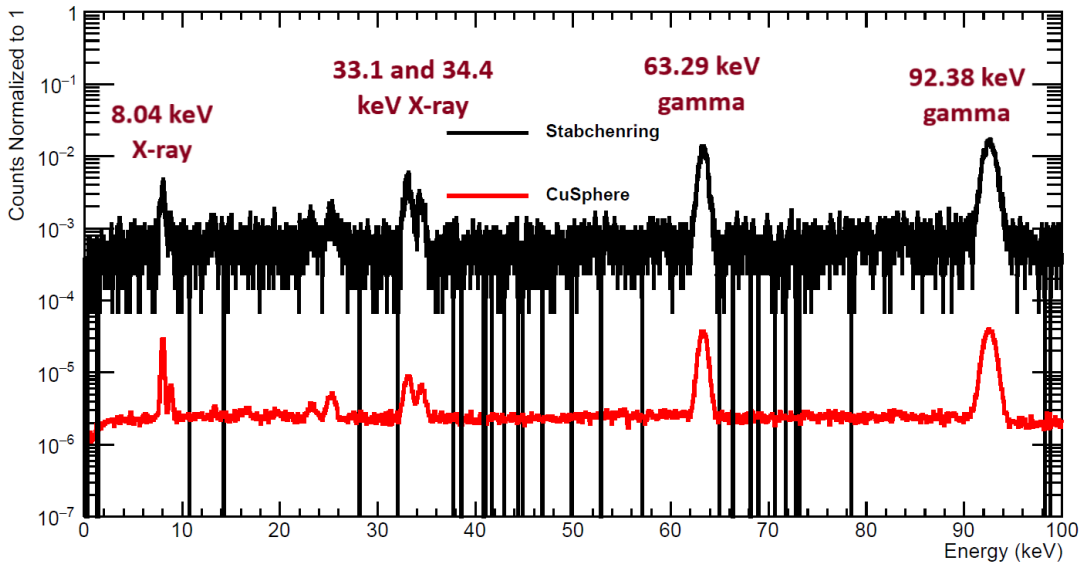

Figure 4.18.: Energy deposition inside the $CaWO_4$ crystal caused by ^{234}Th inside one of the copper holder parts (black) and in the copper spherical shell around the TUM40 detector module (red).

experimental setup is not included in the scope of this work. In order to approximate the copper structure, a simple model is developed: A copper spherical shell with a thickness of 1 mm is created around the TUM40 detector module as shown in fig. 4.17. The nuclides emitting the gamma lines identified in [105] (see also table 5.6) are placed inside this spherical shell and the energy depositions of the decay products of these nuclides in the $CaWO_4$ crystal are collected.

An important consistency check is whether the simulations of the (near) copper holders and the (distant, i.e. outside the copper holders) copper shell give the same result or not. In order to test this, a comparison of templates of the same nuclide simulated in the holders and the copper shell are drawn with respect to each other in fig. 4.18. The energy spectra belong to the beta-/gamma-decay of ^{234}Th. In this comparison, we find two slight differences between the relative heights of some of the peaks in the energies below 100 keV.

The height ratio of $\sim$ 33.1 keV peak to the peak at 92.38 keV is $\sim$ 0.15 in the cop-

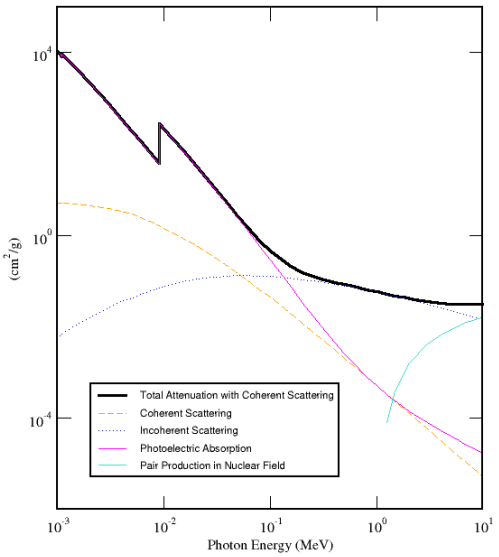

Figure 4.19.: Attenuation of gamma rays in Cu.

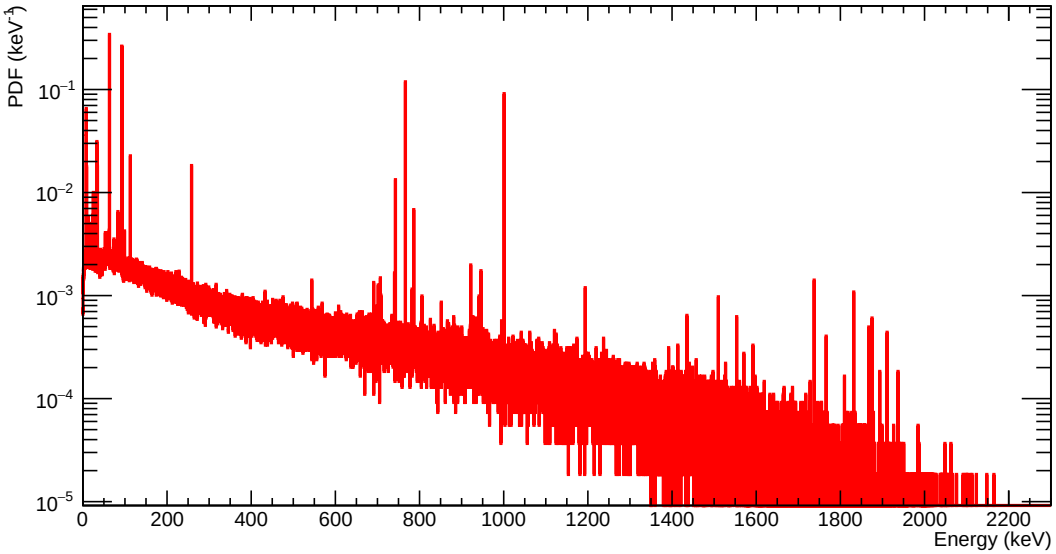

Figure 4.20.: Simulated decay of ^{234}Th inside the copper sphere without applied detector response model.

per holder (black in fig. 4.18), whereas for the same peaks in the copper shell template (red in fig. 4.18) it is ~ 0.08. This can be explained by the attenuation of the decay products from the Cu shell by the full Cu holders, whereas decay products originating inside the Cu holder do not see the full Cu holder as attenuator. As expected, the free path length in Cu decreases with falling gamma energy (see fig. 4.19). Hence, the effect is more pronounced at lower energies.

On the contrary, the ratio of the copper fluorescence line at 8.04 keV to the 92.38 keV peak is higher in the copper shell (red in fig. 4.18) compared to the copper holder (black in fig. 4.18), with ratios ~ 0.18 and ~ 0.07, respectively. The reason for this is similar: as more particles have to go through more copper material, the amount of copper fluorescence emissions increase. For energies higher than 70 keV, the templates match except for the scale because of the amount of particles that can deposit energy inside the crystal is dramatically lower for the copper shell relative to the copper holder.

An example of a template for a distant external beta-decay of ^{234}Th can be seen in fig. 4.20. In this figure, the peaks showing up at various energies along the spectrum correspond to gamma emissions. The continuous part of the spectrum corresponds to a Compton continuum. Spectra of distant external radiogenic decays simulated for all the nuclides used in this work can be found in appendix A.5. How the results of these individual decays are combined is explained in the next chapter (section 5.4).

5. Electromagnetic Background Spectra

In this chapter, detailed information about how the templates are scaled to the activities calculated from the experimental reference data will be given. Finally, the complete scaled templates will be combined to the total background spectra for internal radiogenic, internal cosmogenic and external radiogenic backgrounds.

5.1. Internal Radiogenic Backgrounds

As outlined earlier, internal radiogenic contamination contributes to the background in the ROI mainly via beta-/ gamma-decays. To stay uncorrelated, we will normalize these background to sideband-measurements, i.e. measurements at energies outside the ROI. This will be done in three steps: First, we show how we can use alpha-decays at the MeV-range as sidebands under the assumption of secular equilibrium (section 5.1.1). Second, we will determine the alpha-activities from the experimental reference data (section 5.1.2). Finally, we will calculate the corresponding beta-/gamma-activities and scale the simulated background templates accordingly (section 5.1.3).

5.1.1. Normalisation via Sideband Measurements

For its dark matter analysis, CRESST focuses on the energy regime below 40 keV. At these energies, a great fraction of the observed background is part of continuous beta spectra or Compton continua caused by discrete gamma lines. Because the identification and disentanglement of contamination via their continuous and partial overlapping beta or Compton spectra is hard, these spetra will be connected to clear peaks at higher energies. With this in mind, an analysis is performed in the MeV energy range of 4-7 MeV [105]. Peaks corresponding to contamination by background sources are clearly visible in this energy range. A comparison of the mean energies of these peaks with Q-values of radioactive decays [69] shows that these peaks are caused by alpha decays related to the natural decay chains of ^{238}U, ^{235}U and ^{232}Th. Therefore, it is important to identify these alpha peaks for understanding the background in the low energies. The connection between the MeV-range alpha peaks and keV-range beta and gamma radiation is made via the phenomenon known as *secular equilibrium* [79].

Secular equilibrium is a state of equilibrium between parent and daughter nuclides. There are two criteria that secular equilibrium depends on: the parent nuclide should be long-lived and the daughter nuclide should have a relatively short half-life. In order to

decide if two nuclides are in equilibrium, the first step is to solve the radioactive decay equation [79]:

$$\frac{-\mathrm{d}N_A}{N_A} = \lambda_A \, \mathrm{d}t \tag{5.1}$$

where N_A is the number of atoms of species A present, $\mathrm{d}t$ is the small time interval where $-\mathrm{d}N_A$ number of decays are expected to occur. The decay constant λ of the nuclide in question is defined as

$$\lambda = \frac{\ln 2}{t_{1/2}} \tag{5.2}$$

where $t_{1/2}$ is the half-life of the nuclide.

The solution to eq. (5.1) goes as follows:

$$N(t) = N_0 \, \mathrm{e}^{-\lambda \, t} \tag{5.3}$$

Here, N_0 shows the number of atoms before the decay started and $N(t)$ shows the number of atoms left after time t.

Equation (5.1) deals with the decay of a parent nuclide A which ends at its daughter B. However, if one wants to calculate the consecutive decay of the daughter nuclide, then the following equation should be used [79]:

$$\frac{\mathrm{d}N_b}{\mathrm{d}t} = -\lambda_B \, N_B + \lambda_A \, N_{A0} \, \mathrm{e}{-\lambda_A \, t} \tag{5.4}$$

and the solution of this equation is

$$N_B = \frac{N_{A0} \, \lambda A}{\lambda_A - \lambda_B} \cdot (\mathrm{e}^{-\lambda_A \, t} - \mathrm{e}^{-\lambda_B \, t}) + N_{B0} \, \mathrm{e}^{\mathrm{e}^{-\lambda_B \, t}} \tag{5.5}$$

where N_B is the number of atoms of species B.

In this work, we assume that parent and daughter are in equilibrium, if their activities are closer to each other than 1 % after the 460 days [90] between the crystal growth and the arrival at LNGS passed:

$$\frac{N_A - N_B}{N_A} < 1 \, \% \tag{5.6}$$

We add a second requirement for the secular equilibrium: the initial amount of the daughter, the second summand in eq. (5.5) $N_{B0} \, \mathrm{e}^{\mathrm{e}^{-\lambda_B \, t}}$, should be negligible. We assume that this is the case if the initial amount declined to 10 % during the above mentioned 460 days. Using eq. (5.3), this results in

$$N(460 \, \mathrm{days}) \leq 0.1 \, N_0 \tag{5.7a}$$

$$\lambda_B \leq \frac{\ln(10)}{460 \, \mathrm{days}} \tag{5.7b}$$

Using eq. (5.6) and eq. (5.7), we have established a definition for secular equilibrium in our work. If it is fulfilled, after certain time has passed, the activities of the daughter

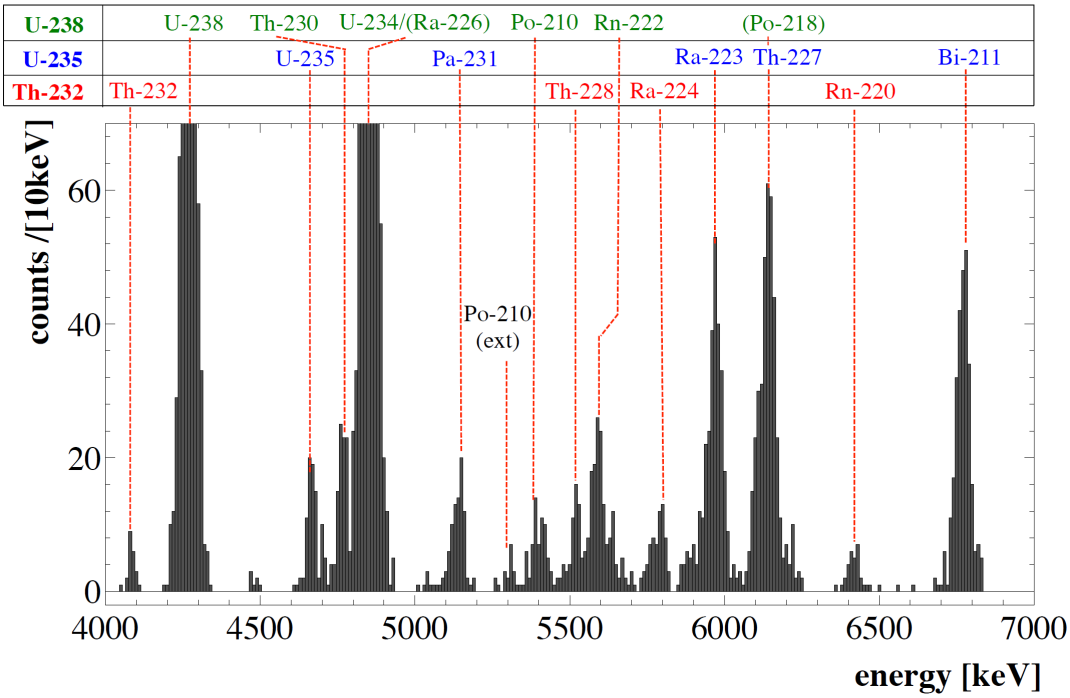

Figure 5.1.: Alpha lines in the energy range between 4 and 7 MeV from the TUM40 training data-set. Figure taken from [105].

nuclide will be equal to that of its parent nuclide. In the event that these conditions are not fulfilled, the result is a broken equilibrium. This means that, a connection between the activities of the parent and the daughter cannot be established. The activities of both should be independently determined.

With this method, one can break down the decay chains into pieces which are in equilibrium. These partitions for each decay chain in question can be found in tables 5.1 to 5.3. The methodology of how the activities of the alpha peaks are determined and how the activities of the subsequent beta and gamma emitters, which are in equilibrium, are calculated will be the subject of the next sections.

5.1.2. Determination of Alpha Activities

For determining the activity A_X of a given alpha-decaying nuclide X, the *high energy reference data* set (see section 3.7.3) is used as reference data. After identifying the

Table 5.1.: An overview of the nuclides of the ^{238}U decay chain. Decay modes, branching ratios, half-lives and activities are included. Nuclides presented in the same colour are in secular equilibrium. Activities of each nuclide are given with systematical errors as deduced in this work.

Parent	**Mode**	**B.R.** (%)	**Half-Life**	**Activity** (μBq/kg)
^{238}U	α	100	$(4.468 \pm 0.006) \cdot 10^9$ y	1073.2 ± 15.4
^{234}Th	β^-	100	(24.10 ± 0.03) d	1073.2 ± 15.4
^{234}Pa	β^-	100	(6.70 ± 0.05) h	1073.2 ± 15.4
^{234}U	α	100	$(2.455 \pm 0.006) \cdot 10^5$ y	1085.5 ± 16.5
^{230}Th	α	100	$(7.54 \pm 0.03) \cdot 10^4$ y	51.2 ± 4.4
^{226}Ra	α	100	(1600 ± 7) y	66.1 ± 5.0
^{222}Rn	α	100	(3.8235 ± 0.0003) d	66.1 ± 5.0
^{218}Po	α	99.98	(3.098 ± 0.012) m	66.1 ± 5.0
^{214}Pb	β^-	100	(27.06 ± 0.07) m	66.1 ± 5.0
^{218}At	α	35.94	(1.5 ± 0.3) s	0.013 ± 0.001
^{214}Bi	α/β^-	99.98	(19.9 ± 0.4) m	66.1 ± 5.0
^{210}Tl	β^-	0.021	(1.30 ± 0.03) m	0.014 ± 0.001
^{214}Po	α	99.979	(164.3 ± 2.0) μs	66.1 ± 5.0
^{210}Pb	α/β^-	100	(22.20 ± 0.22) y	33.1 ± 2.8
^{206}Hg	β^-	1.9×10^{-8}	(8.32 ± 0.07) m	$(62.8 \pm 5.3) \times 10^{-6}$
^{210}Bi	α/β^-	100	(5.012 ± 0.005) d	33.1 ± 2.8
^{206}Tl	β^-	1.339×10^{-6}	(4.202 ± 0.011) m	0.0044 ± 0.0003
^{210}Po	α	100	(138.376 ± 0.002) d	33.1 ± 2.8

Table 5.2.: An overview of the nuclides of the ^{235}U decay chain. Decay modes, branching ratios, half-lives and activities are included. Nuclides presented in the same colour are in secular equilibrium. Activities of each nuclide are given with systematical errors as deduced in this work.

Parent	**Mode**	**B.R.** (%)	**Half-Life**	**Activity** (μBq/kg)
^{235}U	α	100	$(7.04 \pm 0.01) \cdot 10^8$ y	45.5 ± 3.2
^{231}Th	β^-	100	(25.52 ± 0.01) h	45.5 ± 3.2
^{231}Pa	α	100	$(3.276 \pm 0.011) \cdot 10^4$ y	45.0 ± 3.1
^{227}Ac	α/β^-	100	(21.772 ± 0.003) y	143.7 ± 8.6
^{223}Fr	α/β^-	1.38	(22.00 ± 0.07) m	2.0 ± 0.1
^{227}Th	α	98.62	(18.697 ± 0.007) d	141.7 ± 8.5
^{223}Ra	α	99.9999	(11.43 ± 0.05) d	134.8 ± 5.6
^{219}At	α/β^-	8.28×10^{-7}	(56 ± 3) s	$(11.9 \pm 0.7) \times 10^{-5}$
^{215}Bi	β^-	7.75×10^{-7}	(7.6 ± 0.2) m	$(11.1 \pm 0.7) \times 10^{-5}$
^{219}Rn	α	99.9999	(3.96 ± 0.01) s	134.8 ± 5.6
^{215}Po	α/β^-	100	(1.781 ± 0.005) ms	134.8 ± 5.6
^{211}Pb	β^-	99.9998	(36.1 ± 0.2) m	134.8 ± 5.6
^{215}At	α	2.3×10^{-6}	(0.10 ± 0.02) ms	0.031 ± 0.001
^{211}Bi	α/β^-	100	(2.14 ± 0.02) m	147.1 ± 5.5
^{207}Tl	β^-	99.724	(4.77 ± 0.03) m	146.7 ± 5.5
^{211}Po	α	0.276	(0.516 ± 0.003) s	0.41 ± 0.02

Table 5.3.: An overview of the nuclides of the ^{232}Th decay chain. Decay modes, branching ratios, half-lives and activities are included. Nuclides presented in the same colour are in secular equilibrium. Activities of each nuclide are given with systematical errors as deduced in this work.

Parent	**Mode**	**B.R.** (%)	**Half-Life**	**Activity** (μBq/kg)
^{232}Th	α	100	$(1.40 \pm 0.01) \cdot 10^{10}$ y	10.9 ± 1.5
^{228}Ra	β^-	100	(5.75 ± 0.03) y	10.9 ± 1.5
^{228}Ac	β^-	100	(6.15 ± 0.02) h	10.9 ± 1.5
^{228}Th	α	100	(1.9116 ± 0.0016) y	25.4 ± 3.4
^{224}Ra	α	100	(3.6319 ± 0.0023) d	31.1 ± 2.8
^{220}Rn	α	100	(55.6 ± 0.1) s	13.2 ± 1.8
^{216}Po	α	100	(0.145 ± 0.002) s	13.2 ± 1.8
^{212}Pb	β^-	100	(10.64 ± 0.01) h	13.2 ± 1.8
^{212}Bi	α/β^-	100	(60.55 ± 0.06) m	13.2 ± 1.8
^{208}Tl	β^-	35.94	(3.053 ± 0.004) m	4.7 ± 0.7
^{212}Po	α	64.06	(0.299 ± 0.002) μs	8.4 ± 1.2

characteristic alpha lines (the same as in [105], fig. 5.1), the corresponding event number is determined via a Gaussian fit. A Gaussian function is defined as:

$$g(x) = A \cdot \mathrm{e}^{-\frac{1}{2}(\frac{x-E}{\sigma})^2} \tag{5.8}$$

$g(x)$ represents a bell shaped curve where A is the amplitude of the curve, E stands for the mean energy and σ is the variance of the curve. The latter corresponds to the energy resolution of the measurement at the given energy E. In this fit, E, A and σ are free parameters. The mean value of the peak E is initialised with the literature value [69] of the alpha decay in question. The total amount of observed counts $N_{X,\,\mathrm{obs}}$ associated to the alpha line X is obtained by integrating the fitted Gaussian:

$$N_{X,\,\mathrm{obs}} = \int_{-\infty}^{\infty} g(x) \cdot dx = \sqrt{2\pi}\, A\, \sigma \tag{5.9a}$$

$$\delta_{N_{X,\,\mathrm{obs}}} = \sqrt{(2\pi(\delta_A^2 \cdot \sigma^2 + A^2 \cdot \delta_\sigma^2)} \tag{5.9b}$$

We calculated the absolute systematical errors ($\delta N_{X,\,\mathrm{obs}}$) by using error propagation of the errors δ_A and δ_σ obtained from the fit. We assume that the data are not affected by systematic uncertainties.

However, there are two instances in which a simple Gaussian fit cannot be resolved: Two alpha peaks overlap with each other due to the limited detector resolution and give a relatively wider sum-peak. The nuclides in question are ^{234}U/^{226}Ra and ^{218}Po/^{227}Th. Attempts to fit them with the sum of two Gaussians do not converge. However, ^{226}Ra and ^{218}Po are in secular equilibrium with ^{230}Th and ^{222}Rn, respectively. Hence, we perform Gaussian fits to the ^{234}U/^{226}Ra and ^{218}Po/^{227}Th sum-peaks in the experimental data. When the number of events established from the secular equilibrium is subtracted from the integrated sum of the fit to the experimental sum-peak, the number of events for ^{234}U and ^{227}Th nuclides are found. To cross-check the obtained values for $N_{X,\,\mathrm{obs}}$, simulated templates for the alpha decaying nuclide X (see appendix A.2) are scaled accordingly, and after applying the detector response model (section 4.3), compared to the experimental data.

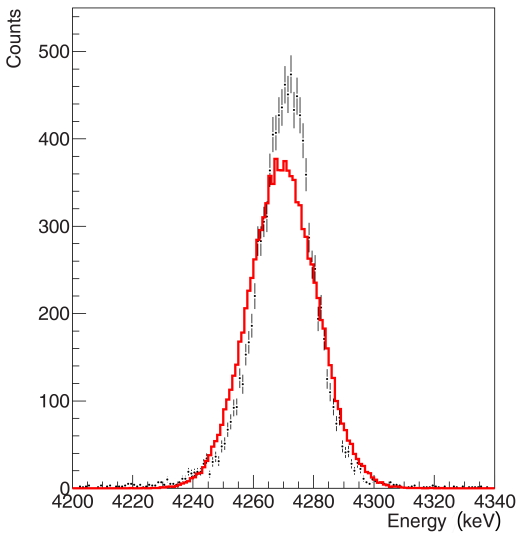

Figure 5.2.: Experimental data (black) and scaled simulated template (red) for the alpha peak corresponding to ^{238}U.

Figure 5.2 shows the comparison between the scaled template and the experimental data for ^{238}U. In this comparison, it is clear that the developed detector response model

overestimate the peak width at these high energies. Because $N_{X,\,\mathrm{obs}}$ is by construction the same between the simulation and the reference data, an overestimation of the simulated peak-width results is an underestimation of the amplitude. However, as fig. 5.3 serves only as a qualitative cross-check, these shortcoming of the detector response model at this energy range is not critial and does not affect the obtained alpha activities. Keeping this in mind, fig. 5.3 shows that the selected alpha-decaying nuclides describe the observed peak structure well.

Finally, the corresponding alpha activity A_X is calculated from the observed number of events $N_{X,\,\mathrm{obs}}$ as:

$$A_X = \frac{N_{X,\,\mathrm{obs}}}{\varepsilon_\mathrm{h} \cdot (T \cdot M)_\mathrm{h}} \tag{5.10a}$$

$$\delta_{A_X} = \frac{\delta_{N_{X,\,\mathrm{obs}}}}{\varepsilon_\mathrm{h} \cdot (T \cdot M)_\mathrm{h}} \tag{5.10b}$$

where $(\mathrm{T} \cdot \mathrm{M})_\mathrm{h}$ stands for the exposure of 129.912 kg $\cdot$ days and $\varepsilon_\mathrm{h} = 86.5\,\%$ is the signal survival probability associated with the *high energy reference data*; see section 3.7.3. The resulting values are listed in Table table 5.4.

When the combination of templates is compared with the high energy experimental data as shown in fig. 5.3, the result shows that (96.7 ± 2.7) % of the data in this range (4-7 MeV) is identified. The errors of this percentage includes both statistical ($\sqrt{N}$ of simulated events N) and systematical (calculated using eq. (5.9b)) contributions.

5.1.3. Scaling of β/γ Templates

After calculating the alpha activities from the reference data, the next step is to obtain the activities of beta-decaying nuclides that are in secular equilibrium with their alpha-decaying parents as discussed in section 5.1.1. The partitioning of the decay chains in elements of piece-wise secular equilibrium and, hence, which daughters (Y) are in equilibrium with their parents (X) can be seen in tables 5.1 to 5.3.

The predicted number of observable events $N_{Y,\,\mathrm{pred}\,(\beta)}$ of the beta-decaying nuclides Y is calculated as follows:

$$N_{Y,\,\mathrm{pred}\,(\beta)} = A_{X,\,\mathrm{obs}} \cdot (\varepsilon \cdot (T \cdot M))_\mathrm{l} \cdot B.R._{X \to Y} \tag{5.11a}$$

$$\delta_{N_{Y,\,\mathrm{pred}\,(\beta)}} = \delta_{A_{X,\,\mathrm{obs}}} \cdot (\varepsilon \cdot (T \cdot M))_\mathrm{l} \cdot B.R._{X \to Y} \tag{5.11b}$$

where $B.R._{X \to Y}$ stand for the cumulative branching ratio between the parent X and the daughter Y.

In this work, the beta-/gamma-background within the ROI is the main focus and it lies within the same energy range which is covered by the *low energy reference data*. To correctly calculate the number of predicted background events $N_{Y,\,\mathrm{pred}\,(\beta)}$ within this energy range, one has to account for the exposure of the low energy spectrum $(T \cdot M)_l =$

Table 5.4.: Gaussian fit values (mean E, amplitude A and variance σ) of the alpha lines observed in the high energy reference data of TUM40. The number of observed events ($N_{\alpha,\mathrm{obs}}$) and the corresponding activities (A_α) are calculated from the integral of the fit. The statistical uncertainties for $N_{\alpha,\mathrm{obs}}$ and A_α are calculated using the fit values as described in the text.

Nuclide	**E (keV)**	**A (#)**	σ **(keV)**	$N_{\alpha,\mathrm{obs}}$ (#)	A_α (μBq/kg)
^{232}Th	4081.6 ± 0.9	4.9 ± 0.6	8.7 ± 0.6	106.1 ± 14.7	10.9 ± 1.5
^{238}U	4270.42 ± 0.09	426.7 ± 5.2	9.74 ± 0.07	10417.4 ± 149.2	1073.2 ± 15.4
^{235}U	4670.3 ± 0.7	12.8 ± 0.8	13.8 ± 0.5	441.5 ± 30.6	45.5 ± 3.2
^{230}Th	4767.1 ± 1.0	11.3 ± 0.7	17.55 ± 1.03	496.8 ± 42.5	51.2 ± 4.4
^{234}U	–	–	–	–	1085.5 ± 16.5[a]
^{226}Ra	–	–	–	–	66.1 ± 5.0[a]
^{231}Pa	5141.6 ± 0.7	11.7 ± 0.7	14.8 ± 0.5	436.1 ± 30.3	45.0 ± 3.1
^{210}Po	5402.7 ± 1.1	6.7 ± 0.5	19.0 ± 0.9	321.4 ± 26.8	33.1 ± 2.8
^{228}Th	5520.6 ± 1.9	5.1 ± 0.5	19.3 ± 2.0	246.6 ± 33.3	25.4 ± 3.4
^{222}Rn	5590.5 ± 0.9	14.2 ± 0.8	18.0 ± 1.0	642.0 ± 48.5	66.1 ± 5.0
^{224}Ra	5789.9 ± 1.8	4.2 ± 0.3	29.0 ± 1.5	301.8 ± 27.3	31.1 ± 2.8
^{223}Ra	5970.1 ± 0.6	24.6 ± 0.9	21.2 ± 0.5	1308.5 ± 54.7	134.8 ± 5.6
^{218}Po	–	–	–	–	66.1 ± 5.0[a]
^{227}Th	–	–	–	–	141.7 ± 8.5[a]
^{220}Rn	6407.7 ± 2.4	2.02 ± 0.23	25.3 ± 2.0	127.9 ± 17.6	13.2 ± 1.8
^{211}Bi	6751.1 ± 0.5	30.05 ± 0.97	19.0 ± 0.4	1428.1 ± 53.5	147.1 ± 5.5

[a] The peaks ^{234}U/^{226}Ra and ^{218}Po/^{227}Th coincide with each other and form sum peaks. Activity of one of the two alpha-lines per peak is obtained via secular equilibrium. The activity of the other alpha-line is calculated by subtracting the activity of the line deduced via secular equilibrium from the activity of the whole peak.

129.912 kg · days (see section 3.7.1) and the bin-wise-calculated signal survival probability ϵ_l shown in fig. 3.10a.

After scaling the simulated templates to the obtained $N_{Y,\,\mathrm{pred}\,(\beta)}$, fig. 5.4 shows the final sum of all beta-decaying nuclides. The associated error bars follow from Equation eq. (5.11b).

To calculate the activities corresponding to $N_{Y,\,\mathrm{pred}\,(\beta)}$ and the associated systematical errors, the following equations should be used:

$$A_{Y,\,\mathrm{pred}\,(\beta)} = \frac{N_{Y,\,\mathrm{pred}\,(\beta)}}{\varepsilon_\mathrm{l} \cdot (T \cdot M)_\mathrm{l}} \tag{5.12a}$$

$$\delta_{A_{Y,\,\mathrm{pred}\,(\beta)}} = \frac{\delta_{N_{Y,\,\mathrm{pred}\,(\beta)}}}{\varepsilon_\mathrm{l} \cdot (T \cdot M)_\mathrm{l}} \tag{5.12b}$$

Comparing with $N_{Y,\,\mathrm{pred}\,(\beta)}$ from eq. (5.11a), one sees that the activity $A_{Y,\,\mathrm{pred}\,(\beta)}$ is independent from the exposure and the signal survival probability of the low energy reference data. Via section 5.1.2 and eq. (5.11), it only depends on the exposure and the signal survival probability of the high energy reference data. The obtained values are listed in tables 5.1 to 5.3.

5.2. Internal Cosmogenic Backgrounds

Internal cosmogenic contaminants contribute to the background in the ROI via X-ray emissions resulting from EC in the case of ^{179}Ta or via beta-decay in the case of ^{3}H. The latter is produced from cosmogenic activation of ^{183}W, together with ^{181}W, which we will use as a proxy for the ^{3}H contamination. Obtaining the contamination quantitatively and scaling for each nuclide needs to be performed in three steps. First, we will fit the peak corresponding to ^{181}W and scale the resulting activity (section 5.2.1). Since the production of ^{3}H occurs in connection with ^{181}W, the resulting activity of the latter will be used to scale the former (section 5.2.2). Finally, the activity of ^{179}Ta will be calculated through fitting the associated X-ray lines in the experimental data (section 5.2.3). After scaling the simulated templates, fig. 5.5 shows the final sum of all cosmogenically activated nuclides. The agreement between the data and the total simulation will be discussed in section 6.1.

5.2.1. Determination of ^{181}W Activity

A similar approach as used for determining the alpha activities (section 5.1.2) will be performed to obtain the numbers for ^{181}W decays. To avoid an overlap of the charateristic peak under investigation by peaks of similar energy from other nuclides, we subtract all the background templates described in section 5.1.3, section 5.3.2 and section 5.4.2 from the reference data before we perform the fit.

However, different from the alpha lines, the fit function will have an additional term. The reason for this is that, unlike the clear alpha lines in the high energy reference data, a

Compton continuum constitutes a linear background in the low energy reference data. In order to account for the linear background, a Gaussian function and a linear background is used:

$$h(x) = (a + b \cdot x) + A \cdot \mathrm{e}^{-\frac{1}{2}(\frac{x-E}{\sigma})^2} \tag{5.13}$$

where a and b are the amplitude and the slope of the linear background component, respectively, and the second summand is the Gaussian function (eq. (5.8)). Using a first order polynomial in the first part of the fit function account for the effect of the linear background of the low energy reference data. This way, the Gaussian part contains only the events under the X-ray peak.

To calculate the corresponding event number, $h(x)$ is fitted with free floating a and b values as well as free floating mean energy E, amplitude A and resolution σ. The mean value of the peak E is initialised with the literature value [69] of the EC and associated gamma emission in question. The total amount of observed counts $N_{^{181}\mathrm{W,\,obs}}$ associated to the X-ray line of ^{181}W, and the corresponding errors are calculated using eq. (5.9a) and eq. (5.9b), respectively. The agreement between the data and the total simulation will be discussed in section 6.1.

With number of events known, the activities corresponding to these numbers can be calculated:

$$A_{^{181}\mathrm{W,\,obs}} = \frac{N_{^{181}\mathrm{W,\,obs}}}{\varepsilon_l \cdot (T \cdot M)_\mathrm{l}} \tag{5.14a}$$

$$\delta_{A_{^{181}\mathrm{W,\,obs}}} = \frac{\delta_{N_{^{181}\mathrm{W,\,obs}}}}{\varepsilon_l \cdot (T \cdot M)_\mathrm{l}} \tag{5.14b}$$

The resulting values are listed in table 5.5.

5.2.2. Determination of ^{3}H Activity

As described in section 3.5.3, proton capture of ^{183}W results in ^{181}W along with ^{3}H. Considering the fact that ^{3}H is also an unstable nuclide, we expect this isotope to contribute to the background. However, if we want to use the clear peak of ^{181}W as a proxy to determine the activity of the ^{3}H beta-spectrum, we have to consider the different decay constants ($\lambda_{^{181}\mathrm{W}}$ and $\lambda_{^3\mathrm{H}}$).

A preliminary ACTIVIA [35] calculation gives the activity of ^{3}H relative to ^{181}W as 62 % [77]. This calculation assumes that ^{3}H ($\mathrm{t}_{1/2} = (12.32 \pm 0.02)$ y) activity is set to zero during the melting of the crystal. Afterwards, the crystal is stored above ground where they are exposed to cosmic rays at sea level for 460 days before it is moved to LNGS. In this time, ^{3}H is cosmogenically produced inside the crystals. Once the crystals arrive at LNGS, the activity of ^{3}H started to decline. Since ^{181}W is short-lived ($\mathrm{t}_{1/2} = (121.2 \pm 0.2)$ d) relative to ^{3}H, it nearly reaches equilibrium during the exposure period. Therefore, it is rather insensitive to the precise exposure history.

Once we obtained $N_{^3\mathrm{H,\,pred}}$, we calculate the corresponding activity similar to eq. (5.14).

5.2.3. Determination of ^{179}Ta Activity

The same method used in section 5.2.1 is also used to determine the activity of ^{179}Ta.

We fit a Gaussian (eq. (5.13)) to each X-ray peak belonging to a decay via EC from the K, L1, L2 and M1 shells and subsequent atomic de-excitations. To calculate the $N_{^{179}\mathrm{Ta},\,X,\,\mathrm{obs}}$ of each line X, we are using eq. (5.9).

Once we obtained $N_{^{179}\mathrm{Ta},\,X,\,\mathrm{obs}}$, we calculate the corresponding activity similar to eq. (5.14). The resulting values are listed in table 5.5.

5.3. External Near Radiogenic Backgrounds

As it is explained in detail in section 4.4.3, there are external background sources, i.e. radioactive contamination of the Cu of the crystal holder, contaminating the experimental data. This contamination contributes to the background in the ROI mainly via beta-/gamma-decays, just as in the case of the internal radiogenic contamination. We want to point out that due to the proximity of the sources to the crystal, also low energy betas are visible, contrary to betas from more distant sources (see section 4.4.3) which are attenuated. The activities of near external radiogenic backgrounds are taken from screening measurements of the copper used by CUORE experiment [15], which is from the same producer (Norddeutsche Affinerie) and grade as the Cu used for the detector holders of TUM40 detector module. First, we show how the activities are calculated (section 5.3.1). Finally, we will scale the simulated templates using the calculated activities (section 5.3.2).

5.3.1. Calculation of Activities

A screening analysis performed on the copper used in the CUORE experiment shows upper limits for the activities of radioactive contaminants ^{238}U and ^{232}Th, i.e. the heads of the corresponding decay chains. The bulk radioactive contaminations of the copper components are given in g/g[1] as follows [15]:

$$A_{\mathrm{bulk\,copper},\,^{238}\mathrm{U}} = 1.8 \cdot 10^{-12}\ \mathrm{g/g}\ (\mathrm{C.L.} = 90\,\%) \tag{5.15a}$$

$$A_{\mathrm{bulk\,copper},\,^{232}\mathrm{Th}} = 1.5 \cdot 10^{-12}\ \mathrm{g/g}\ (\mathrm{C.L.} = 90\,\%) \tag{5.15b}$$

In order to convert these values into the units of μBq/kg, one has to use the following relations [62]:

$$1\ \mathrm{Bq/kg}_{^{238}\mathrm{U}} \mathrel{\hat{=}} 81 \cdot 10^{-9}\ \mathrm{g/g} \tag{5.16a}$$

$$1\ \mathrm{Bq/kg}_{^{232}\mathrm{Th}} \mathrel{\hat{=}} 246 \cdot 10^{-9}\ \mathrm{g/g} \tag{5.16b}$$

[1] This unit shows the amount of contaminant in grams inside the mass of the contaminated material. Here, it shows the amount of ^{238}U (and ^{232}Th) in grams in per gram of copper

Table 5.5.: Gaussian fit values (mean E, amplitude A and variance σ) of cosmogenic X-ray lines observed in the experimental data of TUM40. The number of observed events ($N_{\mathrm{X-ray,obs}}$) and the corresponding activities ($A_{\mathrm{X-ray}}$) are calculated from the integral of the fit. The statistical uncertainties for $N_{\mathrm{X-ray,obs}}$ and $A_{\mathrm{X-ray}}$ are calculated using the fit values as described in the text. Based on simulations, η is the ratio between the activities of the photo peak $A_{\mathrm{X-ray}}$ and the complete spectrum.

Nuclide	E **(keV)**	A (#)	σ **(keV)**	$N_{\mathrm{X-ray,obs}}$ (#)	$A_{\mathrm{X-ray}}$ (μBq/kg)	η	A_{Total} (μBq/kg)
^{179}Ta(M2)	2.620 ± 0.007	162.8 ± 12.2	0.094 ± 0.006	384.0 ± 38.2	49.8 ± 5.0	1.	49.8 ± 5.0
^{179}Ta(L2)	10.83 ± 0.02	37.3 ± 15.7	0.09 ± 0.04	83.2 ± 50.4	10.6 ± 6.4	0.9997	10.6 ± 6.4
^{179}Ta(L1)	11.333 ± 0.004	408.1 ± 18.4	0.097 ± 0.006	990.8 ± 75.8	126.2 ± 10.0	0.9998	126.2 ± 10.0
^{179}Ta(K)	64.994 ± 0.008	233.1 ± 7.8	0.264 ± 0.006	1541.0 ± 63.6	170.6 ± 7.0	0.9719	175.6 ± 7.3
^{181}W	73.49 ± 0.05	19.6 ± 1.9	0.51 ± 0.04	249.3 ± 29.6	27.0 ± 3.2	0.4873	55.5 ± 6.6
^{3}H	–	–	–	–	–	–	40.7 ± 4.8[a]

[a] The activity of ^{3}H is calculated via the activity of ^{181}W (see section 5.2.2).

Hence, we obtain the following values for the activities:

$$A_{\text{copper, }^{238}\text{U}} = 65\ \mu\text{Bq/kg} \tag{5.17a}$$

$$A_{\text{copper, }^{232}\text{Th}} = 2\ \mu\text{Bq/kg} \tag{5.17b}$$

Assuming natural abundance of radioactive nuclides, one can deduce the upper limit for the ^{235}U using the equation [31]:

$$A_{\text{bulk copper, }^{235}\text{U}} = A_{\text{bulk copper, }^{238}\text{U}} \cdot 0.70\,\% = 0.455\ \mu\text{Bq/kg} \tag{5.18}$$

For this work, it is assumed that each decay chain inside the near copper parts is in secular equilibrium, i.e. that each nuclide has the same amount of activity as the nuclide at the top of the chain.

5.3.2. Scaling of β/γ Templates

The final step is to scale each of these nuclides using the upper limits discussed in section 5.3.1. However, in order to do this, one has to take into account the masses of the near copper parts used for this work, which is $m_{\text{Cu}} = 290$ g in total and the spatial arrangement of the parts around the $CaWO_4$.

As discussed in section 4.4.3 and shown in fig. 4.16, there is only a slight dependency of the simulated energy depositions at energies below ~ 40 keV on the individual parts of the detector holder. The part "Stäbchenring" (cf. fig. 4.5a) has the highest contribution to the background per part mass. Hence, as a trade-off between accuracy and simulation performance, we conservatively use only this part to simulate the full three decay chains and scale its background spectra to the mass of all copper parts.

Taking this information into account, the scaling can be done using the following equation:

$$A_{X,\,\text{pred}} = A_{\text{top}} \cdot B.R. \cdot \varepsilon_{\text{l}} \cdot (T \cdot M)_{\text{l}} \cdot 86400\,\text{day}\,\text{Bq}^{-1} \cdot \frac{m_{\text{Cu}}}{\text{M}} \tag{5.19a}$$

$$N_{X,\,\text{pred}} = A_{X,\,\text{pred}} \cdot \varepsilon_{\text{l}} \cdot (T \cdot M)_{\text{l}} \tag{5.19b}$$

where A_{top} is the activity of the top of the particular decay chain (eqs. (5.17) and (5.18)), B.R. is the cumulative branching ratio between the top of the decay chain and nuclide X, m_{Cu} is the total Cu mass (see table 4.1) and M is the crystal mass of 248 g.

Since the activities used in this part are upper limits, no uncertainty is taken into account.

The sum of all these contributions is shown in fig. 5.6.

5.4. External Distant Radiogenic Backgrounds

As explained in section 4.4.4 a number of external gamma emissions are observed in the experimental data (see table 5.6). These gamma lines of external origin can undergo

Compton scattering in the $CaWO_4$ crystal or produce knock-off electrons in the Cu parts close to the crystal, producing significant backgrounds in the ROI of the TUM40 data. The physical place of origin of these nuclides can be e.g. the cryostat thermal shielding around the detector modules. As described in section 4.4.4, this complex shielding structure is approximated in the simulation as a spherical shell made of 1 mm-thick copper which is centered around the TUM40 detector module. The nuclides aforementioned gamma emissions originate from are placed inside this shell and the energy depositions inside the crystal are recorded. In this section, first we will determine the activities using these gamma ray peaks in the observed experimental reference spectra (section 5.4.1). Secondly, we will scale the simulation templates with the activities (section 5.4.2).

5.4.1. Determination of Gamma Activities

A similar approach as used in section 5.2.1 is performed for the external gamma ray emissions. To avoid an overlap of the charateristic peak under investigation by peaks of similar energy from other nuclides, we subtract all previously described background templates (section 5.1.3 and section 5.3.2) from the reference data before we perform the fit.

Since these lines are superimposed over a linear background which originates from other sources, we will fit the sum of a first order polynomial and a Gaussian to each peak using eq. (5.13) with free floating parameters. The mean value of the peak E is initialised with the literature value [69] of the energy of the emitted gamma energy in question. The total amount of observed counts $N_{X,\,\mathrm{obs}}$ associated to each gamma line and the corresponding errors are calculated using eq. (5.9a) and eq. (5.9b), respectively. To calculate the full activity from the observed counts under the peak we use:

$$A_{peak,\,\mathrm{obs}} = \frac{N_{peak,\,\mathrm{obs}}}{\varepsilon_{\mathrm{i}} \cdot (T \cdot M)_{\mathrm{i}}} \tag{5.20a}$$

$$\delta_{A_{peak,\,\mathrm{obs}}} = \frac{\delta_{N_{peak,\,\mathrm{obs}}}}{\varepsilon_{\mathrm{i}} \cdot (T \cdot M)_{\mathrm{i}}} \tag{5.20b}$$

where ε and $(T \cdot M)$ are the signal survival probability and the exposure for the relevant reference data set in which the particular peak is observed: either low energy reference data set ($i = \mathrm{l}$, see section 3.7.1) or medium energy reference data set ($i = \mathrm{m}$, see section 3.7.2). To obtain the full activity of the decay, we scale $A_{peak,\,\mathrm{obs}}$ with η, which is the fraction of events under the peak to all events from the particular decay as deduced from the simulated templates (see table 5.6). The ratio η is therefore defined as:

$$\eta = \frac{N_{peak,\,\mathrm{pred}}}{N_{total,\,\mathrm{pred}}} \tag{5.21}$$

The total activity is therefore:

$$A_{total,\,\mathrm{obs}} = \frac{A_{peak,\,\mathrm{obs}}}{\eta} \tag{5.22a}$$

$$\delta_{A_{total,\,\mathrm{obs}}} = \frac{\delta_{A_{peak,\,\mathrm{obs}}}}{\eta} \tag{5.22b}$$

The obtained values for $N_{gamma,\,\mathrm{obs}}$, A_γ, η and $\mathrm{A}_{\mathrm{Total}}$ are listed in table 5.6.

5.4.2. Scaling of β/γ Templates

The next step is to predict the observable number of events $N_{total,\,\mathrm{pred}}$ in the low energy range as caused by each gamma line observed in the experimental data.

$$N_{total,\,\mathrm{pred}} = A_{total,\,\mathrm{obs}} \cdot \varepsilon_\mathrm{l} \cdot (T \cdot M)_\mathrm{l} \tag{5.23a}$$

$$\delta_{N_{total,\,\mathrm{pred}}} = \delta A_{total,\,\mathrm{obs}} \cdot \varepsilon_\mathrm{l} \cdot (T \cdot M)_\mathrm{l} \tag{5.23b}$$

We note that eq. (5.23a) and eq. (5.23b) can be simplified for the four lines (^{210}Pb, ^{234}Th, ^{226}Ra, ^{212}Pb) which occur in the low energy reference data. In this case, since signal survival probabilities and exposures in both eq. (5.20) and eq. (5.23) are the same, they cancel each other and, therefore, the predicted number of observable events is independent from the signal survival probability and exposure.

The sum of all these contributions is shown in fig. 5.7.

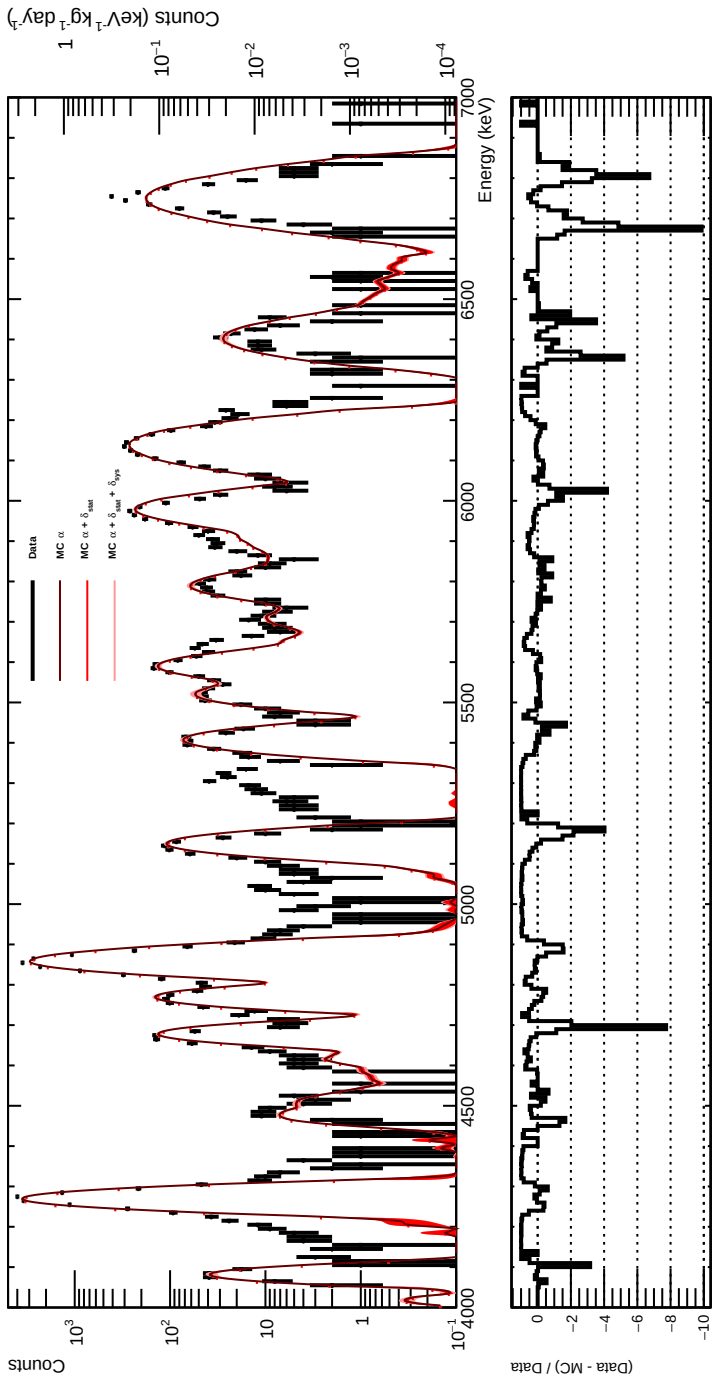

Figure 5.3.: Top panel: comparison of simulated templates for alpha decays (dark red) and the experimental energy spectrum of TUM40 (black) [37]. Light red shows the band of statistical errors and with the pale red the band of statistical and systematical errors. Bottom panel: relative residual between simulation and data.

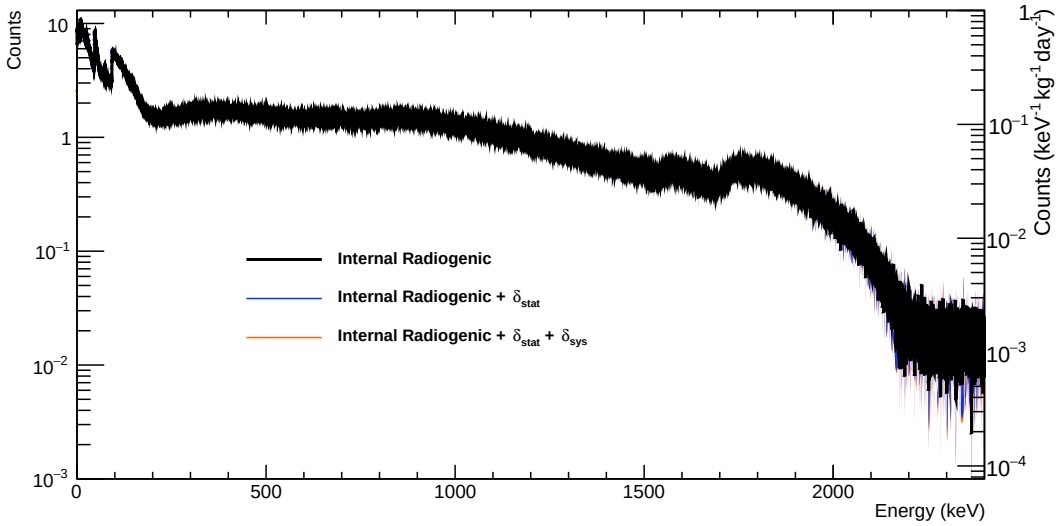

(a)

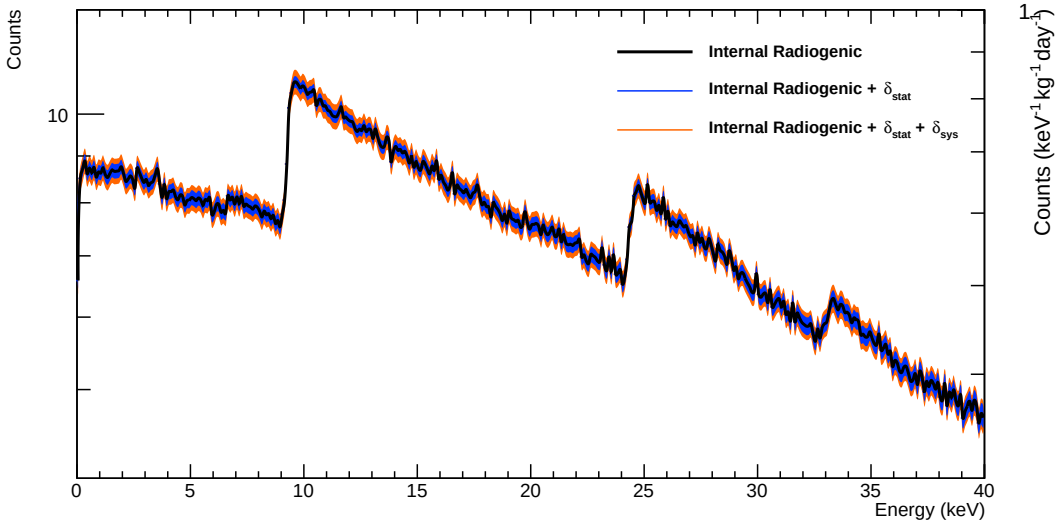

(b)

Figure 5.4.: Combination of all simulated templates for internal beta-decays (a) and zoom on the first 40 keV (b).

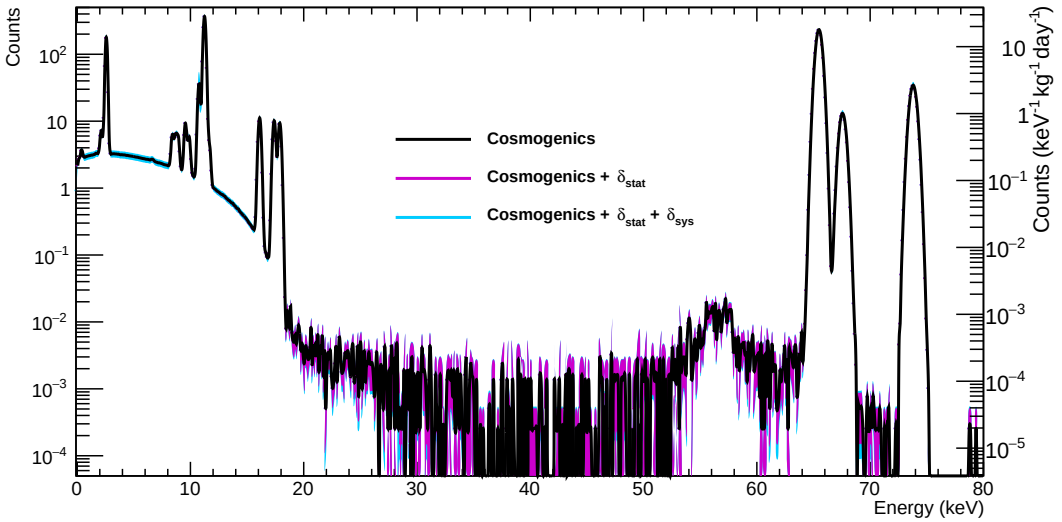

(a)

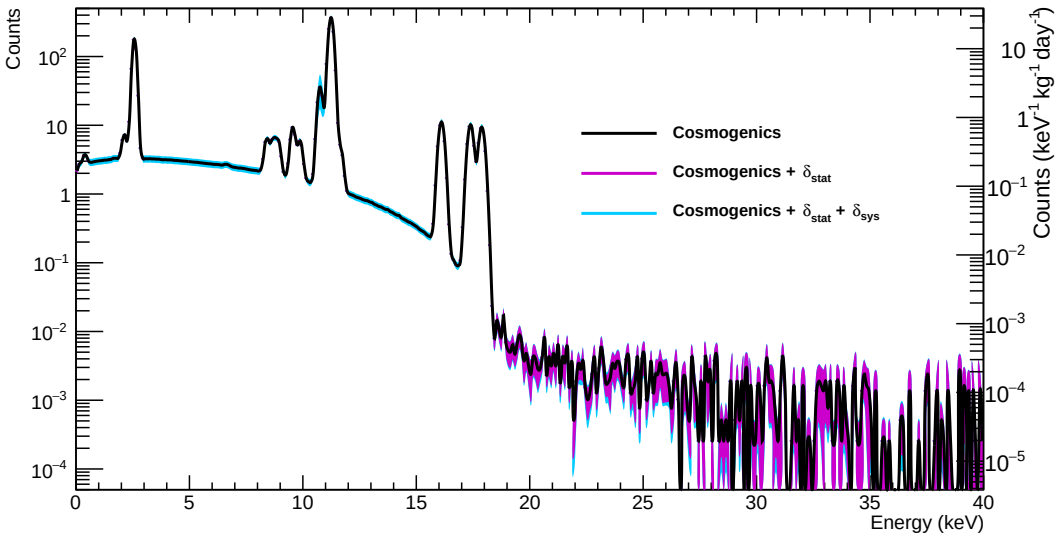

(b)

Figure 5.5.: Combination of all simulated templates for internal decays caused by cosmogenic activation (a) and zoom on the first 40 keV (b).

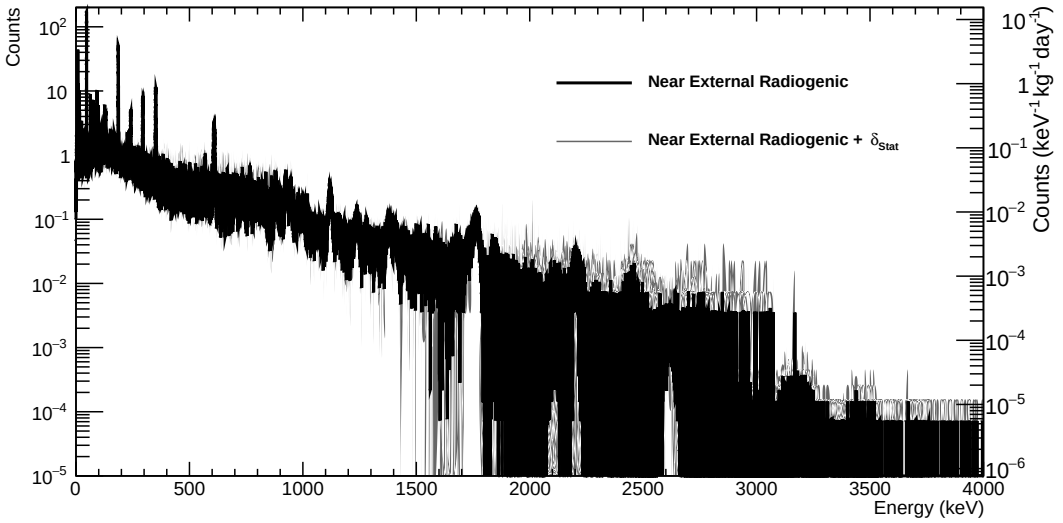

(a)

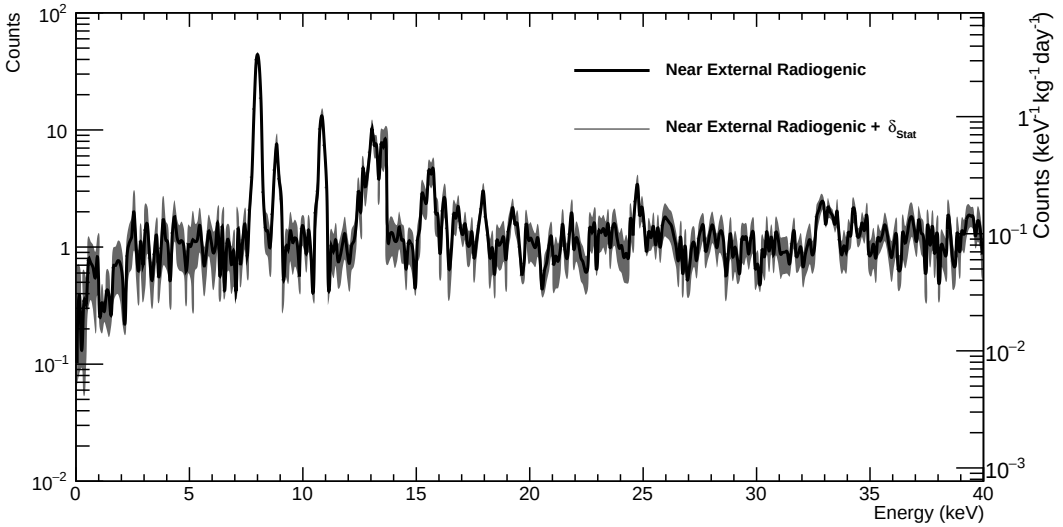

(b)

Figure 5.6.: Combination of all simulated templates for external contaminations in the near copper parts (a) and zoom on the first 40 keV (b).

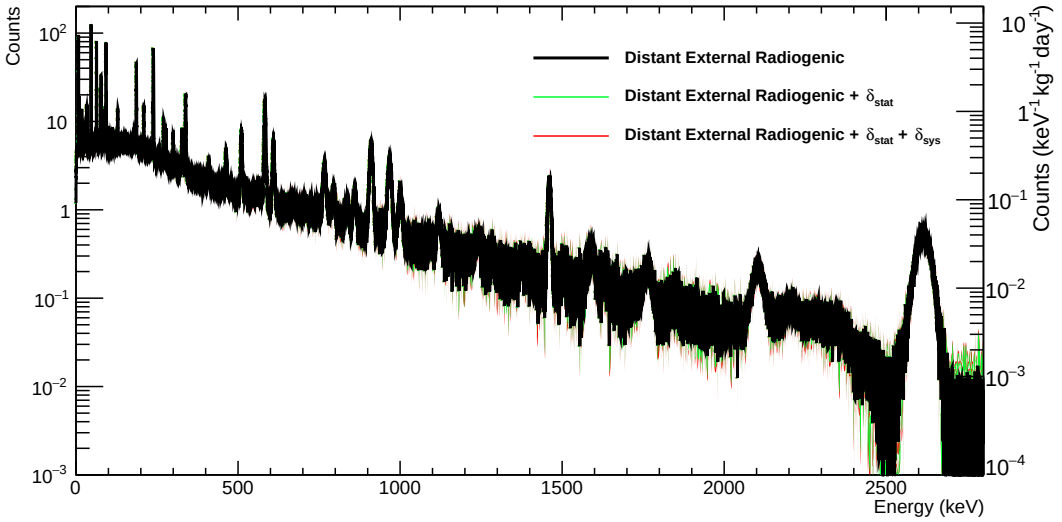

(a)

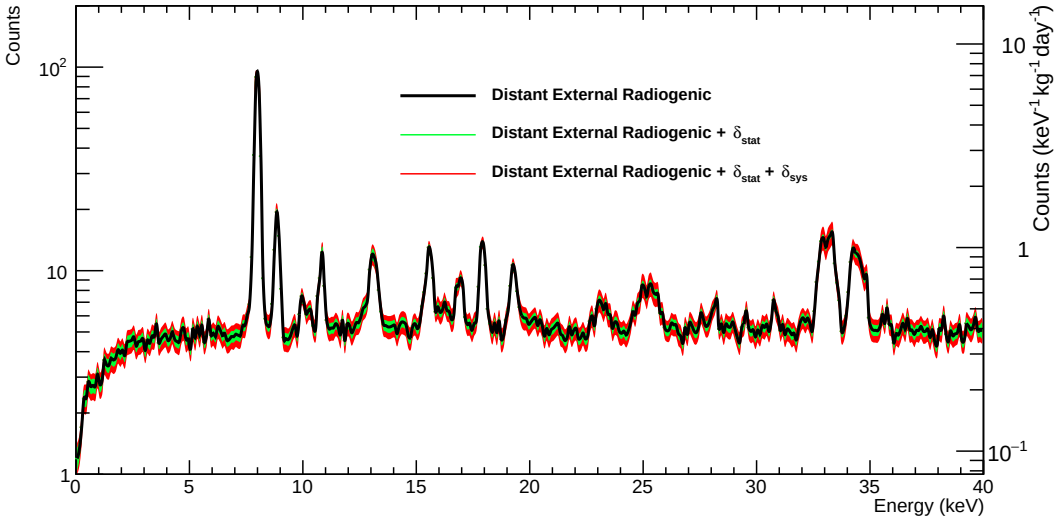

(b)

Figure 5.7.: Combination of all simulated templates of external contaminations in the distant copper parts (a) and zoom on the first 40 keV (b).

Table 5.6.: Gaussian fit values (mean E, amplitude A and variance σ) of gamma lines observed in the experimental data of TUM40. The number of observed events ($N_{\gamma,\mathrm{obs}}$) and the corresponding activities (A_γ) are calculated from the integral of the fit. The statistical uncertainties for $N_{\gamma,\mathrm{obs}}$ and A_γ are calculated using the fit values as described in the text. Based on simulations, η is the ratio between the activities of the photo peak A_γ and the complete spectrum $\mathrm{A_{Total}}$.

Nuclide	E **(keV)**	A (#)	σ **(keV)**	$N_{\gamma,\mathrm{obs}}$ (#)	A_γ (μBq/kg)	η	A_{Total} (μBq/kg)
^{210}Pb	46.29 ± 0.01	105.2 ± 6.0	0.23 ± 0.01	599.3 ± 44.9	66.8 ± 5.0	0.784	85.2 ± 6.4
^{234}Th	92.18 ± 0.04	33.8 ± 2.7	0.45 ± 0.03	377.7 ± 40.4	39.6 ± 4.2	0.027	1479.2 ± 158.3
^{226}Ra	185.62 ± 0.04	36.3 ± 2.3	0.63 ± 0.04	574.0 ± 48.0	60.2 ± 5.0	0.58	103.6 ± 8.7
^{212}Pb	239.77 ± 0.05	614.3 ± 25.6	1.30 ± 0.05	1339.3 ± 78.5	140.4 ± 8.2	0.43	325.2 ± 19.1
^{214}Bi	608.9 ± 0.1	83.6 ± 6.5	1.7 ± 0.1	355.5 ± 37.4	37.3 ± 3.9	0.14	260.8 ± 27.4
^{228}Ac	967.8 ± 0.2	107.1 ± 7.9	2.6 ± 0.2	352.2 ± 33.0	36.9 ± 3.5	0.036	1017.9 ± 95.4
^{40}K	1460.6 ± 0.3	53.1 ± 5.3	3.4 ± 0.3	227.6 ± 30.6	23.9 ± 3.2	0.11	220.8 ± 29.7
^{208}Tl	2615.0 ± 0.3	45.6 ± 3.2	5.8 ± 0.3	331.7 ± 27.9	34.8 ± 2.9	0.052	669.3 ± 56.3

6. Results and Discussion

In this chapter, first, the sum of all scaled simulation templates will be compared to the experimental reference data (section 6.1). Next, the contribution of the individual components to the overall background will be explained quantitatively (section 6.2). Finally, we compare our work quantitatively with the previous work on backgrounds in CRESST and qualitatively with a background analysis of another rare event search (section 6.4).

6.1. Reproduction of the Observed Background

In chapter 5, the determination of the activities corresponding to the backgrounds contaminating the TUM40 detector module internally and externally were explained in detail. After calculating the activities of each nuclide, simulated templates were scaled to the experimental reference data. These contributions are summed according to their place of origin and their decay type.

In order to be able to compare the background model of this work with the reference data, different contributions should be added up. In this section, we will first compare our combined background templates with the medium energy reference data and, then, with the low energy reference data.

A simple summation over the templates scaled to the predicted activities is sufficient:

$$N_{\mathrm{MC,\,m}} = (\varepsilon_{\mathrm{m}} \cdot (T \cdot M)_{\mathrm{m}}) \cdot \sum_i A_i \tag{6.1a}$$

$$\delta_{N_{\mathrm{MC,\,m}}} = (\varepsilon_{\mathrm{m}} \cdot (T \cdot M)_{\mathrm{m}}) \cdot \sqrt{\sum_i (\delta_{A_i})^2} \tag{6.1b}$$

where A_i is the activity predicted for the internal radiogenic backgrounds (eq. (5.12)), internal cosmogenic backgrounds (eq. (5.14)), near and distant external radiogenic backgrounds (eq. (5.19) and eq. (5.22)); ε_{m} and $(T \cdot M)_{\mathrm{m}}$ are the signal survival probability and the exposure of the medium energy data set, respectively (see section 3.7.2).

Figure 6.1 shows the combined templates along with the medium energy reference data (see section 3.7.2). It can be seen that the continuous part, consisting of Compton continua and beta spectra, of the simulated templates is matching the experimental data within the uncertainties.

Also, the annihilation peak at 511 keV (see section 4.4.3) in the simulated templates fits the experimental data. Since this peak occurs due to any external (near or distant) contaminants with Q-values equal to or higher than twice this energy, it shows that the

external contamination predicted for this medium energy reference data (along with the contribution from the internal radiogenic spectrum) is valid within the errors from both the experimental and simulated spectra.

In addition, also the discrete lines of the spectrum match well between simulation and data. Simulated templates of the nuclides which can be seen in the experimental data as prominent peaks originating from distant external contaminants (^{214}Bi, ^{228}Ac, ^{40}K, ^{208}Tl) are fitted to the experimental data both in terms of amplitude and width. Besides these fitted peaks, there are more peaks originating from the same nuclides that are not fitted to the data. However, these peaks are predicted by the normalisation methods (see chapter 5), and the underlying decay processes and nuclear structures. Also, these gamma peaks match the experimental data within the errors. Each of the lines resulting from the aforementioned four nuclides in the medium energy range can be seen in fig. 6.2.

Qualitatively, there is one peak at ~ 725 keV which could not be identified in this work. Because of the sharp sturcture of this peak in the experimental data, without any pile-up with a beta-spectrum, one can conclude that the associated contaminant is probably external to the $CaWO_4$ crystal.

For a quantitative comparison, we use the ratio of the combined spectrum of all simulated templates to the experimental data. For the medium energy range, this is between 511 keV and 4000 keV. However, the experimental data set contains events only up to 2800 keV. Therefore, we use the range between 511 keV and 2800 keV for the comparison:

$$\zeta_\mathrm{m} = \left.\frac{N_\mathrm{MC}}{N_\mathrm{exp}}\right|_{511\,\mathrm{keV}}^{2800\,\mathrm{keV}} \tag{6.2a}$$

$$\zeta_\mathrm{m} = (119.3 \pm 91.4)\,\% \tag{6.2b}$$

where N_exp is the sum over the observed reference data and N_MC is given by eq. (6.1). This means that at face-value, the background model overestimated the observed background in this energy region. However, the resulting value is within the errors[1] of the simulated templates and the experimental reference data as shown in fig. 6.1.

Once the comparison between the simulated templates and experimental reference data in the medium energy region is performed, and the result turns out as a match between them within the errors, the next step is to do the same calculation for the low energy range (1-495 keV), and especially the ROI (1-40 keV). We adapt eq. (6.1) by using the relevant signal survival probability ε_l and exposure $(T \cdot M)_\mathrm{l}$ (see section 3.7.1) instead of

[1] Both statistical and systematical errors are included, except for the near external radiogenic backgrounds. Since the activities used to scale them are the experimental upper limits, systematical errors are not included for them.

ε_m and $(T \cdot M)_\mathrm{m}$, and obtain:

$$N_{\mathrm{MC,\,l}} = \varepsilon_\mathrm{l} \cdot (T \cdot M)_\mathrm{l} \cdot \sum_i A_i \tag{6.3a}$$

$$\delta_{N_{\mathrm{MC,\,l}}} = \varepsilon_\mathrm{l} \cdot (T \cdot M)_\mathrm{l} \cdot \sqrt{\sum_i (\delta_{A_i})^2} \tag{6.3b}$$

The sum of simulated templates is compared with the low energy reference data as shown in fig. 6.3. Also in this energy range, the peaks in the experimental spectrum match well with those of the simulated template. However, the agreement between the template and the experimental data for the continuous part of the spectrum decreases with energy. This indicates that there could be one or more beta-/gamma-decaying nuclides missing which could contribute to this energy range via the low-energy part of their Compton continuum or beta spectrum. This could mean that the Q-value of the missing nuclides are lower than 495 keV.

The copper fluorescence peak at 8.04 keV in the experimental data matches well with that of the simulation within the errors. Because this peak is sensitive to the interaction of the total external gamma/beta background with the copper, this match shows, to some degree, that the contamination external to the TUM40 is well considered. This can be seen more clearly in fig. 6.4, which zoomes into the ROI.

In fig. 6.5, one can see the identified gamma and X-ray peaks in the low energy reference data. The X-rays belonging to ^{179}Ta and ^{181}W are caused by the cosmogenic activation. The other identified peaks originate from the beta-/gamma-decays of ^{210}Pb, ^{234}Th, ^{226}Ra, ^{212}Pb, ^{214}Bi, ^{228}Ac, ^{40}K and ^{208}Tl.

Analogous to eq. (6.6), we can calculate the percentage of known backgrounds for the energy range between 1 keV and 495 keV:

$$\zeta_\mathrm{l} = \left.\frac{N_\mathrm{MC}}{N_\mathrm{exp}}\right|_{1\,\mathrm{keV}}^{495\,\mathrm{keV}} \tag{6.4a}$$

$$\zeta_\mathrm{l} = (86.1 \pm 27.2)\,\% \tag{6.4b}$$

However, since we are interested in the specific part of the background spectrum in CRESST which coincides with the ROI (1-40 keV) of the previous background study of TUM40 [105], we can adapt the calculation accordingly:

$$\zeta_\mathrm{ROI} = \left.\frac{N_\mathrm{MC}}{N_\mathrm{exp}}\right|_{1\,\mathrm{keV}}^{40\,\mathrm{keV}} \tag{6.5a}$$

$$\zeta_\mathrm{ROI} = (75 \pm 19)\,\% \tag{6.5b}$$

Hence, with this first Geant4 model of the electromagnetic background for the CRESST experiment, we were already able to reproduce and identify more than (75 ± 19) % of the background observed with TUM40 in CRESST-II Phase 2. Future studies are necessary in order to increase the amount of knowledge regarding the background contamination of CRESST, and these will be outlined in chapter 7.

6.2. The Composition of the Background

In section 6.1, we presented the comparison of the sum of all templates to the experimental reference data to evaluate the overall quantitative agreement. However, it is also important to understand the contribution of each individual contamination type: internal radiogenic, internal cosmogenic, external near distant contaminants. Hence, we split up the sum in eq. (6.1) into contributions from each type. Again, we will first look at the medium energy range and, then, at the low energy range.

For the medium energy range, fig. 6.6 shows experimental data (black) together with the simulations for internal radiogenic contamination (blue), internal cosmogenic contamination (purple), external near radiogenic contamination (grey), external distant radiogenic contamination (green) and the sum of all these individual contributions (red). It can be seen that the main contributions to the continuous part of the sum spectrum come from the internal radiogenic and external distant radiogenic backgrounds. To quantify this observation. we define the contribution of each type of contamination to the sum as:

$$\xi_X = \frac{N_{\mathrm{MC},X}}{N_{\mathrm{exp,m}}} \tag{6.6a}$$

$$\delta_{\xi_X} = \sqrt{\frac{N_{\mathrm{exp,m}}^2\,\delta_{N_{\mathrm{MC},X}}^2 + N_{\mathrm{MC},X}^2\,\delta_{N_{\mathrm{exp,m}}}^2}{N_{\mathrm{exp,m}}^4}} \tag{6.6b}$$

where X is the type of contamination, e.g. internal radiogenic, internal cosmogenic, near external radiogenic and distant external radiogenic.

Overall, the most prominent contributions are from internal radiogenic and external distant radiogenic with (63.2 ± 38.5) % and (48.8 ± 31.8) %, respectively. It can be seen that these two contributions make up for more than 100 % of the backgrounds in the medium energy range. This could be due to a number of reasons all of which point to an overestimation of the contamination in this energy range. Since the internal beta-/gamma-decays are scaled according to the experimentally measured alpha-peaks, and the distant external radiogenic contaminants are scaled according to the experimentally observed gamma-lines, the only remaining contribution that can cause this overestimation is near external radiogenic contaminants. To scale these contaminants, upper limits of activities of natural decay chains are used (see section 5.3). Hence, an overestimation would most likely indicate that the actual contamination levels of the near copper are lower than the upper limits from the screening. A dedicated copper screening can give more precise values which, in turn, might decrease the contribution of these contaminants in this energy range.

In addition, external distant radiogenic contaminants make up the peaks in this energy region along with a smaller contribution from the external near radiogenic contaminants. The amount of contribution from internal cosmogenic contamination is zero in this region. This is to be expected as the most energetic contribution of internal cosmogenic contamination has an energy of 73.7 keV.

After checking the medium energy region, we move on to the low energy region which is between 0.6 and 495 keV. By adapting the signal survival probabilities accordingly, we move from the medium to low energy reference data. Figure 6.7 shows that external distant contaminants dominate the background at energies above 60 keV. Below this energy level, the dominant contribution comes from the internal radiogenic contaminants. The cosmogenic lines contribute to the sum spectrum at energies below the aforementioned 73.7 keV line. Contribution of each individual background component to the sum in the ROI, that is shown in fig. 6.8 are listed in table 6.1. We note that by considering ^{3}H, we were able to improve the relative contribution of cosmogenic backgrounds by (2.6 ± 0.6) %.

These results mean that if the further purification of the $CaWO_4$ crystal planned for CRESST-III Phase 2 [24] turn out to be as expected, the limiting factor for the background will be the background coming from copper. This highlights the importance of a cleaner copper, to use for the holders and the cryoshielding for the future iterations of CRESST.

6.3. Comparison with the Previous Work

The work done in this thesis gives important information on the backgrounds, and its composition, for the CRESST experiment. However, to assess if the work carried out here is a step in the right direction, one should compare it with other background analyses.

First, we will make a brief quantitative comparison with the earlier background work in CRESST [105]. The comparison of the results of [105] and this work is shown in table 6.1. The sum results show that with this work, we learned 5.4 % more compared to the previous one. For this comparison, we assume that the so-called *excess light events* (see section 3.6) in [105] are caused by external betas as hypothesized in [105]. Hence, we compare them with the *distant external radiogenic* background in this work (see section 4.4.4).

In addition to the quantitative progress, an important qualitative improvement done for this work was to implement the full detector geometry, and this resulted in some of the features to occur naturally, whereas in [105], they were placed either manually (Cu fluorescence peak) or missing (external annihilation peak). This highlights the advantages of the fully Monte Carlo based simulation developed for this work over a semi-empirical model as used in [105].

6.4. Comparison with Another Experiment

In addition to a quantitative comparison with an earlier background model for CRESST, one can also compare this work qualitatively with background analyses performed for other rare event search experiments. There are two different background analyses performed that can be used to compare with this work: works by the CUORE [16] and the COSINE-100 [5] experiments. Since CUORE is a double beta-decay experiment, whereas COSINE-100 is a dark matter search, we will compare this work with the background model of the COSINE-100 Experiment [5]. However, we note that also CUORE uses a template-based

Table 6.1.: Disentanglement of the background sources for TUM40, comparing this work with the previous [105]. Numbers for this work are given rounded up to significant digits.

Source	**Previous Work [105]**	**This Work**
Internal Radiogenic	30 %	(27 ± 5) %
Internal Cosmogenic	18 % [a]	(17.8 ± 3.8) %
Near External Radiogenic	4 %	(6.3 ± 2.1) %
Distant External Radiogenic	17 %	(23.7 ± 6.4) %
Total	69 %	(75 ± 19) %

[a] Includes cosmogenic activation of ^{179}Ta and ^{181}W within the energy range between 1 and 80 keV.

approach to analyse their backgrounds. COSINE-100 is a dark matter search which uses eight ultra-pure crystals made out of NaI(Tl). The primary goal of COSINE-100 is to test the observation of an annual modulation signal asserted by DAMA/LIBRA [41, 42].

In [5], the COSINE-100 collaboration used a Geant4 based simulation to build their background model. The internal background, as with this work, consists of the nuclides in the ^{238}U and ^{232}Th decay chains. Specific for their target material, NaI(Tl), they found also a ^{40}K contamination inside the crystal. Albeit they broke the ^{238}U (^{232}Th) chain into 5 (3) parts during the simulation, they assumed equilibrium along the chain for the comparison with their measurement. On the contrary, we were able to avoid the assumption of an unbroken equilibrium for our target, i.e. $CaWO_4$, due to the clearly identified alpha-peaks in the high energy reference data. Furthermore, we considered also the ^{235}U decay chain in addition to the ^{238}U and ^{232}Th chains. Concerning the external gamma background, COSINE found that the background from individual external parts produces nearly identical spectra and could be well described by one effective spectrum per contaminant where the contaminant is randomly placed outside the crystal. This is very similar to our approach of approximating the whole cryostat geometry by a simple Cu sphere. In terms of cosmogenic activation, the amount and the composition of nuclides is obviously different for NaI(Tl), as used by COSINE, and $CaWO_4$, as used by CRESST. However, they also found an important amount of ^{3}H, just as we hypothesised it. This also proves the importance of this nuclide for a detailed background model.

Differently than this work, COSINE also considered surface contamination. In CRESST, we got rid of most of the surface backgrounds with the addition of the scintillating foil and holder sticks (see section 3.5.6). However, in order to understand the efficiency of this surface rejections and any potential remaining surface backgrounds, one has to study it in detail, which is a necessary continuation to this work in the future.

In addition, COSINE used a log-likelihood method to fit the templates to their observed

data. We will discuss how to adapt a similar approach to the background model developed in this work for CRESST in section 7.1.6.

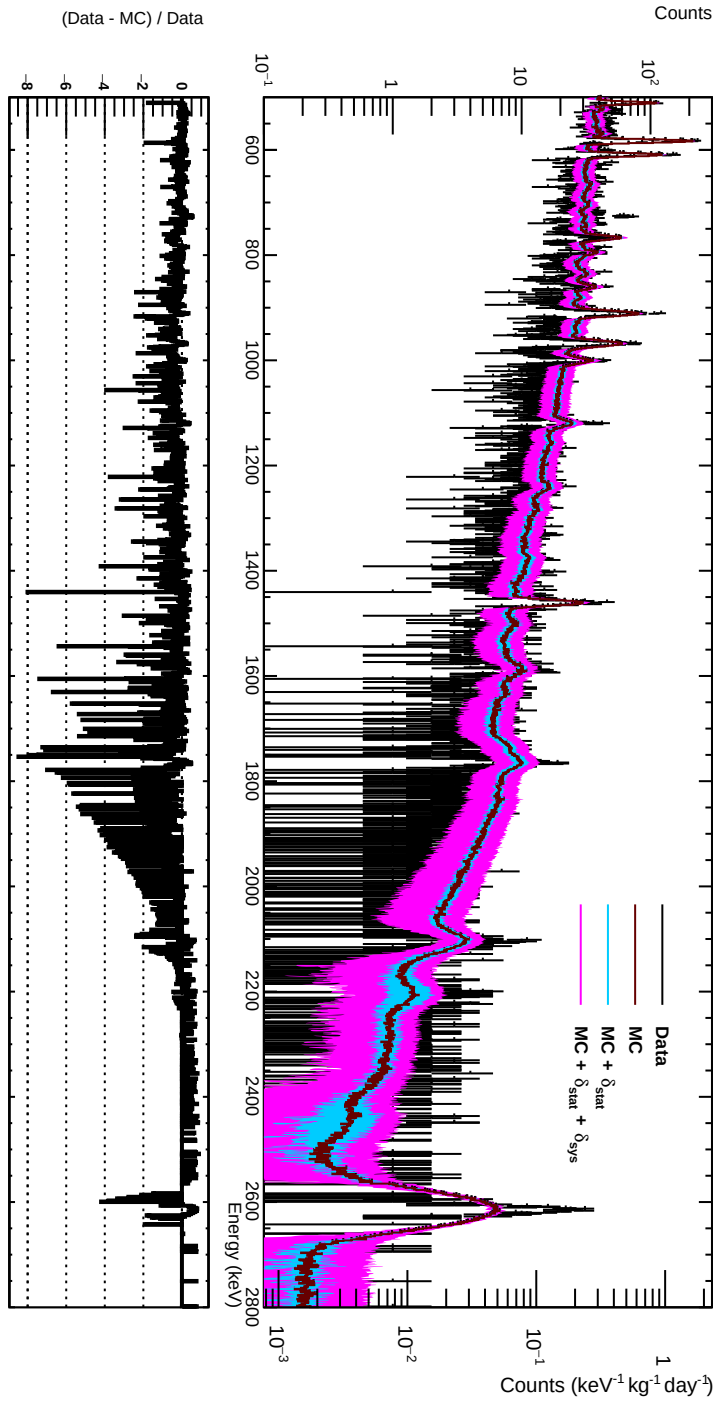

Figure 6.1.: Top panel: sum of all simulated templates with statistical and systematical uncertainties with respect to the experimental data with statistical errors in the medium energy range. Bottom panel: relative residual between simulation and data.

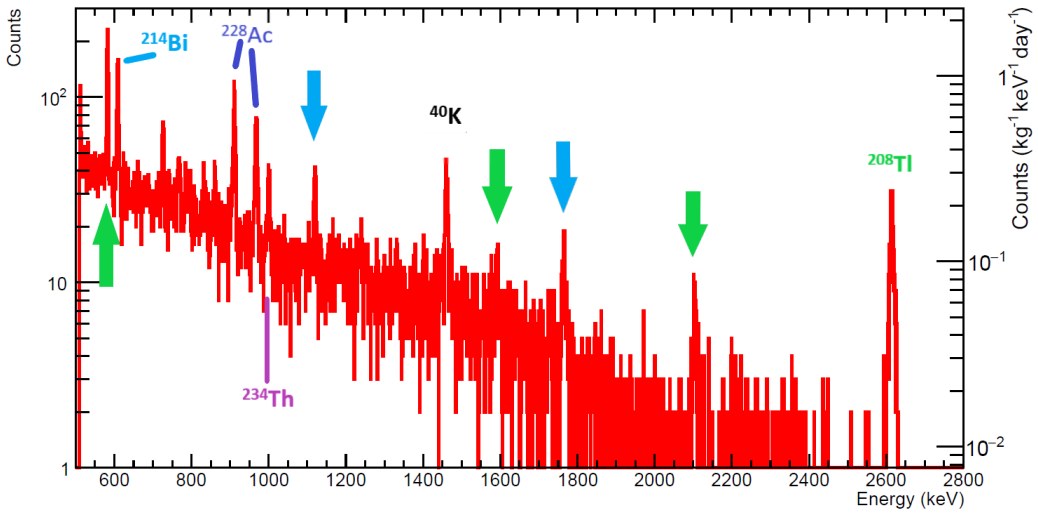

Figure 6.2.: Identified gamma peaks in the medium energy reference data. Gamma emissions originating from the same nuclides are labeled with arrows of the same colour.

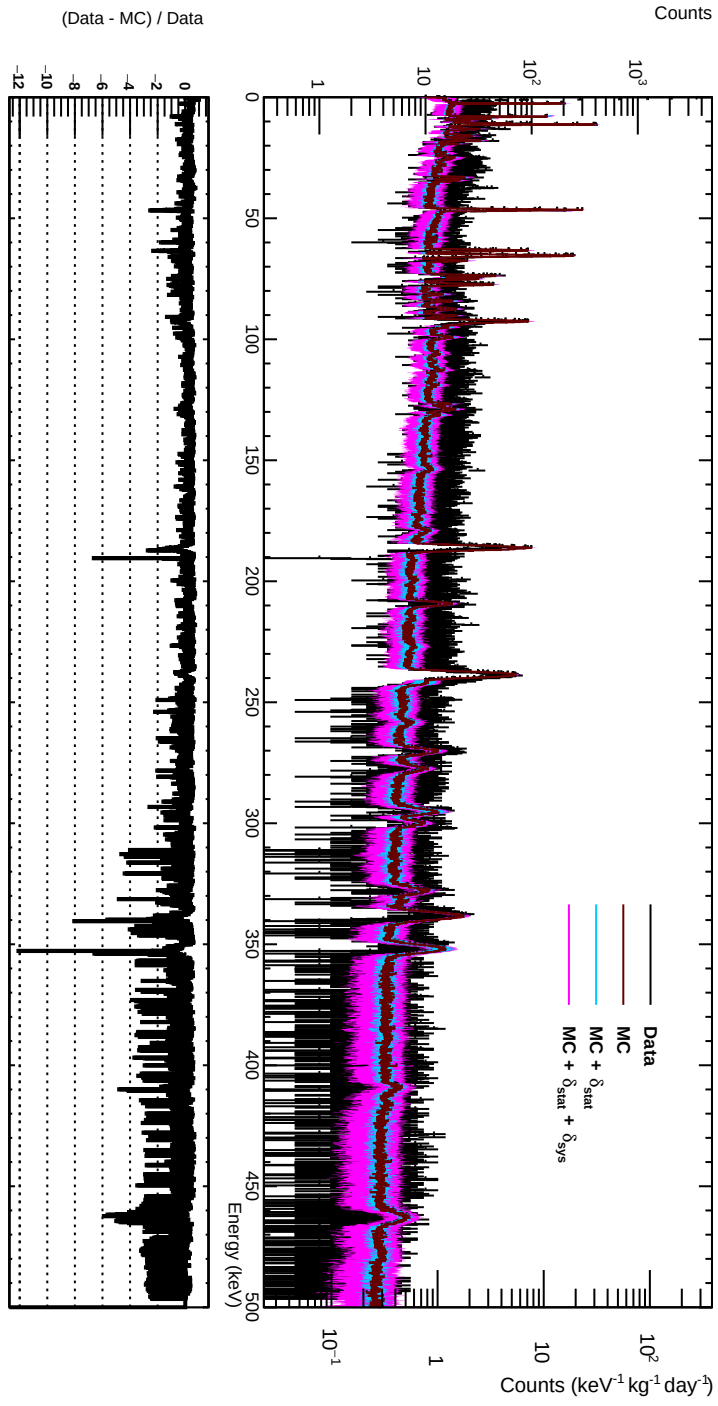

Figure 6.3.: Top panel: sum of all simulated templates with statistical and systematical uncertainties with respect to the experimental data with statistical errors in the low energy range. Bottom panel: relative residual between simulation and data.

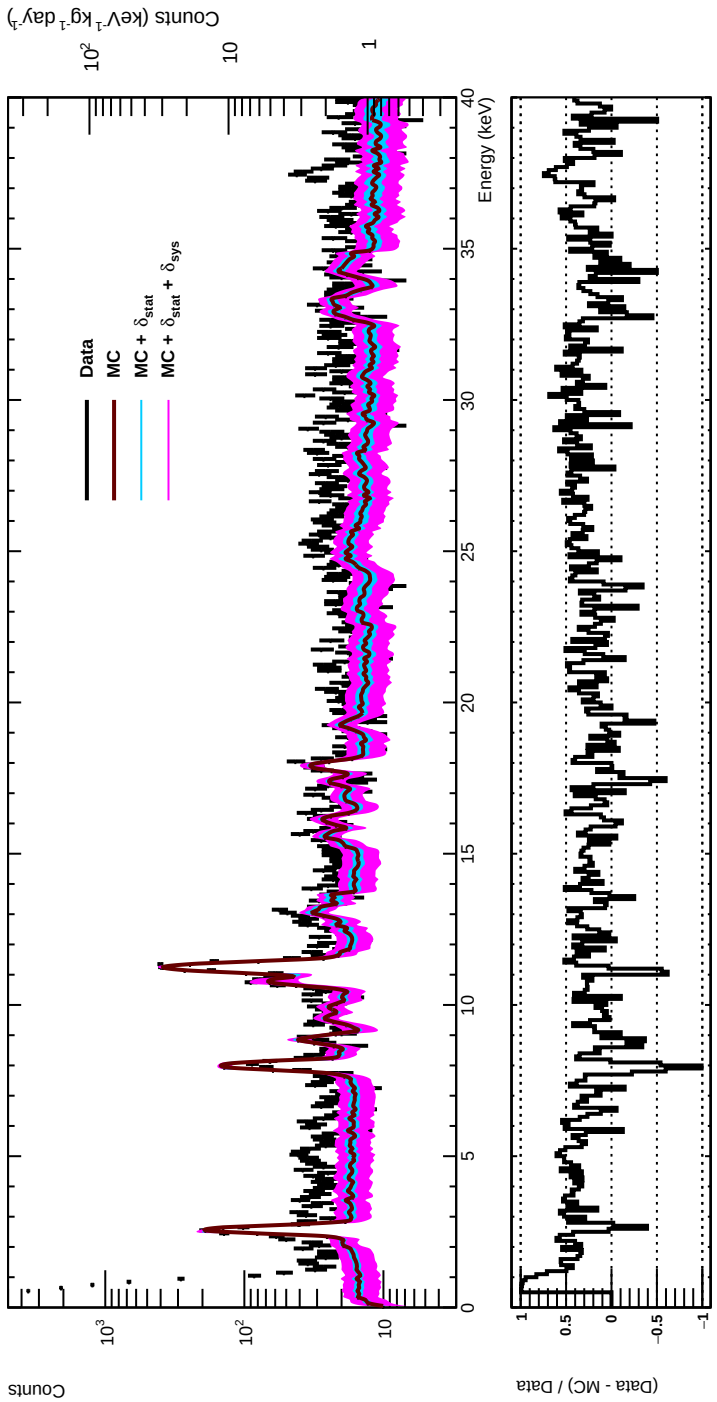

Figure 6.4.: Top panel: sum of all simulated templates with statistical and systematical uncertainties with respect to the experimental data with statistical errors in the ROI both for this work (1-40 keV) and for the dark matter analysis of TUM40 (0.6-40 keV). Bottom panel: relative residual between simulation and data.

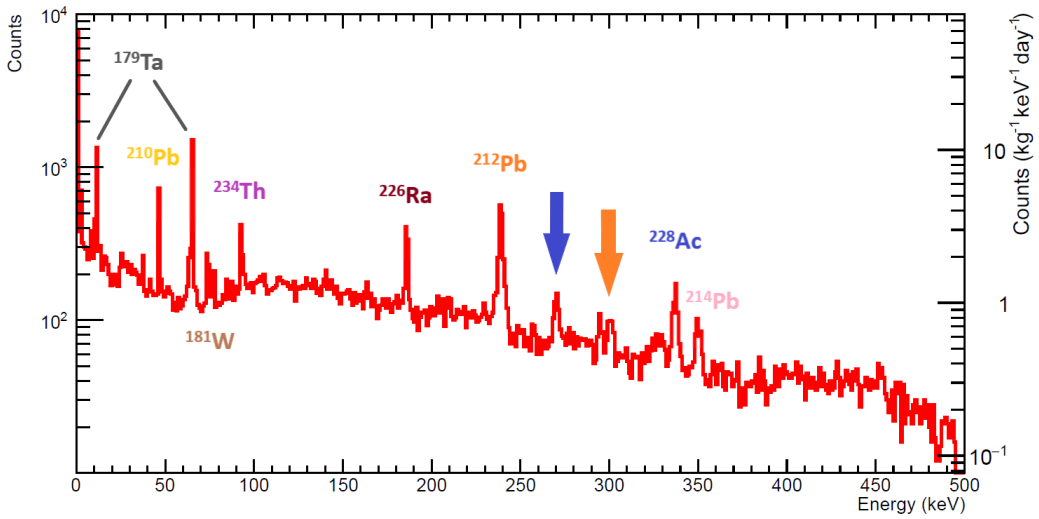

Figure 6.5.: Identified gamma peaks in the low energy reference data. Gamma emissions originating from the same nuclides are labeled with arrows of the same colour.

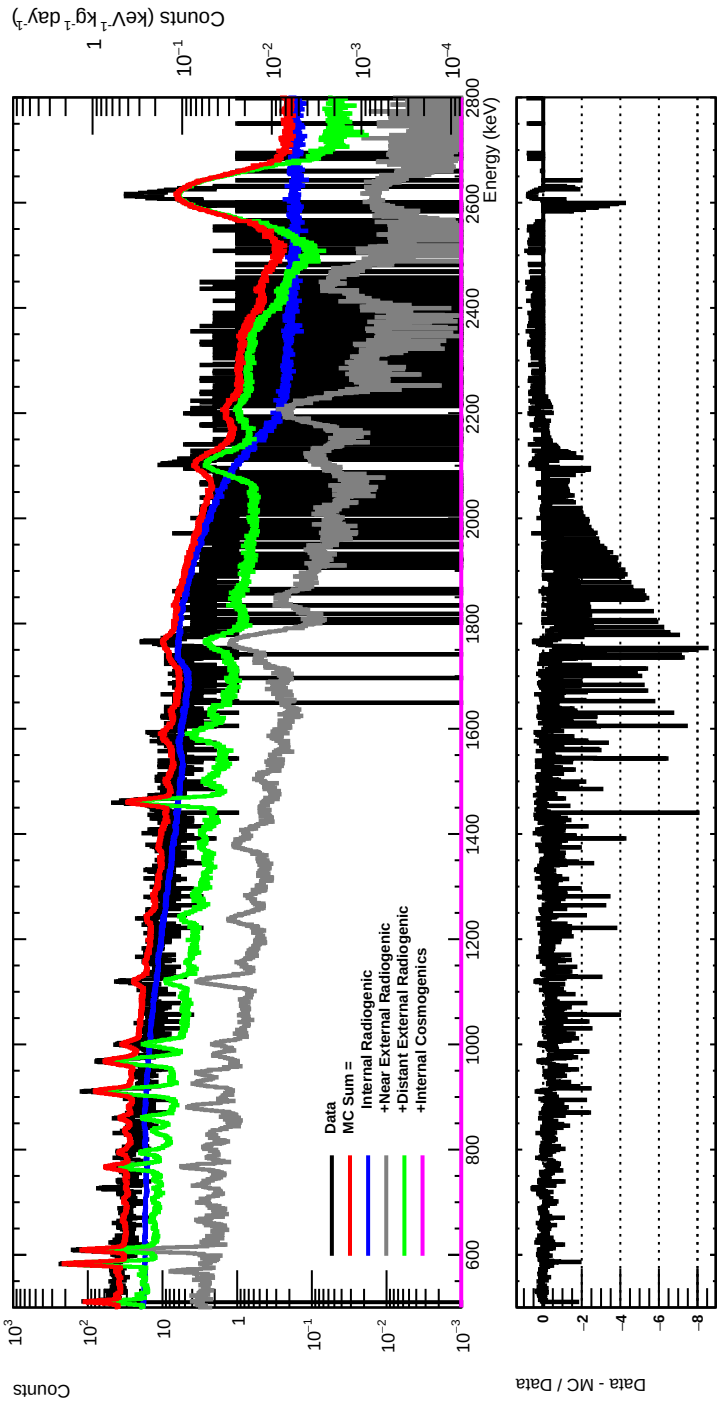

Figure 6.6.: Top panel: individual background components and their sum compared to the medium energy reference data set. Bottom panel: relative residual between simulation and data.

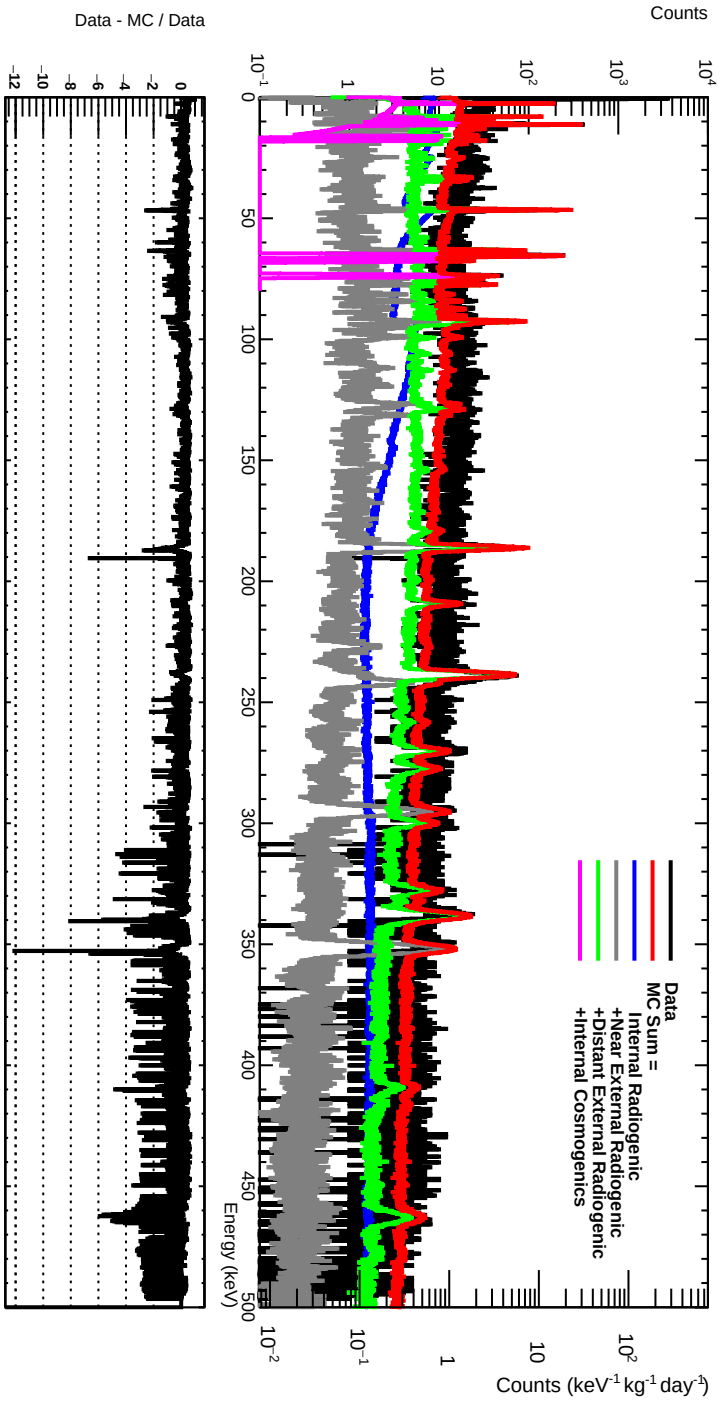

Figure 6.7.: Top panel: individual background components and their sum compared to the low energy reference data set. Bottom panel: relative residual between simulation and data.

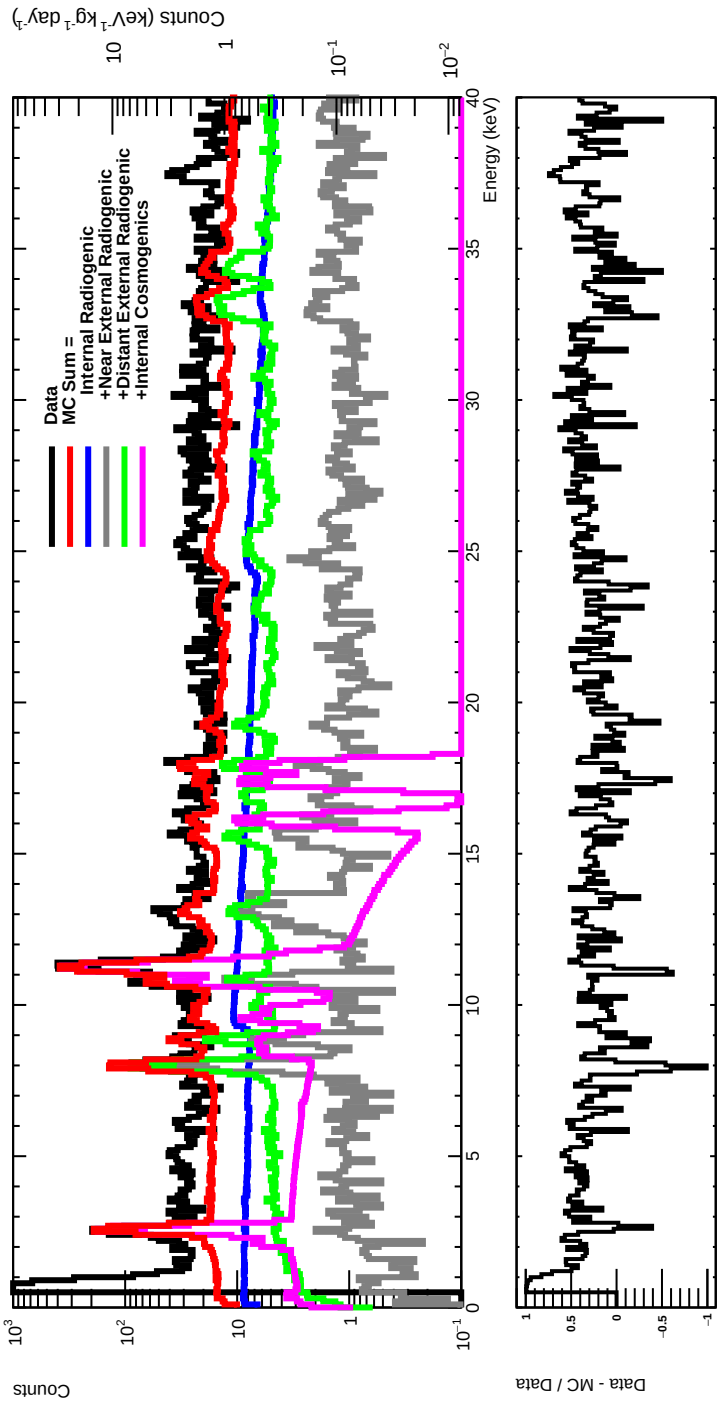

Figure 6.8.: Top panel: individual background components and their sum compared to the low energy reference data zoomed on the ROI (1-40 keV). Bottom panel: relative residual between simulation and data.

7. Future Works

In this chapter, the implications of the result of this work will be discussed. First, the further improvements that can be done will be outlined (see section 7.1). Finally, the impact of this work on the dark matter search of CRESST will be explained (see section 7.2).

7.1. Improvements for Future Simulations

Even though this PhD work is an improvement over the previous work [105], due to its limited time, it can not cover all the topics a complete background model should cover. Hence, in the future, this model can be improved and there are a few ways this can be done. In this section, we will describe the possible improvements such as implementing the full experimental setup, carrying out neutron simulations, performing copper screenings, studying the cosmogenic activation in more detail and improving the detector response model.

7.1.1. Full Experimental Setup

As explained in the section 4.2, the geometry used in this work included the full detector geometry of the TUM40 detector module. Using this geometry helped to understand some features that showed up in the experimental data, such as the copper fluorescence peak at 8.04 keV and the external annihilation peak at 511 keV, but not in the previous semi-empirical background model [105]. These features were explained in detail in section 4.4.3 and section 4.4.4.

However, as it was explained in section 4.4.4, there are other copper parts outside the TUM40 module, e.g. the cryoshields, which were approximated in this work (see section 4.4.4). In order to be able to fully understand the effects of possible contaminants around the detector module, it is imperative to have the full and detailed experimental setup implemented in the simulation code.

Possible advantages of having the full experimental setup implemented are:

1. The contaminants causing external gamma lines in the experimental data can be simulated more accurately using the copper structure inside the cryoshields which holds the detector modules, the so-called *carousel* (see the inner part of fig. 3.1). This way, the attenuation difference between external gamma rays coming from the copper holders of TUM40 and the more distant Cu parts, e.g. the cryoshields, will be considered naturally. Hence, there will be no need anymore to split the simulation in near and distant external radiogenic backgrounds as it was done in this work.

2. In CRESST, detector modules with different designs (see section 3.2) are used in the same experimental runs. Each detector design has their own characteristic features such as geometry, mass and materials. In addition, as explained in section 3.5.7, for most of the detector modules, $CaWO_4$ crystals were supplied from commercial companies. Since using different materials can cause different backgrounds and as the detector modules are placed closely with each other, it is probable that there might be background external to TUM40, which originate from the other detector modules in the vicinity. Therefore, it is better to consider these backgrounds to get a full sense of the interactions between each installed detector.
3. Even though there is an active veto used to reject muons (see section 3.5.1), it could be useful to simulate muons trying to pass through the whole setup in order to consider muon-induced background components.

7.1.2. Neutron Simulation

Neutrons are one of the most dangerous backgrounds as explained in section 3.5.4. Even though CRESST has currently no identication of a prominent neutron background, this may change in the future with new detectors and lower detection thresholds.

The most common sources for neutrons are spontaneous fission and (α,n)-reactions, both in the concrete of LNGS and in the materials of the set-up.

Hence, it is crucial to simulate creation and interaction of neutrons in the full setup. This way, their possible interactions and the rate at which they might induce signals in the detectors can be calculated.

7.1.3. Copper Screenings

As described in section 4.4.3, the upper limits obtained for the Cu used in the CUORE experiment [15] was used for our simulation of CRESST as the Cu supplier of both experiments are the same. However, this can be only a first order approximation for the radiogenic contamination of CRESST's Cu holders to get a tentative understanding of the effect. In order to get the activities accurately, a more detailed study is necessary.

In order to do this, a dedicated screening should be performed for the Cu parts of each of the detector modules. A possibility for doing this would be a precise measurement of the gamma radiation emitted from the Cu with a HPGe detector. After a detailed analysis of the data, one can try to identify each individual contamination using signature gamma and X-ray peaks. This way, more precisely measured activities could be used to improve the background model built in this work.

7.1.4. A More Detailed Study of Cosmogenic Activation

In section 3.5.3, the backgrounds caused by the cosmogenic activation of ^{179}Ta and ^{181}W nuclides are described. In addition, an approximation of the ^{3}H contamination is calculated

in section 5.2.2. However, a more detailed study should be conducted on cosmogenic activation because of two reasons:

- **Additional Tritium** The calculation of the activity of ^{3}H in section 5.2.2 was only a first order approximation. To state the ^{3}H activity more precisely, more research should be conducted both on cosmogenic production of ^{3}H and on other possible ^{3}H sources.
- **Additional Cosmogenics** Cosmogenic activation is difficult to observe unless there are clear lines such as the ones caused by ^{179}Ta and ^{181}W. In addition, there are more materials used in the whole experiment than $CaWO_4$. Therefore, these materials could have not-yet-considered isotopes that can be activated cosmogenically. Since the next step after this work is to implement the full experimental setup in Geant4, these additional materials should be studied in case there are any cosmogenic activation associated with them.

7.1.5. Improved Detector Response Model

In section 5.1.2, how the templates of alpha-decays were scaled was explained, and in fig. 5.3 the comparison between the scaled templates and the high energy reference data was shown. A zoom on the alpha decay of ^{238}U is given in fig. 5.2. In this figure, it can be seen that the width and the amplitudes do not match for templates and experimental data even though the number of events agree within the errors. This is probably caused by the fact that the energy resolution we used in this work is not exactly fitting to that of experimental data. In order to solve this problem, an improved detector response model is needed.

In addition, in section 3.4 we explained that some of the background events in the electron/gamma band leaks into the nuclear recoil bands where we expect a possible dark matter signal. Since this can mimic a possible dark matter signal, we have to understand the amount of leakage into the nuclear recoil bands. Because the bands are defined by the light yield (LY), i.e. the ratio of scintillation light signal over total deposited energy, one has to consider the scintillation light signal in the simulation in addition to the total energy deposition. Hence, the detector response model has to be extended to calculate the scintillation light signal based on the deposited energy and the type of interaction.

7.1.6. Free-Floating Template Fit

In this work, the approach to identify the contaminants in the ROI has been based on the sideband measurements. The activities calculated from the alpha lines in the high energy reference data, and gamma and X-ray lines from the medium and the low reference data were used to calculate the amount of contamination inside the ROI. However, after determining the contaminants and the activities, the scaling could be done more accurately using a *log likelihood* fit [51], as it was performed for the COSINE-100 background model [5]. For our case, we suggest to use a binned log-likelihood fit because the simulated templates H in this work are in the form of binned histograms.

These histograms represent the probability density functions (PDF) to observe the deposition of energy E in the $CaWO_4$ crystal for a given background component. By using a binned log-likelihood, one can estimate the amount of contamination of each previously identified nuclide inside the experimental reference data (rd) divided into N bins each having $\mathbf{n} = (n_1, ..., n_N)$ events. In order to make this estimation, one has to calculate the expectation values $\nu = (\nu_1, ..., \nu_N)$ for this reference data based on the background model. The expectation values ν_i for the i-th bin can be calculated using:

$$\nu_i^{rd}(E, \vec{R}_{rd}) = N_{\text{tot}}^{rd} \int_{E_i^{\min}}^{E_i^{\max}} H_{rd}(E; \vec{R}_{rd}) dE \tag{7.1}$$

where $E_i^{\min}$ and $E_i^{\max}$ are the lower and upper limits of the bin, respectively. Here, $H_{rd}(E; \vec{R}_{rd})$ is the predicted probability at energy E for the template H and the detector response model described by the parameters $\vec{R}_{rd}$. The index rd indicates the used reference data set: low, medium or high energy reference data (see section 3.7). For calculating the PDF, the following equation is used:

$$H_{rd}(E, \vec{R}_{rd}) = \sum_{bg} A_{bg} \cdot H_{bg}(E; \vec{R}_{rd}) \cdot (T \cdot M)_{rd} \cdot \varepsilon_{rd}(E) \tag{7.2}$$

Here, bg stands for *background* and it can be the templates of the internal radiogenic, internal cosmogenic, external near radiogenic or external distant radiogenic backgrounds (see section 4.4), and A stands for the activity of each template.

Hence, the binned log-likelihood can be calculated as follows:

$$\log L^{rd}(\vec{R}) = \sum_{i=1}^{N_{rd}} n_i^{rd} \cdot \log \nu_i^{rd}(E_i, R_{rd}) \tag{7.3}$$

The sum of the binned log-likelihoods calculated for each reference data then gives

$$\log L(\vec{R}) = \log L^l(\vec{R}_{\text{l}}) + \log L^m(\vec{R}_{\text{m}}) + \log L^h(\vec{R}_{\text{h}}) \tag{7.4}$$

where $\vec{R}$ contains the parameters of all three detector response models (see section 4.3.1). With this approach, one can create a fit of the templates to the data with a higher precision as the computation involves calculating the resulting spectrum with different activities.

Even though this method gives more precise results, there is a downside of it: the time needed for the calculation of the binned log-likelihood. For the calculation, it would take all the simulation templates we used in this work, varying the free parameter $(A_i, \vec{R})$ to find a minimum of logL and thereby process each one of them bin-by-bin for many iterations. Given the high amoun of the free parameters, 84 different values for the activities and in total 18 parameters for the three detector response models which consider the detector resolution (section 4.3) and the energy rescaling (sections 3.7.1 and 3.7.2), this process will probably require a long computation time. Hence, it could not be implemented and run within the time limit of this work. However, the outcome of this work may serve as a

valuable input to constrain the parameter space of the fit and, therefore, help to increase speed and robustness of such a future approach.

After calculating the binned log-likelihood, a natural next step would be to include the log-likelihood function in a dark matter analysis and this will be the topic of the next section. However, we note that this is not the only way to combine a background model with a DM analysis.

7.2. Impacts on the CRESST Experiment

The outcome of this work will affect the future of the CRESST experiment in two important aspects: a likelihood based dark matter search and developments of future detectors.

7.2.1. Likelihood-Based Dark Matter Analysis

As discussed in section 7.1.6, a binned log-likelihood method can give more precise results in terms of the activities of the nuclides known to contribute to the observed background. Once this fit is performed, its results can be used in a dark matter analysis.

In order to be able to do this, two different probability distribution functions are needed: one which only models the background and the other for the signal, which in our case is a dark matter signal. The next step is to fit the data twice: once under the hypothesis that they consist only of background and another time under the hypothesis that they consist of background plus signal. Finally, a *likelihood ratio test* can be performed [51]. Using the result of this calculation, one can estimate the signal strength in the data.

7.2.2. Detector Development

Using a full detector geometry in the simulation has advantages beyond building a more accurate background model and identifying the individual background components. One can also use this simulation to estimate the shielding power of a particular detector design against backgrounds. This information could be useful for designing new detector modules.

In this work, we did a preliminary investigation of the shielding effect of the holder structures of the TUM40 module and a CRESST-III module on external gamma radiation, also in comparison with a bare $CaWO_4$ crystal. The geometry implemented in Geant4 for the CRESST-III modules is shown in fig. 7.1. As can be seen there, the new modules are fully covered with Cu plates whereas TUM40 (fig. 4.4 and fig. 4.5) was only partially covered.

To study the effect of the different coverage, we irradiate all three geometries with external gamma rays. For this comparison, external gamma rays with energies of 2614 keV are used as they would originate from the gamma-decay of ^{208}Tl. The photopeak of each spectrum is then normalised to 1 to be able to compare the low energy Compton continuum in each geometry; see fig. 7.2a. As can be seen, the Compton continuum in the bare $CaWO_4$ crystal (red) has the lowest level. The reason for this is that there is no

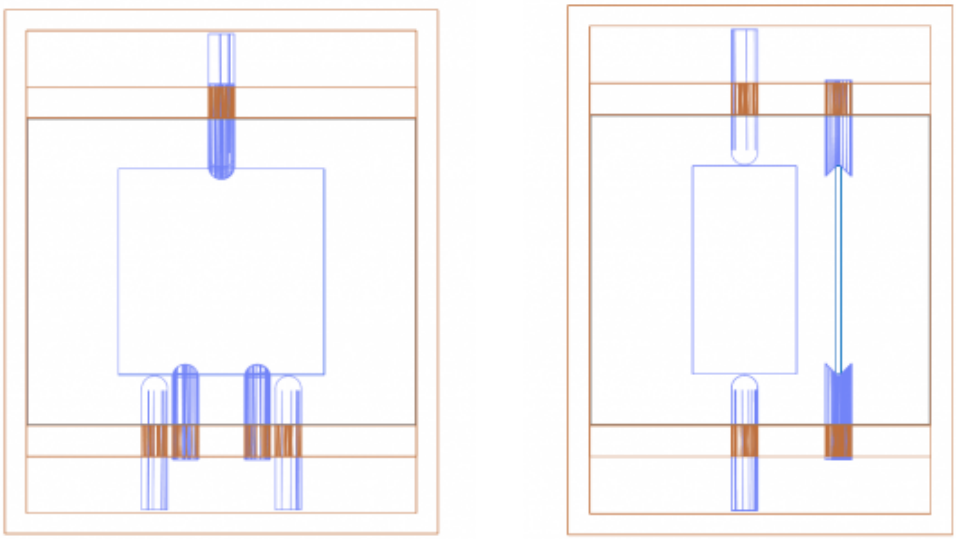

(a) (b)

Figure 7.1.: Visualisation of a CRESST3 detector module as implemented in Geant4: cut-away views parallel to the X-Z plane fig. 7.1a and parallel to the Y-Z plane fig. 7.1b. Main components are the $CaWO_4$ target crystal (big blue box), silicon on sapphire light detector (thick blue line in fig. 7.1b) and Cu holder (brown/orange).

material between the source of the gamma rays and the crystal. Therefore, the gamma rays can only Compton scatter with the crystal itself. On the other hand, for the TUM40 (black) and CRESST-III (purple) detector modules the levels of the Compton continuum increased. The reason is that there is another material, mainly copper, between the crystal and the gamma ray source. TUM40 is only partially covered whereas CRESST-III module is fully covered with copper, which correlates with an increased level of relative activity at low energies. It can be concluded that with more material around the crystal, more gamma rays are shifted to lower energies simply by the fact that they undergo more interactions. Hence, the *relative* contribution of the low energy part of the detected spectrum increase with increased shielding. However, the *absolute* level of the spectrum decrease with increasing shielding as shown in fig. 7.2b.

This observation is an important information we obtained from simulating different detector modules. As especially the background at low energies is cruical for CRESST, a more thorough investigation of new detector designs has to show if the shifting of the remaining background to low energies is acceptable or not. This is an important information to design and build future detectors.

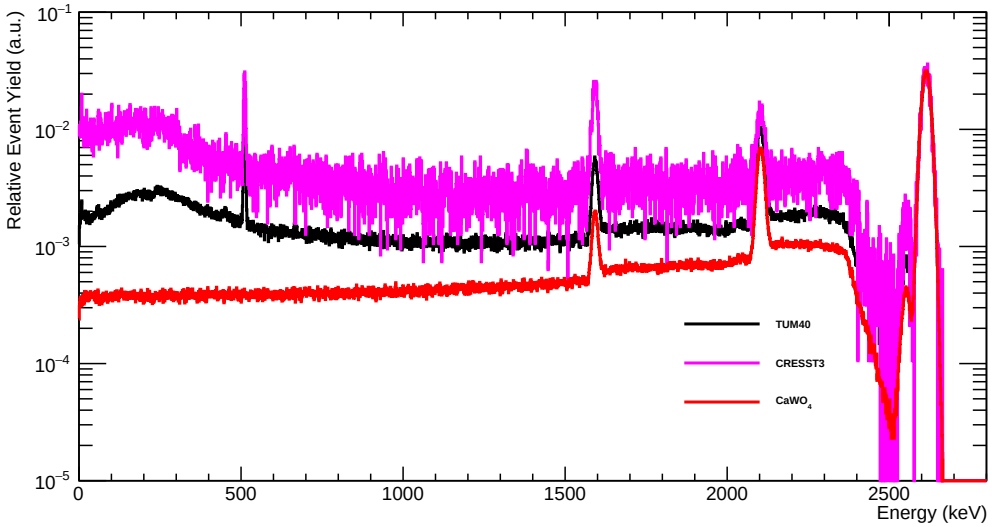

(a)

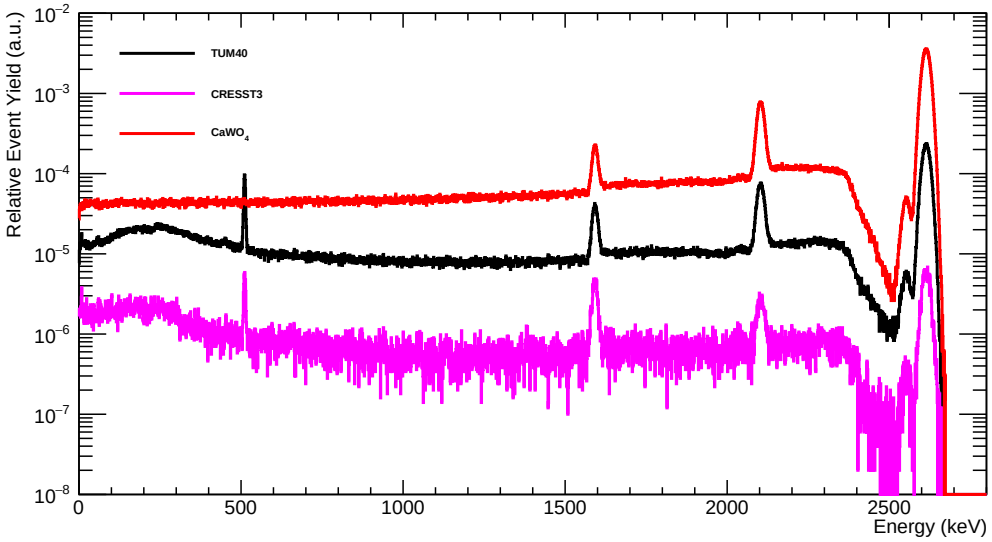

(b)

Figure 7.2.: Simulated energy deposition of a bare $CaWO_4$ crystal (red), TUM40 (black) and a CRESST-III (purple) detector modules caused by irradiation with 2614.0 keV gamma rays (e.g from ^{208}Tl): (a) shows all spectra normalised to the photopeak at 2614.0 keV whereas (b) shows all spectra normalised by the number of all simulated events for each geometry.

8. Conclusion

It is known through various astrophysical and cosmological observations that dark matter exists. Many models propse that dark matter consist of a yet unknown particle. It is known that this hypothetical particle cannot interact electromagnetically or strongly. Dark matter is known to interact gravitationally but for us to be able to detect it, it has to interact with baryonic matter via a weak force, as well. Based on this potential interaction, three different ways to search for a potential dark matter are possible: production, indirect and direct detection.

Direct detection searches for dark matter particles through their scattering off of Standard Model particles. There are various direct detection experiments searching for possible dark matter particles in different mass ranges. One of these experiments is CRESST. CRESST looks for dark matter induced nuclear recoils in $CaWO_4$ crystals operated as cryogenic detectors. With their detectors, CRESST uses phonon and scintillation light signals to measure the total deposited energy and to determine the type of particle which deposited the energy inside $CaWO_4$, respectively. This simultaneous measurement of phonon and light signals enables CRESST to separate the searched-for nuclear recoils from the mostly electromagnetic background, e.g. natural radioactivity. Currently, CRESST is the leading experiment searching for low mass dark matter particles via nuclear recoils with sensitivity to possible dark matter particles with masses down to 350 $\mathrm{MeV/c^2}$ [95].

Considering the fact that dark matter particles scattering off the nucleus inside the targets of the detectors is a potentially rare event, it is crucial to know all the backgrounds in the experiment, since an unknown background can mimic or mask a possible dark matter signal. CRESST is looking for low mass dark matter particles and accordingly, the nuclear recoil energy range below 40 keV is the region of interest (ROI) for CRESST. The lower boundary is set by the detection threshold, which can go as low as 600 eV for the detector module TUM40 used in this work [26]; newer detectors achieved even a detection threshold of around $\sim$ 26 eV [95]. At these energies, no discrimination is possible between electron and nuclear recoils, which makes a background model cruical.

In this work, we have constructed a model of radioactive backgrounds based on simulations implemented using Geant4. In order to construct this model, we have chosen one of the cleanest detector modules, TUM40, which provides us with a large reference data set to test the simulation. The data were taken during a long exposure of 129.912 $\mathrm{kg \cdot days}$. To improve the comparability between experimental data and simulations, we did also a dedicated reanalysis of the reconstructed energy scale and resolution. The first step of this work was to construct an accurate representation of TUM40's geometry. Having an accurate geometry allows us to consider effects caused by the finite target volume (e.g. escape peaks) and by the support material around the target itself (e.g. fluorescence lines

from the Cu of the detector holder).

The next step was to identify the type of backgrounds and, for this, we used the side-band measurements obtained with TUM40. These measurements included alpha decays originating from inside the $CaWO_4$ crystal and external gamma rays penetrating the detector module. From the existence of the alpha decays, we learned about the type and the amount of radioactive backgrounds that also contribute to the contamination in our ROI. Assuming a piecewise secular equilibrium, we have calculated the activities of the beta-/gamma-decaying nuclides originating from the alpha-decaying nuclides that belong to the natural radioactive decay chains.

We split the background contribution from Cu into two: one contribution from Cu close to the $CaWO_4$ target and one from the more distant parts like thermal shields of the cryostat. The former are part of our detailed detector model; the latter was an approximation as Cu sphere around the detector module in the simulation. In our background simulation, we used the same contamination levels as measured by the CUORE [15] to normalise the simulations for the near Cu. We assumed a secular equilibrium throughout the decay chain considering the branching ratios. In addition, we have calculated the activity of ^{235}U decay chain by its natural abundance.

For the distant Cu, we simulate only eight nuclides which were confidently identified in the reference data via their characteristic gamma lines. Any remaining activity in the reference data that could not be explained by the internal contamination or the near Cu, we attributed to this distant Cu which we implemented by creating a spherical Cu shell to approximate the Cu shields.

The last type of background considered in this work is the cosmogenic activation of two nuclides, namely ^{179}Ta and ^{181}W. The existence of these nuclides is confirmed by the distinct X-ray emission peaks observed in the experimental data. Similar to the distant Cu, we normalised these simulations to the characteristic X-ray lines of the associated decays. Moreover, we noticed that along with ^{181}W, also ^{3}H is produced. This means that we have to have some contribution from ^{3}H decays in our data. Based on a preliminary study [77], we scaled the ^{3}H contribution to the observed ^{181}W activity. After this calculation, we added also ^{3}H to our model, and this helped to explain an additonal (2.6 ± 0.6) % of background in the ROI.

After the calculation of activities for each nuclide, we combined these individual spectra and compared the sum with the experimental data. A comparison between the scaled alpha spectra and the experimental data gave compatible results. In the medium energy range, the face-values showed that we might have overestimated part(s) of the spectra, but they are compatible within the uncertainties. However, in the low energies, there is still some part of the background we do not know, as the ratio of summed up templates to the experimental data in the ROI showed that we reproduced only 75 %. If we break this down into individual components, we find internal radiogenic background to be 27 %, internal cosmogenic background to be 17.8 %, near external radiogenic background to be 6.3 % and distant external background to be 23.7 %.

Compared to a previous semi-empirical background study [105], we could improve the

agreement between observation and model from 69% to 75%. Albeit this is a great success for this first fully MC-based model of electromagnetic backgrounds in CRESST, there is of course room for possible future improvements: to implement the full experimental setup in the simulation, to conduct copper screenings to get a more accurate knowledge on the copper contamination levels and to study the cosmogenic activation in more detail. Moreover, one can use the results of this work and implement a free-floating template fit based on a binned log-likelihood function and use this to conduct a dark matter analysis. Finally, a full list of potential future improvements is given, including the optimization of future detector developments: this work shows clearly that if CRESST succeeds with its planned reduction of internal contaminations of the $CaWO_4$ crystal [24], then the Cu around the crystal will be the biggest contributor to the remaining background.

With this work, we have resolved a big part of the observed backgrounds. This knowledge can help CRESST to perform more precise measurements. However, as this was the first step of a bigger analysis on backgrounds, there are many aspects to study in the future in more details.

Acknowledgements

I would like to express my gratitude to my supervisor Prof. Dr. Jochen Schieck, knowledge and wisdom of whom changed my course along my PhD. I could not have finished my research and this thesis without his guidance. I would like to thank him for the encouregement and patience he showed me throughout my whole PhD.

I would like to express my eternal gratitute for my co-advisor Dr. Holger Kluck. He helped me through all the difficulties I faced during my PhD studies. He has always been a great mentor. He was always patient with me, even at times when I could not be patient with myself. I cannot thank him enough because without him, this thesis might not have seen the light of day.

I would like to thank all my colleagues in the CRESST group of HEPHY: Dr. Achim Gütlein, Dr. Florian Reindl, Martin Stahlberg (M.Sc.), Dr. Valentyna Mokina, Rafael Puig (Dipl. Ing.), Alexander Fuss (M.Sc.). They have been amazing colleagues and friends at the same time, who offered their support whenever I needed. Without their encouragement and help, I could not have gotten through many obstacles.

I would like to thank the CRESST collaboration for their support throughout my research. Especially, I would like to thank Dr. Federica Petricca, Dr. Raimund Strauss, Dr. Andrea Münster and Philipp Bauer (M.Sc.). They provided their support each time I needed it.

I would like to thank all fellow scientists working at HEPHY, made working at this institute an amazing experience.

I would like to thank my amazing friend Hanna Lauter, who showed her support since the day I met her. She was there for me even at times when I was the most upset. She is the best friend everyone would love to have and I am hoping that our friendship will last forever. I am so happy to have gotten to known her.

I would like to thank my colleague and friend Dr. Ece Aşılar for all her support. There have been difficult times for both of us during our PhD studies but we managed to survive it while supporting each other throughout. I hope our friendship, which started eight years ago, will be for a lifetime.

I also would like to thank my friends in Vienna Konuralp Esentürk, Ekin Tokatlıgil, Natalija Kostić (M.Sc.), Deniz Dilara Akgün, Jules Beck, Julia Graninger and Ayşegül Turupçu (M.Sc.). In addition, I would like to thank my friends who are physically away but close in heart: Mesut Ünal (M.Sc.), Ramazan Uzel (M.Sc.), Onur Aydoğan, Ava Bagherpoor, Nilüfer Köse, Tuğcan Selimhocaoğlu (M.Sc.), Mert Doğan (M.Sc.), Volkan Acun (M.F.A.), Kerem Alptekin, Boray Değerliyurt (M.Sc.), Berk Bozkır (M.Sc.), Berkan

Zıraman and Serdar Yıldız. They were always there whenever I needed someone to talk to. I am so happy to have these amazing people as friends.

Last but not least, I would like to thank my mother Şennur Türkoğlu for bringing me up, helping me with everything throughout my whole life, being there for me each and every time I needed and for her continuous support. Without her, non of my accomplishments might have seen the light of day. She is the most special person for me in this world. Also, I would like to thank my father Orhan Türkoğlu for believing in and supporting me until his last breath. He lives in my heart and mind, and will continue to do so until my last breath.

A. Appendices

A.1. Abbreviations

BR ..... Branching Ratio
CMB ..... Cosmic Microwave Background
C.L. ..... Confidence Level
CRESST ..... Cryogenic Rare Event Search with Superconducting Thermometers
DM ..... Dark Matter
EC ..... Electron Capture
LNGS ..... Laboratori Natizonali del Gran Sasso
LY ..... Light Yield
MC ..... Monte Carlo
PDF ..... Probability Density Function
PE ..... Polyethylene
ROI ..... Region of Interest
SM ..... Standard Model
WMAP ..... Wilkinson Microwave Anisotropy Probe

A.2. Simulated Templates of Internal Radiogenic Backgrounds

A.2.1. Templates of Alpha Decays

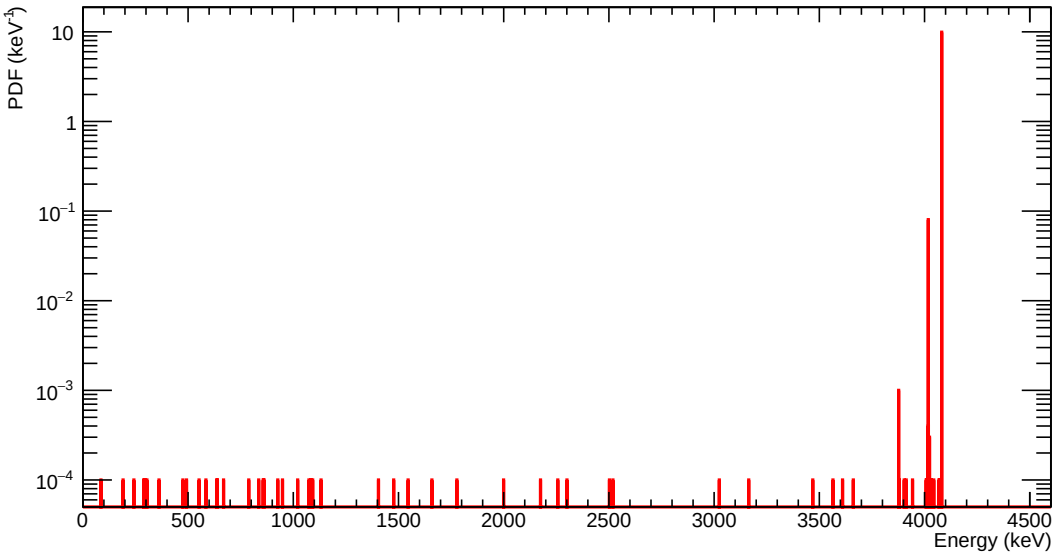

Figure A.1.: Decay of ^{232}Th inside the $CaWO_4$ crystal. Detector response function is not applied.

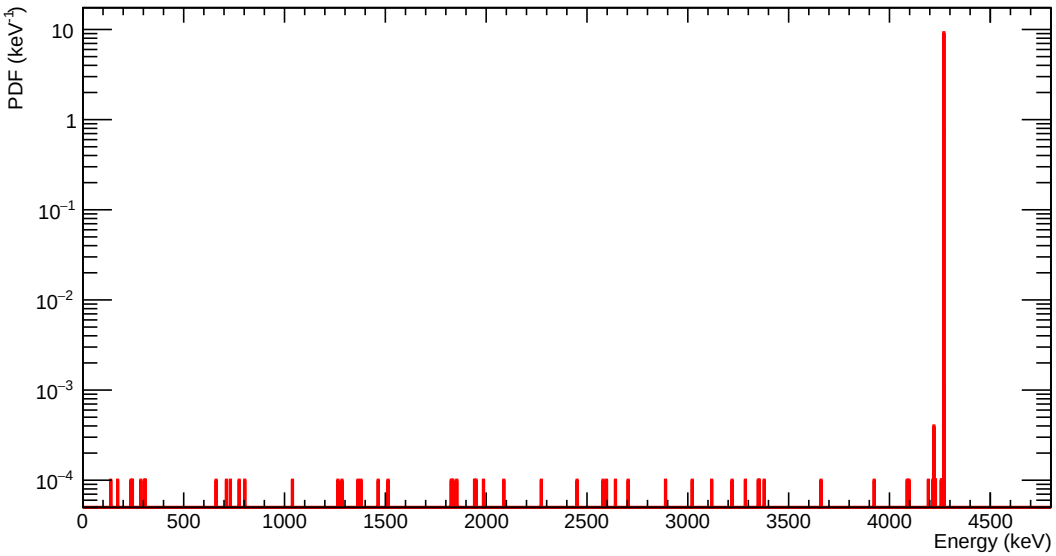

Figure A.2.: Decay of ^{238}U inside the $CaWO_4$ crystal. Detector response function is not applied.

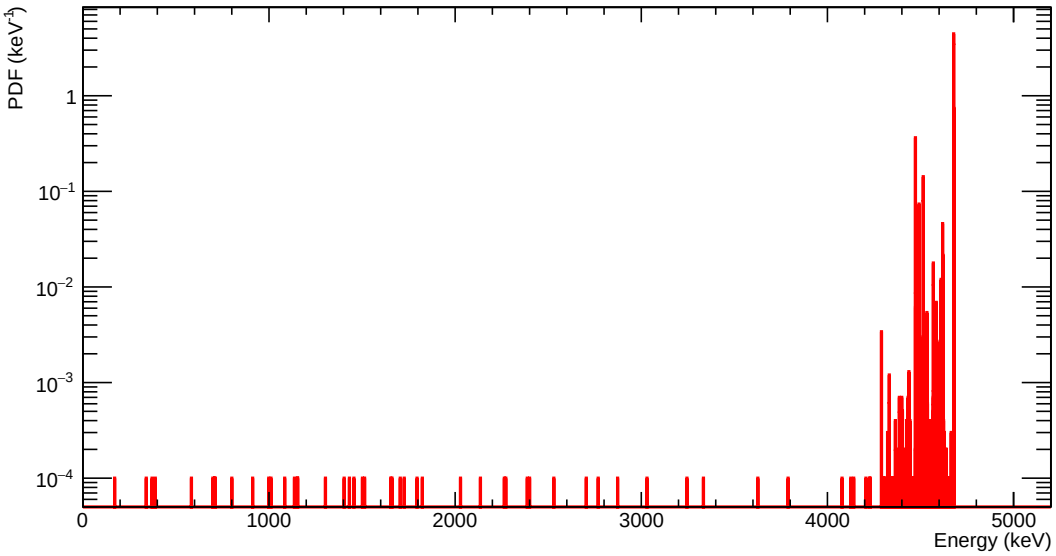

Figure A.3.: Decay of ^{235}U inside the $CaWO_4$ crystal. Detector response function is not applied.

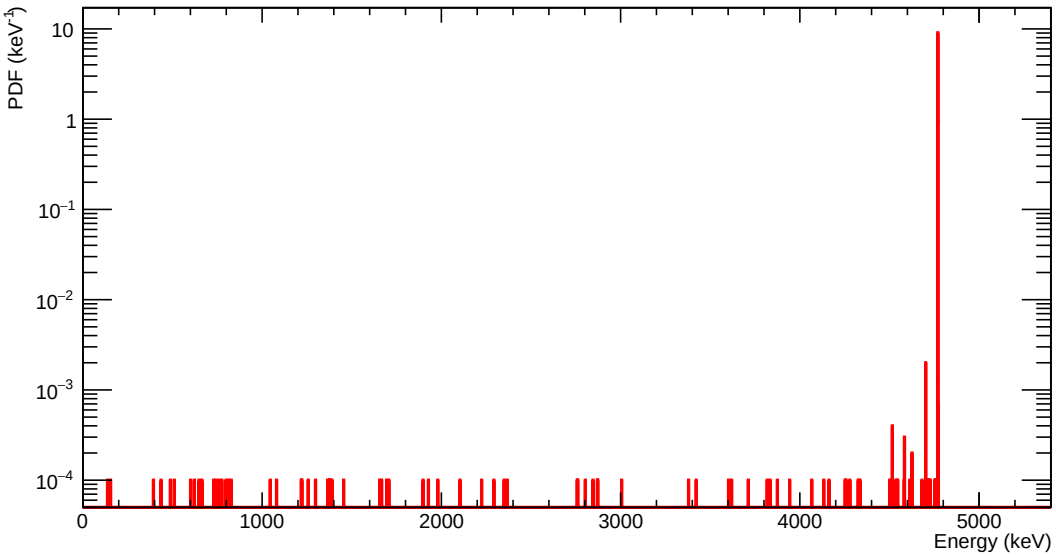

Figure A.4.: Decay of ^{230}Th inside the $CaWO_4$ crystal. Detector response function is not applied.

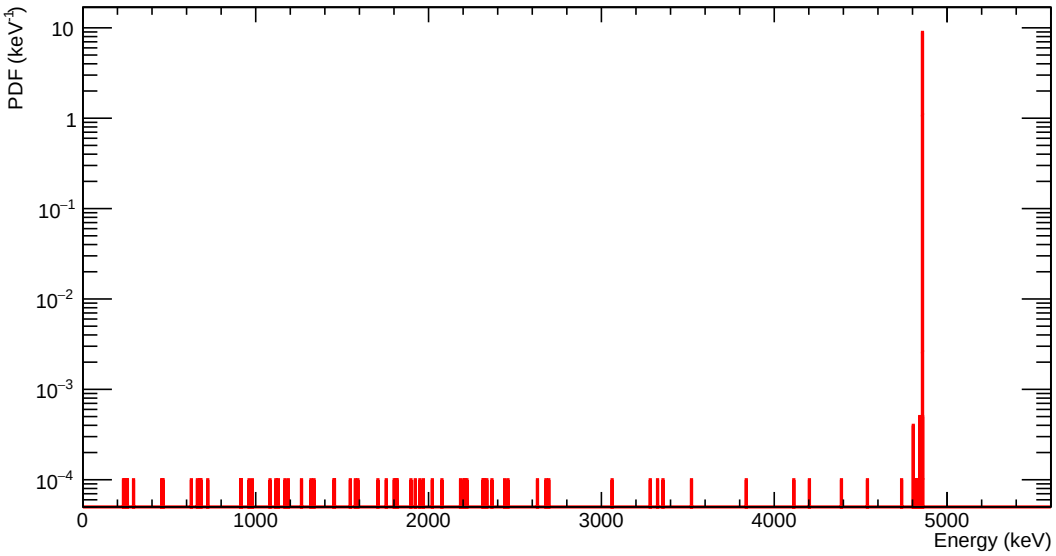

Figure A.5.: Decay of ^{234}U inside the $CaWO_4$ crystal. Detector response function is not applied.

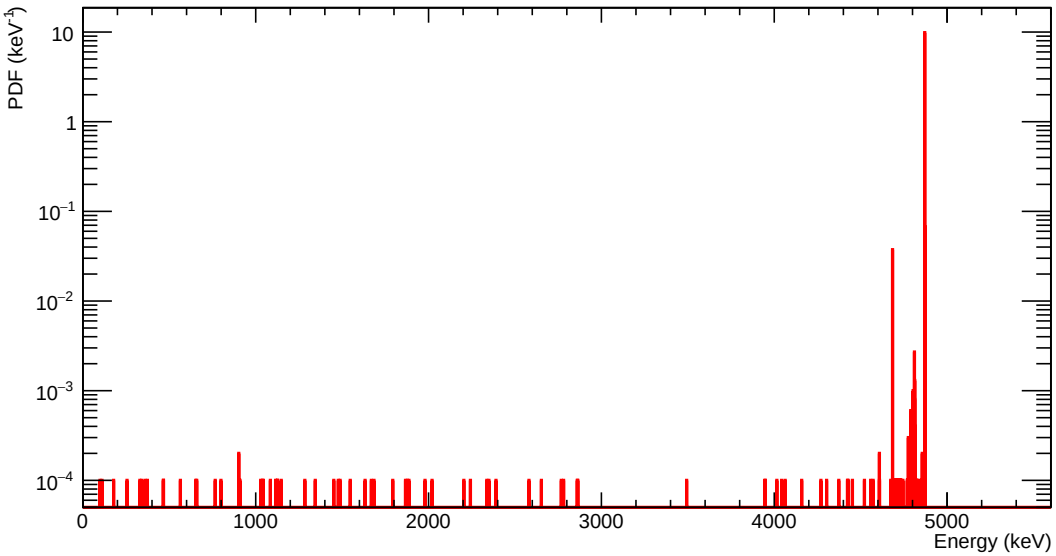

Figure A.6.: Decay of ^{226}Ra inside the $CaWO_4$ crystal. Detector response function is not applied.

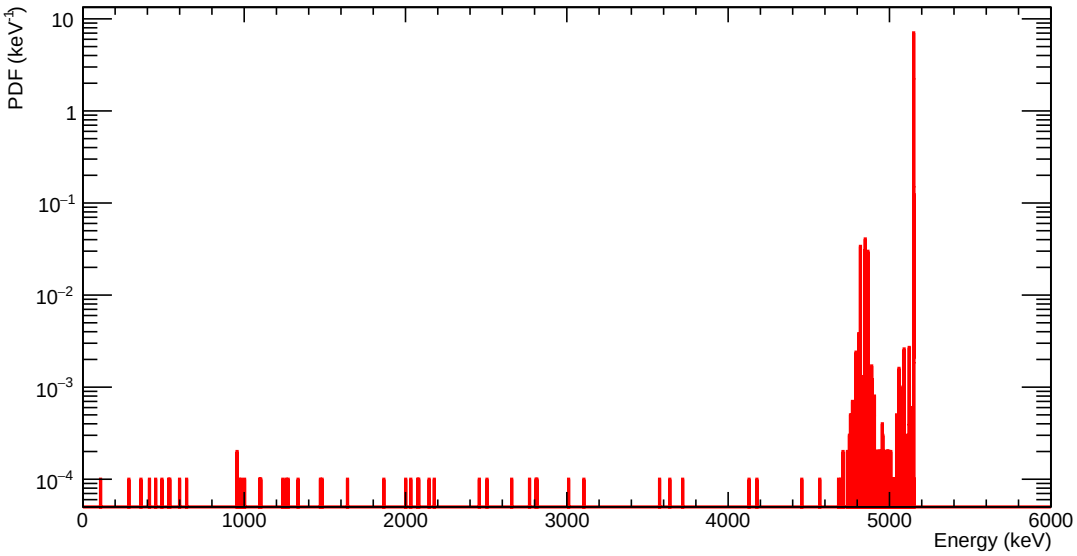

Figure A.7.: Decay of ^{231}Pa inside the $CaWO_4$ crystal. Detector response function is not applied.

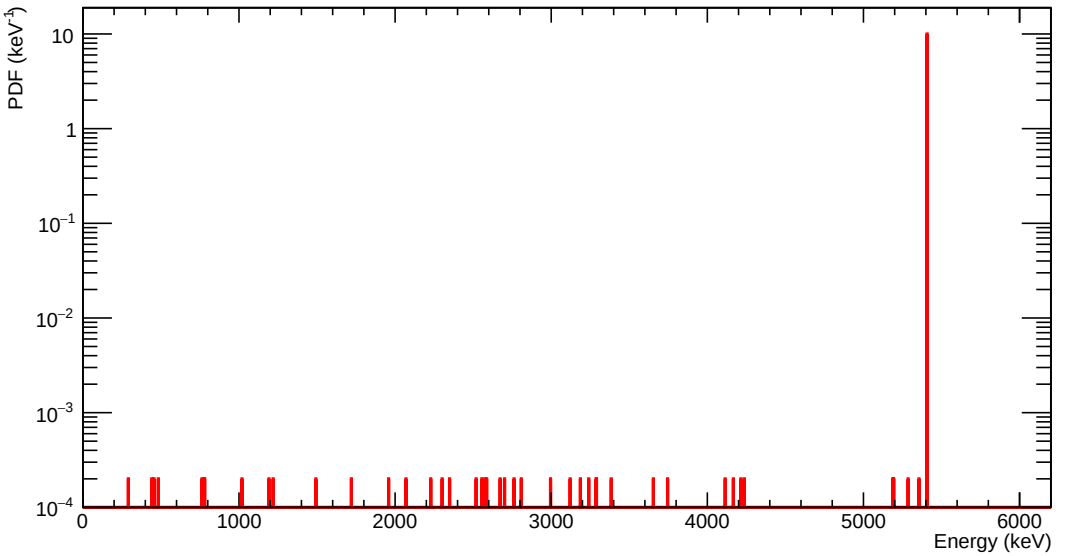

Figure A.8.: Decay of ^{210}Po inside the $CaWO_4$ crystal. Detector response function is not applied.

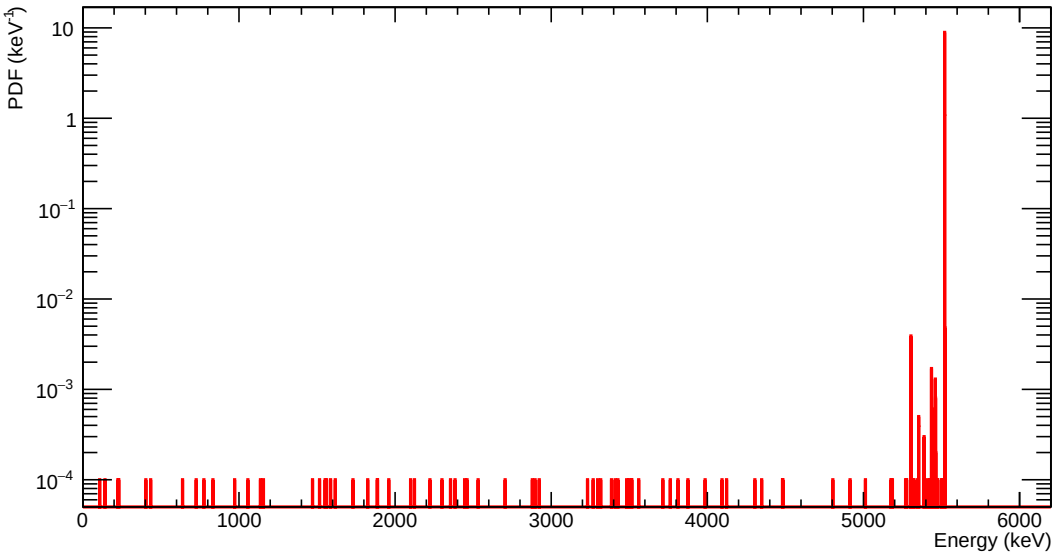

Figure A.9.: Decay of ^{228}Th inside the $CaWO_4$ crystal. Detector response function is not applied.

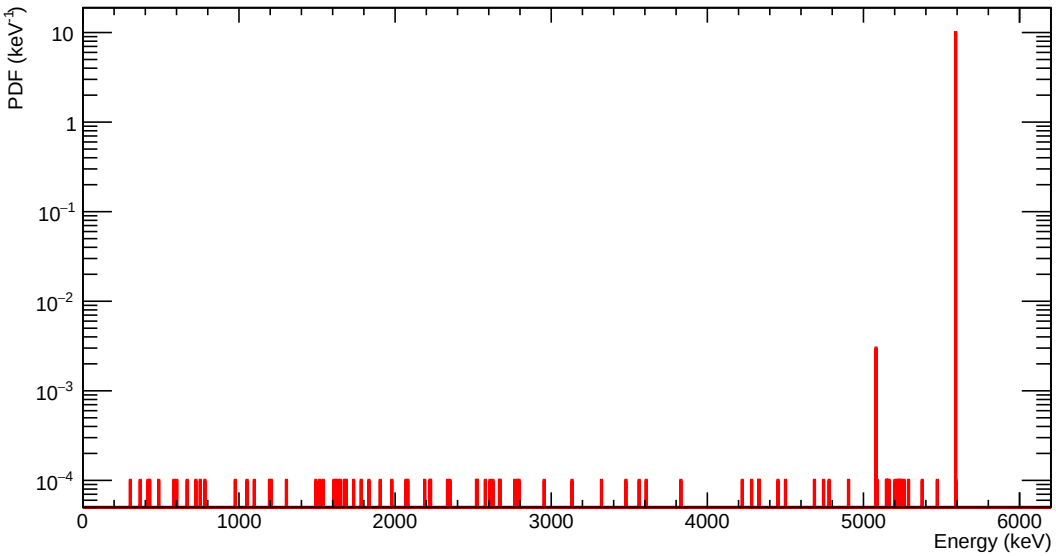

Figure A.10.: Decay of ^{222}Rn inside the $CaWO_4$ crystal. Detector response function is not applied.

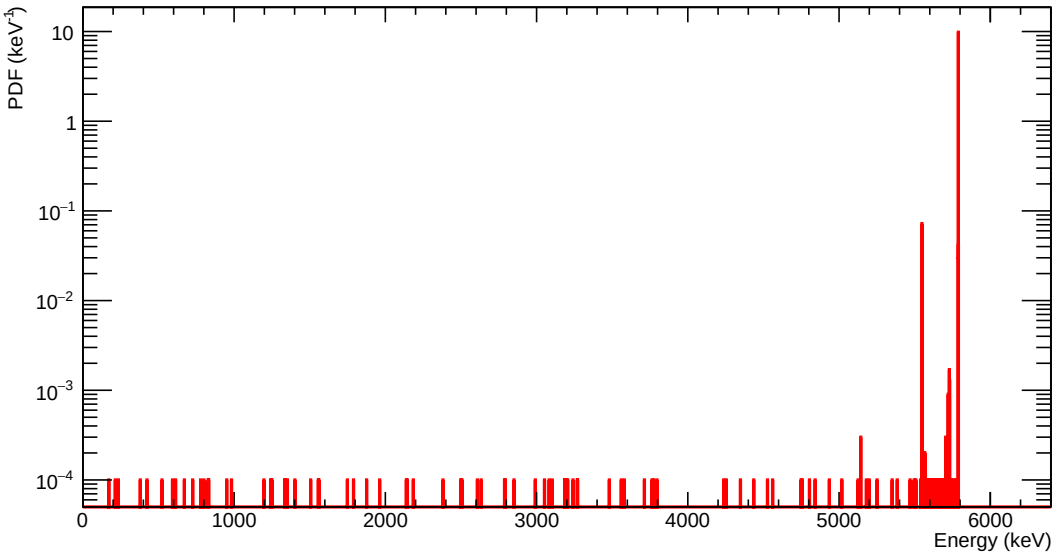

Figure A.11.: Decay of ^{224}Ra inside the $CaWO_4$ crystal. Detector response function is not applied.

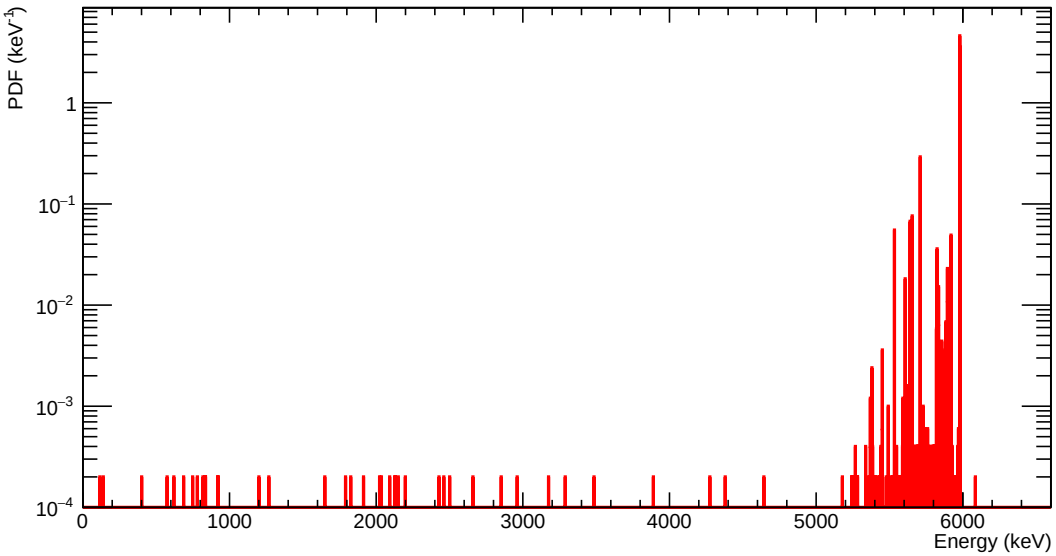

Figure A.12.: Decay of ^{223}Ra inside the $CaWO_4$ crystal. Detector response function is not applied.

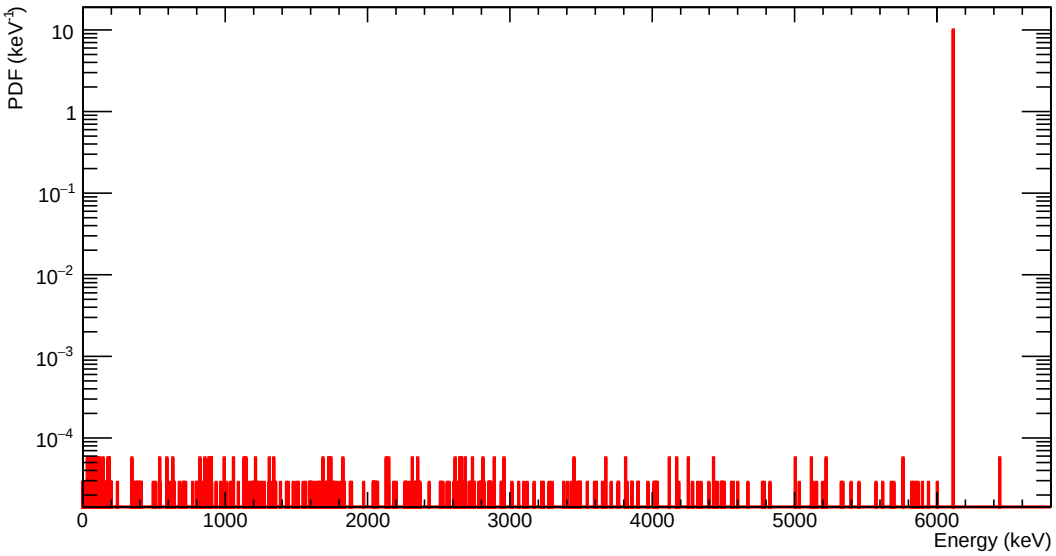

Figure A.13.: Decay of ^{218}Po inside the $CaWO_4$ crystal. Detector response function is not applied.

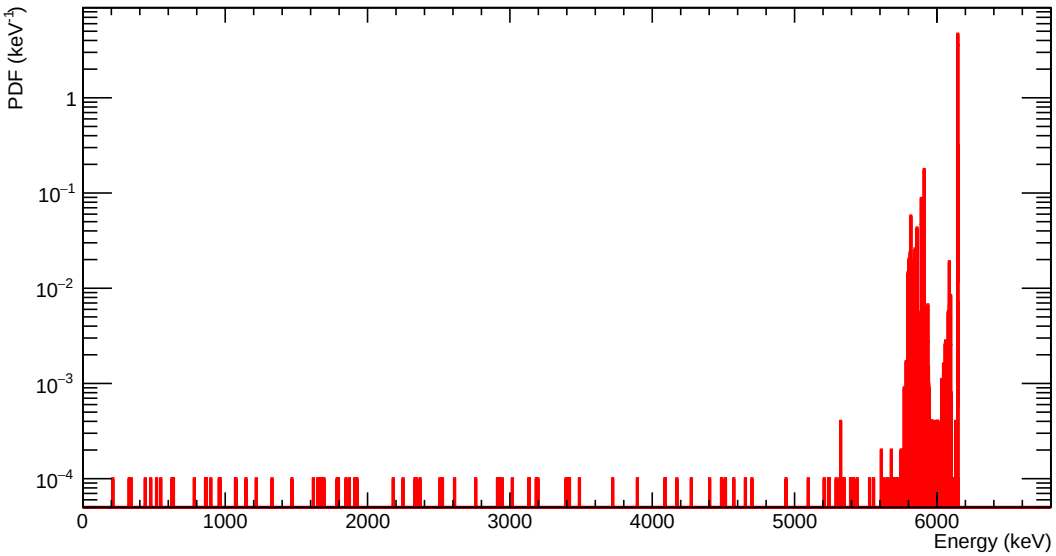

Figure A.14.: Decay of ^{227}Th inside the $CaWO_4$ crystal. Detector response function is not applied.

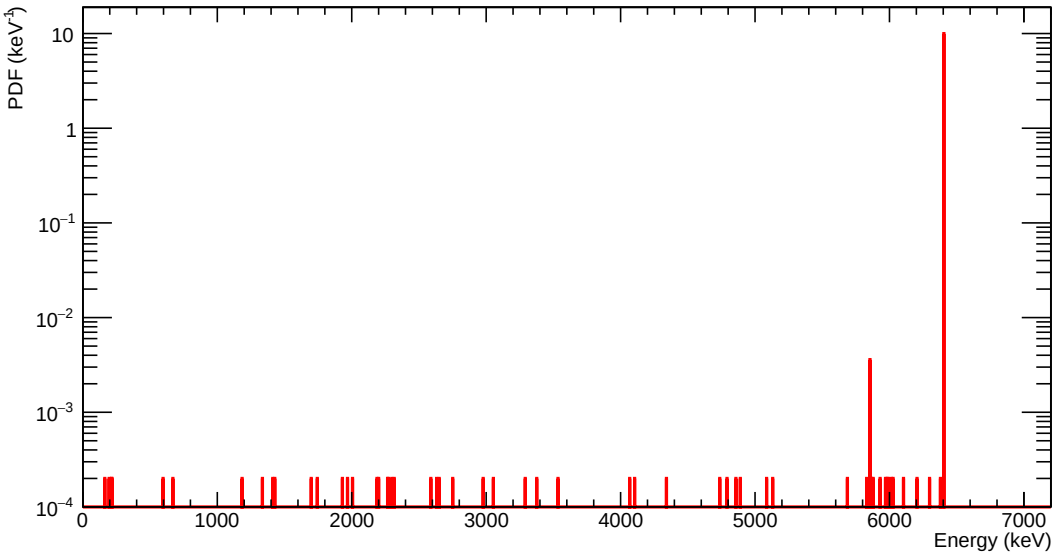

Figure A.15.: Decay of ^{220}Rn inside the $CaWO_4$ crystal. Detector response function is not applied.

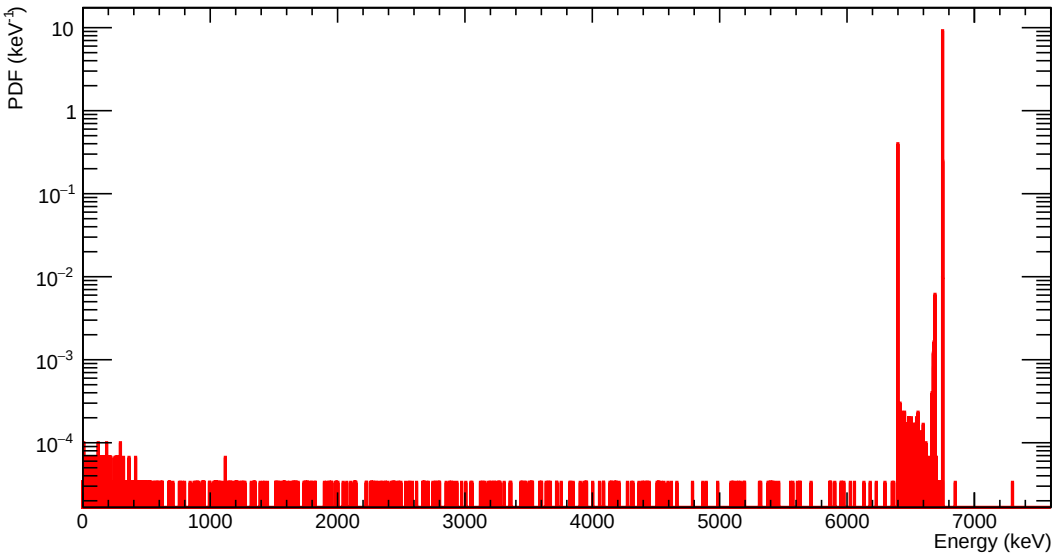

Figure A.16.: Decay of ^{211}Bi inside the $CaWO_4$ crystal. Detector response function is not applied.

A.2.2. Templates of Beta-/Gamma-Decays

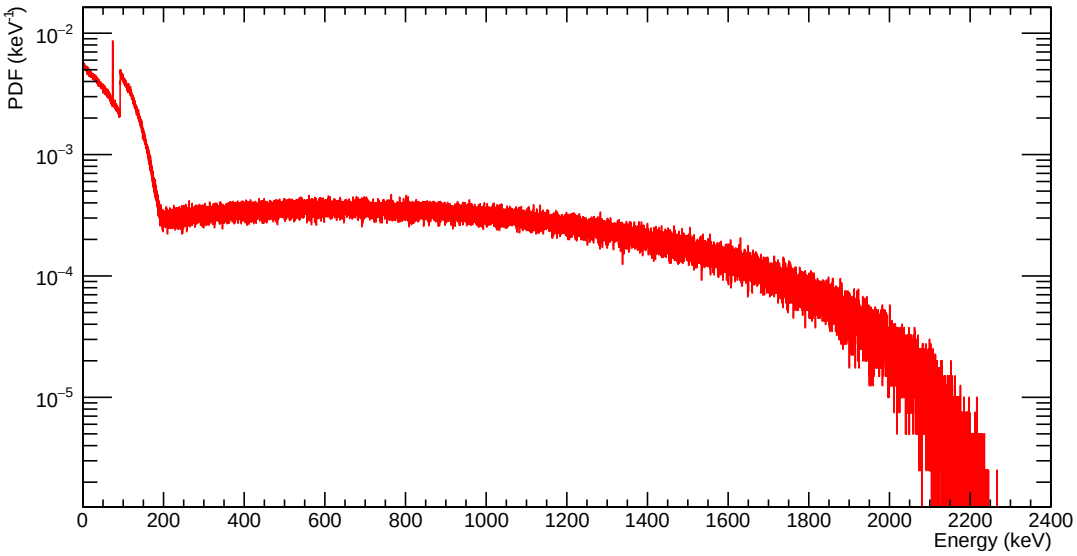

Figure A.17.: Decay of ^{234}Th inside the $CaWO_4$ crystal. Detector response function is not applied.

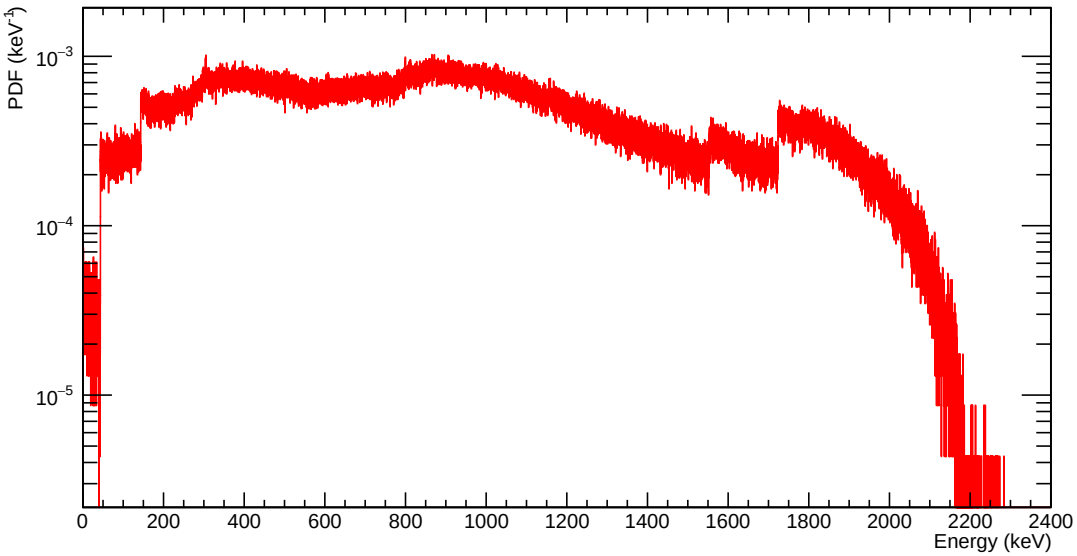

Figure A.18.: Decay of ^{234}Pa inside the $CaWO_4$ crystal. Detector response function is not applied.

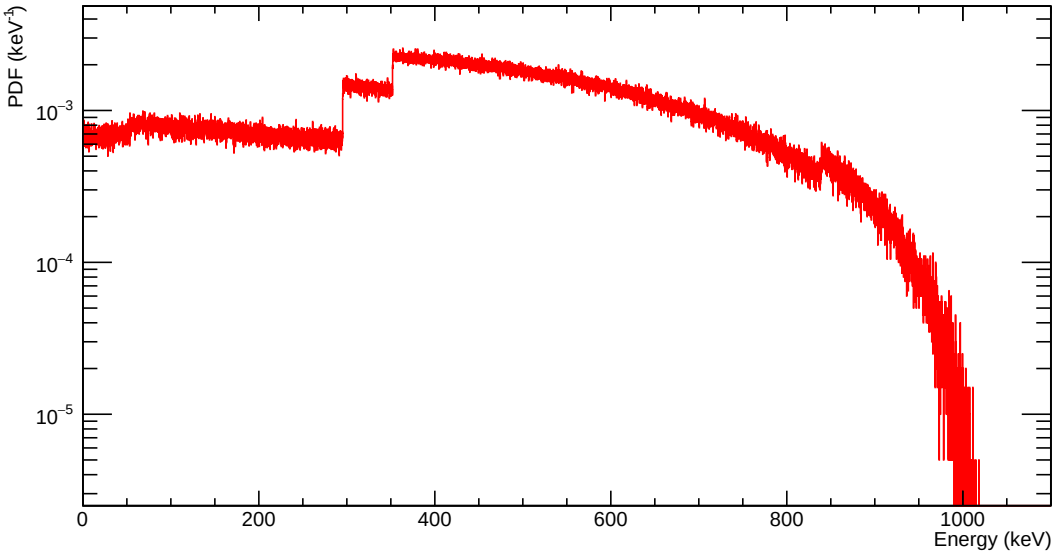

Figure A.19.: Decay of ^{214}Pb inside the $CaWO_4$ crystal. Detector response function is not applied.

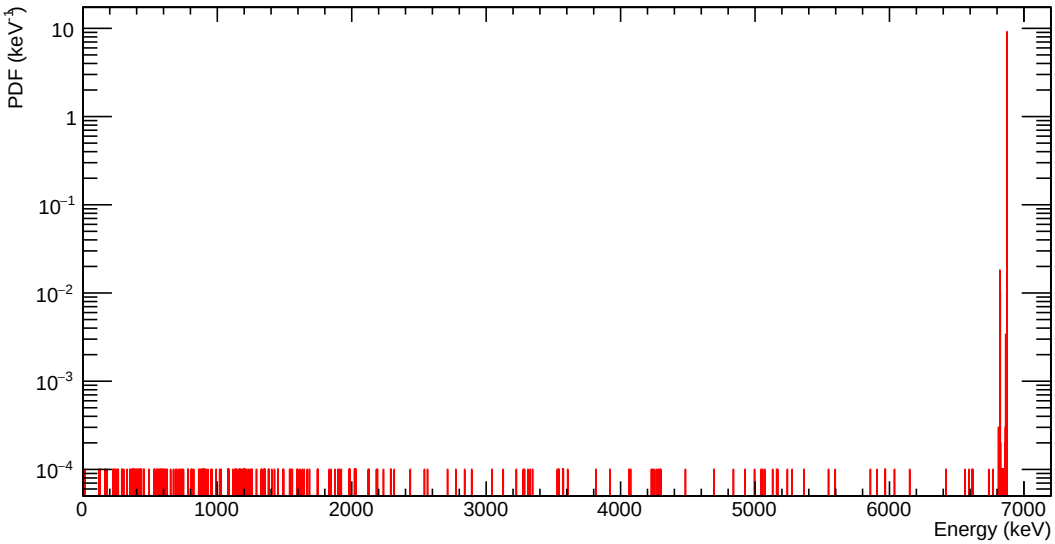

Figure A.20.: Decay of ^{218}At inside the $CaWO_4$ crystal. Detector response function is not applied.

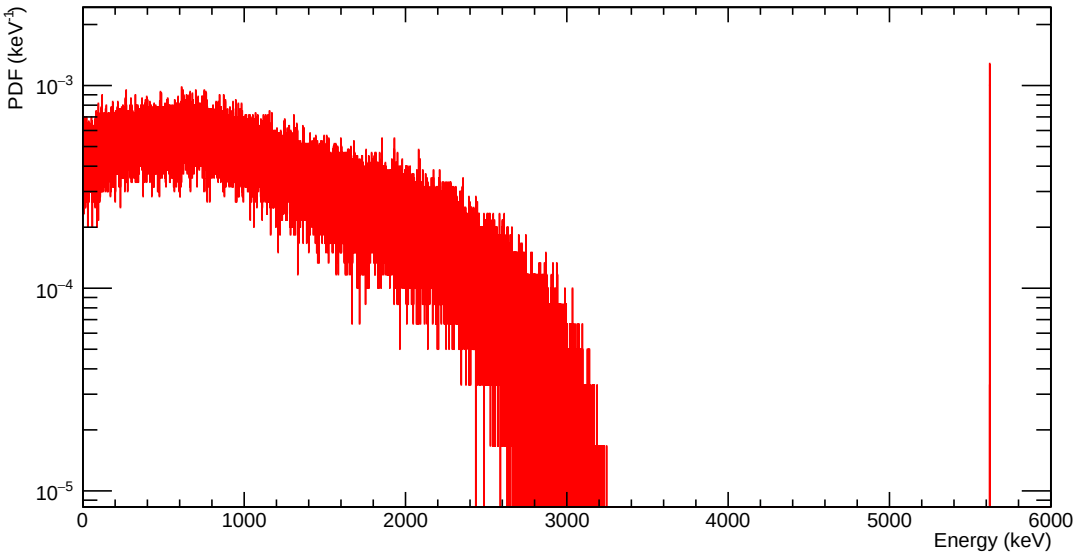

Figure A.21.: Decay of ^{214}Bi inside the $CaWO_4$ crystal. Detector response function is not applied.

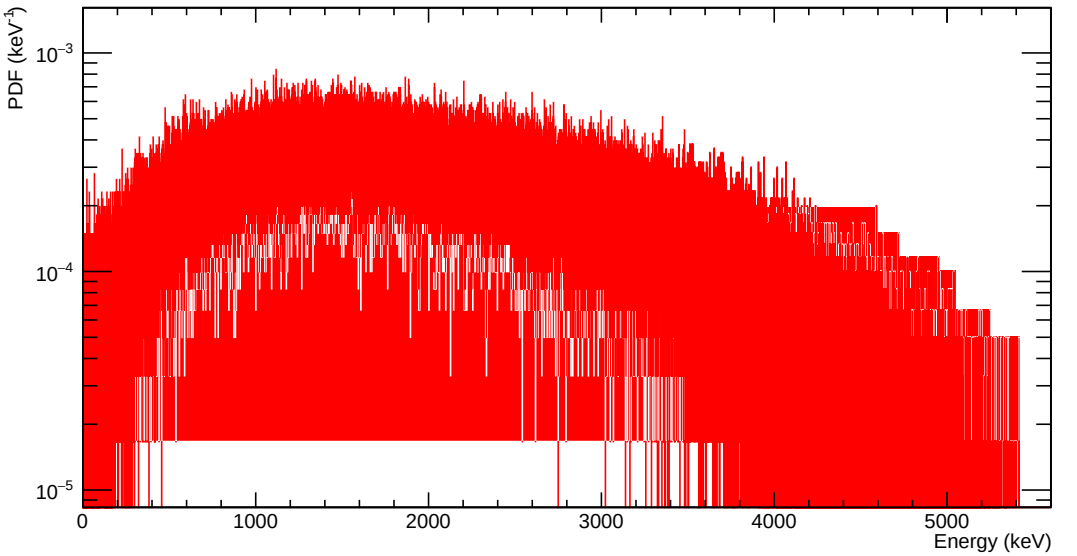

Figure A.22.: Decay of ^{210}Tl inside the $CaWO_4$ crystal. Detector response function is not applied.

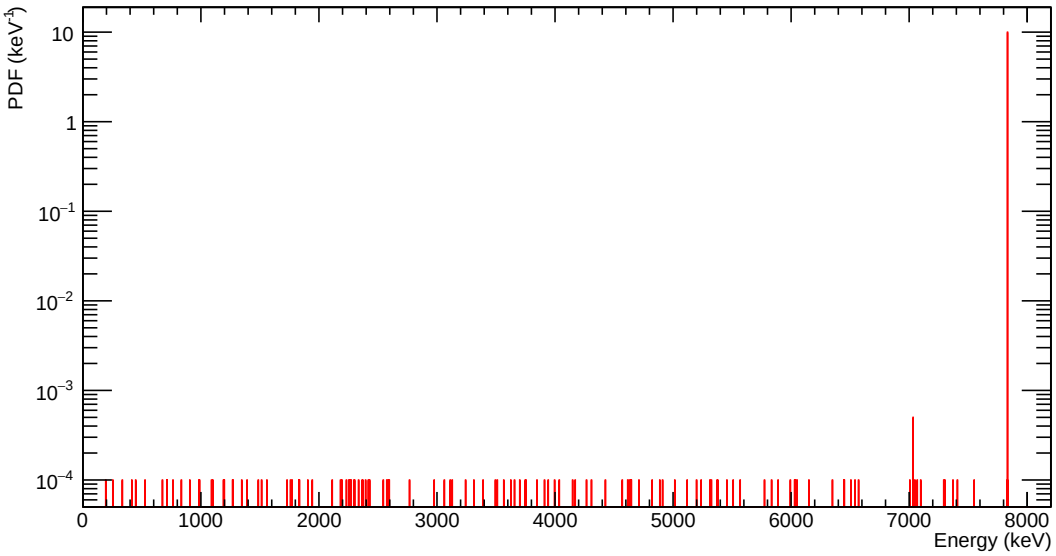

Figure A.23.: Decay of ^{214}Po inside the $CaWO_4$ crystal. Detector response function is not applied.

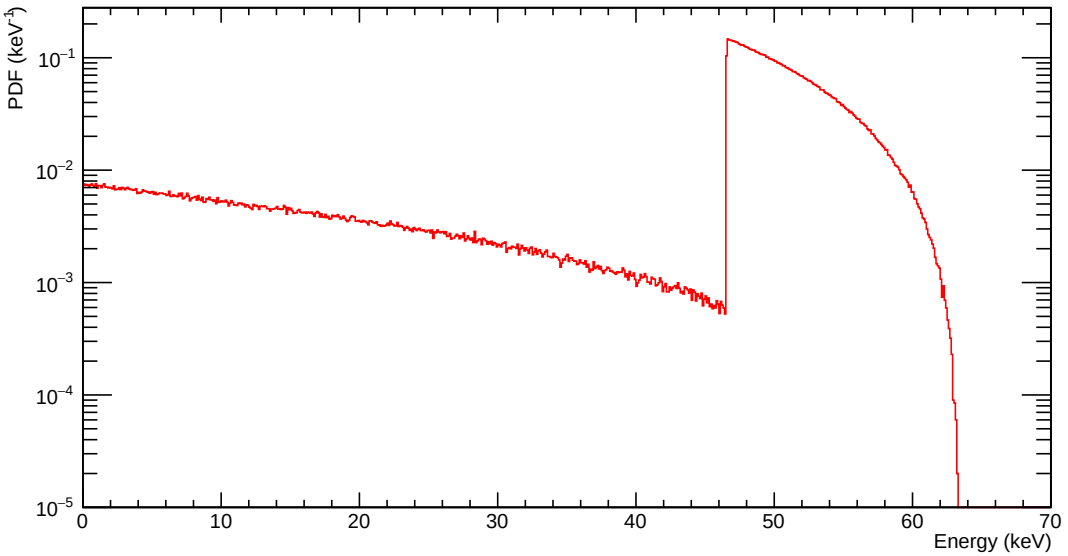

Figure A.24.: Decay of ^{210}Pb inside the $CaWO_4$ crystal. Detector response function is not applied.

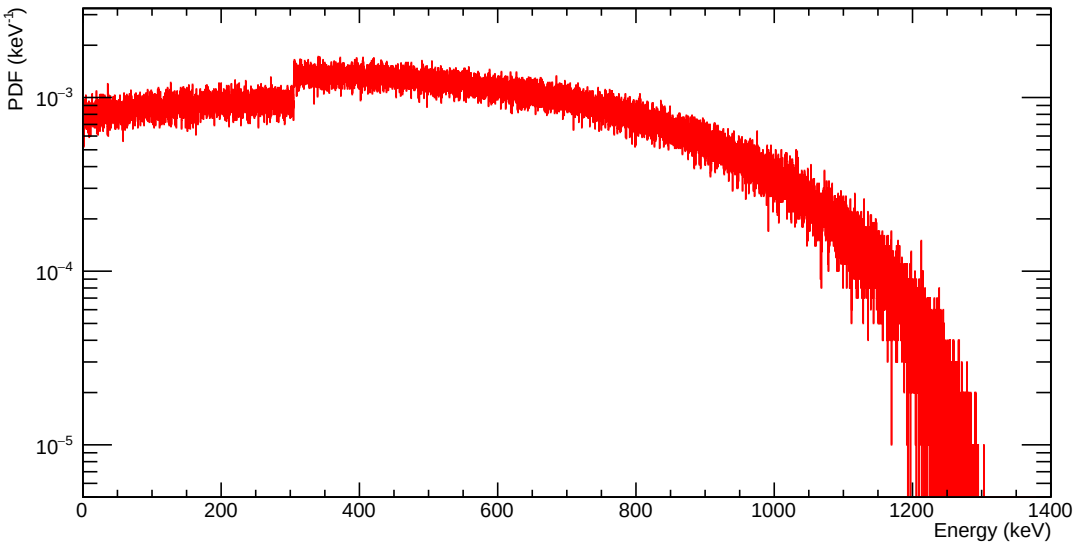

Figure A.25.: Decay of ^{206}Hg inside the $CaWO_4$ crystal. Detector response function is not applied.

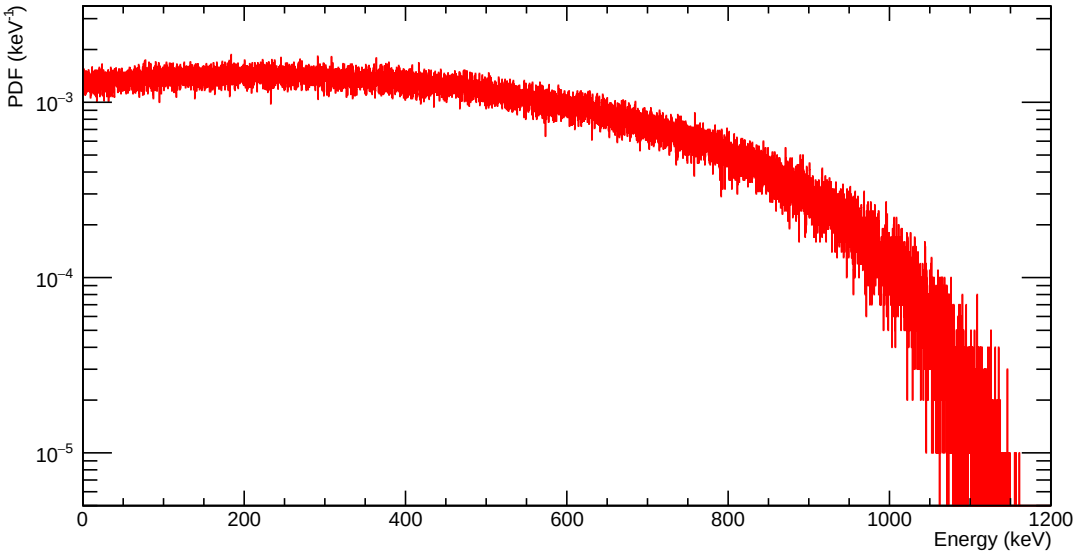

Figure A.26.: Decay of ^{210}Bi inside the $CaWO_4$ crystal. Detector response function is not applied.

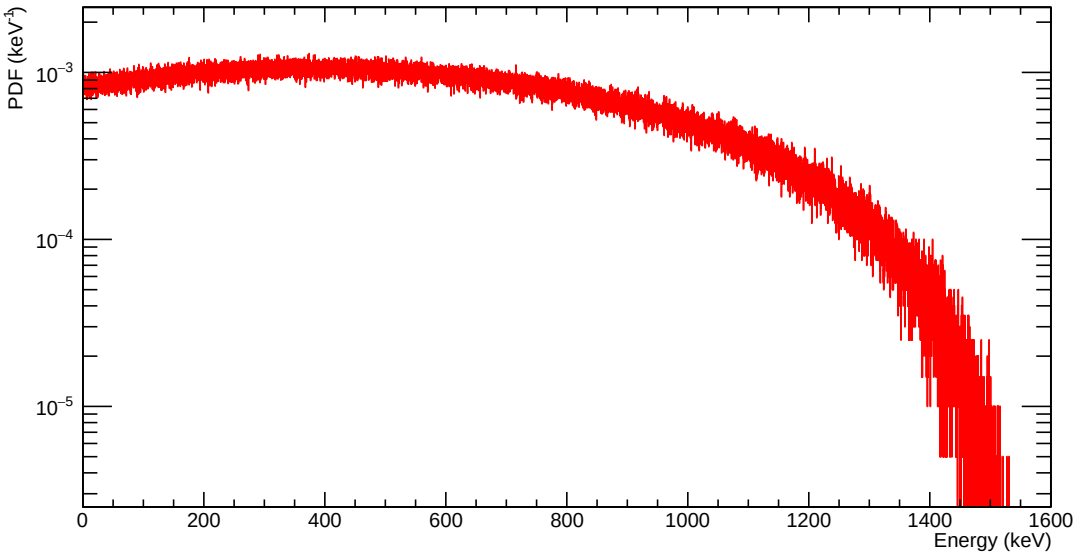

Figure A.27.: Decay of ^{206}Tl inside the $CaWO_4$ crystal. Detector response function is not applied.

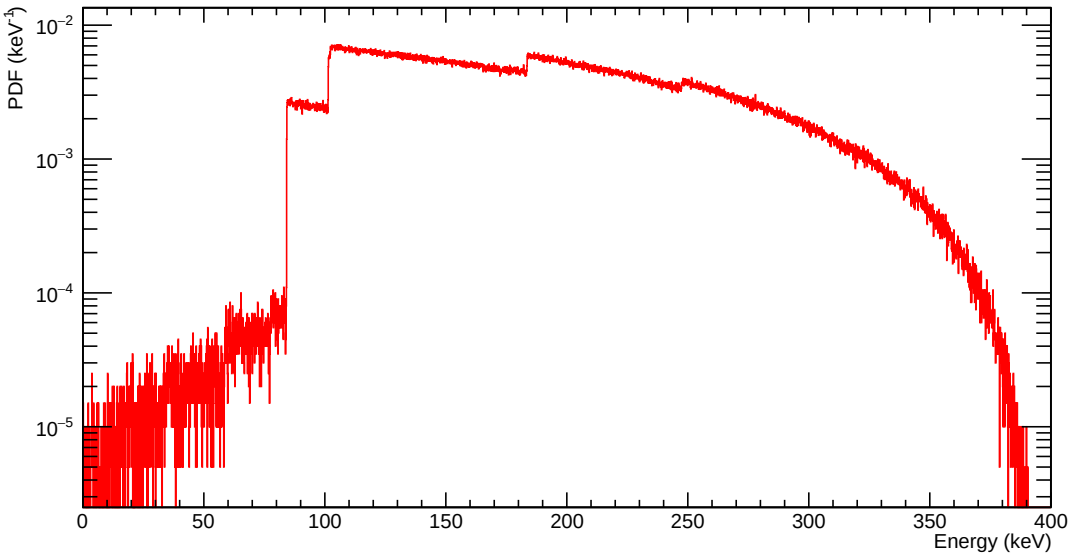

Figure A.28.: Decay of ^{231}Th inside the $CaWO_4$ crystal. Detector response function is not applied.

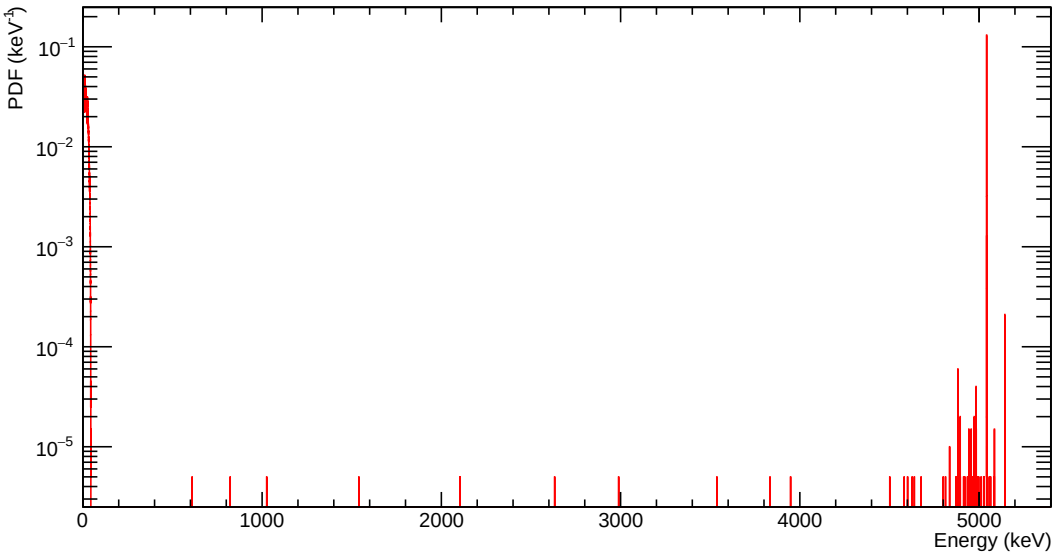

Figure A.29.: Decay of ^{227}Ac inside the $CaWO_4$ crystal. Detector response function is not applied.

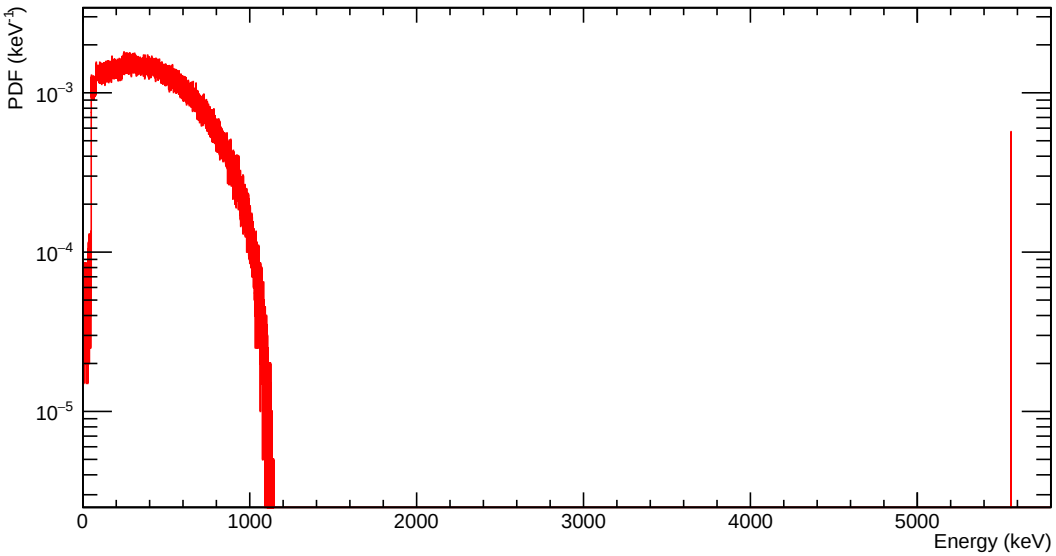

Figure A.30.: Decay of ^{223}Fr inside the $CaWO_4$ crystal. Detector response function is not applied.

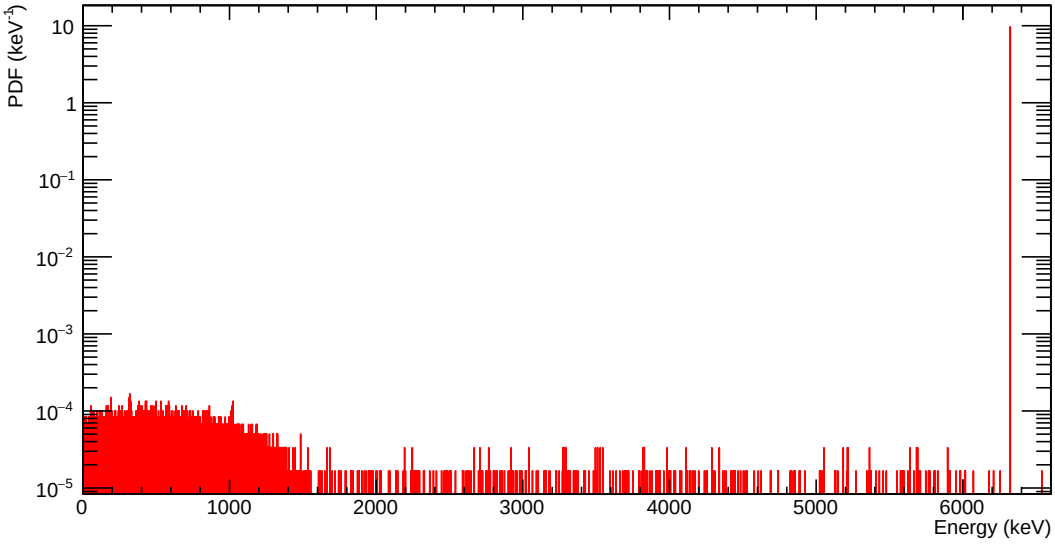

Figure A.31.: Decay of ^{219}At inside the $CaWO_4$ crystal. Detector response function is not applied.

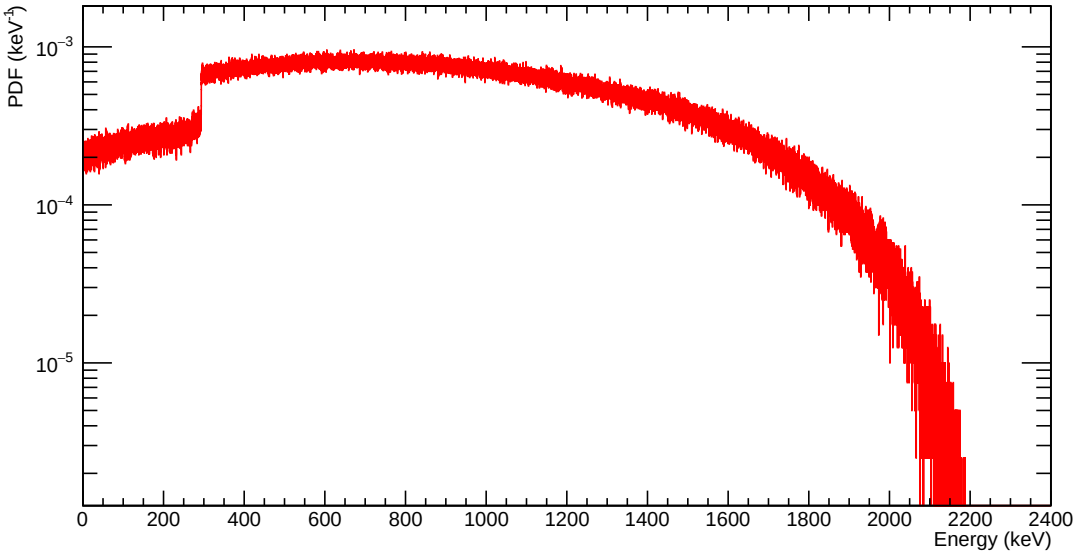

Figure A.32.: Decay of ^{215}Bi inside the $CaWO_4$ crystal. Detector response function is not applied.

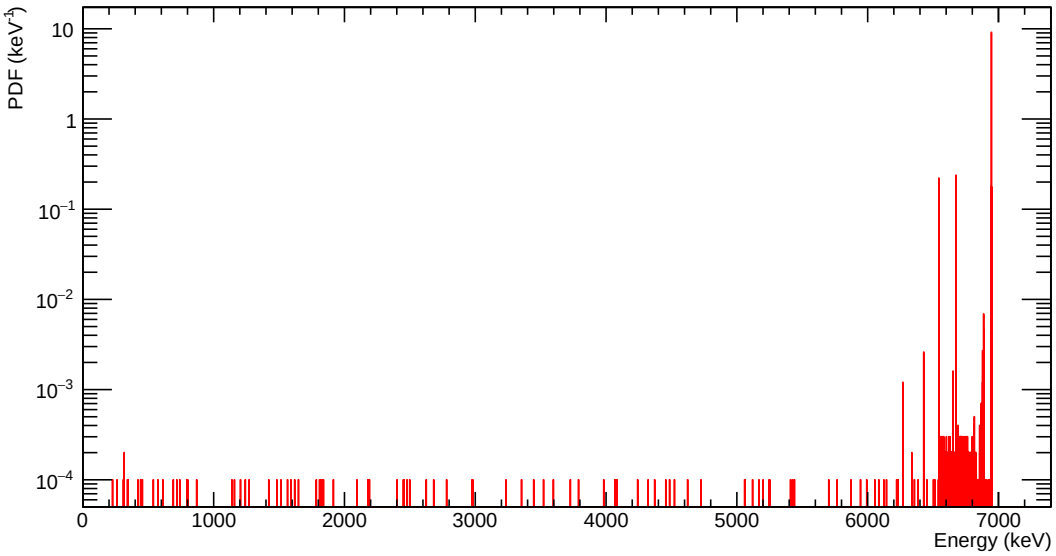

Figure A.33.: Decay of ^{219}Rn inside the $CaWO_4$ crystal. Detector response function is not applied.

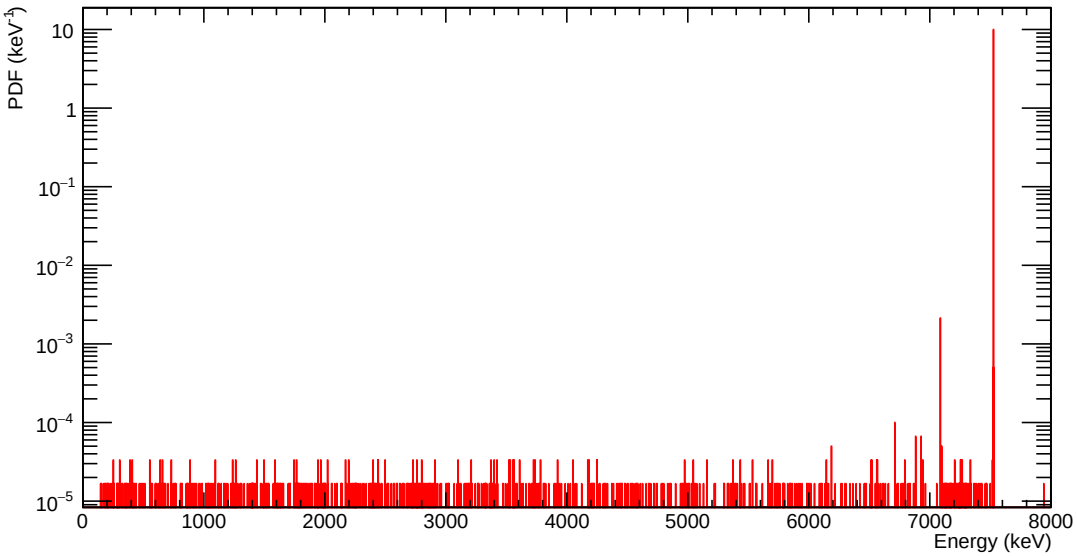

Figure A.34.: Decay of ^{215}Po inside the $CaWO_4$ crystal. Detector response function is not applied.

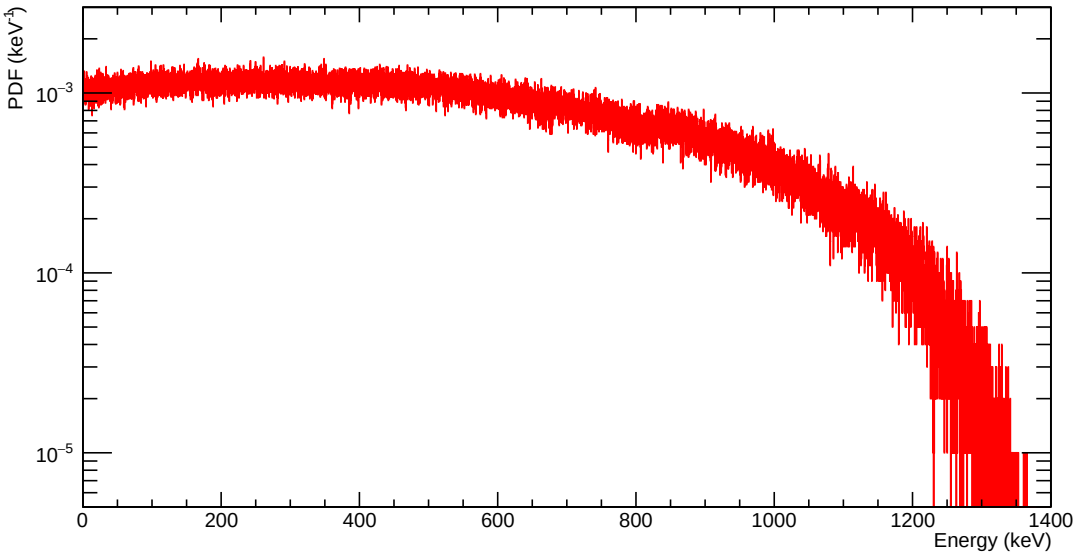

Figure A.35.: Decay of ^{211}Pb inside the $CaWO_4$ crystal. Detector response function is not applied.

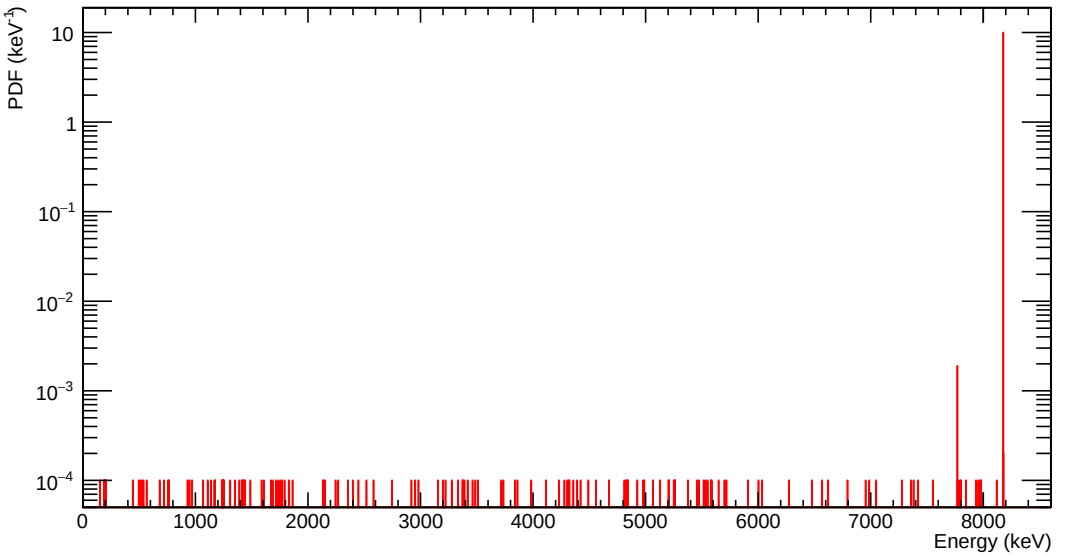

Figure A.36.: Decay of ^{215}At inside the $CaWO_4$ crystal. Detector response function is not applied.

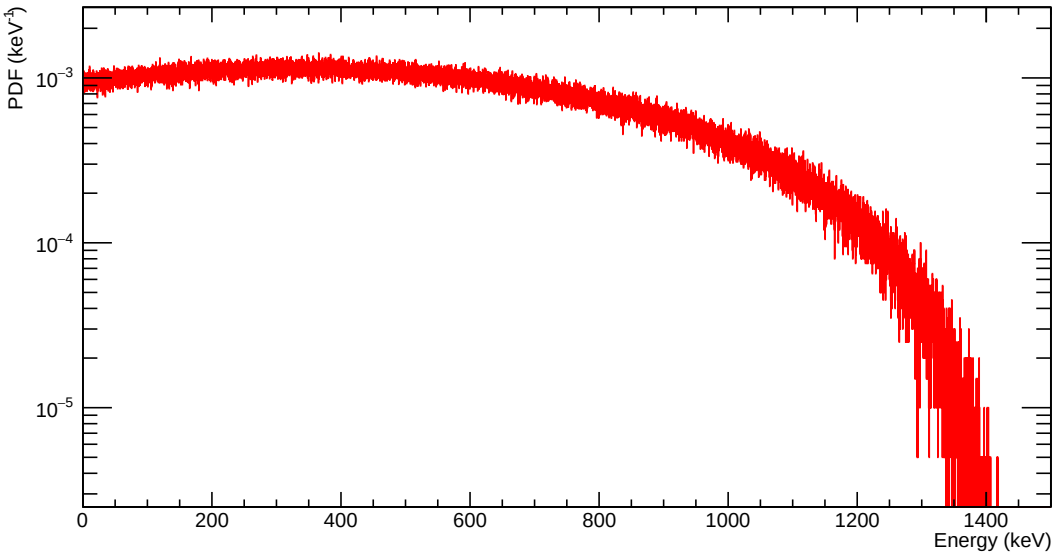

Figure A.37.: Decay of ^{207}Tl inside the $CaWO_4$ crystal. Detector response function is not applied.

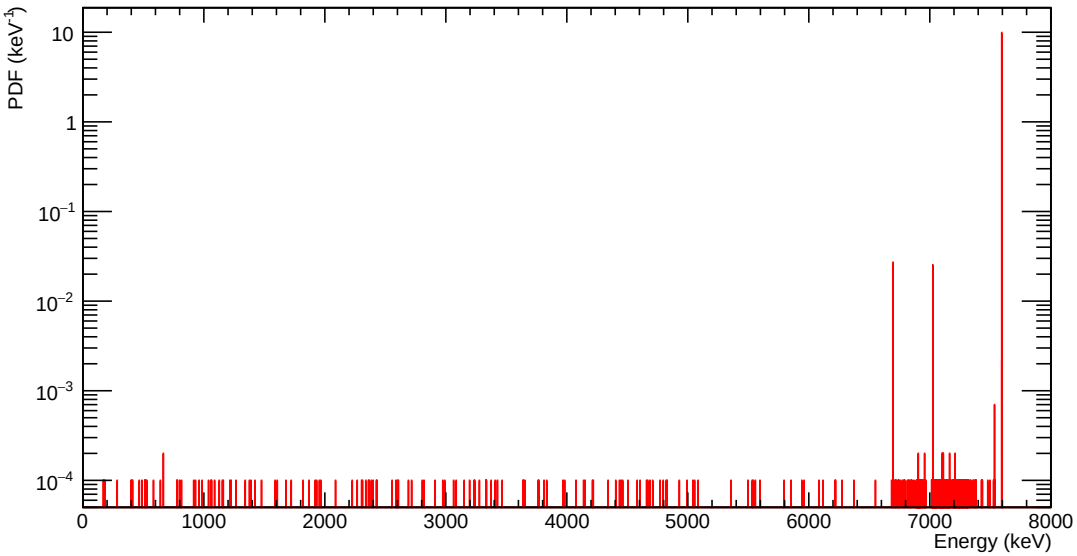

Figure A.38.: Decay of ^{211}Po inside the $CaWO_4$ crystal. Detector response function is not applied.

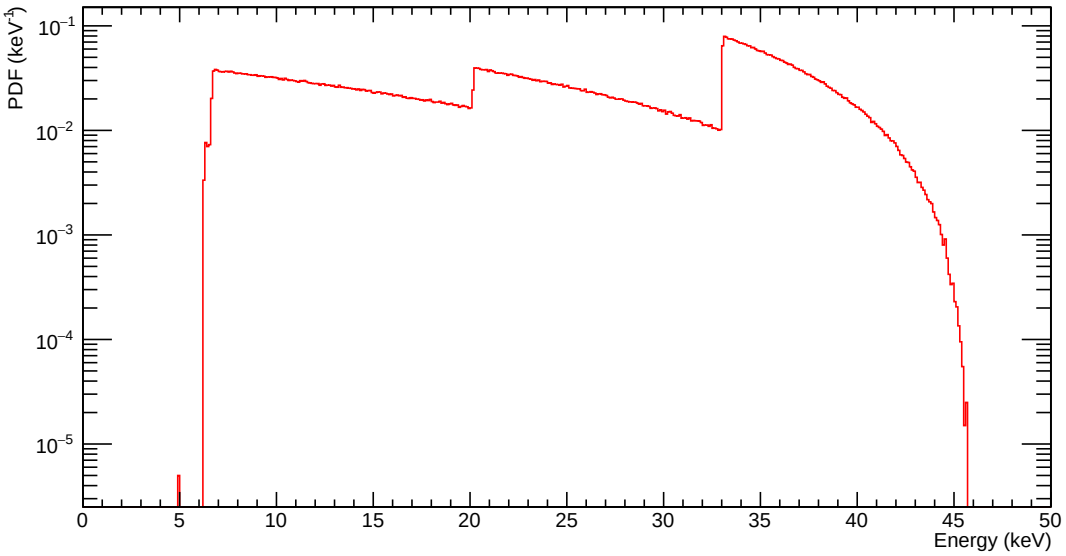

Figure A.39.: Decay of ^{228}Ra inside the $CaWO_4$ crystal. Detector response function is not applied.

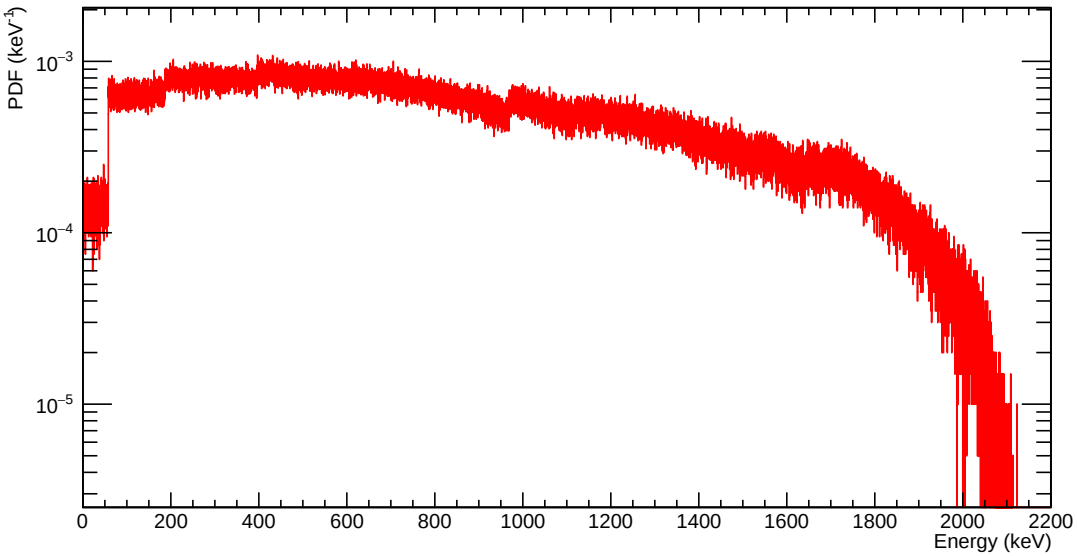

Figure A.40.: Decay of ^{228}Ac inside the $CaWO_4$ crystal. Detector response function is not applied.

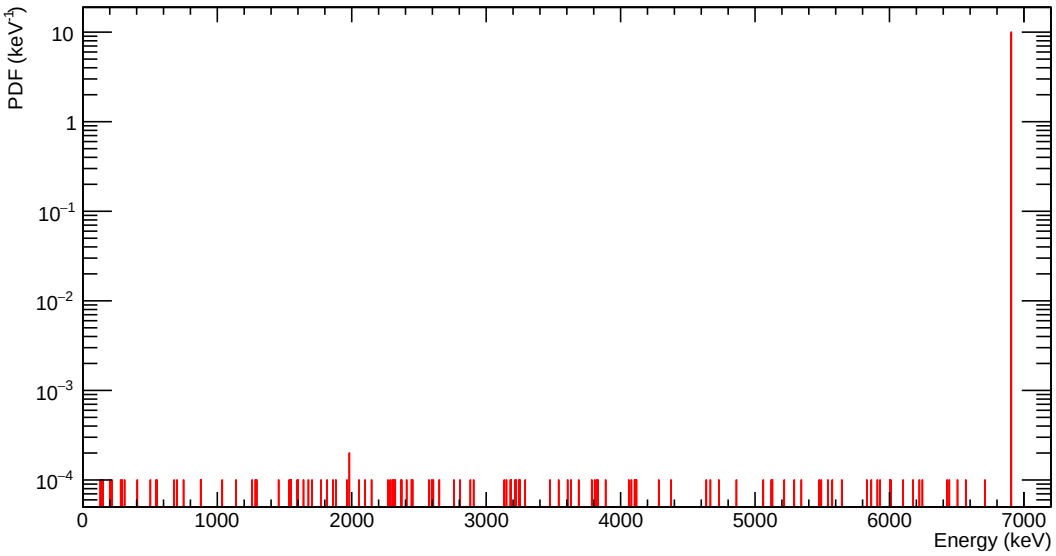

Figure A.41.: Decay of ^{216}Po inside the $CaWO_4$ crystal. Detector response function is not applied.

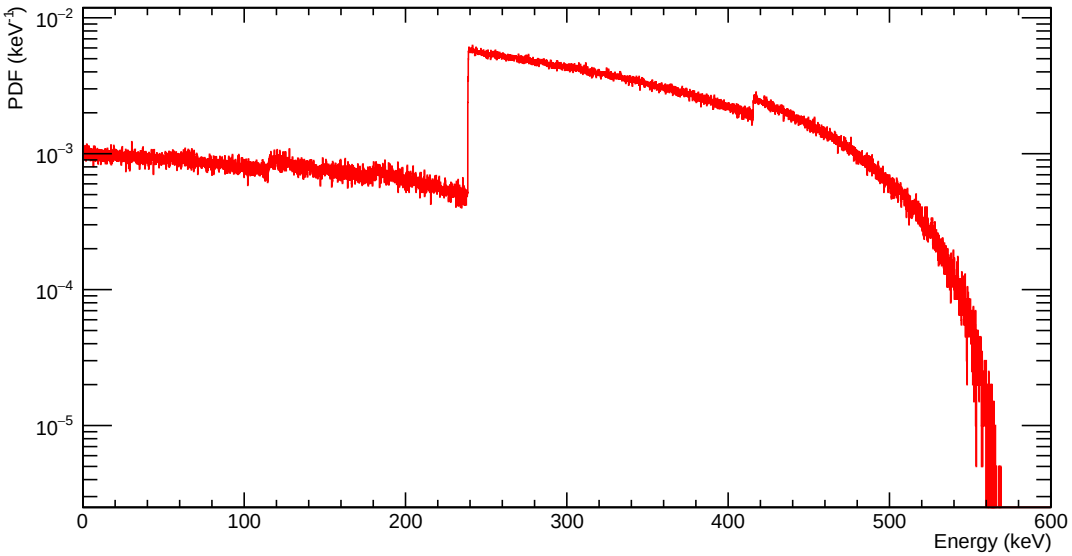

Figure A.42.: Decay of ^{212}Pb inside the $CaWO_4$ crystal. Detector response function is not applied.

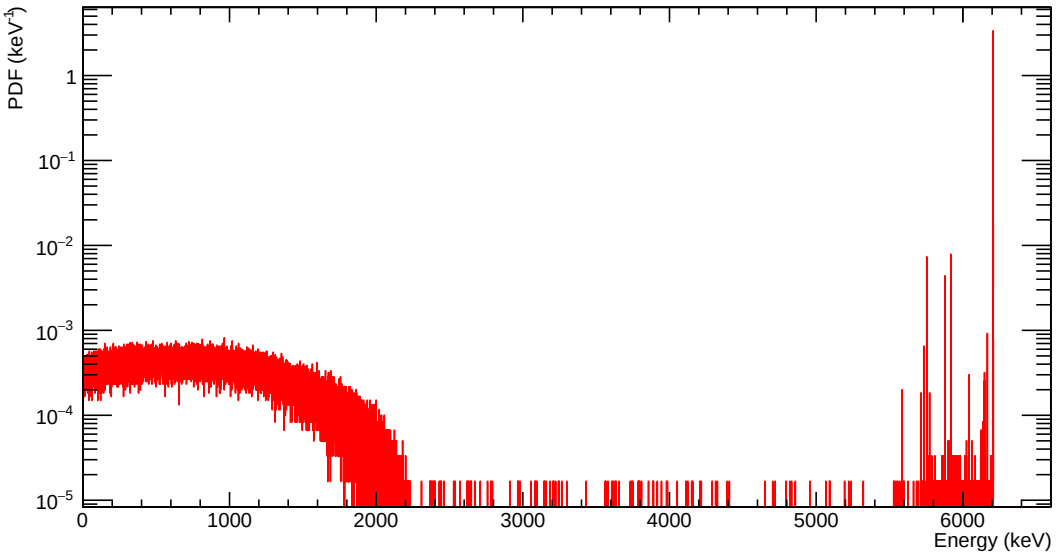

Figure A.43.: Decay of ^{212}Bi inside the $CaWO_4$ crystal. Detector response function is not applied.

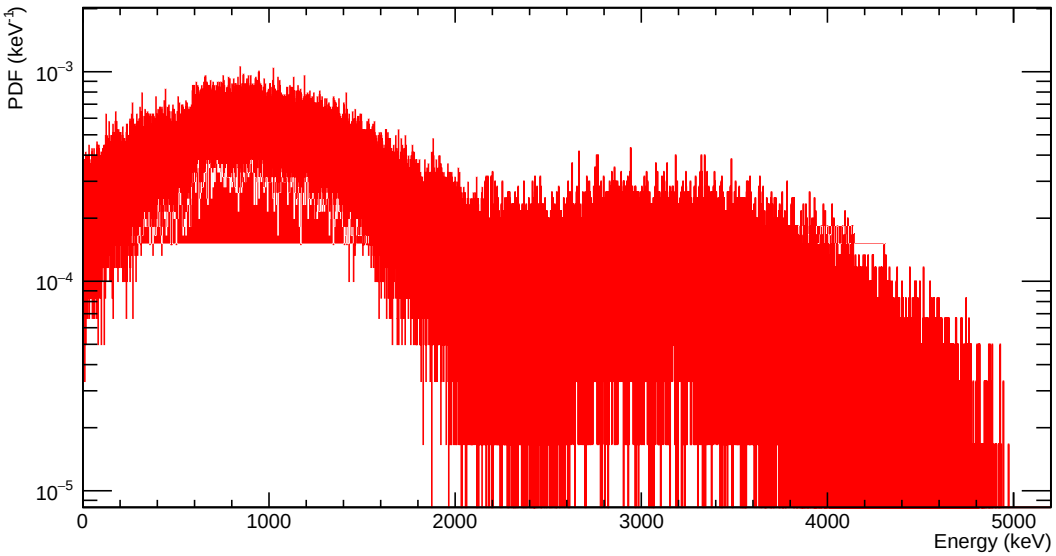

Figure A.44.: Decay of ^{208}Tl inside the $CaWO_4$ crystal. Detector response function is not applied.

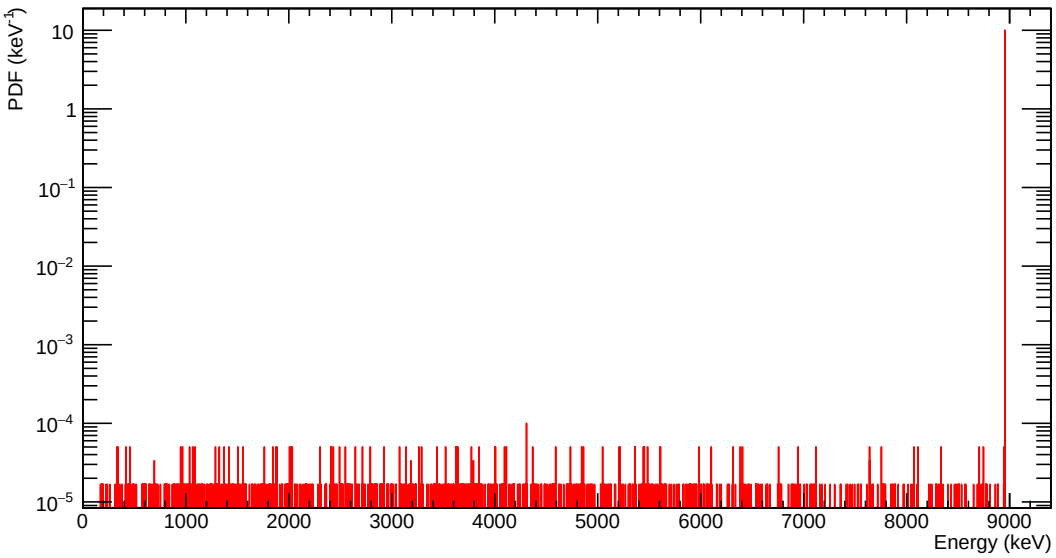

Figure A.45.: Decay of ^{212}Po inside the $CaWO_4$ crystal. Detector response function is not applied.

A.3. Simulated Templates of Internal Cosmogenic Backgrounds

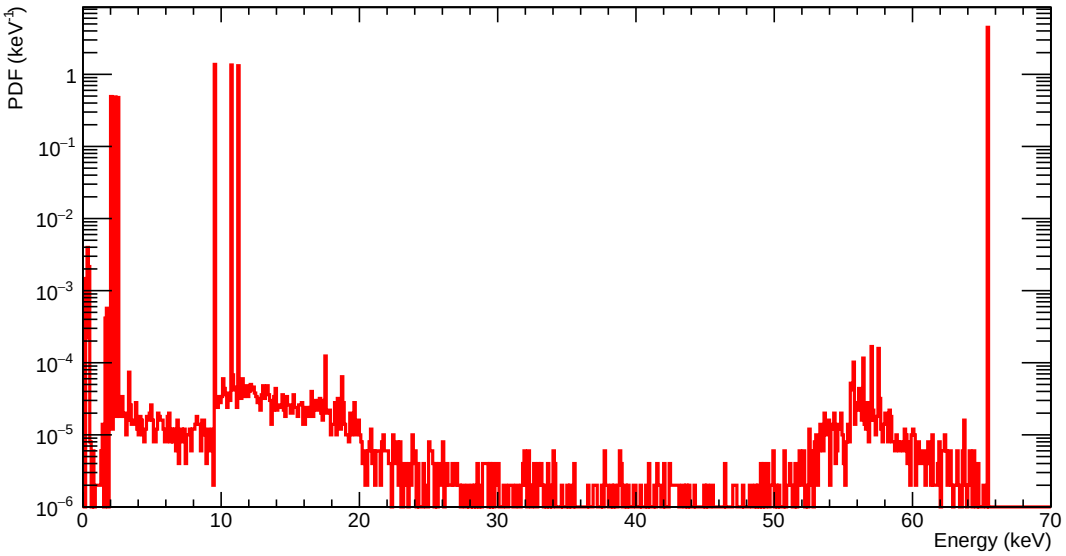

Figure A.46.: Decay of ^{179}Ta inside the $CaWO_4$ crystal. Detector response function is not applied.

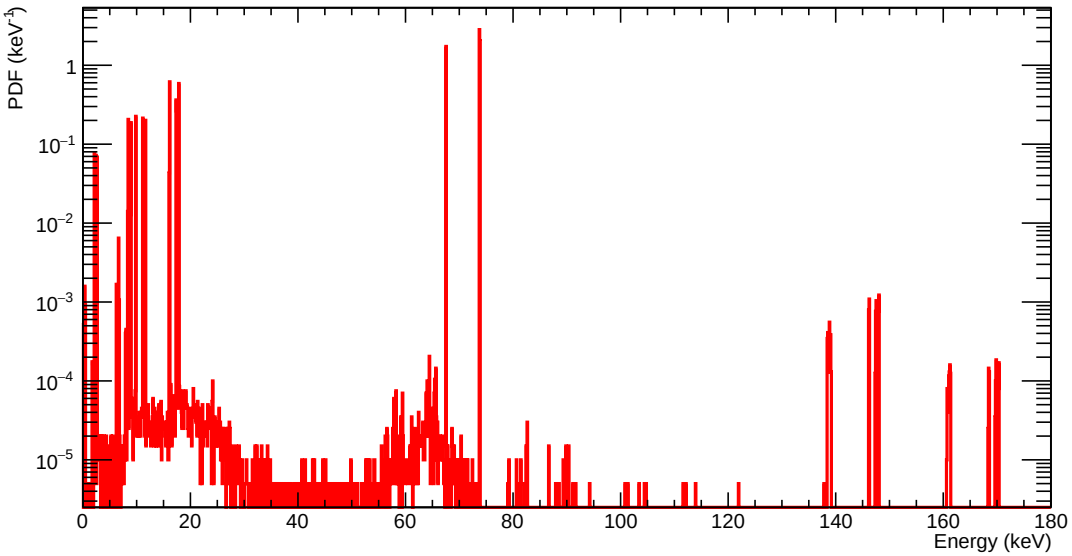

Figure A.47.: Decay of ^{181}W inside the $CaWO_4$ crystal. Detector response function is not applied.

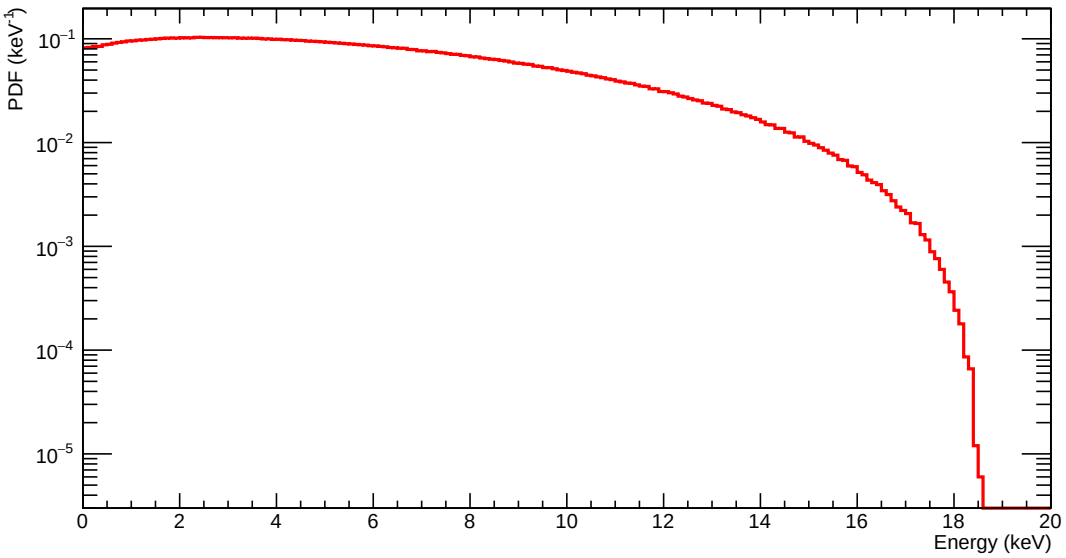

Figure A.48.: Decay of ^{3}H inside the $CaWO_4$ crystal. Detector response function is not applied.

A.4. Simulated Templates of Near External Radiogenic Backgrounds

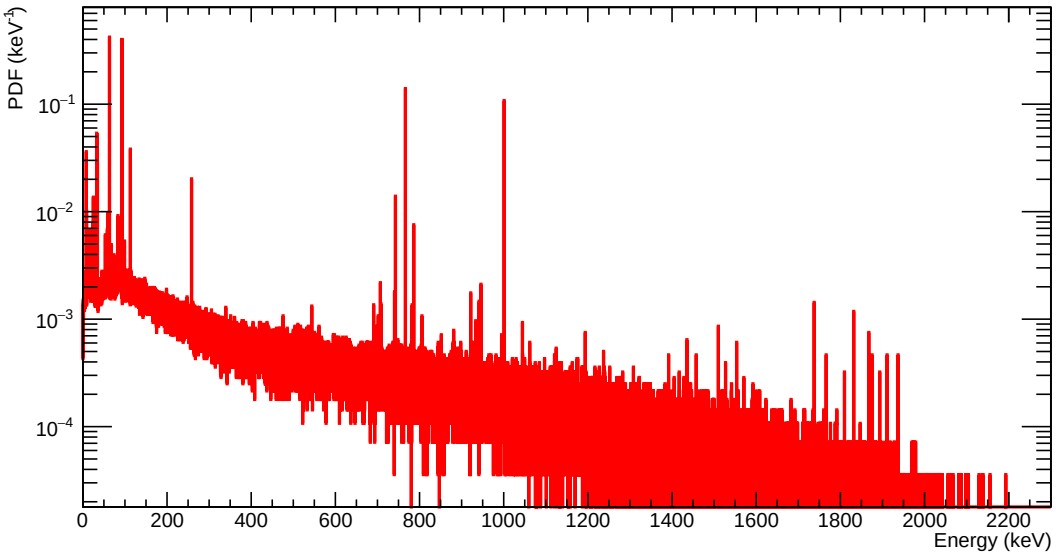

Figure A.49.: Decay of ^{234}Th inside the copper holder part "Stäbchenring". Detector response function is not applied.

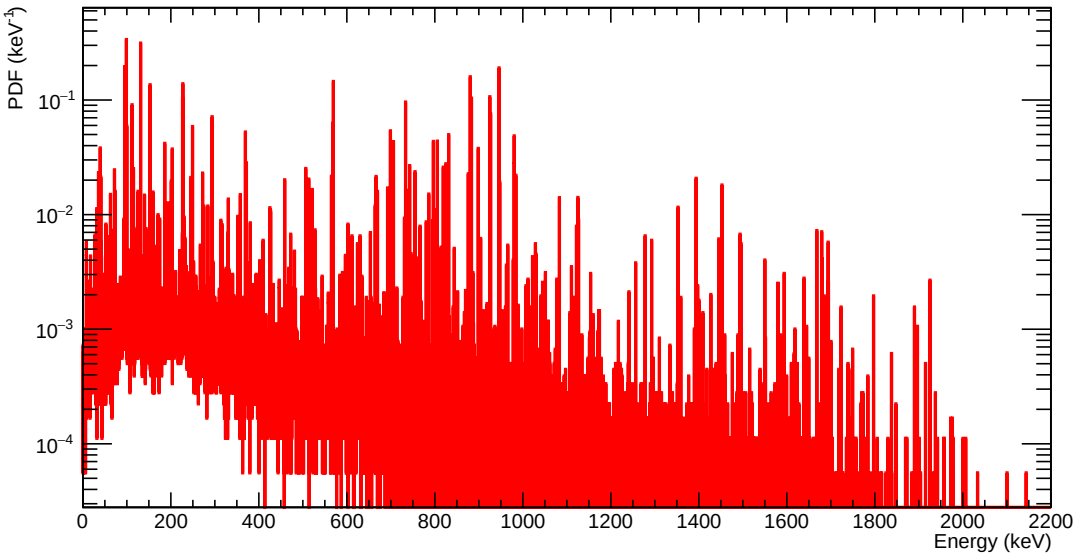

Figure A.50.: Decay of ^{234}Pa inside the copper holder part "Stäbchenring". Detector response function is not applied.

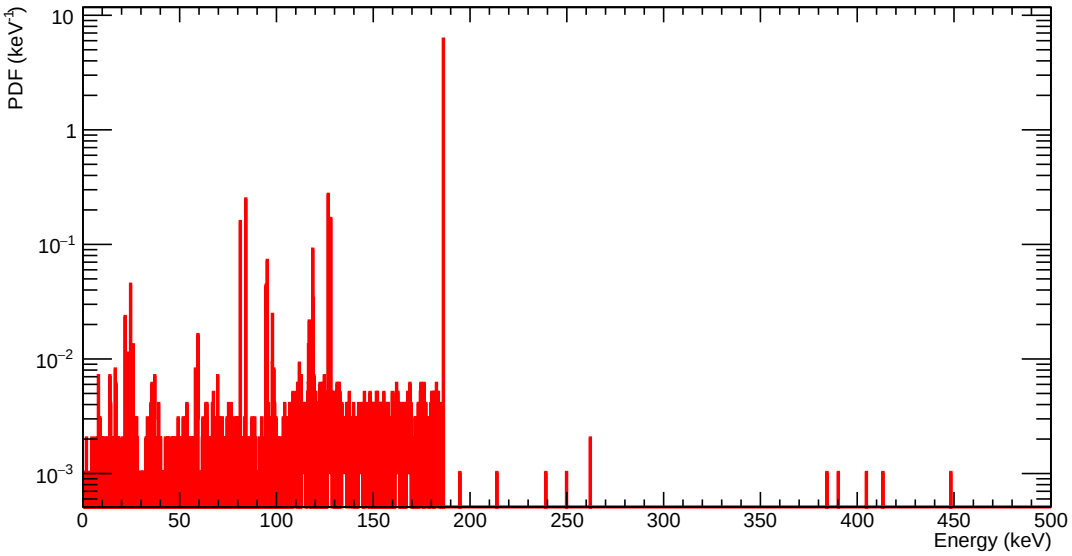

Figure A.51.: Decay of ^{226}Ra inside the copper holder part "Stäbchenring". Detector response function is not applied.

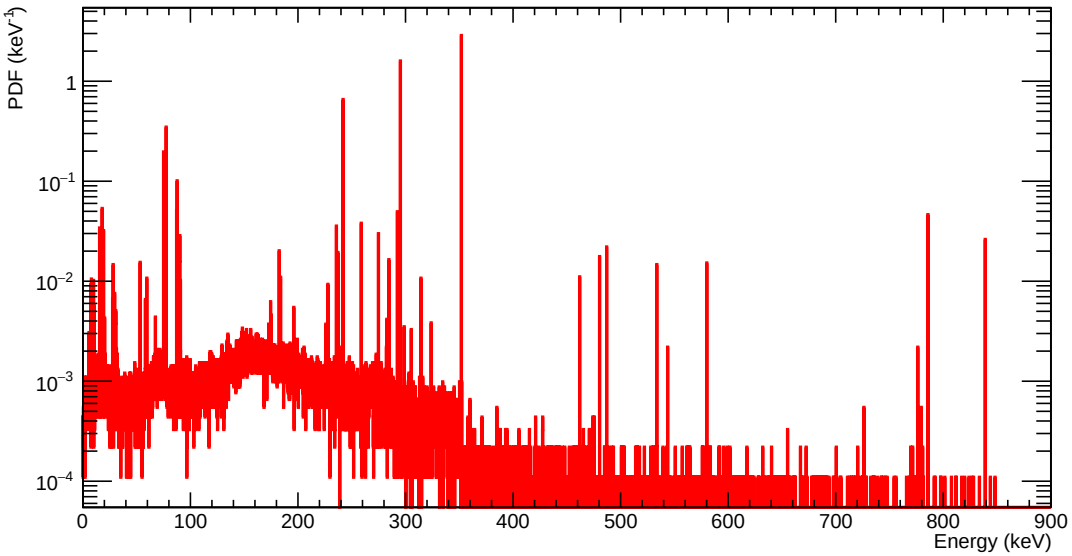

Figure A.52.: Decay of ^{214}Pb inside the copper holder part "Stäbchenring". Detector response function is not applied.

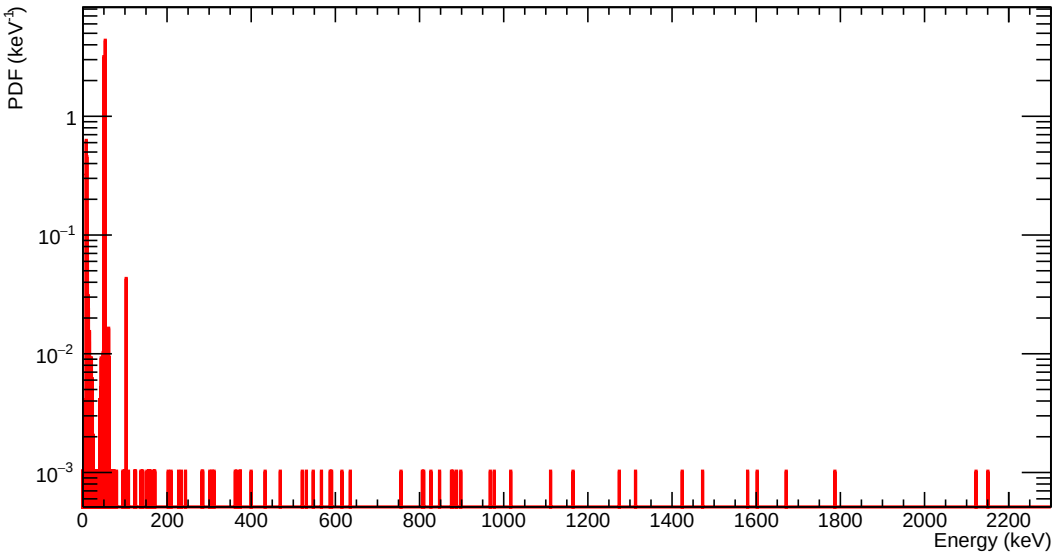

Figure A.53.: Decay of ^{218}At inside the copper holder part "Stäbchenring". Detector response function is not applied.

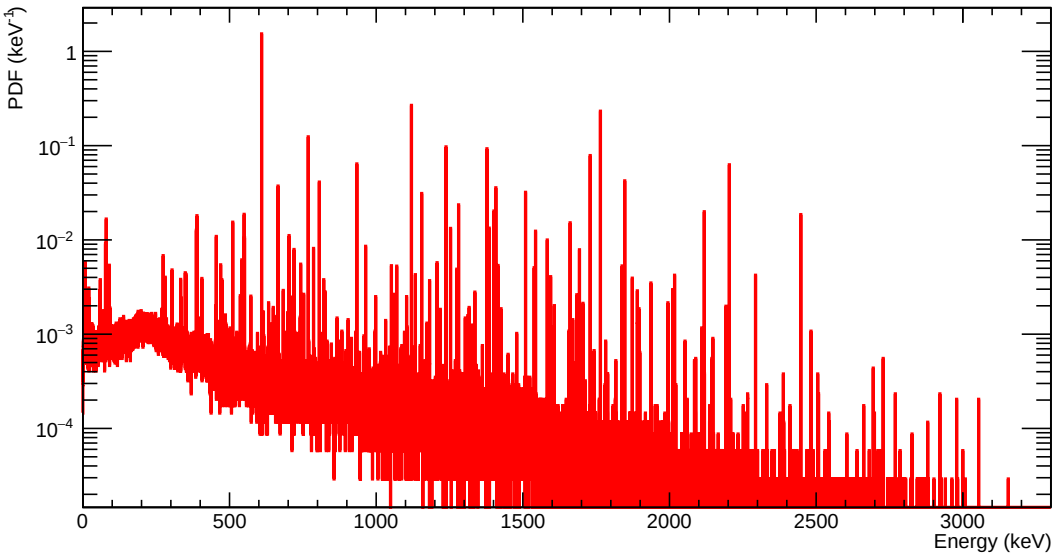

Figure A.54.: Decay of ^{214}Bi inside the copper holder part "Stäbchenring". Detector response function is not applied.

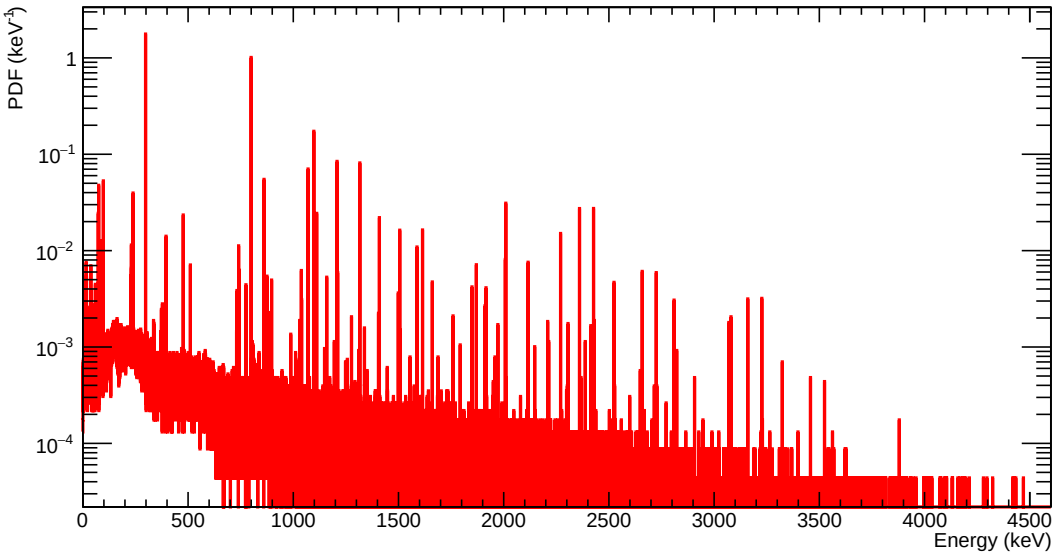

Figure A.55.: Decay of ^{210}Tl inside the copper holder part "Stäbchenring". Detector response function is not applied.

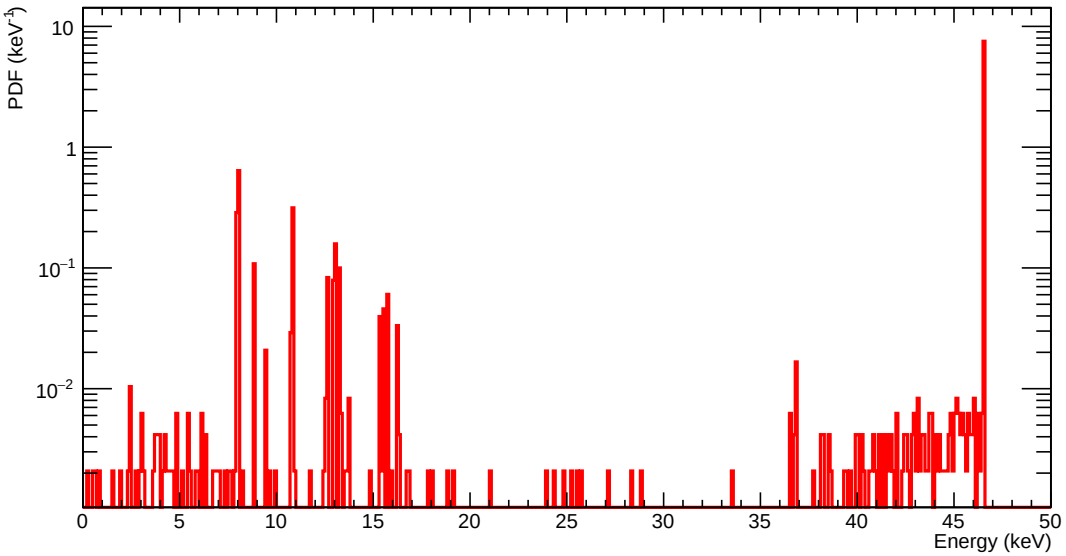

Figure A.56.: Decay of ^{210}Pb inside the copper holder part "Stäbchenring". Detector response function is not applied.

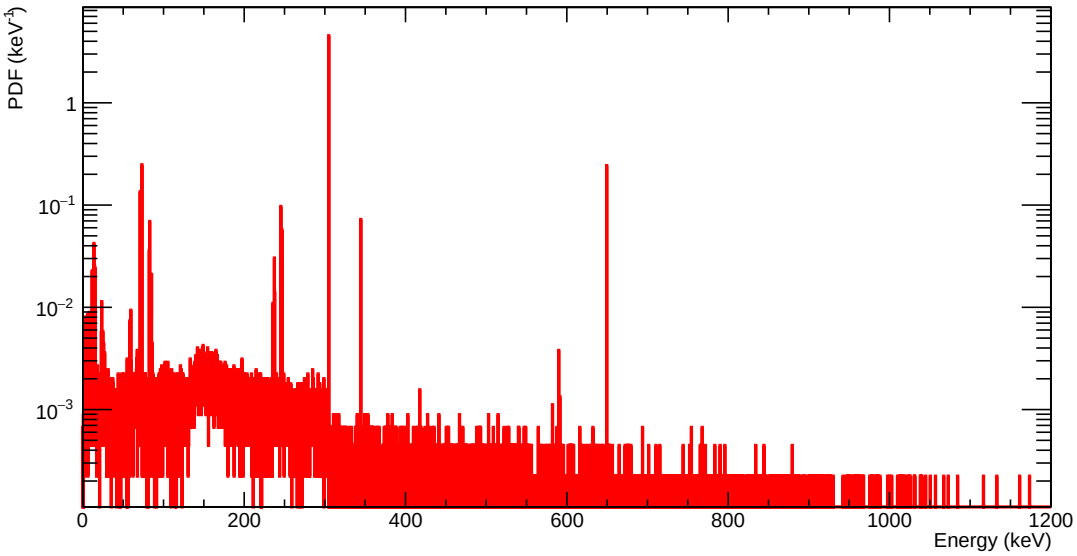

Figure A.57.: Decay of ^{206}Hg inside the copper holder part "Stäbchenring". Detector response function is not applied.

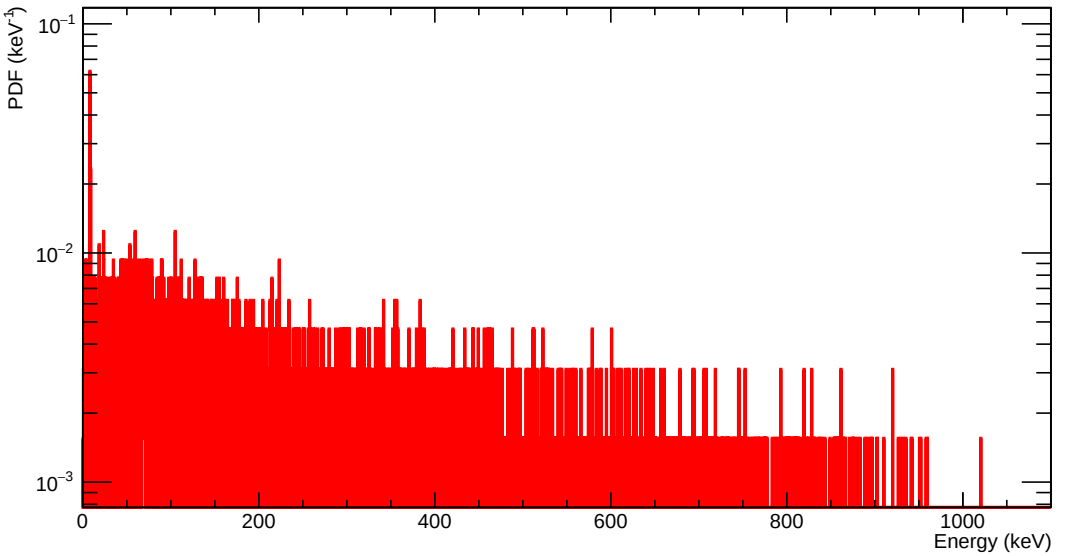

Figure A.58.: Decay of ^{210}Bi inside the copper holder part "Stäbchenring". Detector response function is not applied.

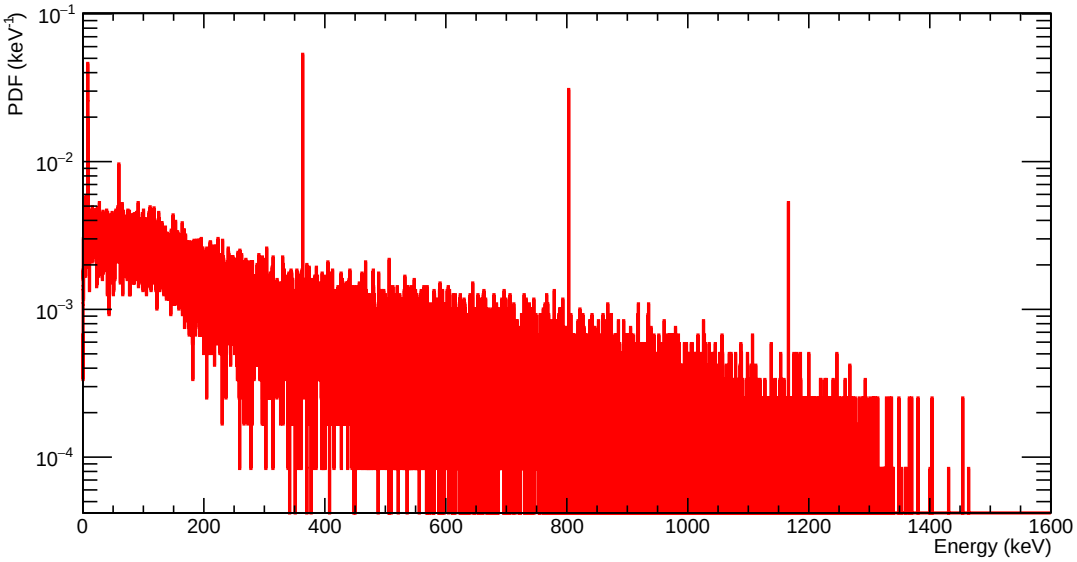

Figure A.59.: Decay of ^{206}Tl inside the copper holder part "Stäbchenring". Detector response function is not applied.

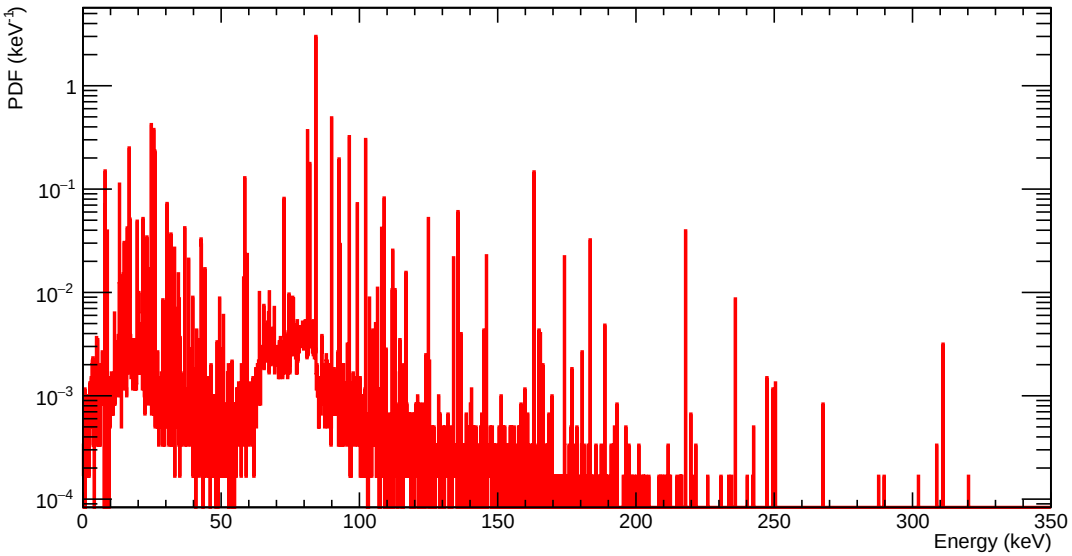

Figure A.60.: Decay of ^{231}Th inside the copper holder part "Stäbchenring". Detector response function is not applied.

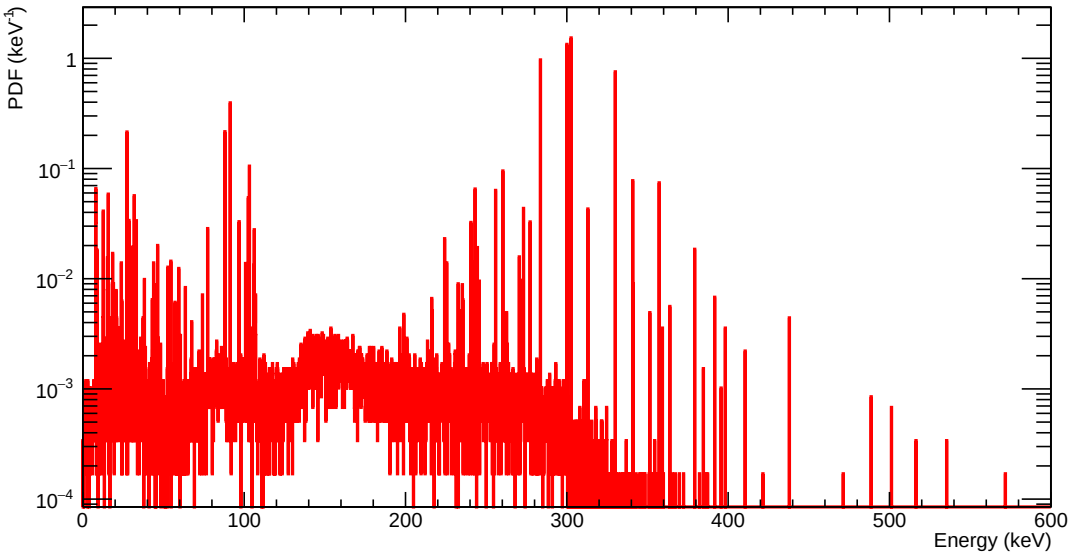

Figure A.61.: Decay of ^{231}Pa inside the copper holder part "Stäbchenring". Detector response function is not applied.

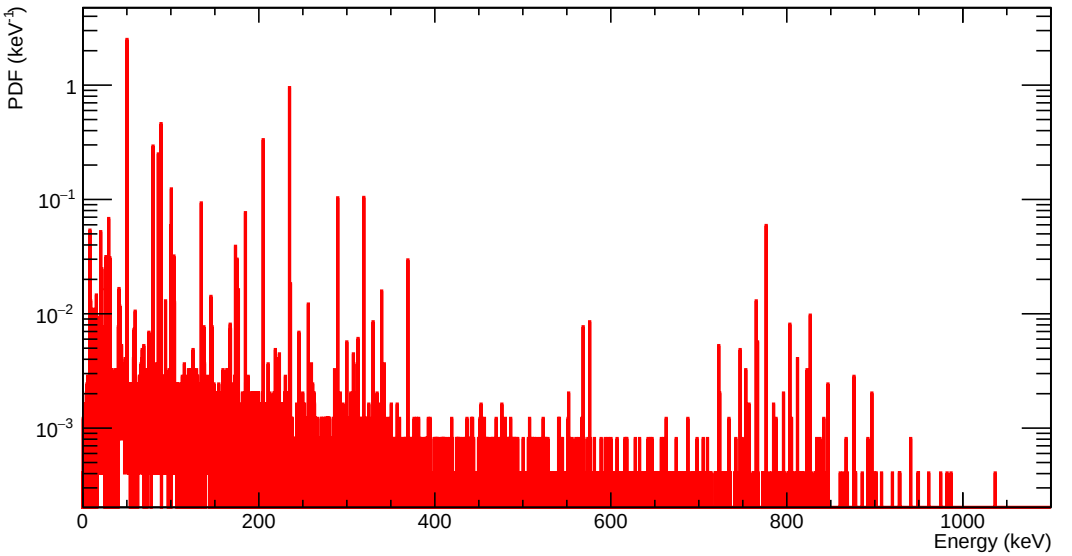

Figure A.62.: Decay of ^{223}Fr inside the copper holder part "Stäbchenring". Detector response function is not applied.

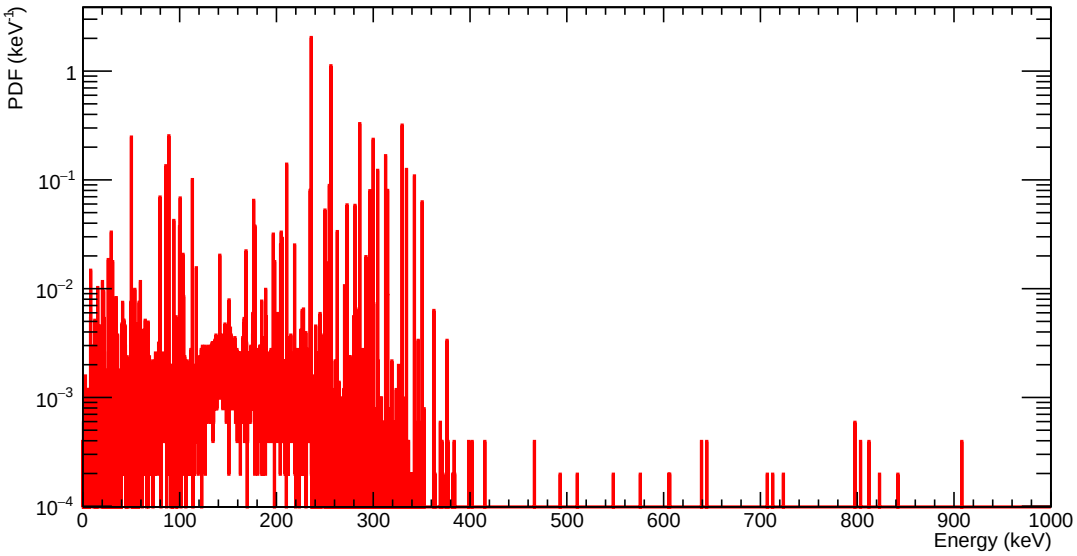

Figure A.63.: Decay of ^{227}Th inside the copper holder part "Stäbchenring". Detector response function is not applied.

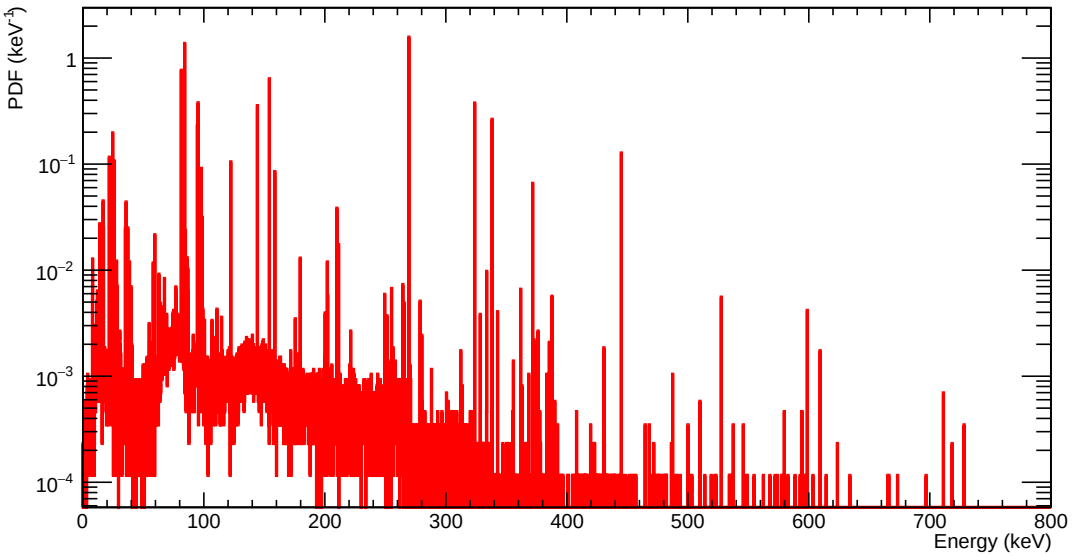

Figure A.64.: Decay of ^{223}Ra inside the copper holder part "Stäbchenring". Detector response function is not applied.

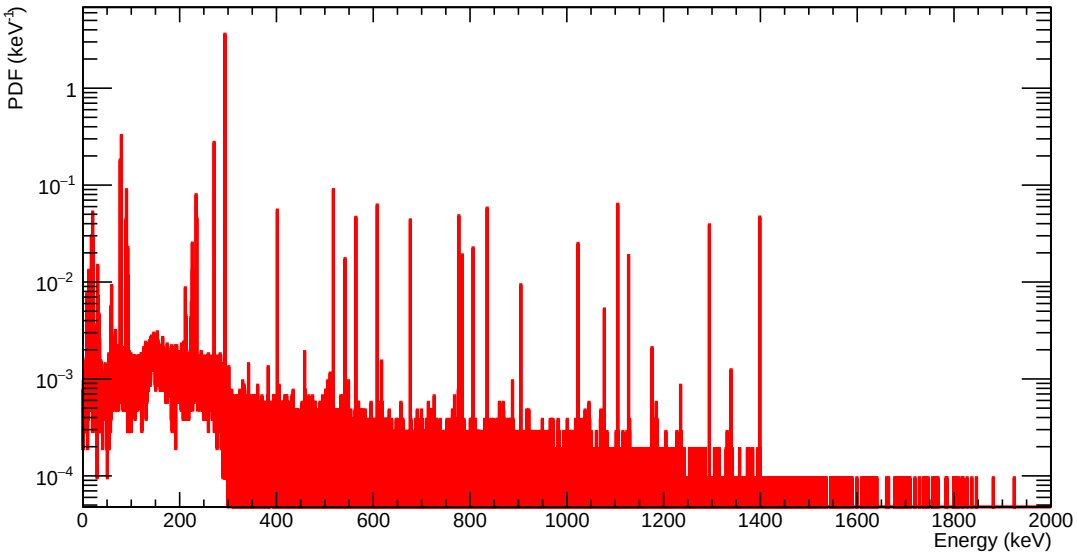

Figure A.65.: Decay of ^{215}Bi inside the copper holder part "Stäbchenring". Detector response function is not applied.

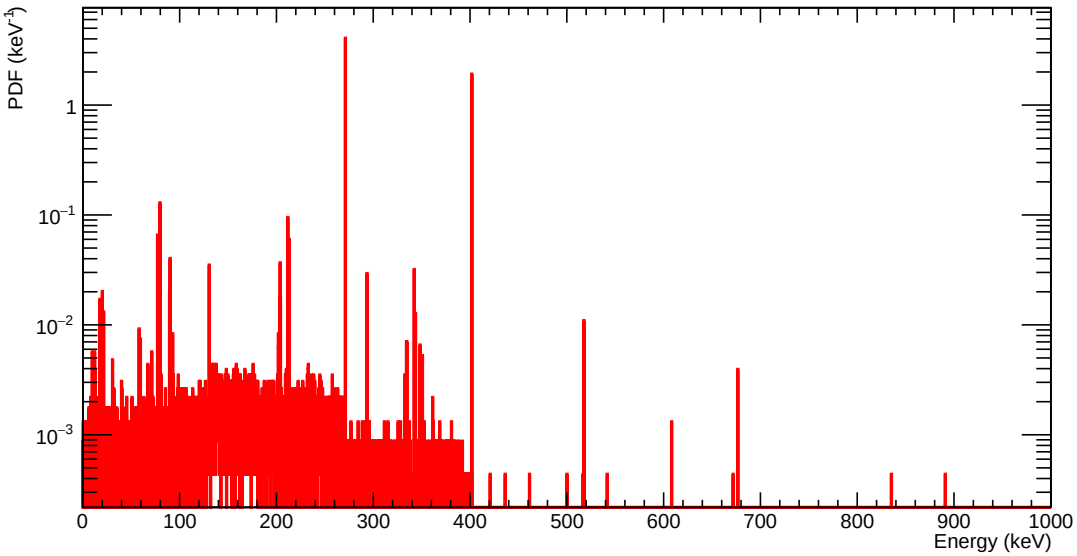

Figure A.66.: Decay of ^{219}Rn inside the copper holder part "Stäbchenring". Detector response function is not applied.

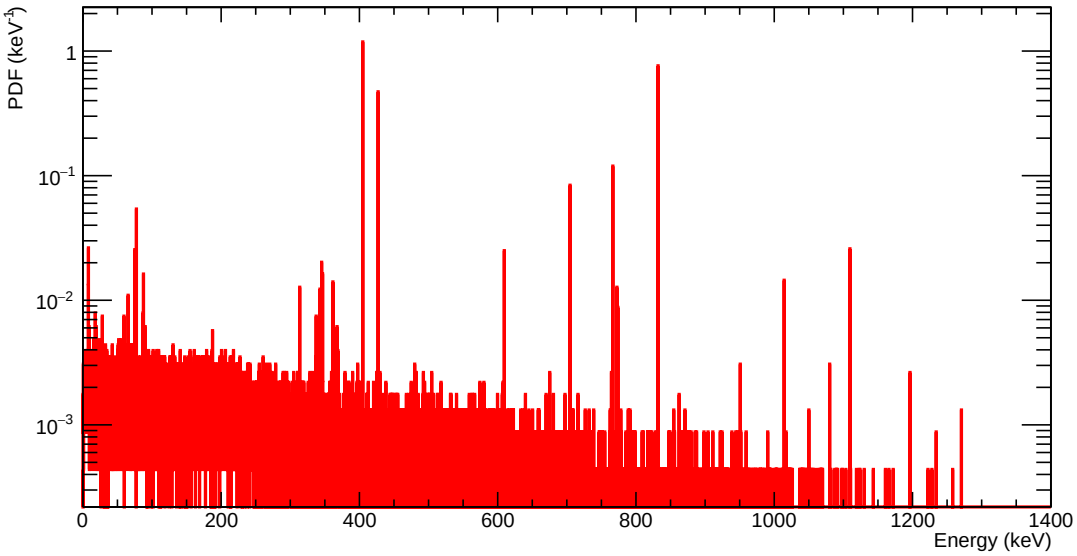

Figure A.67.: Decay of ^{211}Pb inside the copper holder part "Stäbchenring". Detector response function is not applied.

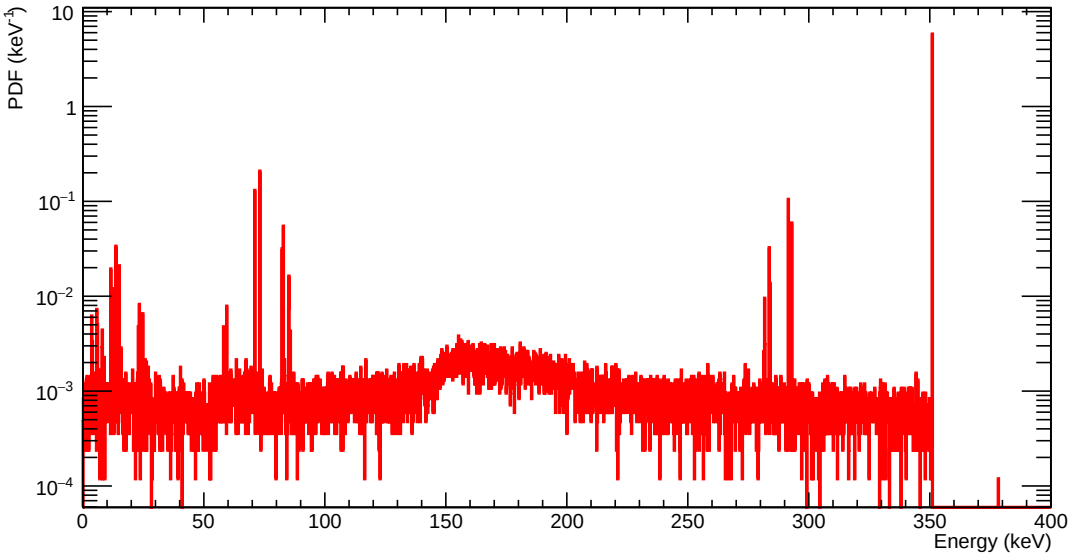

Figure A.68.: Decay of ^{211}Bi inside the copper holder part "Stäbchenring". Detector response function is not applied.

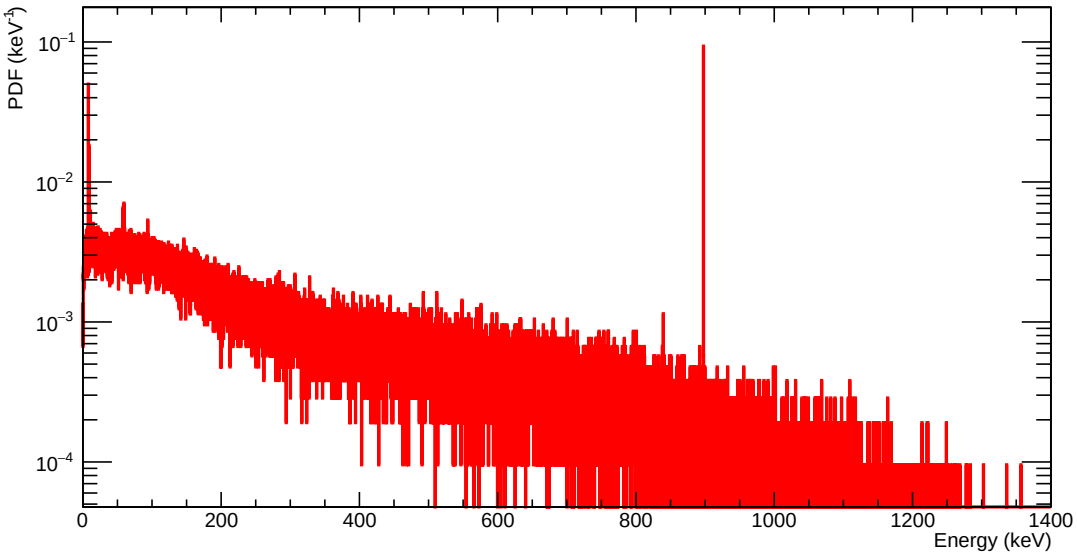

Figure A.69.: Decay of ^{207}Tl inside the copper holder part "Stäbchenring". Detector response function is not applied.

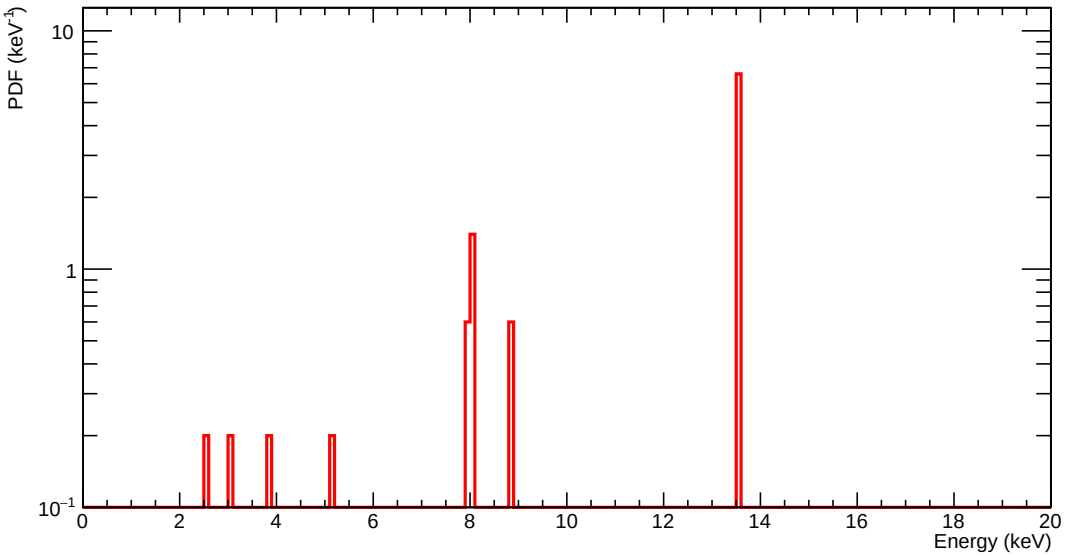

Figure A.70.: Decay of ^{228}Ra inside the copper holder part "Stäbchenring". Detector response function is not applied.

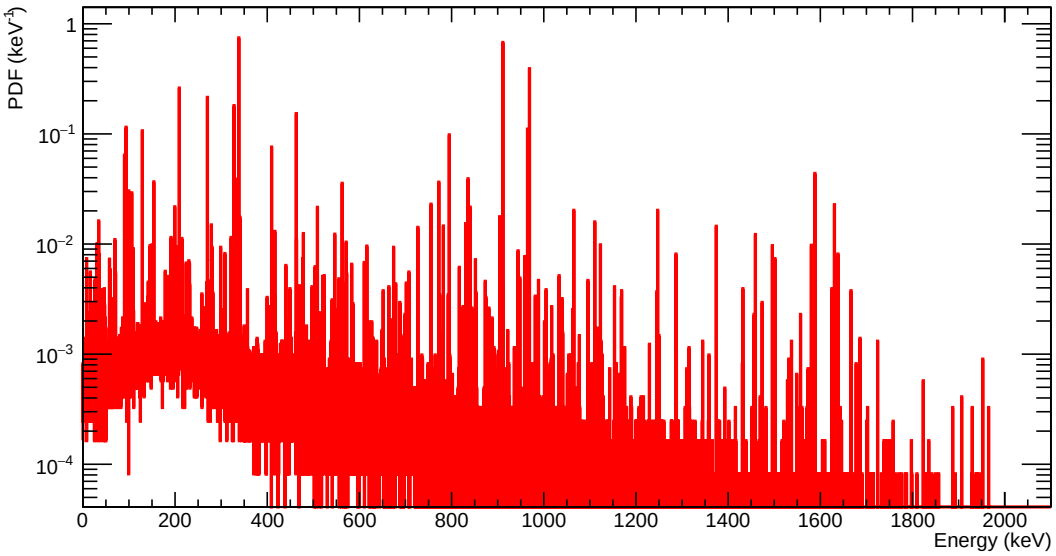

Figure A.71.: Decay of ^{228}Ac inside the copper holder part "Stäbchenring". Detector response function is not applied.

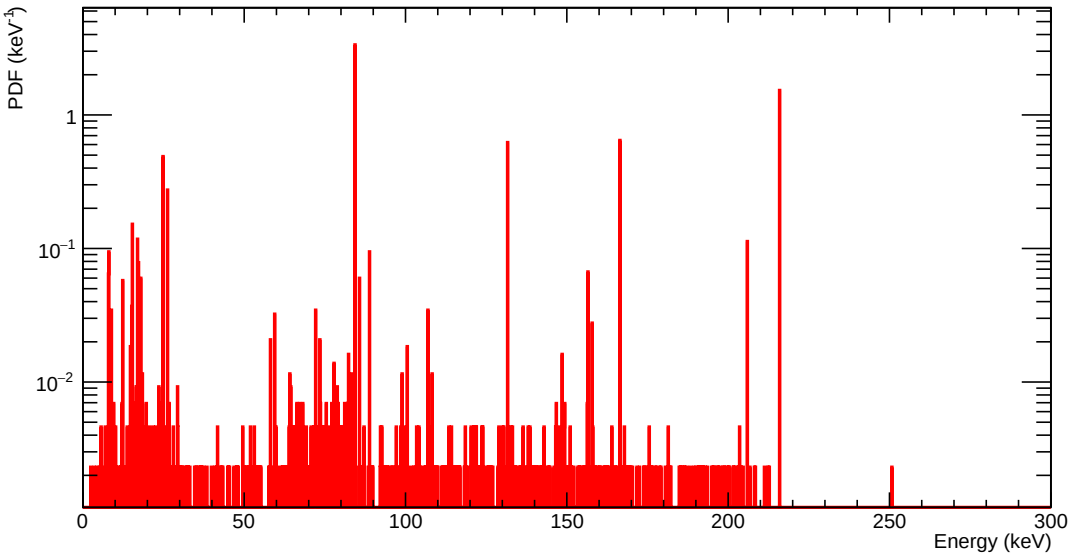

Figure A.72.: Decay of ^{228}Th inside the copper holder part "Stäbchenring". Detector response function is not applied.

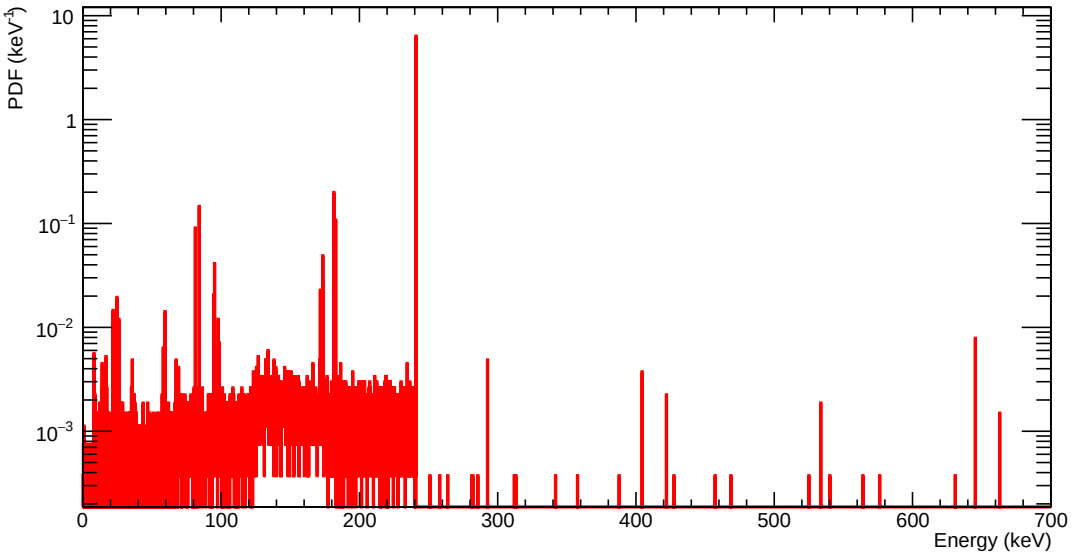

Figure A.73.: Decay of ^{224}Ra inside the copper holder part "Stäbchenring". Detector response function is not applied.

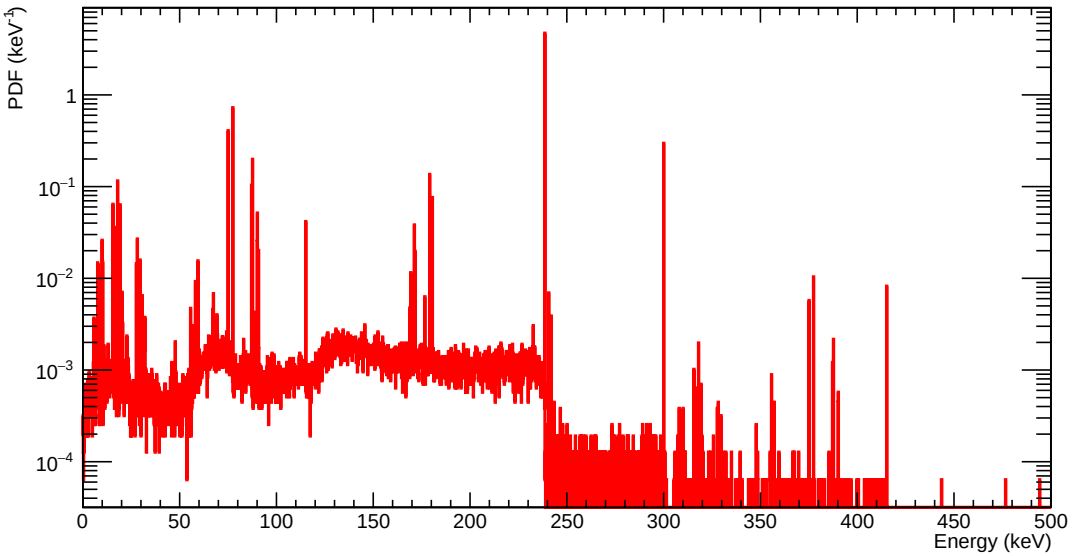

Figure A.74.: Decay of ^{212}Pb inside the copper holder part "Stäbchenring". Detector response function is not applied.

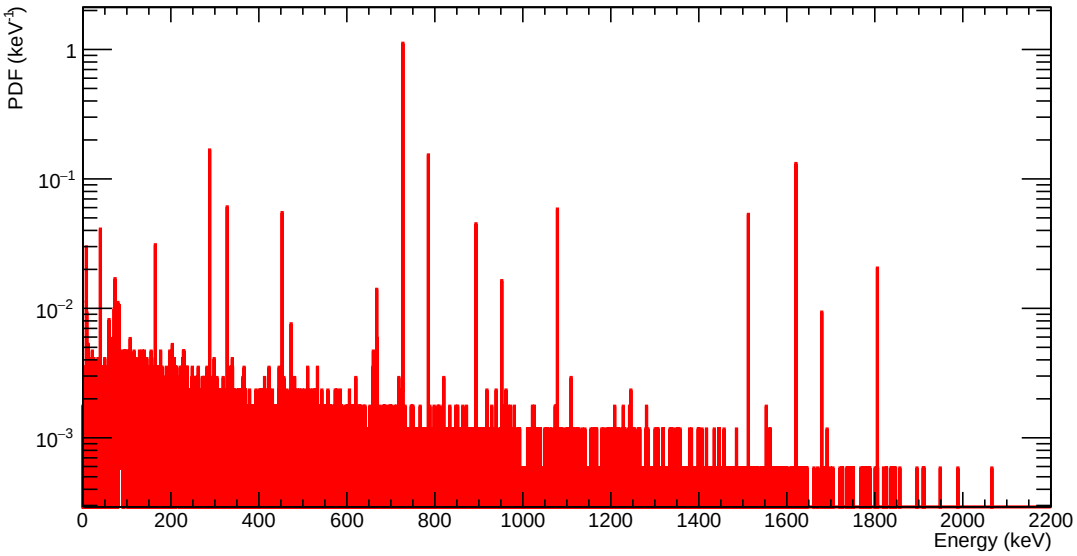

Figure A.75.: Decay of ^{212}Bi inside the copper holder part "Stäbchenring". Detector response function is not applied.

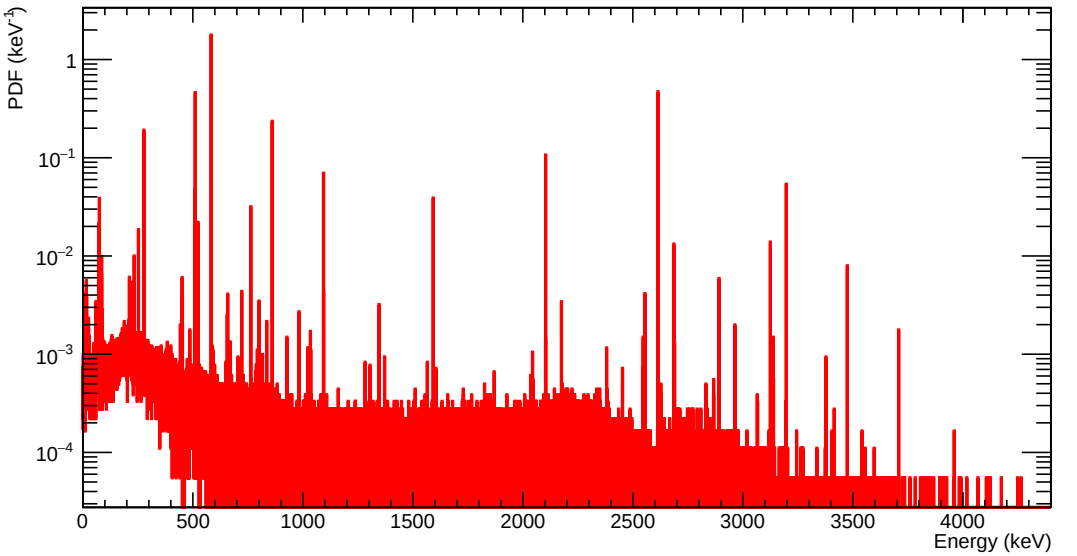

Figure A.76.: Decay of ^{208}Tl inside the copper holder part "Stäbchenring". Detector response function is not applied.

A.5. Simulated Templates of Distant External Radiogenic Backgrounds

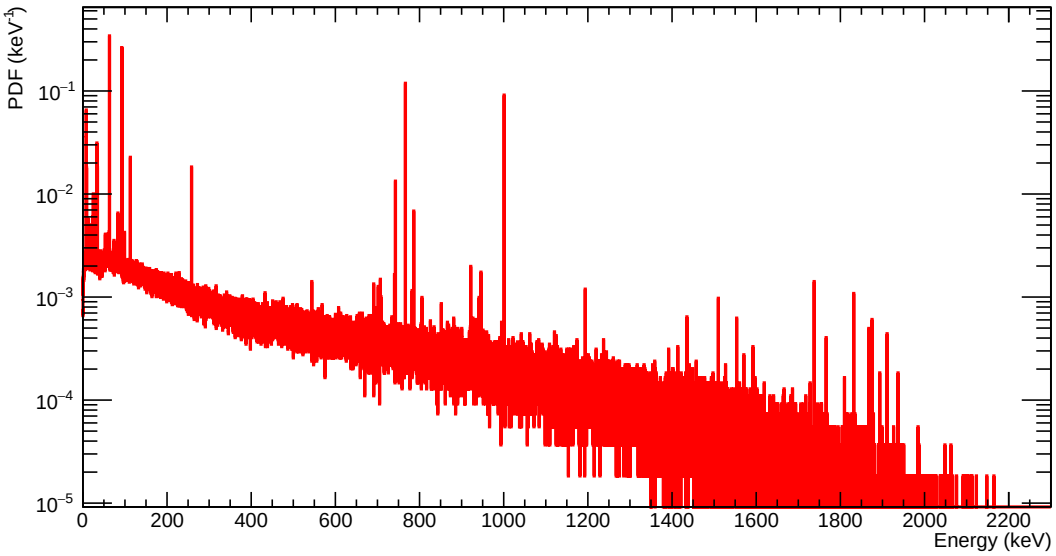

Figure A.77.: Decay of ^{234}Th inside the copper sphere. Detector response function is not applied.

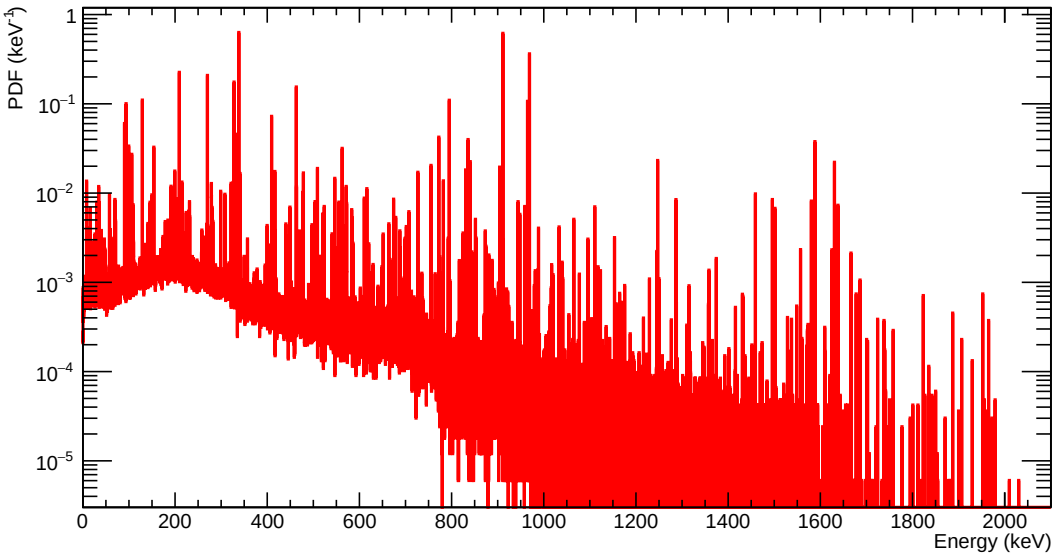

Figure A.78.: Decay of ^{228}Ac inside the copper sphere. Detector response function is not applied.

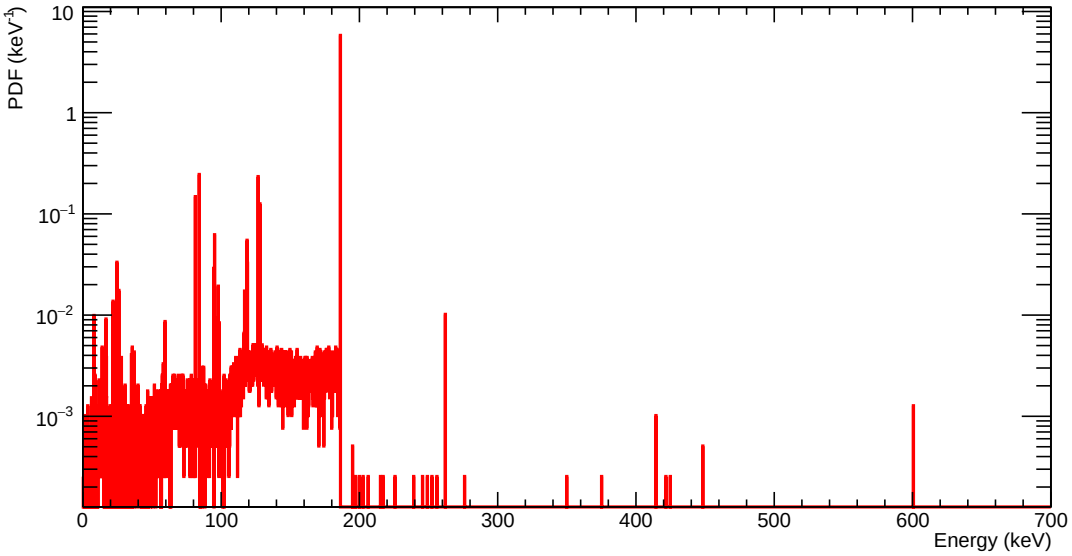

Figure A.79.: Decay of ^{226}Ra inside the copper sphere. Detector response function is not applied.

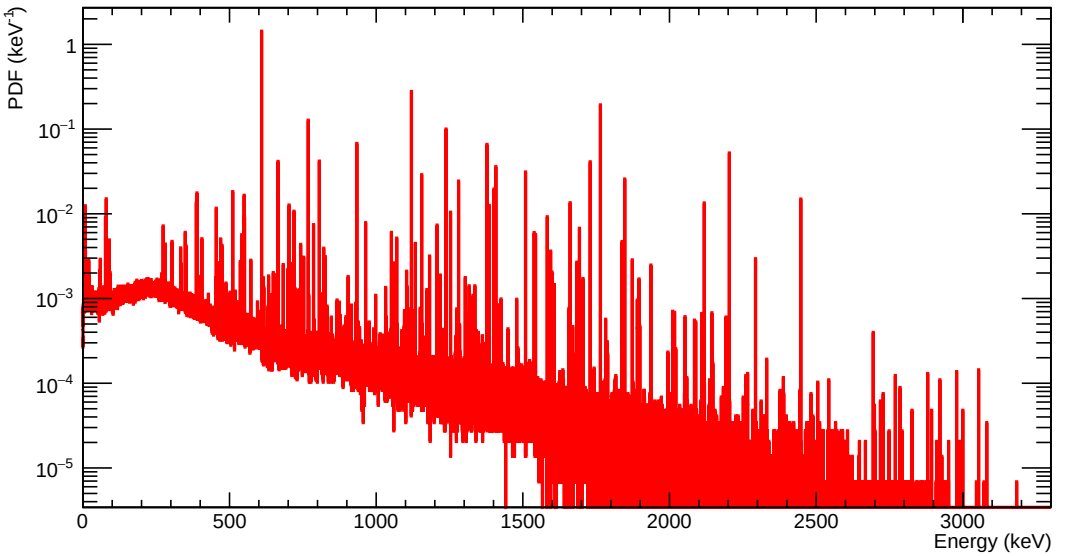

Figure A.80.: Decay of ^{214}Bi inside the copper sphere. Detector response function is not applied.

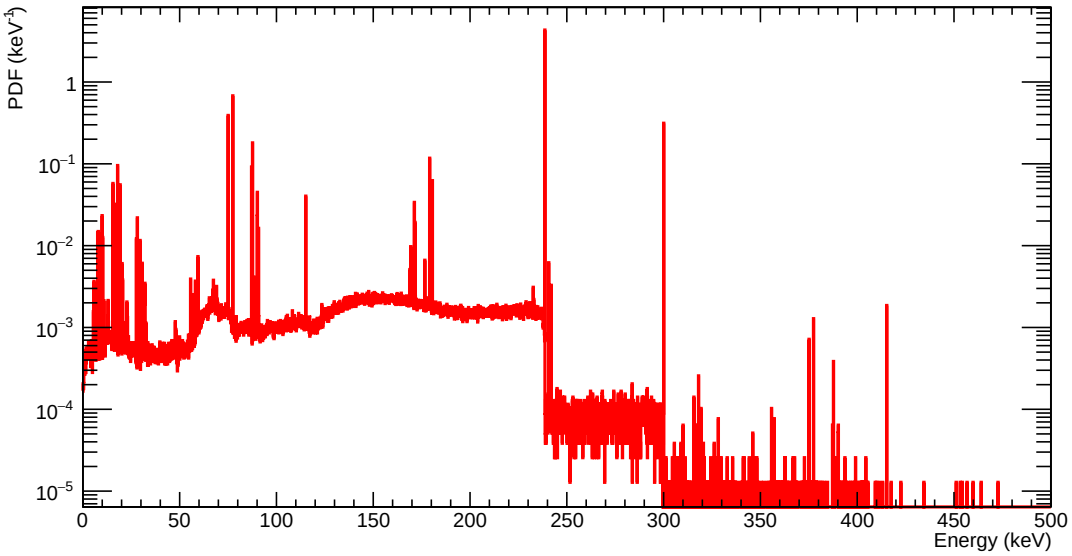

Figure A.81.: Decay of ^{212}Pb inside the copper sphere. Detector response function is not applied.

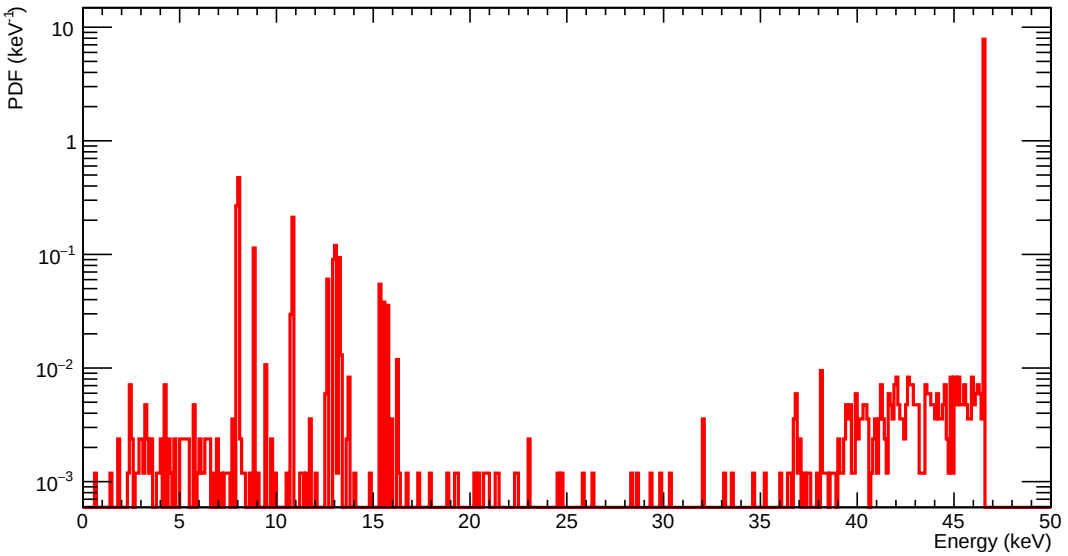

Figure A.82.: Decay of ^{210}Pb inside the copper sphere. Detector response function is not applied.

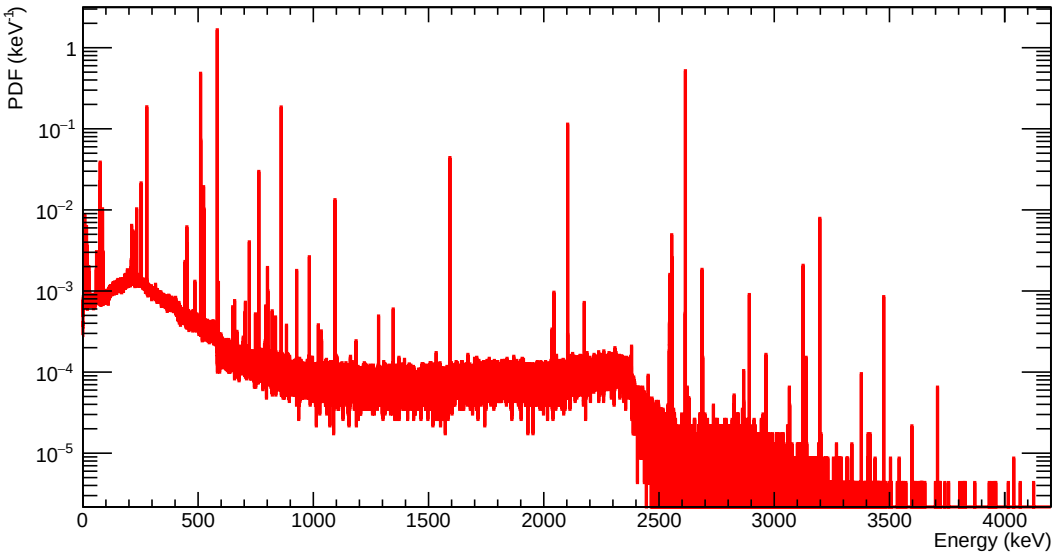

Figure A.83.: Decay of ^{208}Tl inside the copper sphere. Detector response function is not applied.

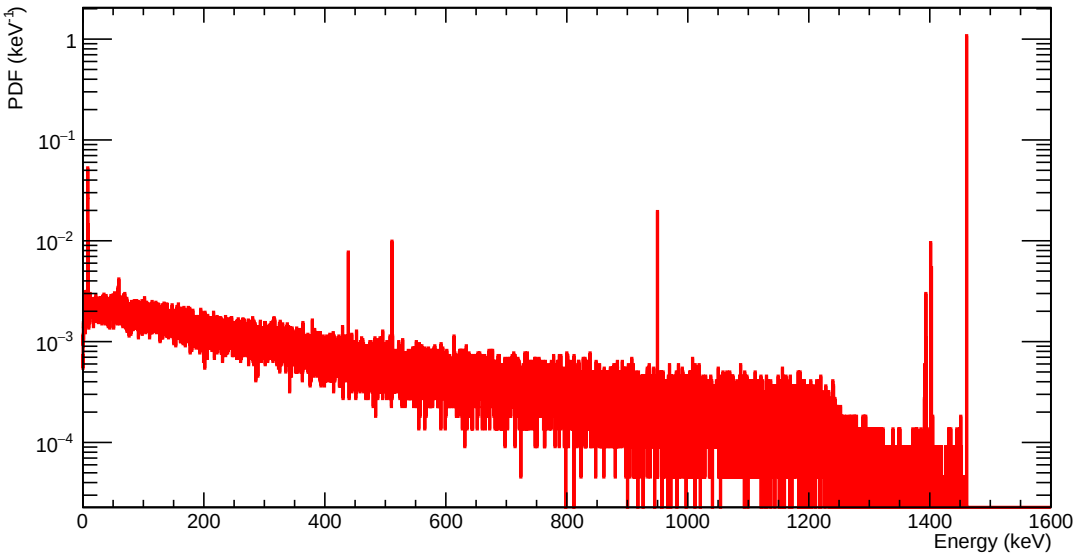

Figure A.84.: Decay of ^{40}K inside the copper sphere. Detector response function is not applied.

A.6. Comparison of Observed Peak Positions with Literature

The following table shows all the identified lines in the TUM40 data (X-ray, gamma and alpha), their energies obtained from the fits to the data, corresponding literature values and the relative difference between experimental[1] and literature values. The footnotes correspond to:

- **a:** Uncertainties might be as large as 10 or 20 eV [56]. For this work, we used the highest possible uncertainty, which is 20 eV.
- **b:** This decay consists of an X-ray and a gamma emission. Only a partial uncertainty is given for this decay in literature [56] that corresponds to the X-ray emission and it is 20 eV. In this work, this value is used as uncertainty of the combined emission of X-ray and gamma.
- **c:** These alpha peaks (^{234}U/^{226}Ra and ^{218}Po/^{227}Th) coincide with each other in the recoil energy spectrum and they cannot be disentangled to be fitted with individual Gaussian functions. Hence, their activities are obtained from the knowledge of secular equilibrium inside their corresponding decay chain. Because of this, these four nuclides don't have any experimental energy values.

[1] The fits were performed on low and medium energy reference data sets after the rescaling functions mentioned in section 3.7.1 and section 3.7.2 were applied.

Table A.1.: Lines corresponding to X-ray and gamma emissions, and alpha decays observed in the TUM40 data. The literature values of the energies of these lines are given along with the mean values of the peaks obtained through fitting.

Source	**Decay Type**	E_{Lit} **(keV)**	E_{Exp} **(keV)**	$\frac{E_{Exp}-E_{Lit}}{E_{Lit}}$
^{179}Ta (M1)	EC	2.601 ± 0.002 [a]	2.620 ± 0.007	-0.008 ± 0.008
^{179}Ta (L2)	EC	10.739 ± 0.002 [a]	10.83 ± 0.02	-0.009 ± 0.003
^{179}Ta (L1)	EC	11.271 ± 0.002 [a]	11.333 ± 0.004	-0.006 ± 0.002
^{210}Pb	γ	46.539 ± 0.001	46.29 ± 0.01	0.0054 ± 0.0003
^{179}Ta (K)	EC	65.351 ± 0.002 [a]	64.990 ± 0.008	0.0054 ± 0.0003
^{181}W	EC	73.7 ± 0.002 [b]	73.46 ± 0.05	0.0028 ± 0.0007
^{234}Th	γ	92.38 ± 0.01	92.18 ± 0.04	0.0022 ± 0.0004
^{226}Ra	γ	186.21 ± 0.01	185.61 ± 0.06	0.0032 ± 0.0002
^{212}Pb	γ	238.632 ± 0.002	239.77 ± 0.05	-0.0048 ± 0.0002
^{214}Bi	γ	609.320 ± 0.005	608.9 ± 0.1	0.0007 ± 0.0002
^{228}Ac	γ	968.97 ± 0.02	967.7 ± 0.2	0.0013 ± 0.0001
^{40}K	γ	1460.820 ± 0.005	1460.6 ± 0.3	0.0002 ± 0.0002
^{208}Tl	γ	2614.51 ± 0.01	2614.9 ± 0.3	0.0002 ± 0.0001
^{232}Th	α	4081.6 ± 1.4	4081.6 ± 0.9	-0.00001 ± 0.00040
^{238}U	α	4269.9 ± 2.1	4270.4 ± 0.1	-0.0001 ± 0.0005
^{235}U	α	4678.0 ± 0.7	4670.3 ± 0.7	0.0017 ± 0.0002
^{230}Th	α	4769.8 ± 1.5	4767.1 ± 1.0	0.0005 ± 0.0004
^{234}U	α	4857.5 ± 0.7	[c]	–
^{226}Ra	α	4870.7 ± 0.3	[c]	–
^{231}Pa	α	5149.9 ± 0.8	5141.6 ± 0.7	0.0016 ± 0.0002
^{210}Po	α	5407.53 ± 0.07	5402.7 ± 1.1	0.0009 ± 0.0002
^{228}Th	α	5520.2 ± 0.2	5520.6 ± 1.9	-0.00008 ± 0.00034
^{222}Rn	α	5590.4 ± 0.3	5590.5 ± 0.9	-0.00001 ± 0.00017
^{224}Ra	α	5788.9 ± 0.2	5789.9 ± 1.8	-0.0002 ± 0.0003
^{223}Ra	α	5979.0 ± 0.2	5970.1 ± 0.6	0.0015 ± 0.0001
^{218}Po	α	6114.75 ± 0.09	[c]	–
^{227}Th	α	6146.6 ± 0.1	[c]	–
^{220}Rn	α	6404.7 ± 0.1	6407.7 ± 2.4	-0.0005 ± 0.0004
^{211}Bi	α	6750.4 ± 0.5	6751.1 ± 0.5	-0.0001 ± 0.0001

A.7. Composition of the Background Sources

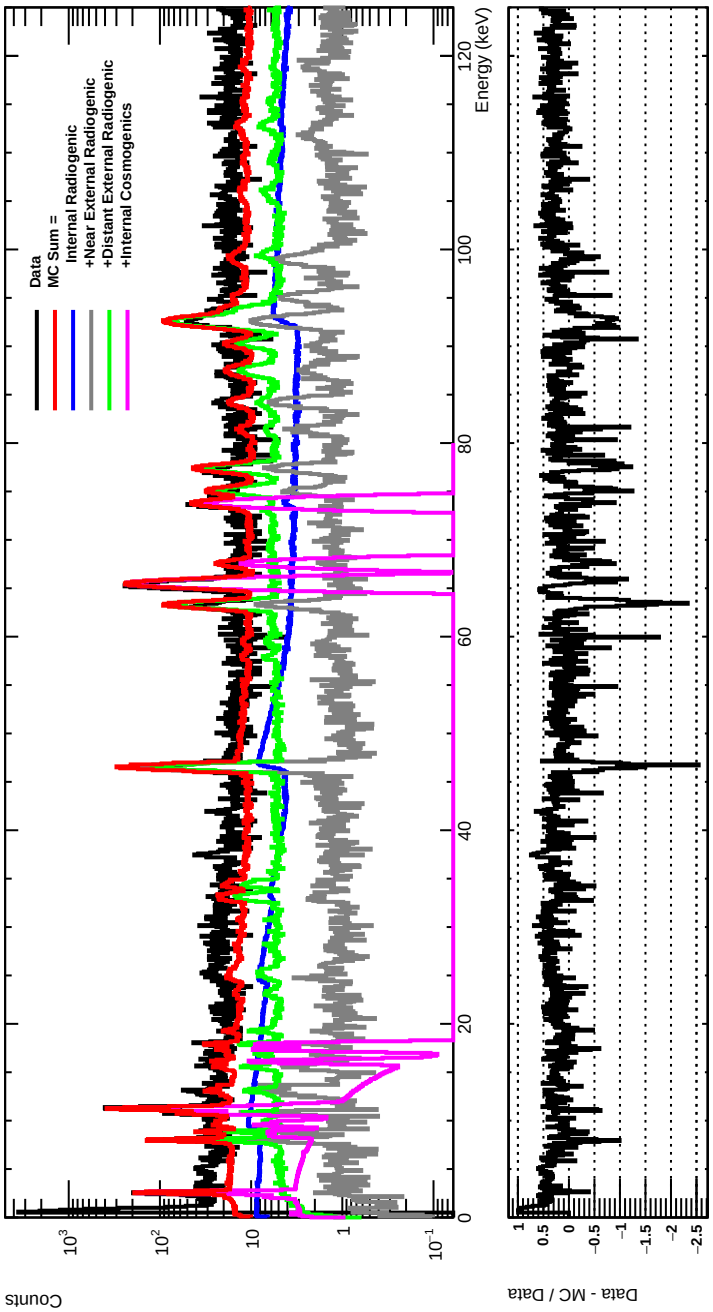

Figure A.85.: Top panel: individual background components and their sum compared to the low energy reference data set between 0 keV and 125 keV. Bottom panel: relative residual between simulation and data.

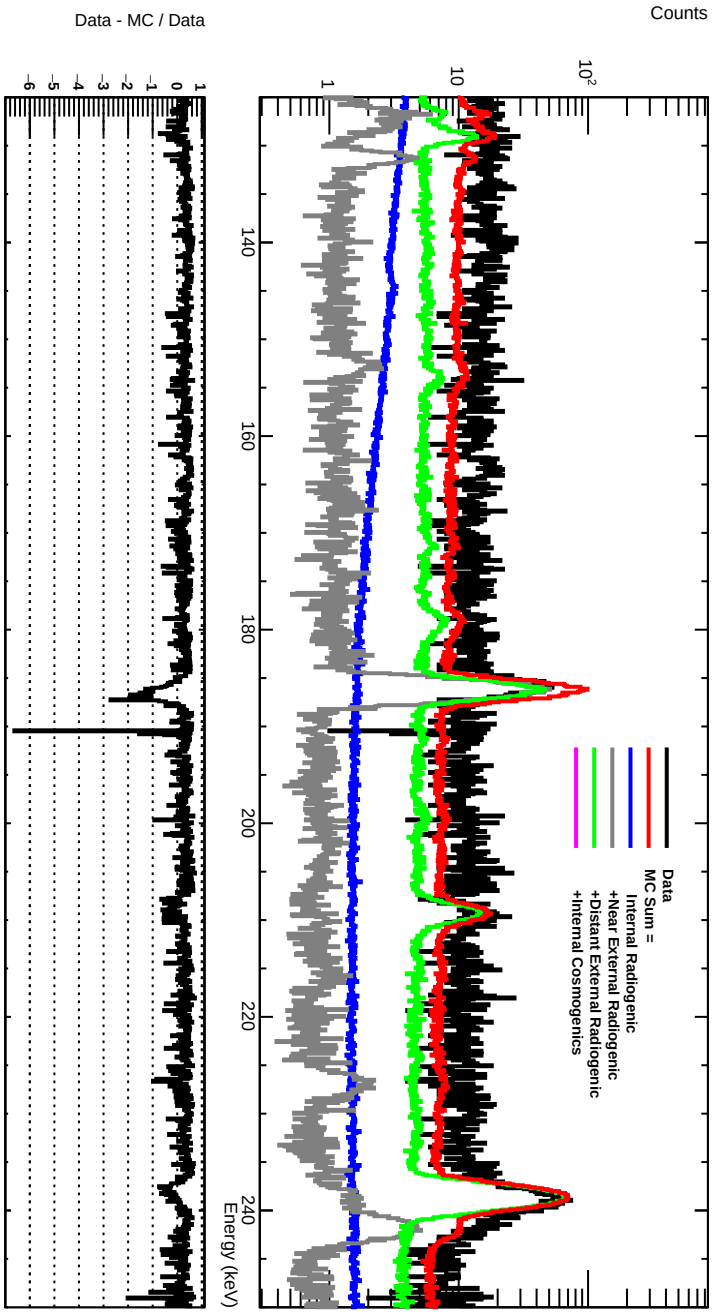

Figure A.86.: Top panel: individual background components and their sum compared to the low energy reference data set between 125 keV and 250 keV. Bottom panel: relative residual between simulation and data.

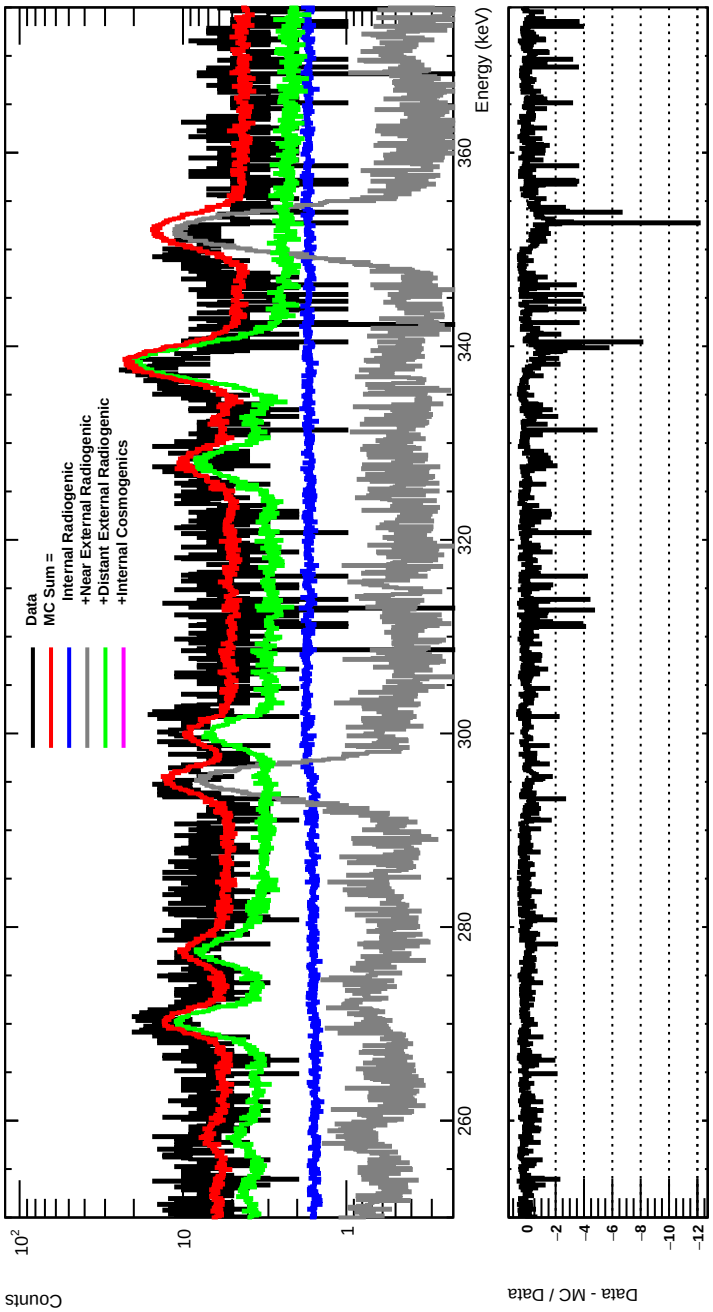

Figure A.87.: Top panel: individual background components and their sum compared to the low energy reference data set between 250 keV and 375 keV. Bottom panel: relative residual between simulation and data.

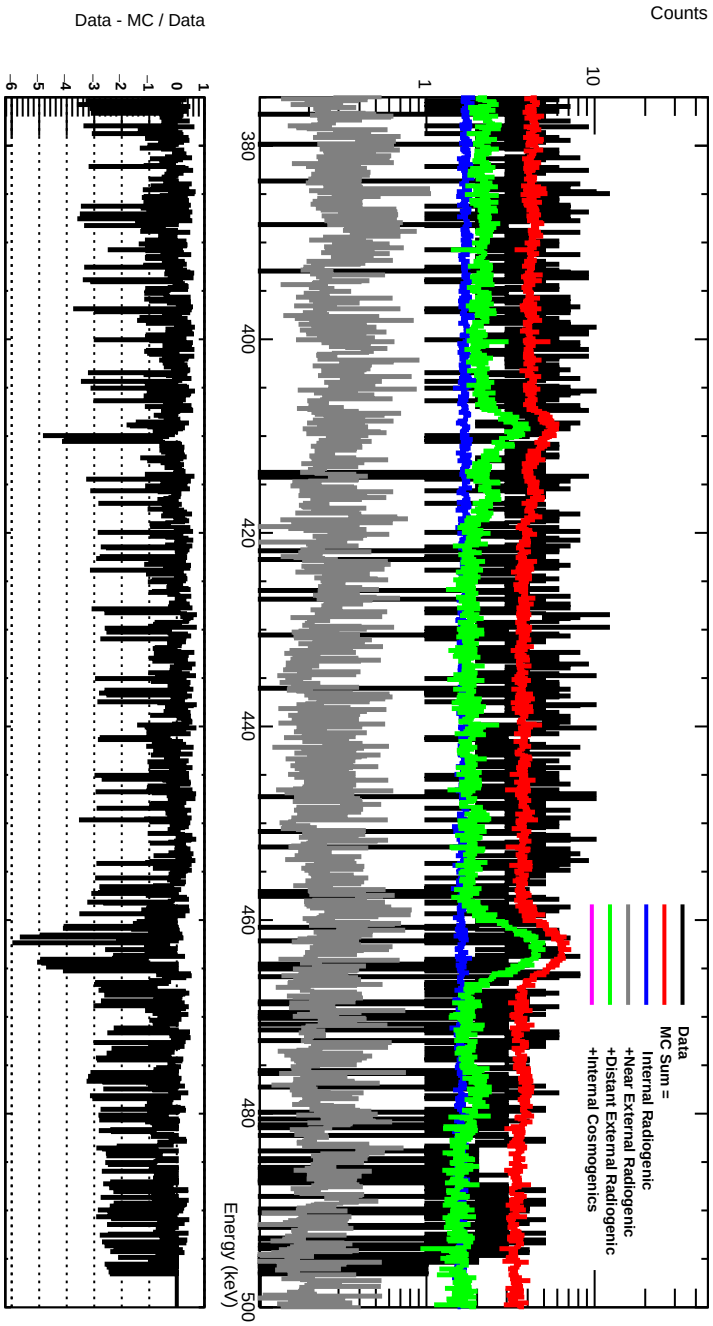

Figure A.88.: Top panel: individual background components and their sum compared to the low energy reference data set between 375 keV and 500 keV. Bottom panel: relative residual between simulation and data.

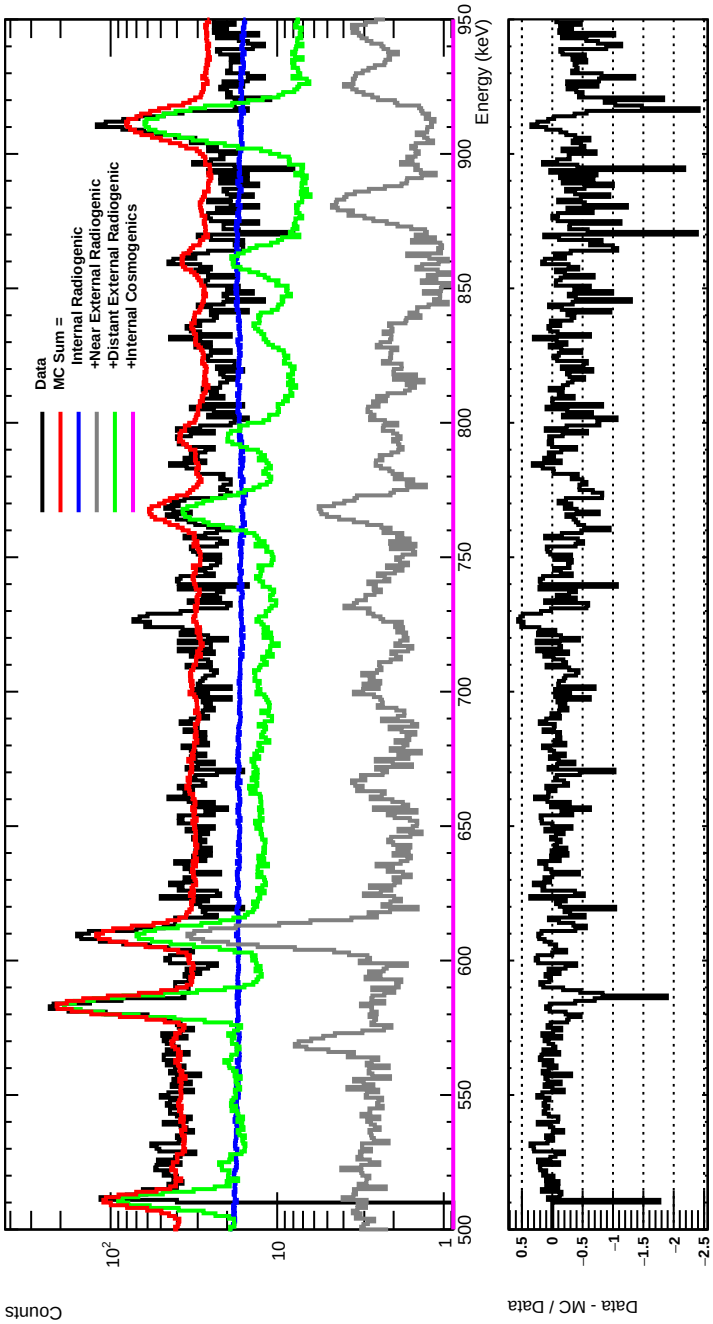

Figure A.89.: Top panel: individual background components and their sum compared to the medium energy reference data set between 500 keV and 950 keV. Bottom panel: relative residual between simulation and data.

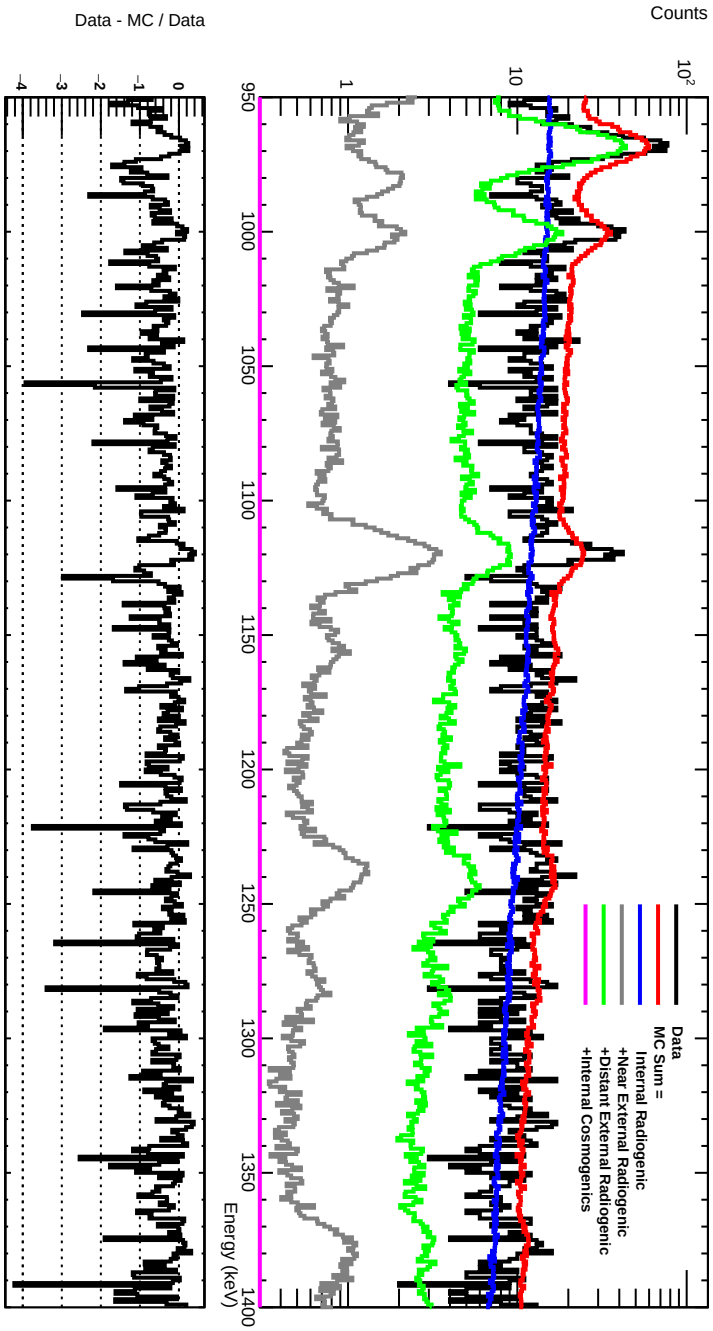

Figure A.90.: Top panel: individual background components and their sum compared to the medium energy reference data set between 950 keV and 1400 keV. Bottom panel: relative residual between simulation and data.

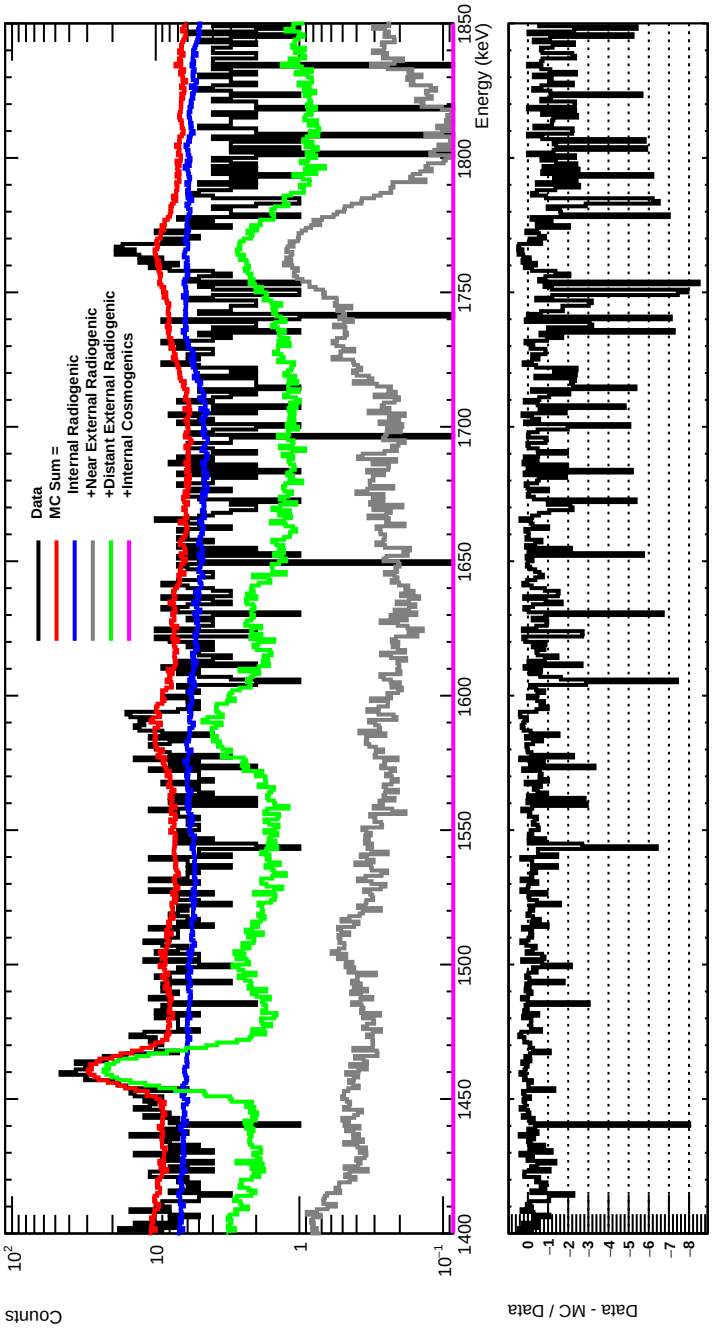

Figure A.91.: Top panel: individual background components and their sum compared to the medium energy reference data set between 1400 keV and 1850 keV. Bottom panel: relative residual between simulation and data.

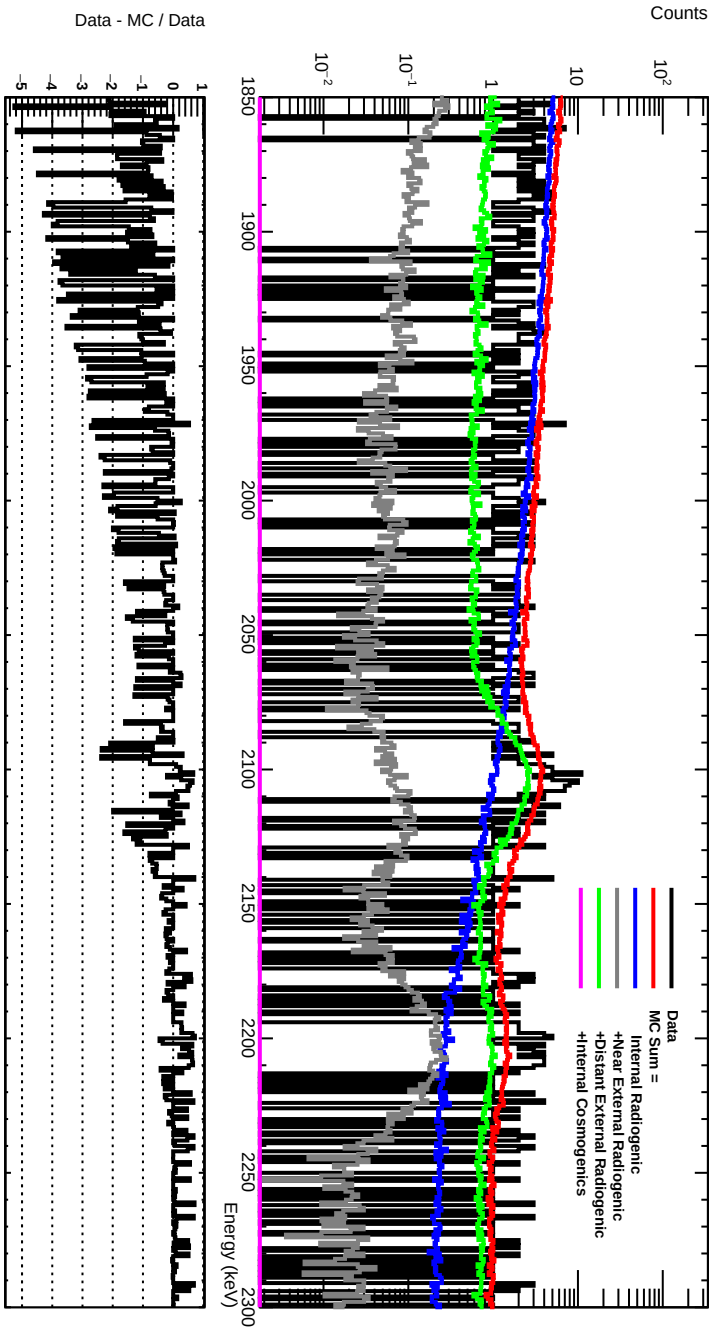

Figure A.92.: Top panel: individual background components and their sum compared to the medium energy reference data set between 1850 keV and 2300 keV. Bottom panel: relative residual between simulation and data.

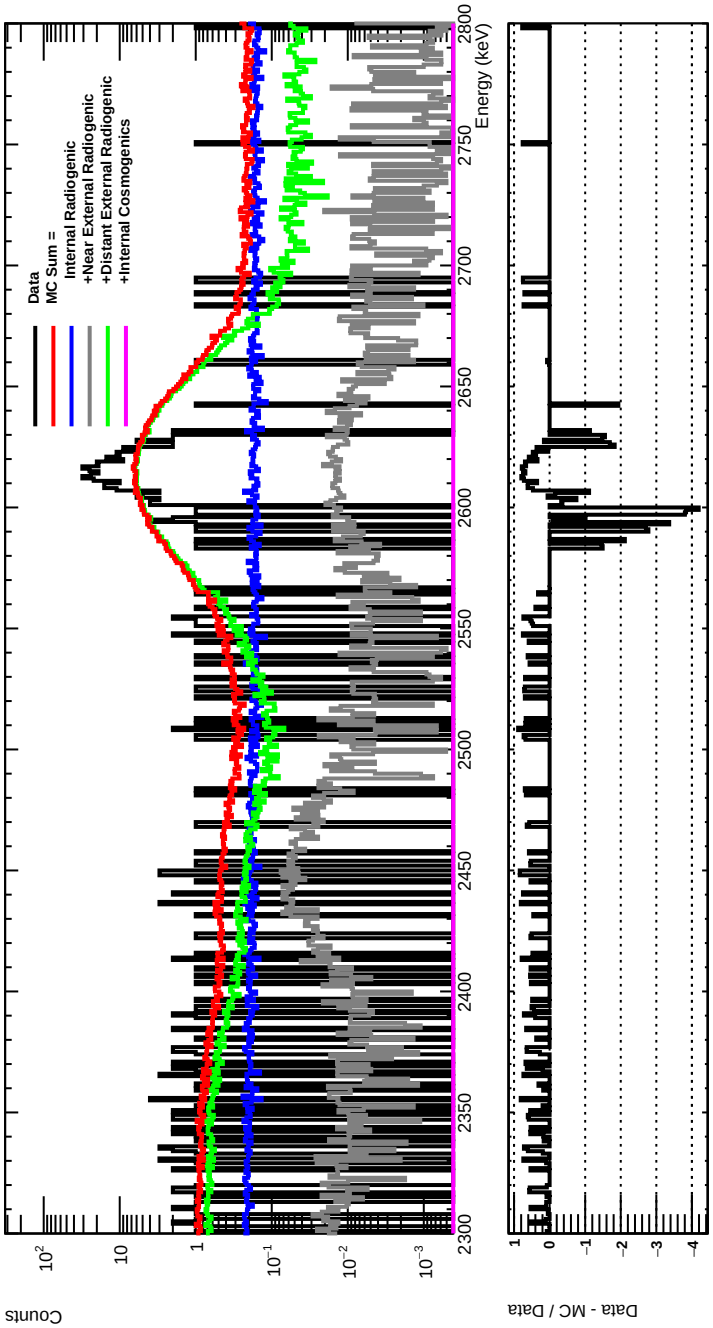

Figure A.93.: Top panel: individual background components and their sum compared to the medium energy reference data set between 2300 keV and 2800 keV. Bottom panel: relative residual between simulation and data.

A.8. Natural Decay Chains

In this part, the natural decay chains observed in the TUM40 data are given. The colours indicate the following:

- **Red:** Shows the nuclides decaying through the release of an alpha-particle.
- **Blue:** Shows the nuclides decaying through the release of a beta-particle.
- **Red/Blue:** Shows the nuclides decaying through the release of either an alpha-particle or a beta-particle. The corresponding branching ratios are given in tables 5.1 to 5.3.
- **Grey:** Shows the nuclides that are radioactively stable.

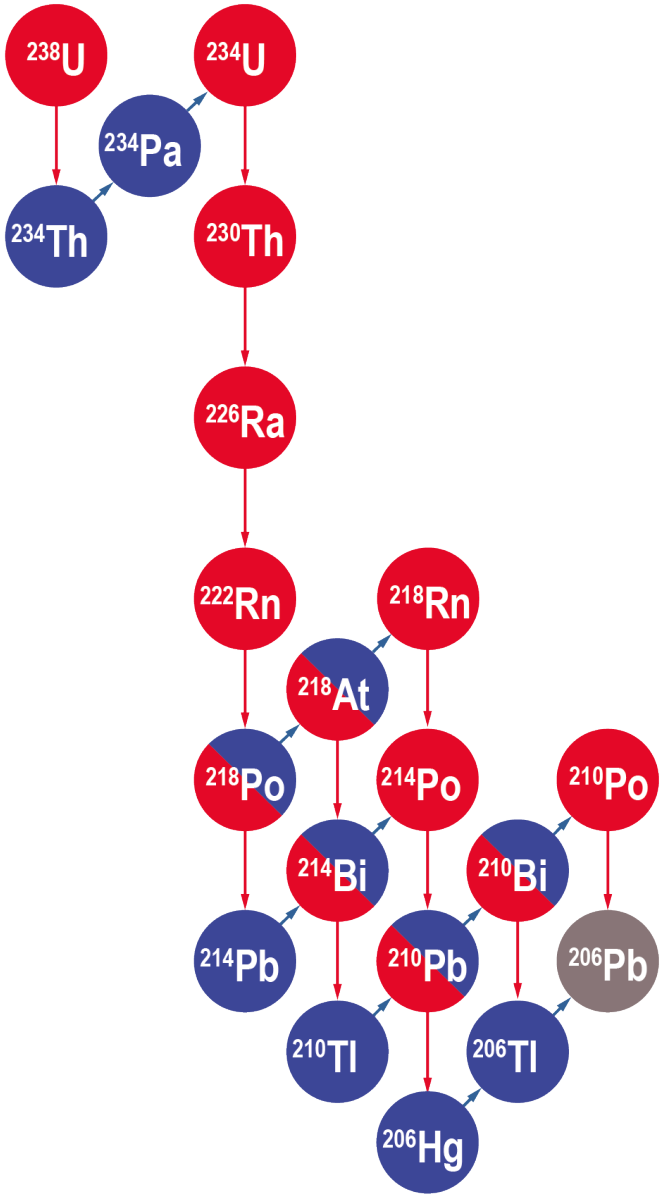

Figure A.94.: ^{238}U natural decay chain. Figure provided by [77].

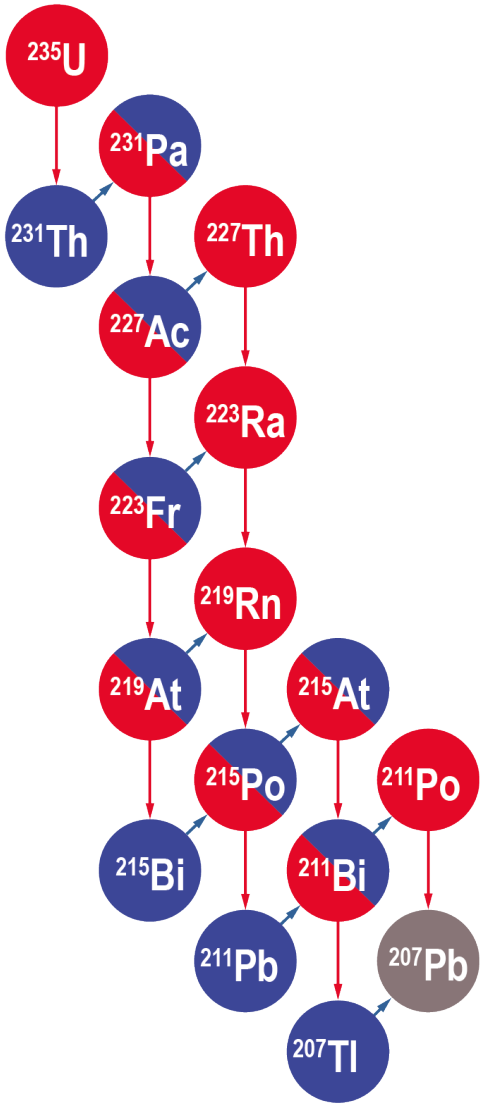

Figure A.95.: ^{235}U natural decay chain. Figure provided by [77].

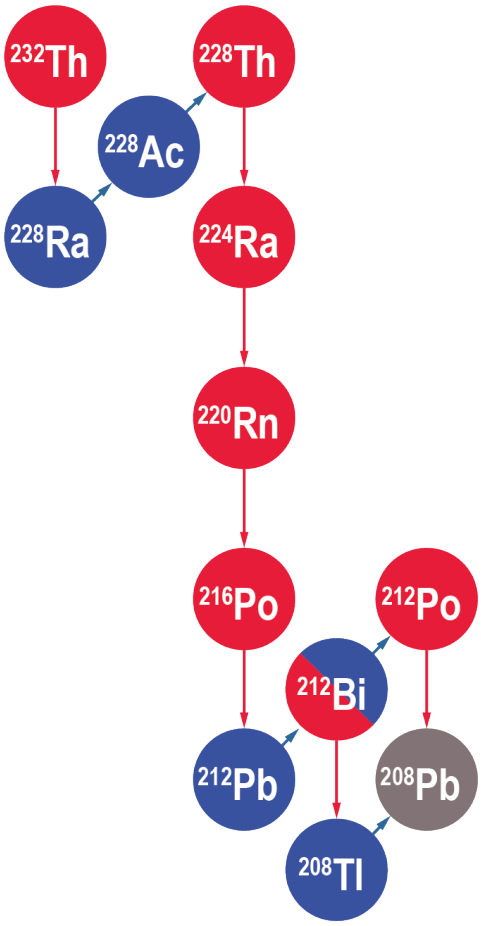

Figure A.96.: ^{232}Th natural decay chain. Figure provided by [77].

Bibliography

[1] C. E. Aalseth et al. "CoGeNT: A Search for Low-Mass Dark Matter using p-type Point Contact Germanium Detectors". In: *Phys. Rev.* D88 (2013), p. 012002. DOI: 10.1103/PhysRevD.88.012002. arXiv: 1208.5737 [astro-ph.CO].

[2] M. G. Aartsen et al. "Search for annihilating dark matter in the Sun with 3 years of IceCube data". In: *Eur. Phys. J.* C77.3 (2017), p. 146. DOI: 10.1140/epjc/s10052-017-4689-9. arXiv: 1612.05949 [astro-ph.HE].

[3] M. Ackermann et al. "Fermi LAT Search for Dark Matter in Gamma-ray Lines and the Inclusive Photon Spectrum". In: *Phys. Rev.* D86 (2012), p. 022002. DOI: 10.1103/PhysRevD.86.022002. arXiv: 1205.2739 [astro-ph.HE].

[4] P. A. R. Ade et al. "Planck 2013 results. XVI. Cosmological parameters". In: *Astron. Astrophys.* 571 (2014), A16. DOI: 10.1051/0004-6361/201321591. arXiv: 1303.5076 [astro-ph.CO].

[5] P. Adhikari et al. "Background model for the NaI(Tl) crystals in COSINE-100". In: *Eur. Phys. J.* C78 (2018), p. 490. DOI: 10.1140/epjc/s10052-018-5970-2. arXiv: 1804.05167 [astro-ph.IM].

[6] N. Aghanim et al. "Planck 2015 results. XI. CMB power spectra, likelihoods, and robustness of parameters". In: *Astron. Astrophys.* 594 (2016), A11. DOI: 10.1051/0004-6361/201526926. arXiv: 1507.02704 [astro-ph.CO].

[7] P. Agnes et al. "First Results from the DarkSide-50 Dark Matter Experiment at Laboratori Nazionali del Gran Sasso". In: *Phys. Lett.* B743 (2015), pp. 456–466. DOI: 10.1016/j.physletb.2015.03.012. arXiv: 1410.0653 [astro-ph.CO].

[8] P. Agnes et al. "Low-Mass Dark Matter Search with the DarkSide-50 Experiment". In: (2018). arXiv: 1802.06994 [astro-ph.HE].

[9] R. Agnese et al. "New Results from the Search for Low-Mass Weakly Interacting Massive Particles with the CDMS Low Ionization Threshold Experiment". In: *Phys. Rev. Lett.* 116.7 (2016), p. 071301. DOI: 10.1103/PhysRevLett.116.071301. arXiv: 1509.02448 [astro-ph.CO].

[10] R. Agnese et al. "Search for Low-Mass Weakly Interacting Massive Particles Using Voltage-Assisted Calorimetric Ionization Detection in the SuperCDMS Experiment". In: *Phys. Rev. Lett.* 112.4 (2014), p. 041302. DOI: 10.1103/PhysRevLett.112.041302. arXiv: 1309.3259 [physics.ins-det].

[11] R. Agnese et al. "Search for Low-Mass Weakly Interacting Massive Particles with SuperCDMS". In: *Phys. Rev. Lett.* 112.24 (2014), p. 241302. DOI: 10.1103/PhysRevLett.112.241302. arXiv: 1402.7137 [hep-ex].

[12] S. Agostinelli et al. "GEANT4: A Simulation toolkit". In: *Nucl. Instrum. Meth.* A506 (2003), pp. 250–303. DOI: 10.1016/S0168-9002(03)01368-8.

[13] A. Aguilar-Arevalo et al. "Search for low-mass WIMPs in a 0.6 kg day exposure of the DAMIC experiment at SNOLAB". In: *Phys. Rev. D* 94 (8 2016), p. 082006. DOI: 10.1103/PhysRevD.94.082006.

[14] D. S. Akerib et al. "Results from a search for dark matter in the complete LUX exposure". In: *Phys. Rev. Lett.* 118.2 (2017), p. 021303. DOI: 10.1103/PhysRevLett.118.021303. arXiv: 1608.07648 [astro-ph.CO].

[15] C. Alduino et al. "CUORE-0 detector: design, construction and operation". In: *JINST* 11.07 (2016), P07009. DOI: 10.1088/1748-0221/11/07/P07009. arXiv: 1604.05465 [physics.ins-det].

[16] C. Alduino et al. "The projected background for the CUORE experiment". In: *Eur. Phys. J.* C77.8 (2017), p. 543. DOI: 10.1140/epjc/s10052-017-5080-6. arXiv: 1704.08970 [physics.ins-det].

[17] J. Allison et al. "Recent developments in GEANT4". In: *Nucl. Instrum. Meth.* A835 (2016), pp. 186–225. DOI: 10.1016/j.nima.2016.06.125.

[18] J. Allison et al. "Geant4 developments and applications". In: *IEEE Trans. Nucl. Sci.* 53 (2006), p. 270. DOI: 10.1109/TNS.2006.869826.

[19] P. .-.-A. Amaudruz et al. "First results from the DEAP-3600 dark matter search with argon at SNOLAB". In: (2017). arXiv: 1707.08042 [astro-ph.CO].

[20] M. Ambrosio et al. "Vertical muon intensity measured with MACRO at the Gran Sasso Laboratory". In: *Phys. Rev.* D52 (1995), pp. 3793–3802. DOI: 10.1103/PhysRevD.52.3793.

[21] C. Amole et al. "Dark Matter Search Results from the PICO-60 C_3F_8 Bubble Chamber". In: *Phys. Rev. Lett.* 118.25 (2017), p. 251301. DOI: 10.1103/PhysRevLett.118.251301. arXiv: 1702.07666 [astro-ph.CO].

[22] G. Angloher et al. "Commissioning Run of the CRESST-II Dark Matter Search". In: *Astropart. Phys.* 31 (2009), pp. 270–276. DOI: 10.1016/j.astropartphys.2009.02.007. arXiv: 0809.1829 [astro-ph].

[23] G. Angloher et al. "Limits on WIMP dark matter using sapphire cryogenic detectors". In: *Astropart. Phys.* 18 (2002), pp. 43–55. DOI: 10.1016/S0927-6505(02)00111-1.

[24] G. Angloher et al. "Probing low WIMP masses with the next generation of CRESST detector". In: (2015). arXiv: 1503.08065 [astro-ph.IM].

[25] G. Angloher et al. "Results on light dark matter particles with a low-threshold CRESST-II detector". In: *Eur. Phys. J.* C76.1 (2016), p. 25. DOI: 10.1140/epjc/s10052-016-3877-3. arXiv: 1509.01515 [astro-ph.CO].

[26] G. Angloher et al. "Results on low mass WIMPs using an upgraded CRESST-II detector". In: *Eur. Phys. J.* C74.12 (2014), p. 3184. DOI: 10.1140/epjc/s10052-014-3184-9. arXiv: 1407.3146 [astro-ph.CO].

[27] G. Angloher et al. "Results from 730 kg days of the CRESST-II Dark Matter search". In: *Eur. Phys. J.* C72.4 (2012), p. 1971. ISSN: 1434-6052. DOI: 10.1140/epjc/s10052-012-1971-8.

[28] E. Aprile et al. "Dark Matter Search Results from a One Tonne×Year Exposure of XENON1T". In: (2018). arXiv: 1805.12562 [astro-ph.CO].

[29] E. Aprile et al. "First Dark Matter Search Results from the XENON1T Experiment". In: *Phys. Rev. Lett.* 119.18 (2017), p. 181301. DOI: 10.1103/PhysRevLett.119.181301. arXiv: 1705.06655 [astro-ph.CO].

[30] E. Aprile et al. "Low-mass dark matter search using ionization signals in XENON100". In: *Phys. Rev. D* 94 (9 2016), p. 092001. DOI: 10.1103/PhysRevD.94.092001.

[31] E. Aprile et al. "Material screening and selection for XENON100". In: *Astropart. Phys.* 35.2 (2011), pp. 43–49. ISSN: 0927-6505. DOI: 10.1016/j.astropartphys.2011.06.001.

[32] E. Armengaud et al. "Constraints on low-mass WIMPs from the EDELWEISS-III dark matter search". In: *JCAP* 1605.05 (2016), p. 019. DOI: 10.1088/1475-7516/2016/05/019. arXiv: 1603.05120 [astro-ph.CO].

[33] Q. Arnaud et al. "First results from the NEWS-G direct dark matter search experiment at the LSM". In: *Astropart. Phys.* 97 (2018), pp. 54–62. DOI: 10.1016/j.astropartphys.2017.10.009. arXiv: 1706.04934 [astro-ph.IM].

[34] C. Arpesella. "Background measurements at Gran Sasso Laboratory". In: *Nucl. Phys. B - Proc. Suppl.* 28.1 (1992), pp. 420–424. ISSN: 0920-5632. DOI: 10.1016/0920-5632(92)90207-9.

[35] J. J. Back and Y. A. Ramachers. "ACTIVIA: Calculation of Isotope Production Cross-sections and Yields". In: *Nucl. Instrum. Meth.* A586 (2008), pp. 286–294. DOI: 10.1016/j.nima.2007.12.008. arXiv: 0709.3472 [nucl-ex].

[36] H. Baer et al. "Dark matter production in the early Universe: beyond the thermal WIMP paradigm". In: *Phys. Rept.* 555 (2015), pp. 1–60. DOI: 10.1016/j.physrep.2014.10.002. arXiv: 1407.0017 [hep-ph].

[37] P. Bauer. private communication. 2017.

[38] P. Belli et al. "Deep Underground Neutron Flux Measurement With Large Bf-3 Counters". In: *Nuovo Cim.* A101 (1989), pp. 959–966. DOI: 10.1007/BF02800162.

[39] C. L. Bennett et al. "Nine-Year Wilkinson Microwave Anisotropy Probe (WMAP) Observations: Final Maps and Results". In: *Astrophys. J. Suppl.* 208 (2013), p. 20. DOI: 10.1088/0067-0049/208/2/20. arXiv: 1212.5225 [astro-ph.CO].

[40] M. J. Berger et al. "Report 37". In: *Journal of the International Commission on Radiation Units and Measurements* os19.2 (1984), NP. DOI: 10.1093/jicru/os19.2.Report37.

[41] R. Bernabei et al. "First model independent results from DAMA/LIBRA-phase2". In: (2018). arXiv: 1805.10486 [hep-ex].

[42] R. Bernabei et al. "Final model independent results of DAMA/LIBRA-phase1 and perspectives of phase2". In: *Phys. Part. Nucl.* 46.2 (2015), pp. 138–146. ISSN: 1531-8559. DOI: 10.1134/S1063779615020045.

[43] G. Bertone, ed. *Particle Dark Matter: Observations, Models and Searches*. Cambridge: Cambridge Univ. Press, 2010. ISBN: 9781107653924. DOI: 10.1017/CBO9780511770739.

[44] N. W. Boggess et al. "The COBE mission - Its design and performance two years after launch". In: *Astrophys. J.* 397 (1992), pp. 420–429. DOI: 10.1086/171797.

[45] S. M. Boucenna and S. Morisi. "Theories relating baryon asymmetry and dark matter: A mini review". In: *Front.in Phys.* 1 (2014), p. 33. DOI: 10.3389/fphy.2013.00033. arXiv: 1310.1904 [hep-ph].

[46] T. Bringmann et al. "Fermi LAT Search for Internal Bremsstrahlung Signatures from Dark Matter Annihilation". In: *JCAP* 1207 (2012), p. 054. DOI: 10.1088/1475-7516/2012/07/054. arXiv: 1203.1312 [hep-ph].

[47] A. Brown et al. "Extending the CRESST-II commissioning run limits to lower masses". In: *Phys. Rev.* D85 (2012), p. 021301. DOI: 10.1103/PhysRevD.85.021301. arXiv: 1109.2589 [astro-ph.CO].

[48] S. Cebrián. "Cosmogenic activation of materials". In: *Int. J. Mod. Phys.* A32.30 (2017), p. 1743006. DOI: 10.1142/S0217751X17430060. arXiv: 1708.07449 [nucl-ex].

[49] G. Chabrier and D. Mera. "Determination of the globular cluster and halo stellar mass functions and stellar and brown dwarf densities". In: *Astron. Astrophys.* 328 (1997), p. 83. arXiv: astro-ph/9705065 [astro-ph].

[50] D. Clowe et al. "A direct empirical proof of the existence of dark matter". In: *Astrophys. J.* 648 (2006), pp. L109–L113. DOI: 10.1086/508162. arXiv: astro-ph/0608407 [astro-ph].

[51] G. Cowan. *Statistical Data Analysis*. New York: Oxford University Press, 1998. ISBN: 9780198501558. DOI: 10.1017/CBO9780511770739.

[52] CRESST Collaboration. Accessed: 12.04.2018. URL: https://cresst.de/.

[53] *Dilution refrigerator*. Accessed: 28.02.2018. URL: https://en.wikipedia.org/w/index.php?title=Dilution_refrigerator&oldid=795823283.

[54] J. Ellis and K. A. Olive. *Supersymmetric Dark Matter Candidates*. 2010, pp. 142–163. arXiv: 1001.3651 [astro-ph.CO].

[55] A. Erb and J.-C. Lanfranchi. "Growth of high-purity scintillating CaWO4 single crystals for the low-temperature direct dark matter search experiments CRESST-II and EURECA". In: *Cryst. Eng. Comm.* 15 (12 2013), pp. 2301–2304. DOI: 10.1039/C2CE26554K.

[56] R. B. Firestone. *Table of Isotopes*. Wiley-VCH, 1999. ISBN: 978-0471356332.

[57] K. Freese. "Review of Observational Evidence for Dark Matter in the Universe and in upcoming searches for Dark Stars". In: *EAS Publ. Ser.* 36 (2009), pp. 113–126. DOI: 10.1051/eas/0936016. arXiv: 0812.4005 [astro-ph].

[58] Geant4 Collaboration. *Geant4 A Simulation Toolkit: Physics Reference Manual*. Accessed: 23.03.2018. 2017. URL: http://geant4.web.cern.ch/geant4/UserDocumentation/UsersGuides/PhysicsReferenceManual/fo/PhysicsReferenceManual.pdf.

[59] Geant4 Collaboration. *Hypernews Forum*. Accessed: 22.06.2018. URL: http://hypernews.slac.stanford.edu/HyperNews/geant4/get/hadronprocess/1538/1.html.

[60] Geant4 Collaboration. *Low Energy Electromagnetic Physics Working Group*. Accessed: 05.06.2018. URL: https://new-geant4-dev.web.cern.ch/node/1615.

[61] J. Goodman et al. "Constraints on Dark Matter from Colliders". In: *Phys. Rev.* D82 (2010), p. 116010. DOI: 10.1103/PhysRevD.82.116010. arXiv: 1008.1783 [hep-ph].

[62] P. Gorla. private communication. 2015.

[63] D. S. Graff and K. Freese. "Analysis of a hubble space telescope search for red dwarfs: limits on baryonic matter in the galactic halo". In: *Astrophys. J.* 456 (1996), p. L49. DOI: 10.1086/309850. arXiv: astro-ph/9507097 [astro-ph].

[64] K. Griest. "Galactic Microlensing as a Method of Detecting Massive Compact Halo Objects". In: *Astrophys. J.* 366 (1991), pp. 412–421. DOI: 10.1086/169575.

[65] K. Griest. "The Search for dark matter: WIMPs and MACHOs". In: *Annals of the New York Academy of Sciences* 688.1 (1993), pp. 390–407. DOI: 10.1111/j.1749-6632.1993.tb43912.x. arXiv: hep-ph/9303253 [hep-ph].

[66] G. Grosso and G. P. Parravicini, eds. *Solid State Physics*. Second Edition. Amsterdam: Academic Press, 2014, pp. 391–436. ISBN: 978-0-12-385030-0. DOI: https://doi.org/10.1016/B978-0-12-385030-0.00009-8.

[67] A. Gütlein et al. "Impact of coherent neutrino nucleus scattering on direct dark matter searches based on $CaWO_4$ crystals". In: *Astropart. Phys.* 69 (2015), pp. 44–49. DOI: 10.1016/j.astropartphys.2015.03.010. arXiv: 1408.2357 [hep-ph].

[68] M. Haffke et al. "Background measurements in the Gran Sasso Underground Laboratory". In: *Nucl. Instrum. Meth.* A643.1 (2011), pp. 36–41. ISSN: 0168-9002. DOI: https://doi.org/10.1016/j.nima.2011.04.027.

[69] International Atomic Energy Agency. *Nuclear Data Services*. Accessed: 27.04.2018. URL: https://www-nds.iaea.org/.

[70] I. Jaegle. "Search for the 'Dark Photon' and the 'Dark Higgs' at Belle". In: *Nucl. Phys. Proc. Suppl.* 234 (2013), pp. 33–36. DOI: 10.1016/j.nuclphysbps.2012.11.008. arXiv: 1211.1403 [hep-ex].

[71] D. Javorsek et al. "New Experimental Limits on Strongly Interacting Massive Particles at the TeV Scale". In: *Phys. Rev. Lett.* 87 (23 2001), p. 231804. DOI: 10.1103/PhysRevLett.87.231804.

[72] G. Jungman, M. Kamionkowski, and K. Griest. "Supersymmetric dark matter". In: *Phys. Rept.* 267 (1996), pp. 195–373. DOI: 10.1016/0370-1573(95)00058-5. arXiv: hep-ph/9506380 [hep-ph].

[73] F. Kahlhoefer. "Review of LHC Dark Matter Searches". In: *Int. J. Mod. Phys.* A32.13 (2017), p. 1730006. DOI: 10.1142/S0217751X1730006X. arXiv: 1702.02430 [hep-ph].

[74] M. Kamionkowski. "WIMP and axion dark matter". In: *High-energy physics and cosmology. Proceedings, Summer School, Trieste, Italy, June 2-July 4, 1997*. 1997, pp. 394–411. arXiv: hep-ph/9710467 [hep-ph].

[75] D. B. Kaplan. "A Single explanation for both the baryon and dark matter densities". In: *Phys. Rev. Lett.* 68 (1992), pp. 741–743. DOI: 10.1103/PhysRevLett.68.741.

[76] M. Kiefer. "Improving the Light Channel of the CRESST-II Dark Matter Detectors". PhD Thesis. Technische Universität München, 2012.

[77] H. Kluck. private communication. 2018.

[78] A. J. Koning, S. Hilaire, and M. C. Duijvestijn. "TALYS: Comprehensive Nuclear Reaction Modeling". In: *AIP Conf. Proc.* 769.1 (2005), pp. 1154–1159. DOI: 10.1063/1.1945212. eprint: https://aip.scitation.org/doi/pdf/10.1063/1.1945212.

[79] M. F. L'Annunziata, ed. *Handbook of Radioactivity Analysis*. Third Edition. Amsterdam: Academic Press, 2012. ISBN: 978-0-12-384873-4. DOI: 10.1016/B978-0-12-384873-4.05001-5.

[80] R. Lang et al. "Electron and gamma background in CRESST detectors". In: *Astropart. Phys.* 32.6 (2010), pp. 318–324. ISSN: 0927-6505. DOI: 10.1016/j.astropartphys.2009.09.009.

[81] R. F. Lang. "Search for Dark Matter with the CRESST Experiment". PhD Thesis. Technische Universität München, 2008.

[82] J. Lewin and P. Smith. "Review of mathematics, numerical factors, and corrections for dark matter experiments based on elastic nuclear recoil". In: *Astropart. Phys.* 6.1 (1996), pp. 87–112. ISSN: 0927-6505. DOI: 10.1016/S0927-6505(96)00047-3.

[83] M. Mancuso et al. "A method to define the energy threshold depending on noise level for rare event searches". In: (2017). arXiv: 1711.11459 [physics.ins-det].

[84] T. Marrodán Undagoitia and L. Rauch. "Dark matter direct-detection experiments". In: *J. Phys.* G43.1 (2016), p. 013001. DOI: 10.1088/0954-3899/43/1/013001. arXiv: 1509.08767 [physics.ins-det].

[85] D. Mei and A. Hime. "Muon-induced background study for underground laboratories". In: *Phys. Rev.* D73 (2006), p. 053004. DOI: 10.1103/PhysRevD.73.053004. arXiv: astro-ph/0512125 [astro-ph].

[86] O. Meier et al. "Active thermal feedback for massive cryogenic detectors". In: *Nucl. Instrum. Meth.* A444 (2000), pp. 350–352. DOI: 10.1016/S0168-9002(99)01390-X.

[87] M. Milgrom. "A modification of the Newtonian dynamics as a possible alternative to the hidden mass hypothesis". In: *Astrophys. J.* 270 (1983), pp. 365–370. DOI: 10.1086/161130.

[88] V. A. Mitsou. "Overview of searches for dark matter at the LHC". In: *J. Phys. Conf. Ser.* 651.1 (2015), p. 012023. DOI: 10.1088/1742-6596/651/1/012023. arXiv: 1402.3673 [hep-ex].

[89] A. Münster et al. "Radiopurity of CaWO4 crystals for direct dark matter search with CRESST and EURECA". In: *JCAP* 1405 (2014), p. 018. DOI: 10.1088/1475-7516/2014/05/018. arXiv: 1403.5114 [astro-ph.IM].

[90] A. R. Münster. private communication. 2017.

[91] A. R. Münster. "High-Purity $CaWO_4$ Single Crystals for Direct Dark Matter Search with the CRESST Experiment". PhD Thesis. Technische Universität München, 2017.

[92] National Institute of Standards and Technology (NIST). *Screened Relativistic Nuclear Stopping Power Calculator*. Accessed: 18.05.2018. URL: http://www.srniel.org/index.php/protons-ions-nuclear-stopping-power-calculator.

[93] A. A. Penzias and R. W. Wilson. "A Measurement of excess antenna temperature at 4080-Mc/s". In: *Astrophys. J.* 142 (1965), pp. 419–421. DOI: 10.1086/148307.

[94] K. Petraki and R. R. Volkas. "Review of asymmetric dark matter". In: *Int. J. Mod. Phys.* A28 (2013), p. 1330028. DOI: 10.1142/S0217751X13300287. arXiv: 1305.4939 [hep-ph].

[95] F. Petricca et al. "First results on low-mass dark matter from the CRESST-III experiment". In: *15th International Conference on Topics in Astroparticle and Underground Physics (TAUP 2017) Sudbury, Ontario, Canada, July 24-28, 2017*. 2017. arXiv: 1711.07692 [astro-ph.CO].

[96] F. Pobell. *Matter and Methods at Low Temperatures*. Springer, Berlin, Heidelberg, 2007. ISBN: 978-3-540-46360-3. DOI: 10.1007/978-3-540-46360-3.

[97] F. Reindl. private communication. 2017.

[98] F. Reindl. "Exploring Light Dark Matter With CRESST-II Low-Threshold Detectors". PhD Thesis. Technische Universität München, 2016.

[99] V. C. Rubin, N. Thonnard, and W. K. Ford Jr. "Rotational properties of 21 SC galaxies with a large range of luminosities and radii, from NGC 4605 /R = 4kpc/ to UGC 2885 /R = 122 kpc/". In: *Astrophys. J.* 238 (1980), p. 471. DOI: 10.1086/158003.

[100] V. C. Rubin and W. K. Ford Jr. "Rotation of the Andromeda Nebula from a Spectroscopic Survey of Emission Regions". In: *Astrophys. J.* 159 (1970), pp. 379–403. DOI: 10.1086/150317.

[101] J. Schmaler. "The CRESST Dark Matter Search – New Analysis Methods and Recent Results". PhD thesis. Technische Universität München, 2010.

[102] Y. Sofue, M. Honma, and T. Omodaka. "Unified Rotation Curve of the Galaxy – Decomposition into de Vaucouleurs Bulge, Disk, Dark Halo, and the 9-kpc Rotation Dip –". In: *Publ. Astron. Soc. Jap.* 61 (2009), p. 227. DOI: 10.1093/pasj/61.2.227. arXiv: 0811.0859 [astro-ph].

[103] Y. Sofue. "Pseudo Rotation Curve Connecting the Galaxy, Dark Halo, and Local Group". In: *Publications of the Astronomical Society of Japan* 61.2 (2009), pp. 153–161. DOI: 10.1093/pasj/61.2.153. eprint: /oup/backfile/content_public/journal/pasj/61/2/10.1093_pasj_61.2.153/4/pasj61-0153.pdf.

[104] R. Strauss et al. "A detector module with highly efficient surface-alpha event rejection operated in CRESST-II Phase 2". In: *Eur. Phys. J.* C75.8 (2015), p. 352. DOI: 10.1140/epjc/s10052-015-3572-9. arXiv: 1410.1753 [physics.ins-det].

[105] R. Strauss et al. "Beta/gamma and alpha backgrounds in CRESST-II Phase 2". In: *JCAP* 1506.06 (2015), p. 030. DOI: 10.1088/1475-7516/2015/06/030. arXiv: 1410.4188 [physics.ins-det].

[106] R. Strauss et al. "Gram-scale cryogenic calorimeters for rare-event searches". In: *Phys. Rev.* D96.2 (2017), p. 022009. DOI: 10.1103/PhysRevD.96.022009. arXiv: 1704.04317 [physics.ins-det].

[107] A. Tan et al. "Dark Matter Results from First 98.7 Days of Data from the PandaX-II Experiment". In: *Phys. Rev. Lett.* 117 (12 2016), p. 121303. DOI: 10.1103/PhysRevLett.117.121303.

[108] S. C. C. Ting. *New Results from the Alpha Magnetic Spectrometer on the International Space Station*. 2014.

[109] J. Tuli. "Evaluated nuclear structure data file". In: *Nuclear Instruments and Methods in Physics Research Section A: Accelerators, Spectrometers, Detectors and Associated Equipment* 369.2 (1996), pp. 506–510. DOI: 10.1016/S0168-9002(96)80040-4.

[110] H. Uchida et al. "Search for inelastic WIMP nucleus scattering on ^{129}Xe in data from the XMASS-I experiment". In: *PTEP* 2014.6 (2014), p. 063C01. DOI: 10.1093/ptep/ptu064. arXiv: 1401.4737 [astro-ph.CO].

[111] Q. Yue et al. "Limits on light weakly interacting massive particles from the CDEX-1 experiment with a p-type point-contact germanium detector at the China Jinping Underground Laboratory". In: *Phys. Rev. D* 90 (9 2014), p. 091701. DOI: 10.1103/PhysRevD.90.091701.

[112] C. Zhang et al. "Cosmogenic Activation of Materials Used in Rare Event Search Experiments". In: *Astropart. Phys.* 84 (2016), pp. 62–69. DOI: 10.1016/j.astropartphys.2016.08.008. arXiv: 1603.00098 [physics.ins-det].

[113] J. F. Ziegler. *SRIM - The Stopping and Range of Ions in Matter*. Accessed: 18.06.2018. URL: http://www.srim.org/.

[114] K. M. Zurek. "Asymmetric Dark Matter: Theories, Signatures, and Constraints". In: *Phys. Rept.* 537 (2014), pp. 91–121. DOI: 10.1016/j.physrep.2013.12.001. arXiv: 1308.0338 [hep-ph].

[115] F. Zwicky. "Die Rotverschiebung von extragalaktischen Nebeln". In: *Helvetica Physica Acta* 6 (1933), pp. 110–127.

[116] F. Zwicky. "On the Masses of Nebulae and of Clusters of Nebulae". In: *Astrophys. J.* 86 (1937), pp. 217–246. DOI: 10.1086/143864.